Crystal Structure Studies of Low-Melting Point Organic Compounds At Low Temperature and High Pressure

Pamela A. McGregor

A thesis submitted in fulfillment of the requirements
for the degree of Doctor of Philosophy to the
School of Physics
University of Edinburgh

October 2003

Acknowledgements

My supervisors: Dr. David R. Allan, Dr. Simon Parsons and Dr. Colin R. Pulham. Firstly for help, encouragement and guidance throughout my PhD, teaching me all I need to know about high-pressure diffraction techniques and crystallography. Generally for supporting me through my PhD – you guys are the best! Thank you!

Dr. Stewart J. Clark and Mr. Iain McLeod for *ab-initio* calculations. Dr. Simon Teat for his assistance on beamline 9.8 at Daresbury. Dr. Malcolm I. McMahon for the upkeep of the ruby kit and allowing use of his diffractometer for various data collections. Mr Jim King for help and advice on safety issues and Mr Ronnie Proc for his help with various cell problems – usually of the stuck cell variety! Mr Steven Duffield for computer help.

To all my friends and colleagues in the High Pressure Physics Group and the Edinburgh University Chemical Crystallography Group – especially Mrs Alice Dawson for companionship in the lab and on beamtime and of course our shared love of crystal growing music! To Steve, Andy, Scott, Thiti, Olga, Bob, Iain, James, Francesca, Patty, Stephen. To Lyn in 5202, especially for our poster incidents!

To my longest serving flatmate Louisa. To my Edinburgh friends, Anna and family, Al, Judith, Tiina, Lissa and Kim fae the block and all the rest at Hutchy Vale Ladies. To ex-Edinburgh Uni football friends – Wendy, Nat, Lou, Gubstar, Gayle, Jen, Crystal, Holly, Karen. Past and Present non-football Uni friends – Linette (I'm never wearing that dress again), Lorna, Tina, Angela, Annela, Helen, Mary, Joh. My old school friends Vicki, Nicola, Lorraine. You've all been rocks – the best friends anyone could have hoped for. Cheers!

My family. To Louise. To Linda and Graham. To all Aunts, Uncles and cousins – McGregor and McKay, and Auntie Pearl – too many to mention. The last three years have been so hard, but we've pulled each other through. Finally, to my late parents who supported me, encouraged me and loved me no matter what. This work is dedicated to them: Stuart Maitland McGregor (1942 – 2001) and Margaret McGregor (1944 – 2001).

Gone but never forgotten – this is for you.

Abstract

The application of moderate pressure (0-15 GPa) can cause significant changes in the crystal structures of small molecules. High pressure has become an important tool in science, and is becoming increasingly more important - particularly so in the field of biology. The effect of pressure on molecular materials is not fully understood, in fact, there are very few groups specialising in this particular area of high-pressure research. Differences between low-temperature and the corresponding high-pressure phases have shown a great diversity in molecular packing arrangements, new structural motifs through variations in hydrogen bonding and even molecular conformational changes.

Previous structural analysis of small organic molecules has provided a range of new high-pressure phases of hydrogen bonded systems: low molecular weight mono-alcohols (methanol and ethanol); acetone; and the small carboxylic acids (formic acid and acetic acid). The author has extended these studies to include the mono-alcohols, cyclobutanol and tertiary butanol. The former, cyclobutanol, forms triple helical hydrogen bonded chains with a central hydrogen bonded core at low temperature. The corresponding high pressure phase contains wave-like hydrogen bonded chains where the two molecules in the repeating unit are related by glide symmetry. The latter, tertiary butanol, shows extensive structural diversity in its low temperature phases and one of these was found to be a metastable form of the high-pressure phase. This phase is composed of 6-membered hydrogen bonded rings.

The study of alcohols was further extended to the α-ω di-alcohols [$HO(CH_2)_nOH$]. Ethane-1,2-diol (n=2), propane-1,3-diol (n=3) and pentane-1,5-diol (n=5) have high-pressure phases that are different from their corresponding low-temperature phases. In the case of ethane-diol, not only do we observe major changes in the packing arrangement of the molecules, there is also a primary conformational change in the molecule. Of the three observed phases at high pressures, the *gauche* conformer is found in phases I and II at 1 and 2 GPa

respectively, and the *trans* conformer in phase III at 2.3 GPa. As for ethane-1,2-diol, both propane-1,3-diol and pentane-1,5-diol crystallise in different packing motifs at low-temperature and high-pressure. However, these also exhibit a primary conformational change at high pressure.

A further extension of the study was to include halogenated molecules, and the high-pressure crystal structures of chloroform and bromoform are presented in this thesis. These materials have a rich phase diversity, chloroform showing a centrosymmetric packing arrangement at low temperature, whilst at high pressure, the molecules are arranged non-centrosymmetrically. Bromoform has 3 centrosymmetric phases at low temperature. The high pressure phase of bromoform is polar and has the same non-centrosymmetric space group, $P6_3$, as the high-pressure phase of chloroform.

Contents

Chapter 1

Introduction

1.1 Pressure and Molecular Science

The study of molecules under non-ambient temperatures and pressures is vital for the understanding of materials in the solid state. Many small molecules are gases or liquids under ambient conditions, these solidify at low temperatures or high pressures. Using diffraction techniques at non-ambient conditions to study these molecules in the solid state gives rise to information otherwise unattainable. Variable temperature studies of molecules explore a very limited area of the pressure-temperature phase diagram, extending the pressure range using modern techniques explores a greater area of this and often uncovers new forms of elements, new polymorphs of molecules, and can change the properties of many materials.

Molecular science at extreme conditions ranges from looking at the smallest molecular solids, such as rare gas solids, to macromolecules such as proteins and viruses. Molecules that are gases or liquids under ambient conditions such as hydrogen, helium, water, ammonia, nitrogen, carbon monoxide and carbon dioxide exist as solids under the extremes of temperature and pressure in parts of our Solar System.

The Sun is at the centre of the solar system, containing nine planets. The Earth is the third planet from the Sun and the temperature and pressures inside the Earth reach over 5000 K and 350 GPa. The atmosphere on Earth consists predominantly of nitrogen and oxygen gases and a pressure of approximately 0.1 GPa is reached at the surface. The Earth is one of four terrestrial planets, which also include Mercury, Venus and Mars. In contrast to the Earth's atmosphere, Mercury has almost no atmosphere, the trace amount of gases present are hydrogen and helium. The major component of the atmospheres of both Venus and Mars is carbon dioxide. The conditions on Venus are a pressure of 90 bar at the surface and a temperature of 730 K, while those on Mars are 0.007 bar and 218 K. The terrestrial or rocky planets have similar compositions. The giant planets,

Saturn and Jupiter, account for over 90% of the total mass of all nine planets. Along with Uranus and Neptune, these four planets are the gassy planets, they are composed mainly of hydrogen, helium, ice, ammonia, methane and carbon dioxide.

Some of the planets have satellites, Saturn's largest moon is called Titan and is the only planetary satellite to have a significant atmosphere. The atmosphere consists of nitrogen, methane and other organic molecules. These molecules become trapped inside ice – the clathrates – at elevated pressures. Loveday *et al*[1] have extensively studied the clathrate hydrates of ammonia and methane over a large pressure and temperature range relevant to Titan, the only satellite to have a significant atmosphere. The diffraction technique used for this study was powder neutron diffraction where the Paris-Edinburgh high-pressure cell (figure 1.1) has been developed by the University of Paris 6 and the University of Edinburgh High Pressure Groups to cover a large pressure (0-25 GPa) and temperature (90-350 K) range[2].

Figure 1.1 The Paris-Edinburgh cell for neutron diffraction

There is great interest in the function of macromolecules at high pressures. In the deepest part of the ocean, the Mariana Trench (figure 1.1), the pressure reaches over 1000 atmospheres, in addition to the pressure the environment is pitch dark, acidic, full

of heavy metals and dissolved poisonous gases. Despite this, more than 300 species are found to thrive in the eerie depths of the ocean – among these are types of shrimp, giant crabs and many others. There are also extremophiles in the depths of the Mariana Trench[2], samples recovered have shown that these are related to the *shewanella* family. The *E-coli* and *shewanella* bacteria have both been found to function under extreme conditions[3].

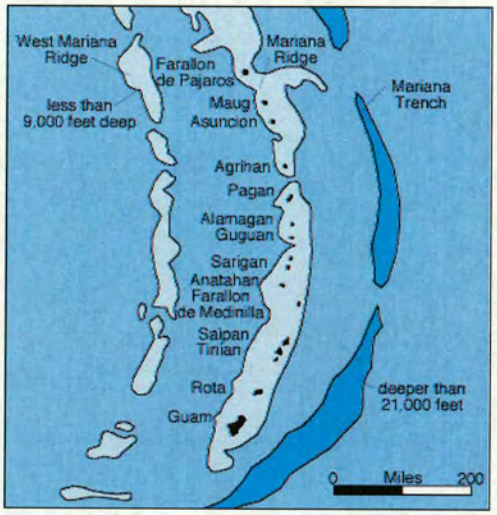

Figure 1.2 A Map of the Mariana Trench

Whilst diving into the depths of the ocean, the pressure increases by 1 atmosphere every 10 m. There are many animals that undergo large changes in pressure in their everyday life, for example the sperm whale takes hour long dives to over 2 km below the surface – a pressure change of over 200 atmospheres.

High pressure is used as a thermodynamic tool to study the mechanics in protein folding. This is of particular use in the pharmaceutical industry, where it is thought that diseases such as Alzheimer's and Parkinson's, possibly even cancer are caused by mistakes in protein folding. The understanding of the mechanism in protein folding will

aid the discovery of ways in the prevention and treatment of these diseases. The application of pressure to a protein causes folding, and it is also possible to stabilise transition states and intermediates using this technique.

Single crystal experiments have been carried out at the ESRF by Fourme *et al*[4], a study of a tetragonal crystal of hen egg-white lysozyme and orthorhombic crystals of bovine erythrocyte. It was possible to study these systems to 0.7 GPa with 2 Å resolution. Single crystal experiments are in the early stages of development, the low completeness of the data due to the x-ray absorbing steel body of the diamond anvil cell restricting this. Other experimental techniques are used such as NMR and other spectroscopic techniques.

Food processing is the means of packaging and preserving a food product from the raw material to a condition that is suitable for the consumer. All food preservation techniques have the main target of the prevention of spoilage which is mostly caused by the growth of microbes that thrive at room temperature, neutral pH, and require water and oxygen to grow. Traditional methods of food processing change these conditions, these are freezing, changing the acidity, drying and anaerobic packaging. Many of these traditional treatments can have an adverse effect on the food quality in terms of texture, taste and colour. High pressure food processing – utilised in many countries – is a novel method of processing food with no heat treatment. Pressure of 300 – 700 MPa can inactivate yeasts and moulds, but have little or no effect on quality and freshness of the product.

Many industrial processes utilise high pressures as a thermodynamic tool. High pressure is used in the activation of reactions, solvent – solute reactions, reactions involving sterically hindered transition states, synthesis of heat sensitive molecules and catalysis. The Haber process (the industrial process of producing ammonia from

hydrogen and nitrogen gas) is performed at high temperatures (400 K) and at an elevated pressure of around 1000 atmospheres. Polymerisation processes also utilise pressure. For example, the polymerisation of ethene to form polythene is carried out under elevated pressures and temperatures, aided by a catalyst to control the synthesis.

Pressure can also change the properties of materials, for example as band gaps are reduced with increasing pressure, many insulators and semi-conductors become metals at high pressures. In the heavy alkali metals, an $s \rightarrow d$ orbital transition occurs with increasing pressure. This is a pressure induced lowering of previously unoccupied d – orbitals, and electrons are gradually transferred to these vacant orbitals.

There is great interest in the effect of pressure on inter- and intra- molecular interactions. It is assumed that with lower pressures, changes in low energy intermolecular interactions would be expected. In molecular studies, a very high pressure would be required to shorten the length of, for example, a covalent bond. Many of these molecular materials will become amorphous before this happens. There is a need for understanding materials under different thermodynamic conditions to aid crystal engineering and polymorph prediction. A study of acetic acid at high pressure (Allan *et al*[5]) found a new polymorph at a relatively low pressure of 0.2 GPa in 1999. The structure matched a predicted polymorph by Mooij *et al*[6] in 1997. They considered 8 different space groups and assumed that there would be one molecule in the asymmetric unit, finding around 100 possible polymorphs within an energy of 5 $kJmol^{-1}$. This is a significant result, proving that high pressure can be used as a test of polymorph prediction. This can also work in the opposite direction, perhaps an unsolved high-pressure phase may be found as a predicted structure in the literature. This will also be of great use to the pharmaceutical industry where now it is imperative that all polymorphs of a new drug must be found.

Different type of intermolecular interactions can be observed within the same molecule. The study of acetone at low temperature and high pressure (Allan *et al*[7]) found that the three types of dipolar carbonyl-carbonyl interactions are all exhibited in the solid state structures of two phases derived at 0.15 GPa and at 150 K. Figure 1.3 shows the three types of interaction.

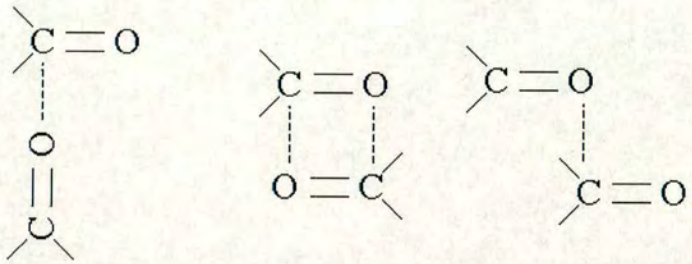

Figure 1.3 Type I, II and III carbonyl-carbonyl interaction

In this thesis, the materials studied are small organic molecules containing functional groups, with a focus on hydrogen bonding. The hydrogen bond is a key interaction in functional molecules such as DNA and proteins. Hydrogen bonds are common in small organic molecules containing electronegative atoms such as oxygen and nitrogen. Understanding hydrogen bonding and changes in hydrogen bonding is key to interpreting and predicting changes in these biological systems.

1.2 Purpose of Research

The purpose of the research carried out in this thesis is to apply the *in-situ* single crystal growth technique to study the high-pressure crystal structures of simple organic molecules with one or more functional group. Where the low-temperature crystal structure is not known, the *in-situ* single crystal growth at low-temperature and ambient pressure techniques is applied. This thesis presents low-temperature crystal structures of cyclobutanol and tertiary butanol; and high-pressure crystal structures of cyclobutanol, tertiary butanol, ethane-1,2-diol, propane-1,3-diol, pentane-1,5-diol, chloroform and bromoform.

1.3 Thesis Outline

This thesis is organised in the following manner:

Chapter 2 contains an introduction to the experimental techniques for high-pressure single crystal x-ray diffraction. Although the author was not involved in the implementation of these techniques, the methods used are essential to the experimental results presented in this thesis. It is therefore necessary to include them here for the understanding of the subsequent chapters.

Chapter 3 presents a structural study of the mono-alcohols cyclobutanol and tertiary butanol, following on from initial studies of methanol[8], ethanol[5] and phenol[9] by Dr. David R. Allan. A new polymorph of tertiary butanol stable at low-temperature and high-pressure which contains hydrogen bonded rings is compared to the known polymorph stable under ambient conditions which contains helical chains. The low-temperature and high-pressure phases of cyclobutanol both form hydrogen bonded

chains, although the chains in each polymorph are different. The trend is strikingly similar to the phase behaviour of phenol.

Chapter 4 is an extension to the work on mono-alcohols, and it contains the results and analysis on a high-pressure structural study of the di-alcohols. The most striking result obtained in this chapter is the fact that higher energy conformers are found to be stable in the new high-pressure phases of ethane-1,2-diol, propane-1,3-diol and pentane-1,5-diol.

Chapter 5 details a study on the tri-halogenated derivatives of methane. It is found that the new high-pressure phases of both chloroform and bromoform are strikingly similar, both polymorphs crystallise in the polar hexagonal space group $P6_3$. With the exception of the low-temperature and ambient pressure phase I of chloroform, all known phases of chloroform, bromoform and iodoform contain the same layer type. Different polymorphs are formed by these layers stacking in different forms.

Chapter 6 concludes the thesis, summarising what has been achieved and outlining the possible future developments in this field.

1.4 References

1. Loveday J.S., Nelmes R.J., Guthrie M., Belmonte S.A., Allan D.R., Klug D.D., Tse J.S., Handa Y.P., *Nature*, **410**, 661 (2001).

2. Loveday J.S., Nelmes R.J., Marshall W.G., Besson J.M., Klotz S., Hamel G., Hull S., *High Pressure Res.*, **14**, 303 (1996).

3. Sharma A., Scott J.H., Cody G.D., Fogel M.L., Hazen R.M., Hemley R.J., Huntress W.T., *Science*, **295**, 1514 (2002).

4. Fourme R., Kahn R., Mezouar M., Girard E., Hoerentrup C., Prangé T., Ascone I., *J. Synchrotron Rad.*, **8**, 1149 (2001).

5. Allan D. R., Clark S. J., *Phys. Rev. B.*, **60**, 6328 (1999).

6. Mooij W. T. M., Van Eijck B. P., Price S. L., Verwer P., Kroon J., *J. Comput. Chem.*, **19**, 459 (1998).

7. Allan D. R., Clark S. J., Ibberson R. M., Parsons S., Pulham C. R., Sawyer L., *Chem. Commun.*, 751 (1999).

8. Allan D.R., Clark S.J., Brugmans M.J.P, Ackland G. J. and Vos W.L., *Phys. Rev. B*, **58**, 11809 (1998).

9. Allan D.R., Clark S.J., Dawson A., McGregor P.A. and Parsons S., *Acta Cryst.*, **B58**, 1018 (2002).

Chapter 2

Techniques

2.1 Introduction

This chapter will outline the techniques required to complete the work for this thesis. Section 2.2 gives a brief overview of diffraction theory, section 2.3 details growing single crystals suitable for x-ray diffraction from low-melting point compounds at low-temperatures, and section 2.4 gives the high-pressure equivalent of this crystal growth technique. Section 2.5 serves as a brief overview of data collection, processing, structure solution and refinement procedures. Finally, section 2.6 will detail the current research undertaken to overcome limitations in these techniques.

2.2 Diffraction Theory

In 1913, W.L. Bragg used diffraction theory to determine the crystal structure of sodium chloride. This theory has been the basis of the development of diffraction techniques for almost a century, and the basis of the determination of solid state structures ranging from the "simple" structures containing only a few atoms in the unit cell to macromolecular crystal structures of proteins containing thousands of atoms in the unit cell.

Bragg's Law (equation 2.1) relates the diffracted x-ray beam with the so called "Miller Planes" within the unit cell of the crystal structure, defined by the Miller Indices, h, k, and l. λ, the wavelength of the incident radiation is directly proportional to the spacing between a given set of Miller planes, d_{hkl} and half the angle between the incident x-ray beam and the x-ray beam diffracted from the given set of Miller planes, θ_{hkl}.

$$\lambda = 2d_{hkl} \sin \theta_{hkl}$$

Equation 2.1 Bragg's Law

There are two experimental variables, the wavelength, λ and the diffracting angle, θ. An experiment using a fixed λ is called angle dispersive x-ray diffraction where data are collected with varying 2θ. Energy dispersive x-ray diffraction uses a white x-ray beam, where the diffracting angle is fixed and data are collected over all wavelengths in the spectrum. The angle dispersive technique is the most successful and widely used, although the development of synchrotron radiation sources and neutron diffraction techniques has allowed great development in the energy dispersive technique. All experiments in this thesis use the angle dispersive technique, and all are single crystal experiments. The intensity of the reflections gives the vital information of the atomic positions within the repeating unit of the crystal. This information is obtained through the structure factor, F, the intensities of reflections are related to F^2. The structure factor is related to the scattering factors of all j atoms in the unit cell with atomic positions x_j, y_j and z_j, equation 2.2.

$$F_{hkl} = \sum_{j=1}^{n} f_j e^{2\pi i(hx_j + ky_j + lz_j)}$$

Equation 2.2 The Structure Factor Equation

The crystal structure is determined using equations 2.1 and 2.2. Firstly, the unit cell dimensions can be derived from the d-spacings of each reflection, calculated from θ using Bragg's Law (equation 2.1). Secondly, the atomic positions within the unit cell are determined from the intensities of these reflections using the structure factor equation (equation 2.2). These principles, described here in very basic terms, form the basis of x-ray diffraction studies.

An alternative expression of Bragg's law which involves the reciprocal lattice is the Ewald reflecting sphere (see figure 2.1). The construction considers a single crystal in the diffracting position for the reflecting plane hkl. The primary beam travels along IO, passing through the single crystal sample at point A.

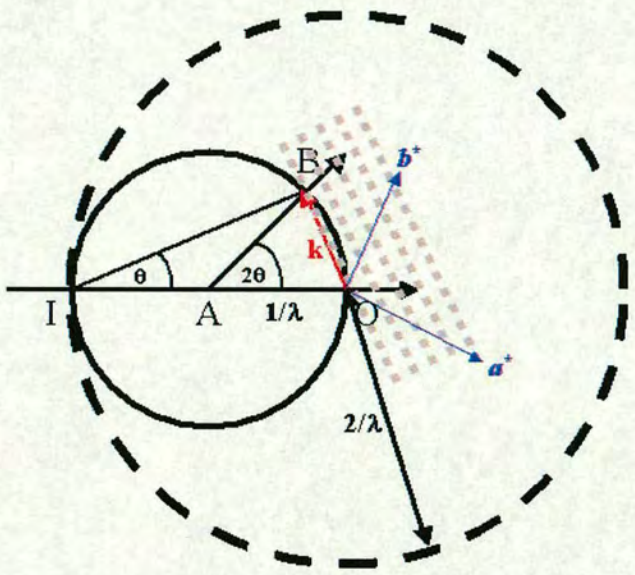

Figure 2.1 The Ewald reflecting sphere

A sphere of radius $1/\lambda$ and a diameter of IO is drawn. The point O serves as the origin of the reciprocal lattice, defined as $a^*=1/a$, $b^*=1/b$ and $c^*=1/c$. a, b and c are vectors defining the direct lattice of the crystal where a^* is normal to the bc plane, b^* is normal to the ac plane and c^* is normal to the ab plane. When the reciprocal lattice vector k is in the diffracting position, the corresponding direct lattice planes will lie parallel to the vector IB, and make an angle θ with the primary beam along IO. The relationship $OB = k = 1/d_{hkl} = IO \sin\theta = (2 \sin\theta) / \lambda$ holds, and the reciprocal lattice point B lies on the surface of the Ewald sphere. The limit of observable reciprocal lattice points for a given λ is shown by the dashed circle (figure 2.1) with radius $2/\lambda$. Only lattice points inside this sphere can be measured in the diffraction experiment.

From the data itself, the unit cell parameters can be determined from the positions of the observed reflections, the space group from systematic absences in the data, and the intensity of each reflection is measured. The location of the atoms in the unit cell, or the structure solution, have to be determined. The electron density, $\rho_{xyz,}$ can be calculated using equation 2.3 if the structure factors with their phases are known. This process is a Fourier summation, and the electron density map produced is often called the "Fourier map" or the "difference map".

$$\rho(\mathbf{x}) = \frac{1}{V}\sum_{\mathbf{h}} \mathbf{F}(\mathbf{h})\exp(-2\pi i\mathbf{h}\cdot\mathbf{x})$$

Equation 2.3 The Electron Density Equation

The experimental measurements give only the intensities of the reflections at a given x,y,z, all the phase information of the scattered x-ray is lost. This is the underlying phase problem of crystal structure determination. Structure solution methods such as the Patterson method and direct methods overcome this problem.

The scattering amplitude in x-ray diffraction is proportional to the square of the atomic number, Z, x-rays are diffracted by the electron density around each atom. Accurate hydrogen atom placement is hampered by this as hydrogen with Z=1, has only one electron and therefore the information obtainable for the positions of hydrogen atoms compared to other atoms within the unit cell is very small. In neutron diffraction, the scattering amplitude is independent of Z, this is perhaps a more favourable method of studying hydrogen bonded materials. Currently, there are very limited facilities in single crystal studies at high pressures. In this work, quantum mechanical *ab-initio* calculations are used to determine accurate hydrogen atom co-ordinates.

For single crystal diffraction there are four main factors that affect accurate structure determination. These factors are well understood and documented. A brief outline is included here:

i). The data should contain all independent Bragg reflections up to the required resolution limit, in Sin θ/λ. This includes a number of symmetry equivalent reflections. The volume of reciprocal space covered should be uniform to avoid any bias in the structural model.

ii). The background should be as low as possible, and vary smoothly so that the intensity of each reflection can be integrated accurately.

iii). The effects of absorption from the crystal itself and any other absorbing sample environment, such as glass from a capillary, must be corrected for each reflection in the data set.

iv). The crystal should be well centered and within the incident x-ray beam to avoid angle-dependent intensity variations.

2.3 Single Crystal X-ray Diffraction of Low Melting Point Compounds

This technique was pioneered by Prof. R. Boese[1]. This involves the loading of the low-melting material into a capillary, cooling to below the melting point of the sample to acquire a solid sample and using intimate laser heating to grow a single crystal suitable for x-ray diffraction. The laser is built into the diffractometer housing such that x-rays and the laser beam can be used simultaneously if required. The detector used is an area detector, its major advantage in this situation is the monitoring of crystal quality. Figure 2.2 shows the goniometer head with the attached capillary on the diffractometer. The red guide laser indicates where the laser is positioned on the sample. Intimate heating of specific areas of the sample can therefore be achieved.

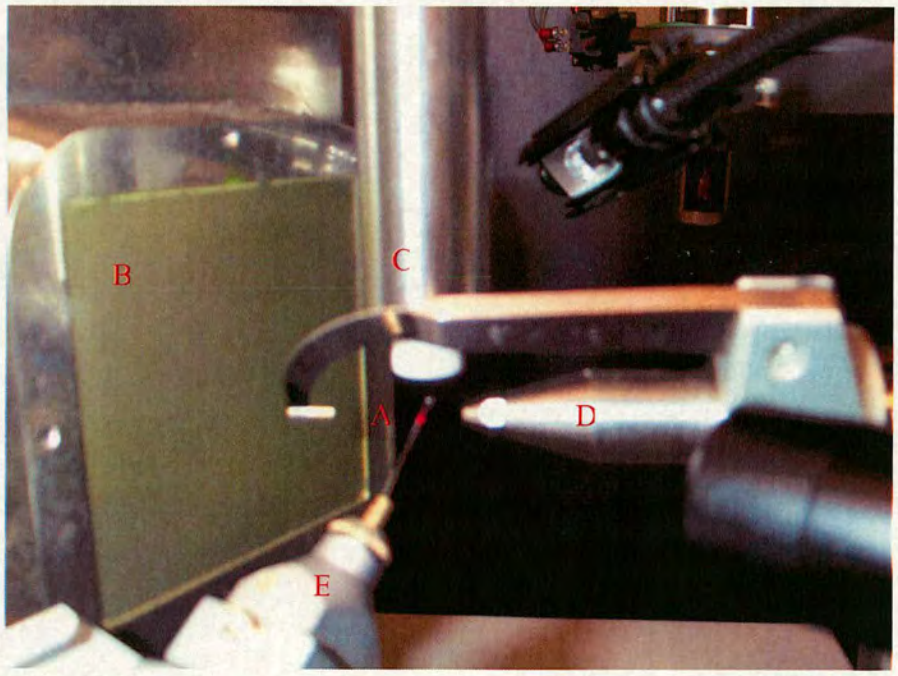

Figure 2.2 A capillary containing a low melting point compound mounted on the goniometer attached to the SMART diffractometer. (A) The red guide light of the laser can be seen on the capillary, (B) the area detector screen, (C) the cryostat, (D) the collimator, (E) the goniometer.

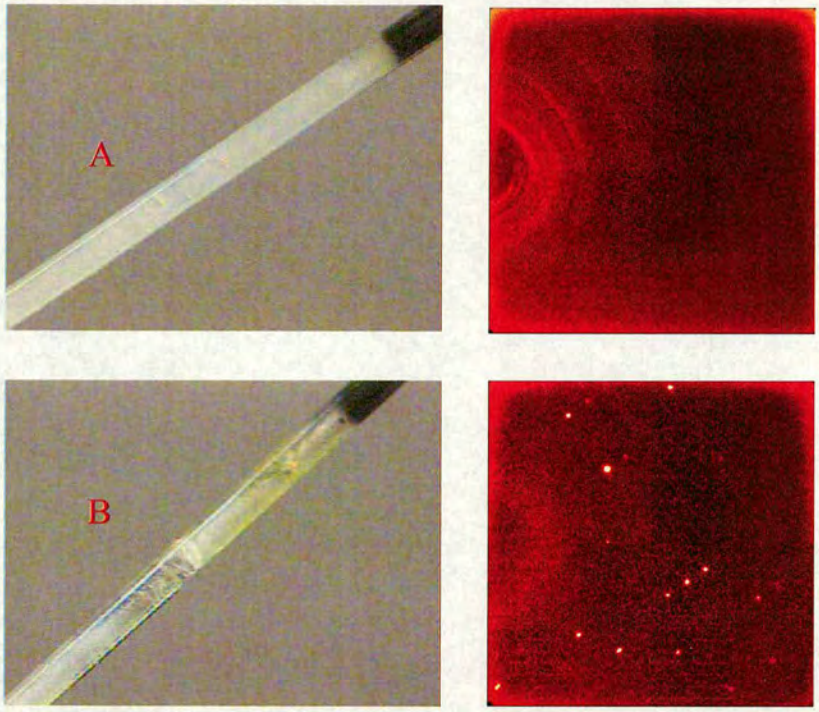

Figure 2.3 A capillary containing a low melting point compound mounted and the corresponding 10s exposure. (A) A polycrystalline material with corresponding powder diffraction rings; (B) A single crystal with corresponding reflections.

When the sample is mounted and centered on the diffractometer, it is cooled to below the melting point using a low temperature cryogenic unit. Often, due to the lack of nucleation points on the smooth surface of the capillary, supercooling occurs, when the sample stays in the liquid state although it is held at a temperature below the melting point. It is necessary to flash freeze the sample by dabbing liquid nitrogen onto the capillary. In most cases, glass formation will occur, and using the laser at a low power, so that heating is still below the melting point, will provide sufficient energy to convert the sample to a polycrystalline form. An example of this and the corresponding diffraction pattern is shown in figure 2.3 (A). The laser is then concentrated on one area of the sample where the minimum power required to melt the sample is found. Using

this power, the laser is programmed to move down the capillary over an adequate area and for a period of 20 minutes. The power is then lowered at the end of this cycle over a further 20 minutes. This procedure creates a solid – liquid interface where the single crystal can be grown. This does not necessarily work routinely, so the variables of time, power and cryostream temperature can be altered. For example, some crystals have been grown over 10 minute periods, others over 10 hour periods.

A set of matrix frames are then collected, usually 3 runs of 25 frames each measuring 0.5° in ω. If indexing is successful, usually a hemisphere of data is collected for these samples to get the best refinement possible. If indexing fails using the SMART[2] software, the next step is to use GEMINI[3] for twin indexing. If a reasonable solution is not found using GEMINI[3], there are three options: collect more matrix frames to aid indexing; collect a hemisphere of data as back-up and subsequently work on all data; or grow another crystal. It is preferred to collect the data set before growing another crystal, this is because it may never be possible to grow a better crystal of the material.

Routine data collection strategies are applied for samples that index easily. The amount of data collected depends on the point group of the crystal, although in this case to enable the absorption correction to be as accurate as possible given the presence of the glass capillary, a hemisphere of data is usually collected. To select the framewidth of the data collection, the reflections collected in the matrix runs are analysed, and the framewidth set to be half of the minimum halfwidth of the peaks. The exposure time for each frame is the last variable, the time selected should ensure that spots are clearly visible at higher values of 2θ.

There are many variables available when integrating the data set. This integration is carried out using the program SAINT[4]. SAINT[4] uses 3D profiling algorithms to reduce raw crystallographic data frames to HKLs and Lorenz polarization corrected intensities

with their associated standard deviations. The data are then corrected for absorption using SADABS[5]. The errors this software corrects for are: variation of the volume of crystal irradiated; crystal decay; absorption by crystal support; and variations in the intensity of the incident beam.

The space group is determined by analyzing the systematic absences in the data set. Programs such as WinGX[6] or XPREP (from the SHELXTL suite[9]) are used for this. Structure solution is carried out using SHELXS[7] or SIR92[8] and refinement using Shelxl (from the SHELXTL suite[9]).

2.4 High Pressure Single Crystal X-ray Diffraction of Low Melting Point Compounds

2.4.1 The Diamond-Anvil Cell for X-ray Diffraction

The high-pressure cell used for the single crystal x-ray diffraction techniques in this thesis is the Merrill-Bassett diamond anvil cell[10,11]. Figure 2.4 shows the principle components of the cell – the opposing diamond anvils and the gasket. The sample is contained in a small hole drilled into the gasket that is situated between the two opposing faces of the diamonds. The faces, or culets, are flat and parallel and measure between 400 and 600 μm for this work. Typically the sample diameter is 150 – 200 μm, with a height of around 100 μm indented in the 250 μm tungsten gasket (figure 2.5 (A)). The pressure is applied when a load is applied to both diamonds onto the sample. The environment in which the sample is contained means the pressure generated is hydrostatic i.e. equal across all areas of the sample.

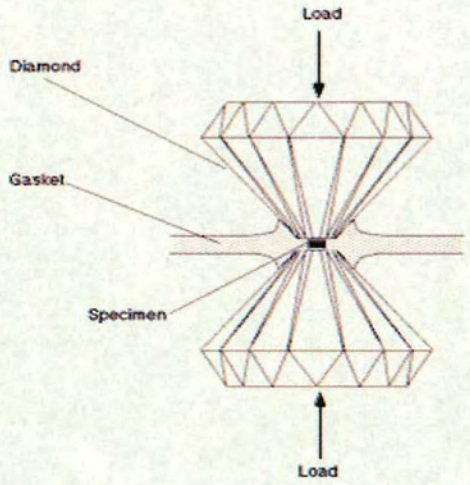

Figure 2.4 The main components of the Diamond - Anvil Cell

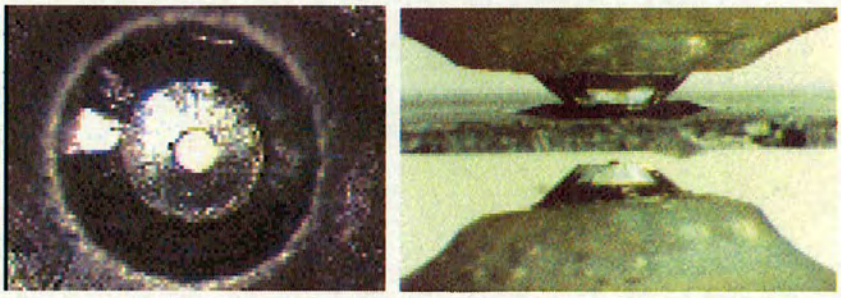

(A) (B)

Figure 2.5 (A) A hole which has been eroded in a pre-indented tungsten gasket. (B) The culets and gasket. A small chip of ruby can be seen on the face of the lower diamond.

Each diamond is glued onto a beryllium backing disc that has been finely manufactured with a tapered hole. Beryllium is used as it is essentially transparent to x-rays. The beryllium is then backed by a steel platen containing holes for Allen screws. Tightening these brings the two halves of the cell together, thus increasing the load on the sample. A schematic diagram is shown in figure 2.6. Although the beryllium is transparent to x-rays, the steel is not. The diffracted beam is absorbed at an angle where it passes through the steel outer body of the cell. This means that only 30-40 % of data is measurable. The opening angle of the cell is 90°, this allows reflections up to a 2θ of 45° to be measured. Figure 2.7 shows the cell mounted on a BRUKER-SMART^2 diffractometer.

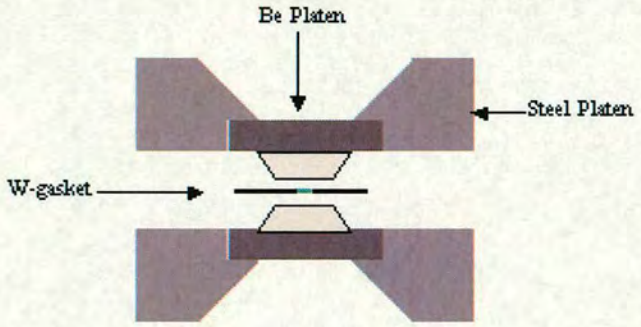

Figure 2.6 Schematic Diagram of the Diamond Anvil Cell

To measure the pressure inside the cell, ruby fluorescence spectroscopy is used for all work in this thesis, although it is also possible to measure pressure by using the equation of state of a known calibrant material, such as salt. A small (5-15 μm) chip of ruby, Cr^{3+} doped Al_2O_3, is placed on the upper culet with a small smear of grease. The ruby fluoresces when excited by laser light, which is shone through the diamond window. The fluorescence consists of a doublet, with the R lines R_1 at a wavelength of 6927 Å and R_2 at 6942 Å under ambient conditions. Up to pressures of 29 GPa, well in excess of any pressure reached in this work, the ruby scale is considered linear (Piermarini and Block[12]). The pressure is calculated from the equation $P = A(\lambda_1 - 6942)$, where λ_1 is the resultant wavelength of the resultant R_2 line and A is the proportionality constant (0.2740 $GPaÅ^{-1}$). Pressure measurements are carried out using a Jobin –Yvon Labram 300 instrument with excitation by a He-Cd laser operating at 441.61 nm.

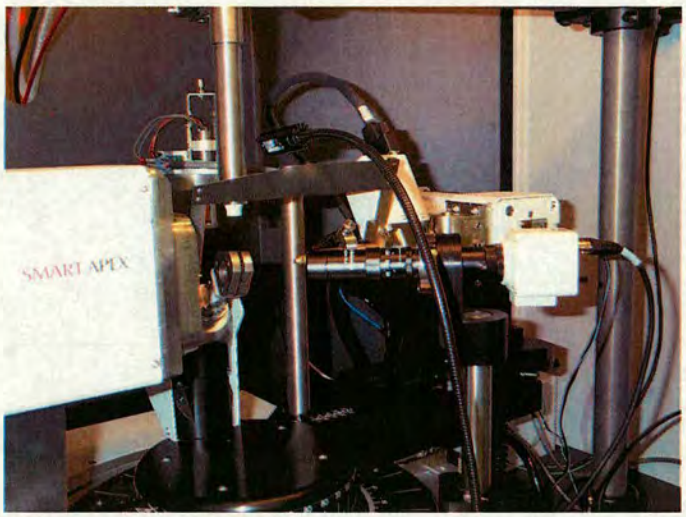

Figure 2.7 The diamond anvil cell situated on the SMART diffractometer

With the diamond anvil cell equipped with a tungsten gasket, and ruby chip placed on the upper culet, the sample may be loaded. For non-volatile and non-air sensitive low melting compounds, the sample is carefully dropped into the gasket hole on the bottom half of the cell and the top half is then placed onto the bottom half. A microscope is used to check for any air bubbles, if there are none the pressure is increased until crystallisation occurs.

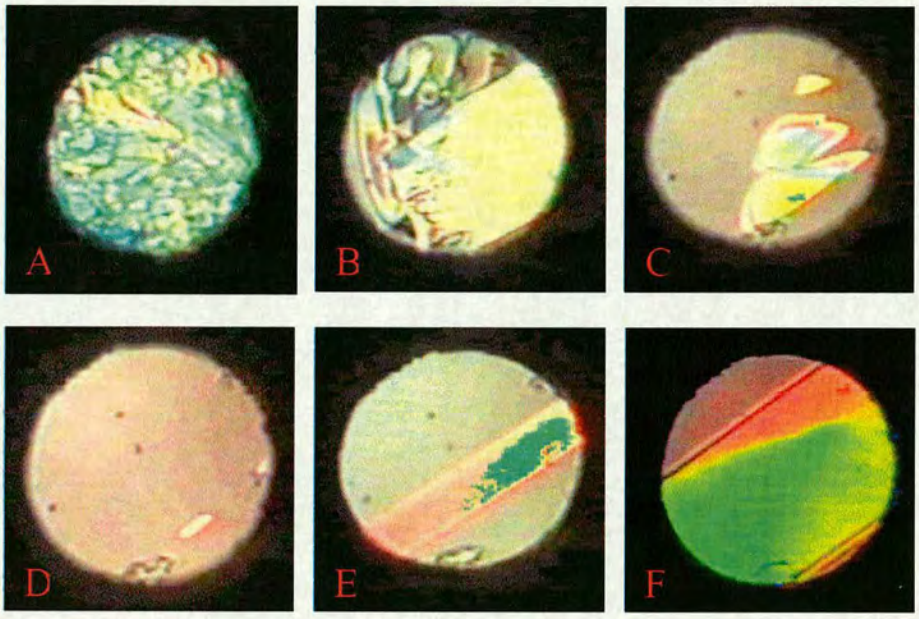

Figure 2.8 Animation of the growth of a single crystal of acetic acid (courtesy of D. R. Allan) (A) Polycrystalline (B) Melting (C) Further melting (D) Seed crystal (E) Single crystal growing on cooling (F) Fully grown single crystal[13]

After polycrystalline material is formed, heat is applied by means of a heat gun, aimed in the general direction of the sample between the steel platens. The heat and also the pressure is cycled until the melting process begins (figure 2.8 (B)). Heat is applied until there is one remaining crystallite (figure 2.8 (D)), and then the heat is removed to allow the cell to cool to room temperature and the crystal to grow to fill the gasket hole.

2.4.2 X-ray Sources

All data collected for this work are from either a sealed tube x-ray source in the laboratory, or synchrotron radiation at the SRS in Daresbury.

The sealed tube x-ray source is the most commonly used laboratory source, although is now beginning to be replaced by the rotating anode, which is 10 times more intense. X-rays are produced when a beam of electrons, accelerated by a high voltage (50 kV in the lab) strike a metal target. The electrons are slowed down by the impact with the metal, and their energy is lost gradually producing white radiation – a continuous spectrum of x-

rays. A secondary spectrum with very sharp peaks is produced over the white spectrum when the energy of the electrons striking the target metal is higher then a certain threshold value. This secondary spectrum has peaks that are found at specific wavelengths characteristic to the metal target. These are the K, L and M lines that correspond to transitions from higher energy orbitals to the K, L and M orbitals that have principal quantum numbers n = 1,2 and 3. When the orbitals involved in the transition are adjacent, the emission line is called α, if they are separated by one shell they are called β. So the Mo-Kα line is produced by a molybdenum target in which the atoms lost an electron in the orbital of n = 1 and the vacancy was filled by an electron of the orbital of $n = 2$.

The most frequently used targets for laboratory instruments are copper (Cu K_α) and molybdenum (Mo K_α) with wavelengths of 1.5418 Å and 0.7107 Å respectively. Molybdenum is used for high-pressure data collections in the laboratory – the higher wavelength copper radiation is too highly absorbed by the diamond anvil cell. The volume of reciprocal space attainable is limited by the Ewald Sphere which has a radius of $2/\lambda$. Shorter wavelength radiations therefore give access to a larger volume of reciprocal space.

The synchrotron radiation facility, development of which began in the 1960's and is developing further today with the proposed fourth generation source – the TESLA project in Hamburg, Germany, provides the opportunity to carry out diffraction experiments at a much brighter source. A laboratory x-ray source has a brilliance of 10^7 photons/s/0.1%BW/mrad^2/mm^2/mA, whereas the Second Generation source at SRS Daresbury has a brilliance of 10^{15}. Figure 2.9 shows a schematic diagram of a synchrotron light facility.

White synchrotron radiation is produced when the path of high-energy electrons, traveling at over 99.99 % of the speed of light, is deflected by a magnetic field. The electrons are produced from a cathode and are injected into a linear accelerator. High-energy microwave radiation is used to accelerate the electron beam. These are fed into a

booster ring that ramps the energy up to 2 GeV, enough energy to produce synchrotron radiation from the infra-red to the hard x-ray range. The booster ring feeds the pulses of electrons into the vacuum storage ring where a series of magnets steer the electrons along circular arcs. Synchrotron radiation is emitted tangentially from these magnets to be used at the experimental chambers.

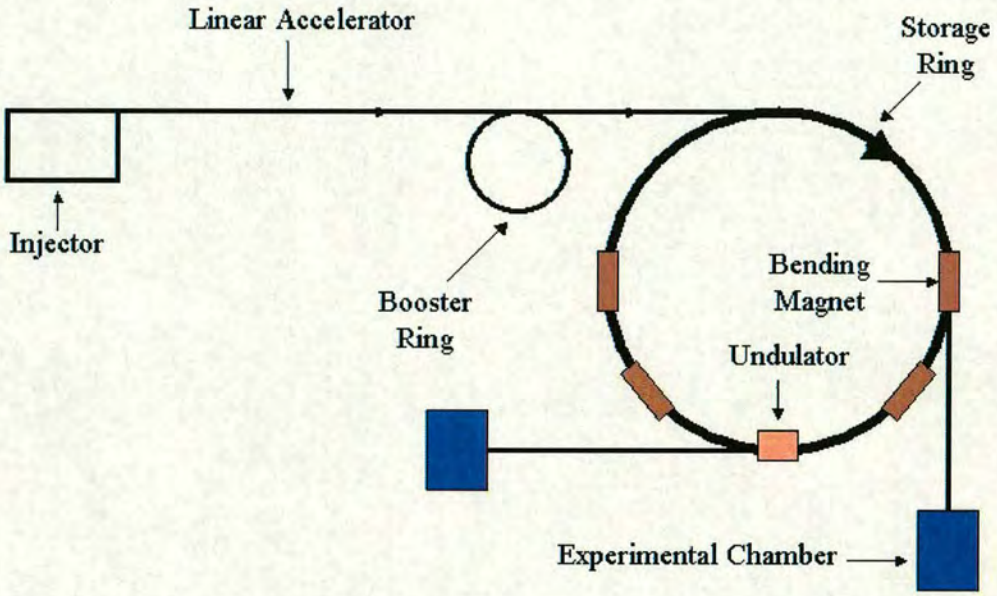

Figure 2.9 Schematic Diagram of a Synchrotron Light Facility

The insertion devices, wigglers and undulators, are situated on straight regions of the storage ring. The single crystal station at the SRS Daresbury, Station 9.8, is an experimental station on beamline 9 on which the insertion device is a 5T wiggler. A wiggler increases the brightness of the beam by causing multiple direction changes (wiggles). The wavelength of radiation available is from 0.3 – 1.5 Å, depending on the set up of monochromation and mirrors. The station is set for normal use at around 0.68 Å at the Zirconium edge. This is the wavelength used for all data sets collected at the SRS for this work. To be able to attain a bigger area of reciprocal space, it is possible to collect at shorter wavelengths.

2.4.3 Data Collection and Processing Strategies

As was discussed in section 2.4.1, the steel outer body of the diamond anvil cell restricts the amount of accessible reciprocal space for data collection. There are two diffractometers used for data collection in this work, the CAD-4[14], which is a four-circle diffractometer with kappa geometry and a point detector, and the BRUKER-SMART[2], which is a three-circle diffractometer with an area detector. Station 9.8 at Daresbury is equipped with a BRUKER-SMART[2] diffractometer, the procedure is essentially the same as data collection using the laboratory set up.

CAD-4 Data Collection and Processing

The diamond anvil cell containing the sample is mounted and centered on the diffractometer. A rotation photograph is collected using an x-ray sensitive image plate. The positions of the reflections are measured, and subsequently centered. DIRAX[15] is used to index a list of up to 25 reflections. Lisgen, a program written by Dr. J. S. Loveday and modified by Dr. R. O. Piltz in the Edinburgh University High Pressure Group, takes the UB matrix (relating the orientation matrix to the diffractometer axes), the opening angle of the diamond anvil cell, the axis along which the diamond anvil cell is situated and the wavelength and calculates the observable reflections which are then printed to a file containing h, k, l and Ψ. These reflections are then collected using a θ dependent scan width in ω, determined by the width of a sample reflection.

This data collection technique was modified by Finger and King[16]. Their method is a fixed ϕ technique where the ϕ-axis is fixed to zero (or some other value defined by the direction of the diamond –anvil cell) and the desired reflection is moved to the diffracting position by rotating around ψ with the ω and χ motors. By measuring the reflection this way the cylindrical axis of the diamond anvil cell is constrained to lie in the diffraction plane of the diffractometer and the maximum number of reflections can be observed. In this position, the path lengths of the x-rays through the diamonds and beryllium are reduced. This leads to lower background scattering and less absorption.

In an ambient pressure data collection on a four circles instrument, the intensity of a reflection is routinely measured using an ω-2θ scan where both the sample and the detector are rotated simultaneously. This type of scan ensures that the diffracted x-ray beam strikes the centre of the detector throughout the scan. If this were adopted into the collection of data of a sample at high pressure, the detector would sweep across the powder lines generated by both the beryllium and the tungsten gasket. These powder lines will appear as extra peaks in the reflection profile, making accurate integration of the intensities extremely difficult. In the pure ω-scan, the reflections are scanned parallel to the powder lines. Their profile lies on a relatively flat background. However, the horizontal detector aperture must be increased so that all the intensity is recorded over the scan range. This results in a higher background, but the low signal-to-noise ratio can be compensated for by increasing the count time for each scan. The level of the flat background can be determined accurately, so the ω-scan method is used widely in high-pressure crystallography.

The data collection takes around a week to complete. Processing of data starts with the integration using the program DECCOR2 (Written by Prof. R. J. Angel and modified by Dr. S. A. Belmonte, University of Edinburgh High Pressure Group) that produces a file containing h, k, l, F^2 and σF^2. This is then corrected for absorption by the cell and gasket using the program ABSORBU2 (Prof. R. J. Angel, Virginia Polytechnic Institute and State University).

SMART Data Collection and Processing

The data collection strategy used for the area detector (laboratory source and SRS) is to set up a series of scans to cover the maximum amount of reciprocal space. This is independent of the orientation matrix of the sample. This is a major advantage the area detector has over the point detector whereby indexing is difficult, the full data set can be used to facilitate this step after a "blind" data set is collected. Tables 2.1 and 2.2 below contain the scan ranges for the laboratory and SRS diffractometers. Data collection

requires 8 hours at the SRS, generally using a scan time of 1s and a step size of 0.1° in ω. In the laboratory, the scan time generally used is 10s, coupled with a step size of 0.3° in ω and a data collection time of 12 hours is achieved.

Run	2θ (°)	Ω range (°)	ψ (°)	No. of Frames
1	-28	-8 → -40	90	106
2	28	40 → -40	90	266
3	-28	-140 → -215	90	250
4	28	-140 → -172	90	106
5	-28	-140 → -218	270	260
6	28	-140 → -172	270	106
7	-28	-8 → -40	270	106
8	28	35 → -40	270	250

Table 2.1 Scan sequence for high-pressure data collection on Bruker SMART diffractometer

Run	2θ (°)	Ω range (°)	ψ (°)	No. of Frames
1	27	40 → 320	90	400
2	27	40 → 320	270	400
3	27	220 → 190	270	154
4	27	220 → 190	90	154
5	-27	220 → 140	90	400
6	-27	220 → 140	270	400
7	-27	175 → 140	270	175
8	-27	175 → 140	90	175

Table 2.2 Scan sequence for high-pressure data collection on Bruker SMART diffractometer at the SRS Daresbury

Selecting reflections for indexing can be done either computationally using the threshold function in SMART[2], ensuring that the lower limit for a reflection is greater than the highest value observed from the Be powder ring. Using this method, it is best to collect peaks from all 8 runs of data, and use GEMINI[3] to index the sample, and also both diamonds. If this does not work, selecting reflections by hand using the pick function in

SMART[2] and subsequent use of either SMART[2] or GEMINI[3] to index is usually adequate. Least squares refinement of the cell in SMART[2], determination of the Bravais lattice and more least-squares refinement cycles provide the best orientation matrix for SAINT[4].

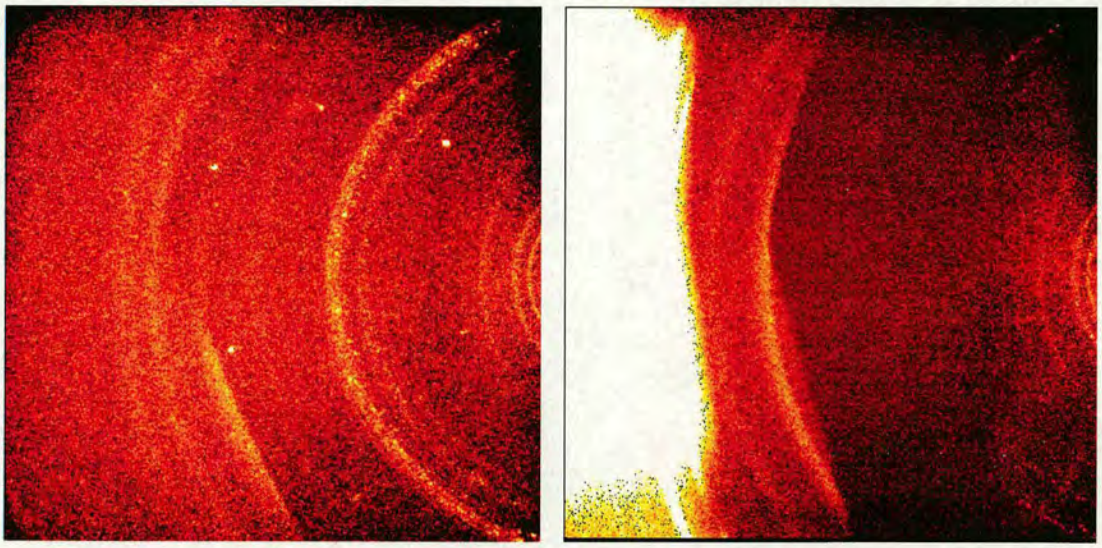

(A) (B)

Figure 2.10 (A) shows a "normal" SMART frame where diffraction is observable in all areas. The Be powder rings and sample reflections are observed. Part (B) shows a shaded SMART frame where the positioning of the diamond anvil cell is such that the area on the left of the frame contains intensity that has been reflected by the steel body of the cell.

The data processing procedure is modified slightly from that discussed in section 2.3 for samples held at low temperature. In addition to the BRUKER programs, SAINT[4] and SADABS[5], the program SHADE[17] written by Dr. S. Parsons is utilised to facilitate the integration process. Figure 2.10 (A) shows a "normal" SMART frame where diffraction is observable in all areas. Part (B) shows a shaded SMART frame where the positioning of the diamond anvil cell is such that the area on the right of the frame contains intensity that has been reflected by the steel body of the cell. Spurious reflections for which the incident or reflected beam is completely absorbed by the steel body of the cell are removed by SHADE[17]. Also, SHADE[17] will reject reflections with poor correlations (<0.3) between the measured and calculated profiles. SHADE[17] is used after the integration by SAINT[4] and before the absorption correction using SADABS[5].

The space group is determined by analyzing the systematic absences in the data set using either WinGX[6] or XPREP (part of the SHELXTL suite[9]). Software used for structure solution are shelxs[7] and sir92[8]. Refinement software used are shelxtl[10] and CRYSTALS[18]. Using restraints on bond lengths is common, this is due to the fact that the data to parameter ratio is low, as is the completeness of the data set due to the restrictions of the diamond anvil cell.

2.5 Details of the *Ab-Initio* Calculations

Ab-initio calculations for t-butanol, ethane-1,2-diol, propane-1,3-diol, pentane-1,5-diol, chloroform, bromoform and iodoform were carried out by Dr. S. J. Clark of the University of Durham. For cyclobutanol, these were carried out by Mr. I. R. McLeod of the University of Edinburgh. The calculations are utilised here for two main reasons: the first to determine accurately the positions of hydrogen atoms; the second for the comparison of energies of polymorphs under different conditions.

For each given material and structural configuration *ab-initio* pseudopotential calculations within the density functional formalism are carried out. In each of the calculations described, the experimental structure is used as a starting model and subsequently the structure is fully optimised. Throughout, the CASTEP[19] density functional code is used to perform the calculations.

2.6 References

1. Boese R. & Nussbaumer M., (1994) *Correlations, Transformations, and Interactions in Organic Crystal Chemistry*, IUCr Crystallographic Symposia, Vol. 7, edited by D. W. Jones and A. Katrusiak, pp. 20-37. Oxford University Press.
2. SMART: Area Detector Software Package. (1993) Siemens Industrial Automation, Inc.: Madison, WI, USA.
3. GEMINI, Sparks R. A. (1999), Bruker AXS, Madison, WI, USA.
4. SAINT: Area Detector Integration Software. (1995) Siemens Industrial Automation, Inc.: Madison, WI, USA.
5. SADABS, Sheldrick G. M. (2001), University of Gottingen and Bruker AXS, Madison, WI, USA.
6. WINGX, Farrugia L. J., *J. Appl. Cryst.*, , **32**, 837 (1999).
7. SHELXS, Program for Crystal Structure solution. Sheldrick, G. M., Institüt für Anorganische Chemie der Universität, Tammanstrasse 4, D-3400 Göttingen, Germany, 1986.
8. SIR92, A program for crystal structure solution. Altomare, A., Cascarano, G., Giacovazzo, C. & Guagliardi, A. *J. Appl. Cryst.* **26**, 343-350 (1993).
9. SHELXL, Sheldrick, G. M. (1997). Programs for Crystal Structure Analysis (Release 97-2). University of Göttingen, Germany.
10. Jamieson J. C., Lawson A. W. and Nachtrieb N. D., *Rev. Sci. Inst.* **30**, 1016 (1959).
11. Weir C. E., Block S. and Peirmarini G. J., *J. Res. Mat. Bur. Stand.*, **C69**, 275 (1969).
12. Peirmarina G. J., Block S, Barnett J. D., Formen R. A., *J. Appl. Phys.*, **44**, 5377 (1973).
13. From http://www.ph.ed.ac.uk/~dra
14. CAD4 Express Software. Enraf-Nonius, Delft, The Netherlands, 1994.
15. DIRAX: Duisenberg A. J. M, *J. Appl. Cryst.*, **25**, 92 (1992).
16. Finger L. W. and King H., *American Mineralogist*, **63**, 337 (1978).

17. SHADE, Allan D.R., Clark S.J., Parsons S. and Ruf M., *J. Phys. Condens. Matter.*, **12**, L613 (2000).
18. CRYSTALS, Watkin, D. J., Prout, C. K., Carruthers, J. R., Betteridge, P. W. & Cooper R. I., Issue 11 (2001), Chemical Crystallography Laboratory, OXFORD, UK.
19. CASTEP: Payne M.C., Tefer M. P., Allan D. C., Arices T. A. and Joannopolou J., *J. Appl. Phys.*, **64**, 1045 (1992); CASTEP 4.2, Academic Version, licensed under the UKCP-MSI agreement (1999).

Chapter 3

High Pressure and Low Temperature Structural Studies of the Mono Alcohols Cyclobutanol and Tertiary Butanol

3.1 Introduction

The work in this chapter is an extension of previous work undertaken in the Edinburgh University High Pressure Group by Dr. David Allan, where the effect of pressure on the solid state structures of small linear chain mono-alcohols, $H(CH_2)_nOH$ (where the integer n denotes the chain length) was investigated[1,2,3]. More recently, this work was extended to involve phenol, a mono-alcohol which undergoes pressure induced polymorphism (Allan *et al*, 2002)[4]. Mono-alcohols are compounds that have a hydroxyl group bonded to an sp^3 hybridised carbon atom. They are organic derivatives of water, which itself has 16 known phases at varying temperature and pressure (see figure 3.1).

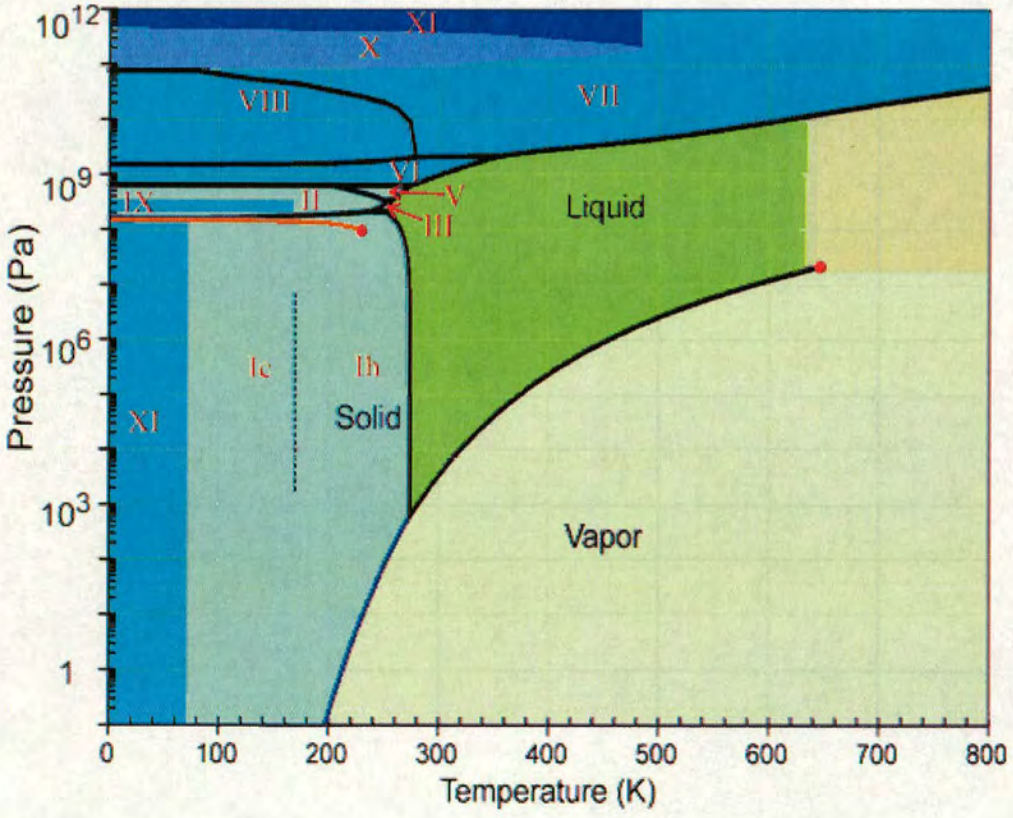

Figure 3.1 The Phase Diagram of Water[5]

In fact only 2 of the different phases of water are stable under ambient pressure, the remaining 12 are high-pressure phases at varying temperature – this provides significant motivation for studying the organic derivatives of water at elevated pressures.

In water and alcohols, the oxygen atom is sp^3 hybridised and the ROH angle is approximately tetrahedral due to the presence of two lone pairs of electrons completing the valence shell. In solution, alcohols are highly associated due to the formation of weak hydrogen bonds between neighbouring molecules. In the solid state, this neutral hydroxyl group acts as both a hydrogen bond donor and acceptor - this gives rise to many different ways of packing the molecules together and the possibility of many new polymorphs. These neutral, moderate (in terms of energetics) hydrogen bonds are the important and essential components of the structure and function of biological molecules essential to life e.g. DNA, proteins. In alcohols, we expect that, as the chain length increases, the relevance of hydrophobic interactions between the alkyl groups will increase and the effect of hydrogen bonding in the structure will consequently decrease.

Rules governing the packing of mono alcohols, and space group frequencies from the Cambridge Structural Database have been discussed most recently by Taylor and Macrae (2001)[6] and prior to that by Brock and Duncan (1994)[7]. The hydrogen bonding pattern in these structures fall into four types: infinite hydrogen bonded chains involving only the hydrogen bond donor and acceptor of the hydroxyl group; hydrogen bonded rings containing the same type of hydrogen bond as the chains; hydrogen bonded dimers; and, finally, structures which have no hydrogen bonds. The latter are mostly stabilised by hydroxy - π interactions. Steric effects are the most dominant in the formation of these bonds, with the least sterically hindered hydroxyl groups generally forming chains. The order of favoured structure then goes through from rings to dimers with increased steric hinderence, and finally structures with no hydrogen bond present where bulky groups prevent their formation. The

application of pressure will reduce the volume that a molecule can occupy – essentially a different type of steric hinderance. It is, therefore, intuitive that under pressure the type of changes one would expect to see are, for example, chains under ambient pressure forming rings under elevated pressure.

There are different types of chains and rings. Chains fall into four categories: planar zig-zag; three-fold helical; four-fold helical; and wave-like. Planar zig-zag chains consist of molecules that are either related by a 2_1 screw axis, or by translation when $Z' > 1$. A three-fold helice is formed either by symmetry in a trigonal space group, or by translation where $Z' = 3$. Four-fold helices are formed either by a four fold screw axis or where $Z' = 2$ and the molecules are related by a two-fold screw axis. The chains termed "wave-like" involve two crystallographically independent molecules related by a glide plane. Three, four and six membered hydrogen bonded rings occur in the CSD, the four membered rings are most common and split equally between puckered and planar configurations, puckered is more common for tertiary alcohols. It was also found that the six membered rings all adopt the "chair conformation", similar to the molecular form of cyclohexane.

Methanol (n=1) and ethanol (n=2) both exhibit new phases at ambient temperature and high-pressure which are different to the corresponding low temperature and ambient pressure structures. Propan-1-ol, propan-2-ol and butan-1-ol were found to vitrify at both low temperature and high pressure. Vitrification has proven to be a problem when it occurs at high pressure, unlike at low temperature where zone refinement using laser heating at a temperature below the melting point can be used to convert the glass into a polycrystalline material. This process is carried out in-situ on the BRUKER-SMART diffractometer, where collecting a series of "still" shots - ie 10s exposures at a fixed gonimeter setting, can be used to monitor the crystalline quality of the sample. The laser heating technique is challenging at high pressures due to the nature of the diamond anvil cell with the reflective properties of the steel body, combined with the accuracy of the laser beam on the laboratory apparatus. It is difficult to tell optically whether a sample has solidified, and this

can lead to a pressure increase well in excess of freezing. The melting point might then be so high that subsequent heating will be insufficient. Challenges for the future are to develop calorimetric methods to find the onset of glass formation, by measuring the heat capacity of the sample in contact with the gasket, or in-situ monitoring and frequent exposures to laser heating for such glassy materials.

This chapter will discuss the results obtained in Edinburgh on two mono alcohols each containing four carbons. The first, a secondary alcohol, cyclobutanol with the four carbon atoms in a ring, and the second a tertiary alcohol, tertiary butanol with three terminal methyl groups in a structure which is isoelectronic to butanol itself. Low temperature phases were obtained using the laser refinement technique described in chapter 2.3, and the high pressure single crystals grown after the onset of crystallisation in the diamond anvil cell as described in chapter 2.1.

Firstly it is important to discuss the low temperature structures of methanol, ethanol and phenol and compare these to the corresponding high-pressure polymorphs, concentrating on the intra-molecular similarities and the inter-molecular differences.

3.2 A Comparison of the Low Temperature and High Pressure Phases of Methanol, Ethanol and Phenol

3.2.1 A Comparison of the Crystal Structures of Methanol at Low Temperature and High Pressure

Methanol (CH_3OH) is the first member in the mono-alcohol series, characterised by the presence of a methyl group attached to the hydroxyl functional group (Figure 3.2).

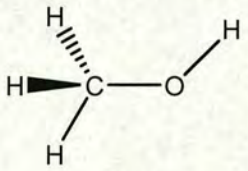

Figure 3.2 Methanol (CH_3OH)

The phase diversity is quite complicated. Below the melting point of 175 K there are two known crystalline phases (the α and β phases) and an amorphous phase that is produced by vapour deposition at low temperatures. Upon warming to 130 K, this amorphous phase converts to the α-phase. The β-phase is stable on cooling below the melting point to 157 K. The positions of the carbon and oxygen atoms were determined by Tauer and Lipscomb[8] in the space group *Cmcm*. In this setting, the hydrogen atoms must be disordered about a mirror plane. More recently, this was repeated by Boese[9] and with the hydrogen atoms, the space group symmetry was found to be $Cmc2_1$, and the hydrogen atoms are no longer disordered as the mirror perpendicular to the *c*-axis is lost. On cooling to 157 K the transition to the α–phase occurs. The structure of the deutero-form was characterised by Torrie *et al*[10] using neutron powder diffraction experiments, where they found the phase crystallised in the orthorhombic space group $P2_12_12_1$.

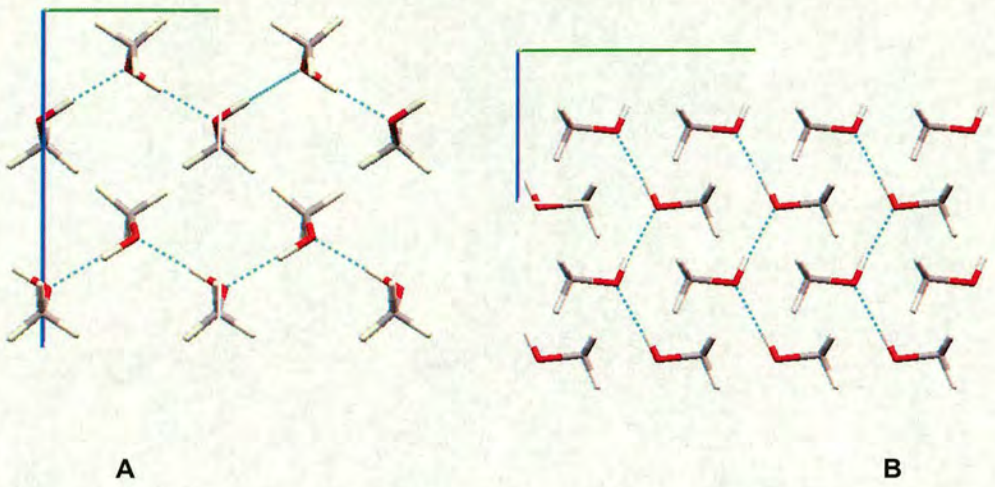

Figure 3.3 (A) The α–phase of methanol showing the "zig-zag" chains aligned parallel and anti-parallel to the *b*–axis.

Figure 3.3 (B) The β-phase of methanol showing the "zig-zag" chains aligned parallel to the *c*–axis. [*b*–axis in green, *c*–axis in blue]

There are two main structural differences between the phases, the first illustrated in figure 3.3: in the α-phase the hydrogen bonded chains are aligned parallel and anti-parallel to neighbouring chains; whereas in the β-phase, the chains are aligned so that the hydrogen bonds are parallel. The second difference, shown in figure 3.4, is the alignment of the methanol molecule with respect to the plane of the hydrogen bonded chain. In the α-phase, neighbouring methanol molecules have the C-O bond aligned above and below the plane of the hydrogen bonds at an approximate tetrahedral angle, whereas in the β-phase neighbouring molecules are aligned in the plane to the left or right at the fulcrum of the "zig-zag".

Figure 3.4 show the packing of the hydrogen bonded chains, in the α-phase, the chains are aligned parallel to the 4 0 3 or parallel to the –4 0 3 lattice plane. In the β-phase, the chains are aligned parallel to the crystallographic *c*-axis.

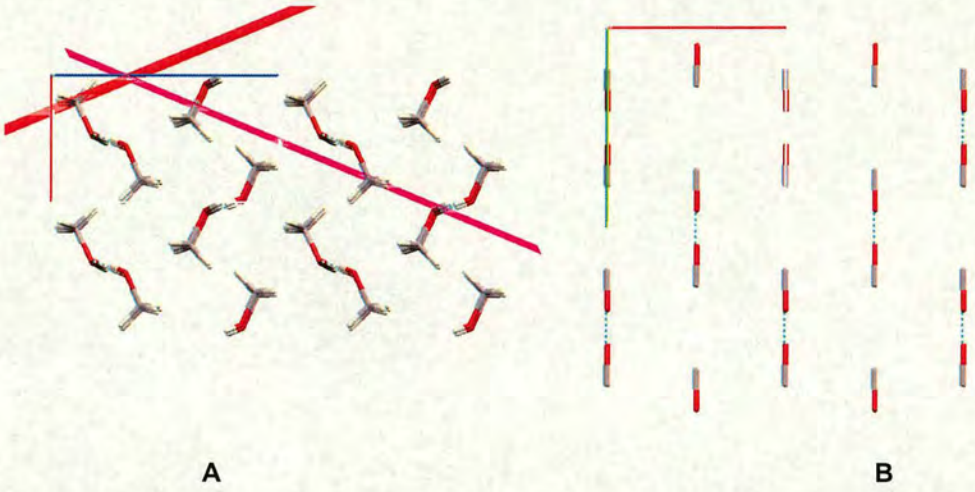

A B

Figure 3.4 (A) The α-phase of methanol showing the herring bone arrangement of the chains. [*b*-axis in green, *c*-axis in blue, 4 0 3 lattice plane in red, -4 0 3 lattice plane in purple]

Figure 3.4 (B) The β-phase of methanol showing the layers of chains aligned parallel to the *b*-axis. The *a*-axis is shown in red and the *b*-axis in green.

In the β-phase there is one unique hydrogen bond that measures 2.650 Å in length and connects two neighbouring oxygen atoms. The molecular volume is 53.95 $Å^3$ at 150 K. There is also a strong implication of disorder where the molecule can be modelled over two different positions, each with a common central carbon atom. However, the characteristic hydrogen bonded "zig-zag" chains are conserved in this disorder model.

In the deutero α-phase, the hydrogen bond measures 2.753 Å and this is, of course, longer for the O-D…O over the O-H…O. The ODO angle measures 175.28° and as a consequence of this, it would be expected that the molecular volume aught to be greater. Surprisingly this is not the case. In fact, each molecule occupies 50.13 $Å^3$, which is almost 4 $Å^3$ less than the hydrogenated form. This can be accounted for by the disorder in the β-phase resulting in the molecule occupying a larger volume in the overall structure.

In sharp contrast to the α and β-phases, the high pressure γ-polymorph (Allan *et al*[1]) has only inversion symmetry, the molecules pack in the triclinic space group P-1 with three molecules in the asymmetric unit. The molecules pack into chains that are characterised by the three unique hydrogen bonds, and the chains are subsequently aligned parallel and anti-parallel to the 2 –1 0 lattice plane (figure 3.6). The dimensions of the hydrogen bonds are: O1…O3 2.703 Å; O3…O2 2.425 Å; and O2…O1$^{\#1}$ 2.516 Å (where #1 denotes x, y, z-1). The latter two hydrogen bonds have considerably smaller donor – acceptor distances than in the β-phase, this difference will contribute substantially to the reduction in molecular volume between the β and γ-phases.

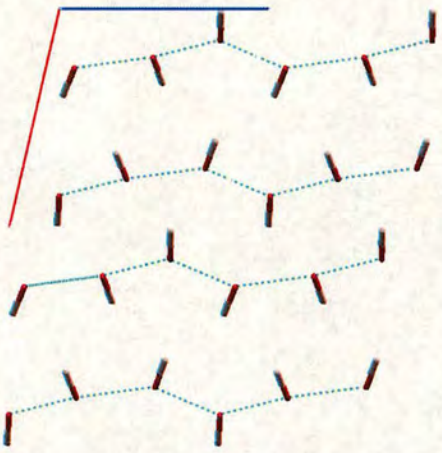

Figure 3.5 The high-pressure crystal structure of methanol, viewed down the crystallographic *b*-axis. Hydrogen atoms are omitted for clarity. [*c*-axis in blue, *a*-axis in red]

The unit cell volume for this phase is 236.19 Å^3, which gives a molecular volume of 39.4 Å^3 at 4.0 GPa. This corresponds to a substantial 36 % reduction in molecular volume in comparison to the low temperature β-phase.

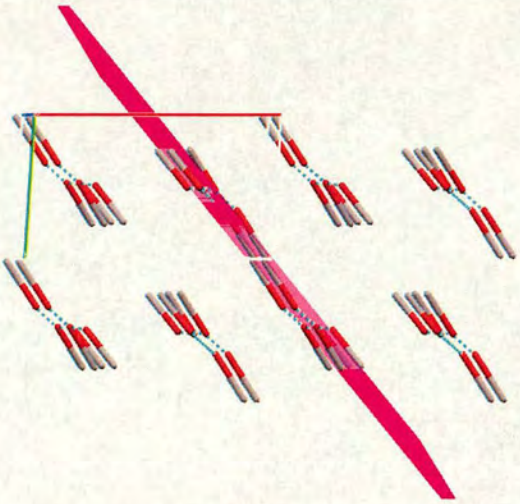

Figure 3.6 The hydrogen bonded chains in the high-pressure crystal structure of methanol are aligned parallel to the 2 –1 0 lattice plane, which is shown in purple. Hydrogen atoms are omitted for clarity. [*a*-axis in red, *b*-axis in green, *c*-axis in blue]

3.2.2 A Comparison of the Crystal Structures of Ethanol at Low Temperature and High Pressure

Ethanol (CH_3CH_2OH) is the second member of the mono-alcohol series, having an ethyl group attached to the hydroxyl functional group (figure 3.7).

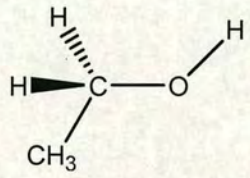

Figure 3.7 Ethanol (C_2H_5OH)

There is only one known crystalline phase of ethanol at low temperature, determined by Jonsson[11] in 1976 at 87 K and ambient pressure. The crystal was grown in a capillary just below the melting point of 156 K. There are two molecules in the asymmetric unit of this monoclinic *Pc* polymorph. The major difference between the two molecules is the positioning of the hydrogen atom. One molecule is the *trans* conformer with a C3-C2-O2-H2 torsion angle of 179°, and the other is the

gauche conformer which has a C4-C1-O1-H1 torsion angle of -63 °. Each forms a unique hydrogen bond to the other molecule, O1-H1…O2 (x, -y, ½+z) has a donor-acceptor distance 2.730 Å and O2-H2…O1 (x, y, z-1) slightly shorter at 2.716 Å. The structure contains hydrogen bonded "wave-like" chains that are aligned approximately anti-parallel to the crystallographic *c*–axis (figure 3.8). Each chain has two alternating planes of hydrogen bonds that are aligned approximately parallel to the 5 2 0 and the –5 2 0 lattice planes as shown in figure 3.8 (B). The unit cell volume is 298.6 $Å^3$, which gives an average volume of 74.7 $Å^3$ per molecule.

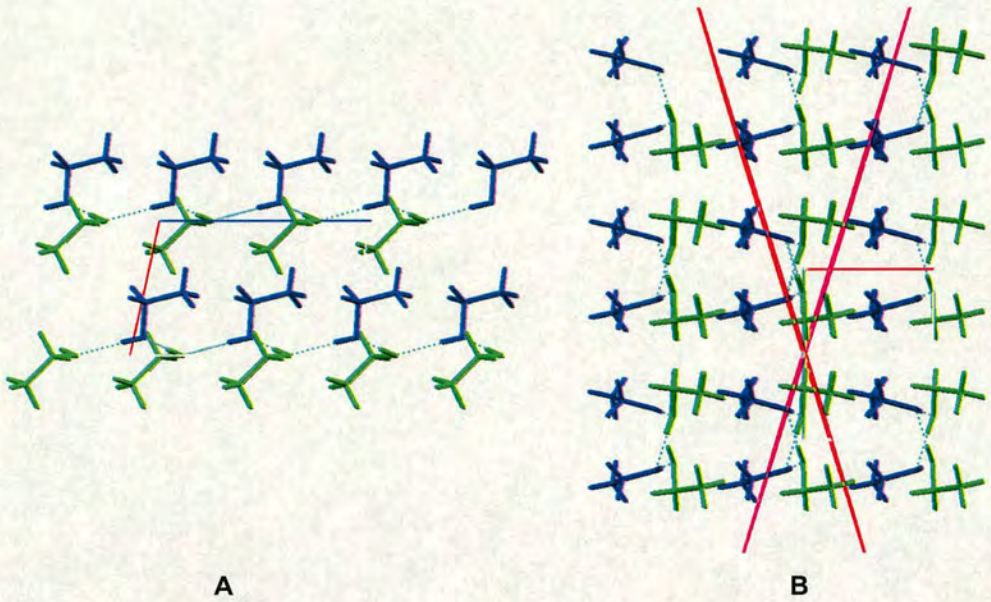

Figure 3.8 (A) Hydrogen bonded chains in the low temperature polymorph of ethanol. The wave-like chains are aligned approximately anti-parallel to the *c*–axis. [*a–axis* in red, *c*–axis in blue]

Figure 3.8 (B) A projection of the structure viewed down the *c*–axis showing the alternating planes of the hydrogen bonded chains parallel to the 5 2 0 (purple) and –5 2 0 (red) lattice planes [*a*–axis in red, *c*–axis in blue, *trans* conformer in blue, *gauche* conformer in green]

At a pressure of 3.0 GPa and room temperature, ethanol crystallises in the monoclinic space group $P2_1/c$ with only one molecule in the asymmetric unit (Allan *et al*)[2]. In this study, non-hydrogen atoms were located using single crystal x-ray diffraction and hydrogen atoms by *ab-initio* calculations. The molecule adopts the *trans* conformation, the C2-C1-O1-H1 torsion angle measuring –171.2°. There is one unique hydrogen bond O1-H1…O1 (2-x, ½+y, ½-z) with a donor acceptor distance of 2.693 Å. These form "zig-zag" chains which are aligned approximately parallel and anti-parallel to the -2 0 2 lattice plane. This polymorph has a unit cell volume of 239.0 $Å^3$, resulting in an average molecular volume of 59.75 $Å^3$, a 25 % decrease compared to the low temperature / ambient pressure phase.

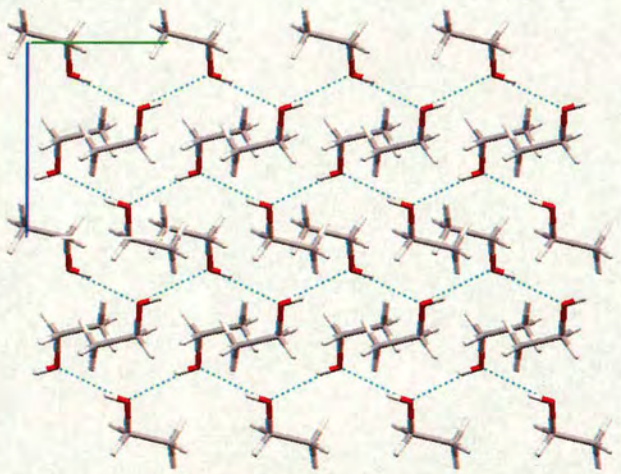

Figure 3.9 The high-pressure phase of ethanol, viewed down the crystallographic *a*–axis. [*b*–axis in green, *c*–axis in blue]

The striking difference between the two phases is the difference in the number of conformers in each phase. This has a major effect on the packing of the molecules which is observed in Figure 3.10. As discussed above, at low temperature the chains are "wave like" and at high pressure, they are "zig-zag".

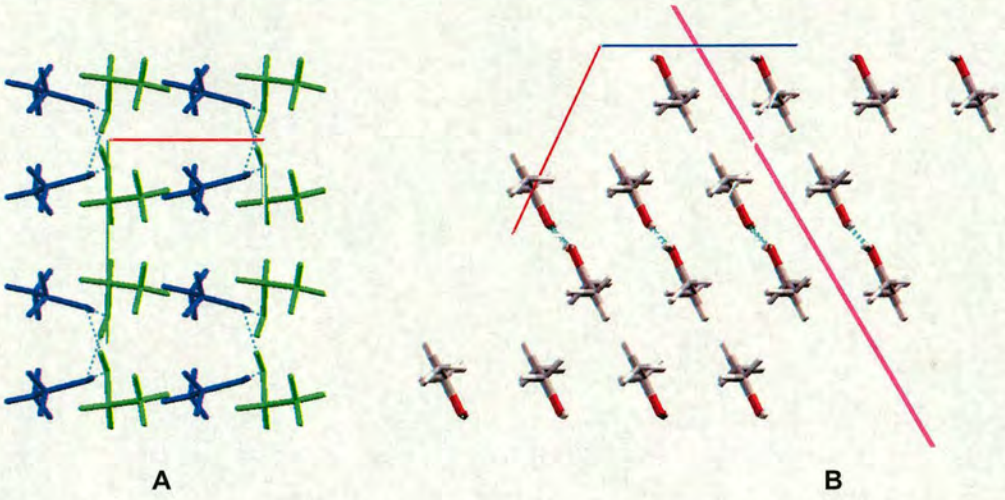

Figure 3.10 (A) The low temperature phase of ethanol showing the arrangement of the "wave - like" chains. [*a* – axis in red, *b* – axis in green]

Figure 3.10 (B) The high-pressure phase of ethanol showing the "zig-zag" layers of chains aligned approximately parallel to the -2 0 2 lattice plane (purple). [*a*–axis in red, *c*–axis in blue]

The more recent study of Allan *et al*[3] using synchrotron radiation to locate the hydrogen atoms used a single crystal of ethanol at 2.75 GPa and found that the hydroxyl hydrogen atom is actually disordered over two sites in the molecule. This implies that both the *trans* and *gauche* molecules are present in the structure. The refined occupancies are 0.7 (1) for the *trans* [C3-C2-O1-H11 = 177 (4)°] and 0.3(1) for the *gauche* [C3-C2-O1-H12 = -44 (9)°]. Both phases contain two different conformers in two different fashions, these conformational changes are discussed in more detail in chapter 4.

3.2.3 A Comparison of the Crystal Structures of Phenol at Low Temperature and High Pressure

The third mono-alcohol to be studied is phenol (C_6H_5OH) for which pressure induced polymorphism occurs at a very low pressure of 0.16 GPa. In phenol, the hydroxyl group is bonded to an aromatic ring rather than an sp^3 hybridised carbon

atom. Although this has consequences on properties such as acidity, phenol is a stronger acid than either methanol or ethanol due to the relative stability of the phenoxide anion due to resonance stabilisation, the hydrogen bonding properties in the solid state are certainly comparable to the other mono-alcohols discussed in this chapter. Zavodnik *et al*[12] reported the low temperature phase in 1987, Allan *et al*[4] the high pressure phase in 2002. Both polymorphs have the space group $P2_1$, although the characteristic hydrogen bond type for each phase differs. The low temperature phase has pseudo-3 fold helices whereas in the high-pressure polymorph, there are two unique "zig-zag" chains (figure 3.11).

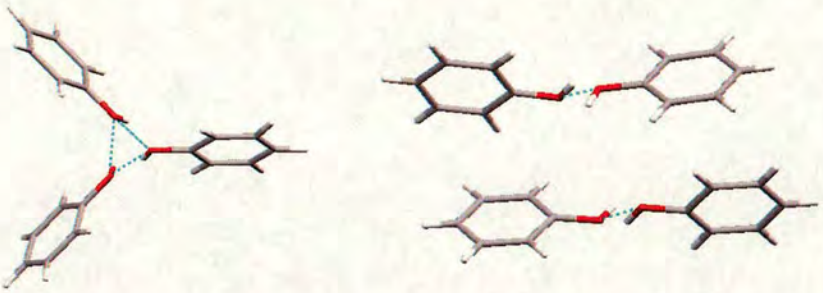

A B

Figure 3.11 (A) The low temperature phase of phenol showing the pseudo 3-fold helices viewed down the crystallographic *a*–axis.

Figure 3.11 (B) The high-pressure phase of phenol showing the "zig-zag" chains viewed down the crystallographic *b*–axis.

Each set of chains have two main properties: first the hydrogen bond length, and second the angle of the phenyl ring with respect to the alignment of the hydrogen bonded chains. As both polymorphs have Z' = 3, each has 3 unique hydrogen bonds but in the low temperature phase, these are involved in the same unique chain which is 3 fold helical by translational symmetry, whereas at high pressure there are two distinct chains. These chains are both planar "zig-zag", described by Taylor and Macrae[6], and complete the structure. One involves a single crystallographically

independent phenol molecule that is hydrogen bonded to the neighbouring molecules around a 2_1 screw axis, and the other involving two crystallographically independent phenol molecules which are also related to their neighbours within the chain by simple translational symmetry (figure 3.12).

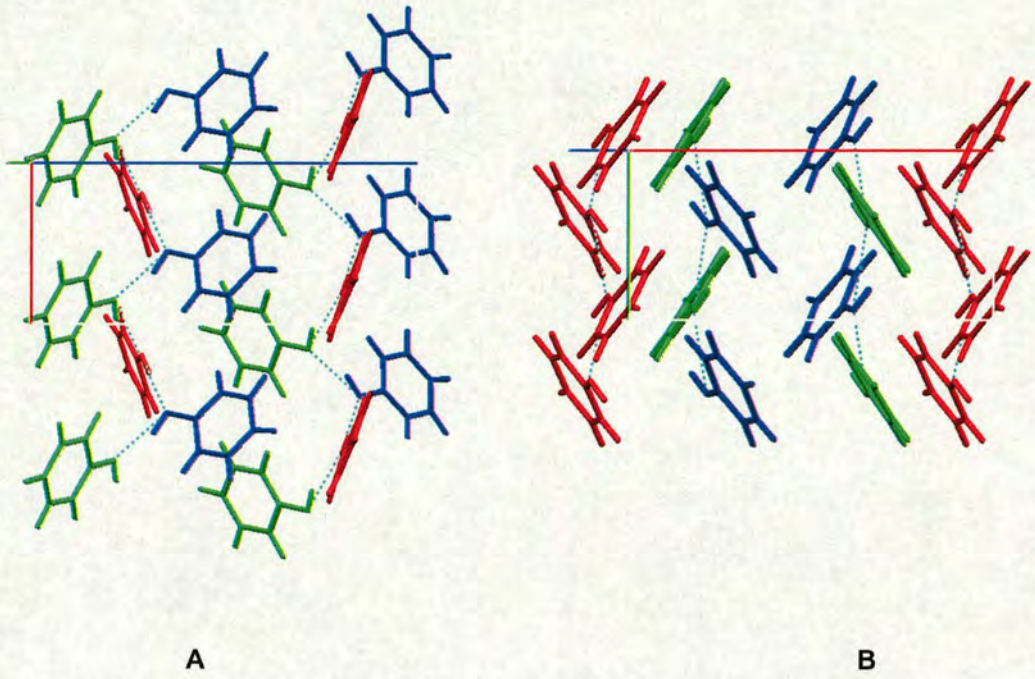

A B

Figure 3.12 (A) The low temperature phase of phenol showing the hydrogen bonded chains aligned parallel and anti parallel to the *b*–axis. Crystallographically unique molecules are shown in red, green and blue. [*a*–axis in red, *b*–axis in green, *c*–axis in blue]

Figure 3.12 (B) The high-pressure phase of phenol showing the two unique hydrogen bonded "zig-zag" chains. The different types of chains have the hydrogen bond aligned in opposite directions parallel to *b*. Crystallographically unique molecules are shown in red, green and blue. [*a*–axis in red, *b*–axis in green, *c*–axis in blue]

The donor – acceptor distances in the hydrogen bonded chains are longer in the high pressure structure compared to the low temperature structure. In the low temperature phase, the distances are 2.693, 2.664 and 2.655 Å for O3 – O2, O2 – O1 and O1 – O3 (x y+1, z) respectively. At a pressure of just 0.16 GPa, these increase to 2.996 Å for O1C – O1C (2-x, ½+y, 3-z) for the red chain (chain C) shown in figure 3.12 (B), 2.941 Å for O1B – O1A and 2.957 Å from O1A – O1B (x, y+1, z)

for the chain involving both blue and green molecules (chain AB). The question arises, is this an electrostatic effect, or a packing effect? There are two possible interactions between neighbouring phenyl groups, one is C – H … π and the other π - π stacking.. For π - π stacking to occur, the phenyl rings must be parallel to each other and at a distance of approximately 3.4 Å. In this case, the rings tilt at an average angle of 22.9° from the direction of the hydrogen bonded chains, whereas at high pressure, the average value for chain AB is 32.6° and for chain C it is 32.0°. The molecules are separated by 1 unit cell length, in the low temperature phase this is a distance of 6.05 Å, and at high-pressure 5.44 Å. To conclude, in both polymorphs these distances are too far away from the dimensions for ideal π - π stacking, (90° and 3.4 Å) to have any effect. It is postulated that with increasing pressure, these values could approach the ideal settings for π - π stacking. For the C-H…π interactions, again the distances observed are far longer than the ideal values required for this interaction to occur. Therefore, this lengthening of the hydrogen bond under pressure must be a steric effect. It is also important to note that the differences in intermolecular distances and angles are very large considering the relatively small pressure applied (0.16 GPa).

3.3 The Low Temperature and High Pressure Crystal Structures of Cyclobutanol

3.3.1 Introduction

Cyclobutanol (C_4H_8O) is a clear, colourless liquid with a melting point of 221 K and a boiling point of 395 K. It is a secondary alcohol which consists of four sp^3 hybridised carbon atoms arranged in a puckered four membered ring (figure 3.13). The puckering of the ring increases the angle strain in the molecule, but relieves the eclipsing interactions of adjacent C-H bonds.

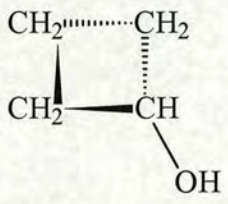

Figure 3.13 Cyclobutanol

The high-pressure and low-temperature crystal structures of cyclobutanol have been determined using a combination of single-crystal x-ray diffraction techniques and *ab-initio* density functional calculations. At temperatures below the melting point of 221 K, we find that the structure crystallizes in the orthorhombic space group *Aba*2, with 2 discreet cyclobutanol molecules in the asymmetric unit. The molecules form triple helical chains with a hydrogen bonded central core. At high pressure, just above the onset of crystallization at 1.3 GPa, we find a new phase where the molecules pack in the orthorhombic space group $Pna2_1$ with one molecule in the asymmetric unit. The major difference between the low temperature and high-pressure phases is that under pressure, wave-like hydrogen bonded chains are formed.

3.3.2 Experimental

3.3.2.1 Differential Scanning Calorimetry (DSC)

The DSC results were obtained using a Perkin Elmer Pyris DSC 1. The sample of cyclobutanol was loaded into a sealed aluminium pan. Figure 3.14 shows that super-cooling occurs in the sample, and the liquid does not crystallise until it is warmed where the exothermic crystallisation peak occurs at 180 K (event C in figure 3.14). The small event which occurs in this first scan at approximately 138 K (event B in figure 3.14) is probably glass formation or some degree of ordering in the glassy phase. This is not present in the polycrystalline material. Melting occurs at 221 K (event A in figure 3.14).

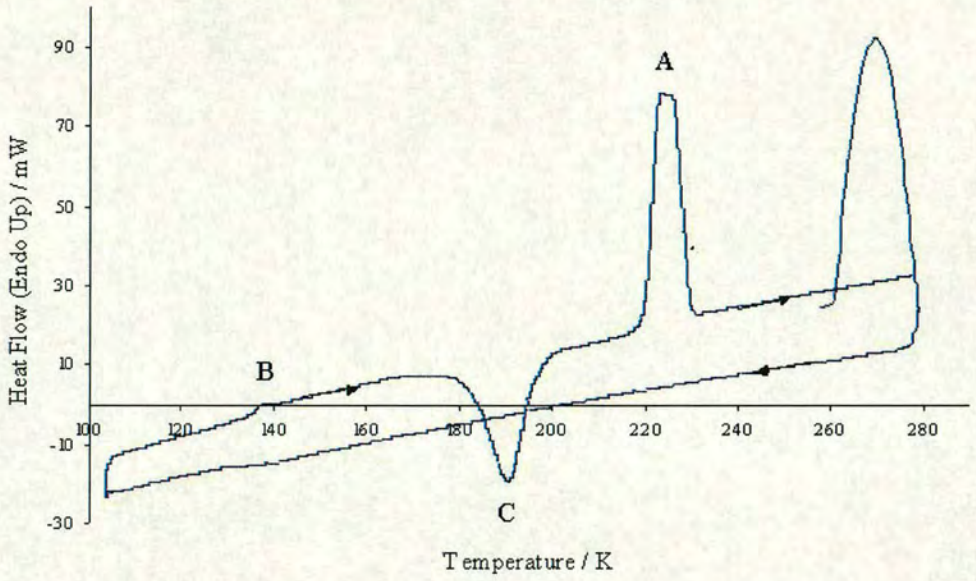

Figure 3.14 Graph of Heat Flow v Temperature for cyclobutanol loaded as a liquid at room temperature, scanning from 273 K to 105 K, then from 105 K to 273 K at 10 K per minute.

In order to test the phase stability of the solid, it was decided to cool the sample to 153 K and warm to 203 K where the crystallisation process is complete (event B in figure 3.15), and below the melting point of the sample at 221 K. The solid sample was cooled to 100 K and subsequently warmed through the melting point to 273 K (event A in figure 3.15). Figure 3.15 shows this temperature scan, and it is observed that no further events occur below the melting point down to a temperature of 100 K. This experiment was beneficial in that before carrying out the X-ray diffraction experiment, it was known that no phase change occurs, so a crystal can be grown at a temperature below 221 K, and cooled for data collection.

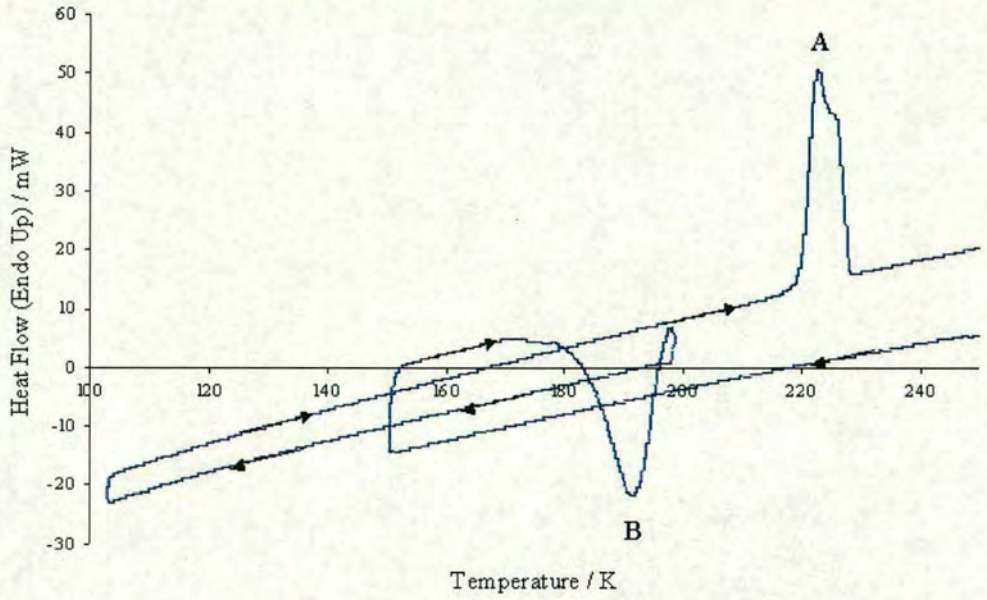

Figure 3.15 Graph of Heat Flow v Temperature for cyclobutanol loaded as a liquid at room temperature, scanning from 273 K to 153 K, then from 153 K to 203 K just above the onset of crystallisation, then from 203 K to 105 K back to 273 K at 10 K per minute.

3.3.2.2 Low Temperature Crystal Growth of Phase I

Liquid cyclobutanol was loaded into a capillary of 0.33 mm diameter that was attached to the goniometer head, mounted and centered on a BRUKER-APEX SMART[13] diffractometer, equipped with a cryogenic low-temperature unit and a laser heating system. The sample was cooled to just below the melting point of 221 K. A solid – liquid equilibrium was established at 60 % laser power, and a crystal was grown by applying 60 % laser power along approximately 0.5 mm of the capillary over 30 minutes, then reducing the laser power at the end of the cycle to 0 % for a further 20 minutes.

A set of matrix frames were obtained and although the diffraction was very weak at 10 s exposures, the pattern was indexed using GEMINI[14] where 23 out of 27 reflections gave the unit cell a = 9.350, b = 9.601, c = 9.651 Å and α = 89.98, β = 89.49, γ = 89.66. Using the 18 Å^3 rule for volume occupied by non-hydrogen atoms,

the volume of this cell is approximately 833 $Å^3$ which accounts for 8 molecules in the unit cell (720 $Å^3$), with hydrogen bonding accounting for the remaining space. As the diffraction was weak, it was decided to collect a hemisphere of data at this temperature, scanning 0.3° in ω for a 30 s exposure time.

After data collection, the sample was re-indexed using SMART[13], which gave the unit cell $a = 9.708$, $b = 9.741$, $c = 9.419$ Å, $\alpha = 89.91$, $\beta = 90.02$, and $\gamma = 90.02°$ with a cell volume V = 888.06 $Å^3$. Determination of the Bravais lattice yielded the following possibilities, listed in table 3.1:

Bravais Lattice	***a* / Å**	***b* / Å**	***c* / Å**	***α* /°**	***β* /°**	***γ* /°**
Tetragonal P	9.668	9.673	9.328	90.154	90.002	90.095
Orthorhombic C	13.665	13.687	9.328	90.107	90.111	89.971
Orthorhombic P	9.328	9.668	9.673	90.095	90.154	90.002
Monoclinic C	13.665	13.687	9.328	90.107	90.111	89.971
Monoclinic P	9.328	9.668	9.673	90.095	90.154	90.002
Triclinic P	9.328	9.668	9.673	90.095	90.154	90.002

Table 3.1 Possible Bravais Lattices for the low temperature phase of cyclobutanol

The data were integrated as triclinic P, and an absorption correction applied using SADABS[15]. The merging in xprep suggested the crystal system to be monoclinic with the space group *C*2. The structure solved and refined to 5.5 % using SHELXS[16] and SHELXTL[17] respectively with all the alkyl hydrogens fixed geometrically to ride on their parent carbon atoms and the hydroxyl hydrogens were found on the difference map. Using the MISSYM facility in PLATON[18] to check for additional symmetry it was found that there were two glide planes in addition to the 2-fold axis. The suggested new Bravais lattice was orthorhombic mmm in the space group *Aba*2. Referring back to the BRUKER SMART[13] program, the Bravais lattice was then re-determined as Orthorhombic C and after subsequent reintegration of the data using SAINT[19], the structure was subsequently solved and refined in the same manner as above, but now in the correct space group.

As the first data set was collected just below the melting point, the sample was then cooled to 100 K for subsequent data collection in order to slow thermal vibrations, again scanning 0.3° in ω although a shorter exposure time of 20 s was used. Refinement statistics are shown in table 3.3 on page 23.

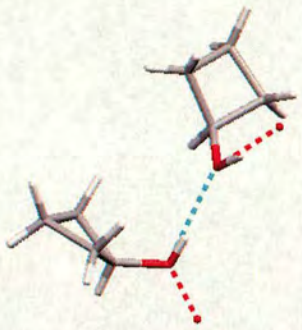

Figure 3.16 The asymmetric unit of phase I of cyclobutanol

Below the 221 K melting point of cyclobutanol, the solid crystallises in the orthorhombic space group *Aba*2 with unit cell dimensions a = 9.379 (2), b = 13.658 (2), c = 13.661 (2) Å at 220 K. There are two unique molecules in the asymmetric unit (figure 3.16), each acting as both a hydrogen bond donor and hydrogen bond acceptor. Table 3.2 shows the dimensions of both hydrogen bonds at 220 K and 100 K.

Donor – Acceptor	220 K	100 K
O1…O2$^{\#1}$	2.742 (2) Å	2.736 (2) Å
O2…O1	2.709 (3) Å	2.703 (3) Å

Table 3.2 The donor - acceptor distance of the hydrogen bonds in cyclobutanol at 220 K and 100 K [#1 = x-½, ½-y,z].

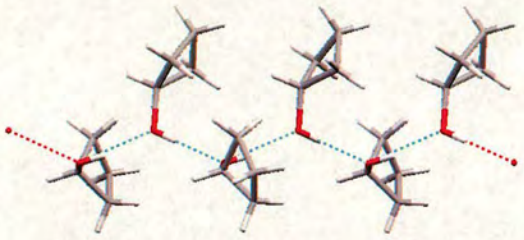

Figure 3.17 Hydrogen bonded chains of cyclobutanol molecules, aligned parallel to the crystallographic *a*-axis

The crystal structure is characterised by the presence of basic, binary hydrogen bonded chains of cyclobutanol molecules aligned parallel to the crystallographic *a* – axis. The chains are assigned the graph set notation $C_2^2(4)$ – having two unique hydrogen bond donors and two unique hydrogen bond acceptors involving four atoms - the hydroxyl groups in neighbouring molecules. Figure 3.17 shows a hydrogen bonded chain. The molecules on the lower side of the chain in the figure have the alkyl group alternating in front and behind the hydroxyl group of the chain, giving the chain its helical nature as shown in figure 3.18 (A).

In the packing plot projected down the same crystallographic *a*-axis, it is observed that neighbouring chains intertwine where the alkyl groups of molecules on neighbouring chains lie on top of one another (figure 3.18 (B)). The chains themselves are aligned in layers perpendicular to the crystallographic *a*–axis. As neighbouring layers lie on top of each other, it can be considered to have 8 nearest neighbouring chains.

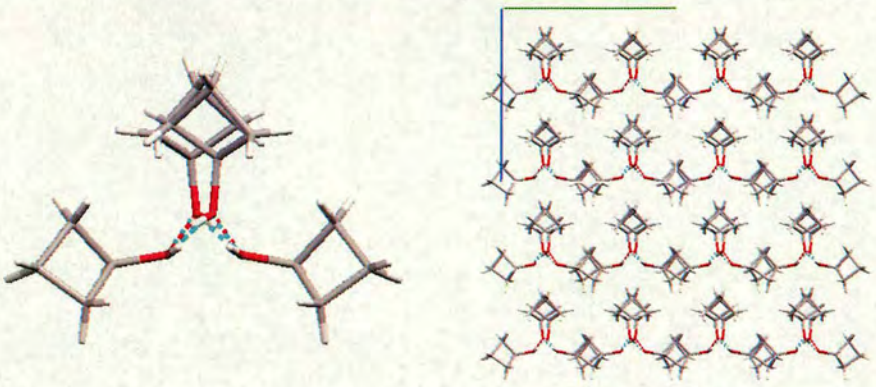

(A) (B)

Figure 3.18 (A) Hydrogen bonded chains of cyclobutanol phase I viewed down the crystallographic *a*-axis showing the pseudo 3-fold nature

Figure 3.18 (B) Packing plot of cyclobutanol phase I viewed down the crystallographic *a*-axis showing the intertwining of the chains via neighbouring alkyl groups [*b*–axis in green, *c*–axis in blue]

In figure 3.19, the projection down the crystallographic c – axis shows the layers of symmetry equivalent molecules. In the crystal structure, each molecule occupies a volume of 109.4 (1) $Å^3$ at 220 K and 108.4 (1) $Å^3$ at 100K, a difference of 0.9 %. To account for this difference there are slight decreases in cell dimensions and a small decrease in hydrogen bond length. This is due to the decreased thermal motion of the molecules with reduced temperature.

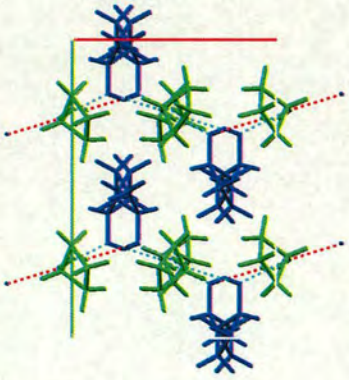

Figure 3.19 View down the crystallographic *c* - axis showing the hydrogen bonded chains of symmetry equivalent molecules [*a* – axis in red, *c* – axis in blue]

Temperature / Pressure	220 K / 0 GPa	100 K / 0 GPa	293 K / 1.3 GPa
Formula	C_4H_8O	C_4H_8O	C_4H_8O
Weight	72.10	72.10	72.10
Radiation	Mo K-α	Mo K-α	Mo K-α
Crystal System	Orthorhombic	Orthorhombic	Orthorhombic
Space Group	Aba2	Aba2	$Pna2_1$
a/Å	9.379(2)	9.331(2)	4.9208(4)
b/Å	13.658(2)	13.642(2)	8.230(1)
c/Å	13.661(2)	13.619(2)	9.598(2)
Volume ($Å^3$)	1749.9(5)	1733.7(5)	388.71(9)
Z	16	16	4
No. reflections for cell	2278	3363	479
2θ range (°)	$6 < 2\theta < 52$	$6 < 2\theta < 52$	$6 < 2\theta < 40$
D_c (Mg/m^3)	1.095	1.105	1.232
μ mm^{-1}	0.076	0.077	0.086
Reflections collected	4279	5003	747
Unique data	918 [R(int) = 0.0456]	1093 [R(int) = 0.0508]	225 [R(int) = 0.0731]
No. of data with $I > 2\sigma$	824	922	197
T_{min}/ T_{max} [SADABS[15]]	0.693 / 1.000	0.766 / 1.000	0.425 / 0.928
Parameters	108	108	23
R_1	0.0454	0.0468	0.0708
wR_2	0.1043	0.1049	0.1553
S	1.074	0.995	1.131
$\Delta\rho_{max}$ ($eÅ^3$)	0.167	0.248	0.196
$\Delta\rho_{min}$ ($eÅ^3$)	-0.170	-0.217	-0.186

Table 3.3 Refinement Statistics for Cyclobutanol

3.3.2.3 High Pressure Crystal Growth of Phase II

Liquid cyclobutanol was loaded and pressurised in a Merrill-Bassett diamond-anvil cell[20] that had been equipped with 600 μm culet diamonds and a tungsten gasket. After the nucleation of several crystallites the temperature was cycled close to the melting curve, in order to reduce the number of crystallites. Finally, a single crystal was obtained at approximately 1.3 GPa that entirely filled the 175 μm gasket hole.

The diamond-anvil cell was mounted and centred on a Enraf-Nonius CAD-4[21] diffractometer (equipped with a monochromated Mo x-ray tube). Indexing of 24 reflections ($3.25 < \theta < 9.64$) using Dirax[22] gave the orthorhombic unit cell $a = 4.924$ (4), $b = 8.243$ (7) and $c = 9.601$ (11) Å.

On account of there being only 154 unique, strong data points collected using the CAD[21], a further data set was collected on a BRUKER-SMART[13] diffractometer. To gain the best coverage of reciprocal space that can be obtained from the diamond anvil cell, 8 runs of data were collected in the manner and sequence shown in table 3.4. Data were collected for an exposure time of 30 s per frame over a scan range of 0.3° in ω. After data collection, each set of frames were utilised for reflection indexing with GEMINI[14], and of the 283 thresholded spots over a raw count threshold of 500, 94 of these fitted the cell obtained from the CAD-4[21] for the high pressure phase of cyclobutanol, $a = 4.877$, $b = 8.151$, $c = 9.546$ Å, $\alpha = 89.74$, $\beta = 89.92$, and $\gamma = 89.81°$ with a cell volume V = 379.45 Å^3. The remaining 189 reflections were all accounted for as those arising from the diamonds in the pressure cell. The Bravais lattice was determined as orthorhombic P, and subsequent least squares optimisation gave the worst fitting reflection –2 –3 0 that was within 0.002 of the integer value of hkl.

Run	2θ (°)	ω range (°)	ψ (°)	No. of Frames
1	-28	-8 → -40	90	106
2	28	40 → -40	90	266
3	-28	-140 → -215	90	250
4	28	-140 → -172	90	106
5	-28	-140 → -218	270	260
6	28	-140 → -172	270	106
7	-28	-8 → -40	270	106
8	28	35 → -40	270	250

Table 3.4 Scan sequence for high-pressure data collection on Bruker SMART diffractometer. Data were collected using a scan step of –0.3° in ω for an exposure time of 30s.

At a pressure of 1.3 GPa, cyclobutanol crystallises in the orthorhombic space group $Pna2_1$ with unit cell dimensions a = 4.921 (1), b = 8.230 (1), c = 9.598 (2) Å, which were refined using 479 reflections in SAINT[19] (the CAD-4[21] cell refinement could only be done on 24 reflections). After integration, the program SHADE[23] was used to reject reflections for which either the incident or diffracted beam was completely absorbed by the steel body of the diamond anvil cell resulting in complete shading of the detector. Also, reflections with poor correlations (< 0.3) between the measured and calculated profiles were rejected. The remaining reflections are corrected for absorption by the pressure cell components (diamond, beryllium and tungsten) using SADABS[15] and the transmission ranged from 0.425 to 0.928. The low minimum transmission factor arises from partial shadowing of reflections by the highly absorbing tungsten gasket.

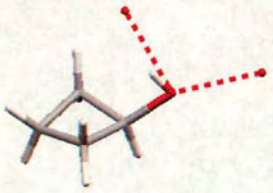

Figure 3.20 One molecule in the asymmetric unit of cyclobutanol phase II - the high pressure phase

There are 4 molecules in the unit cell with one unique molecule in the asymmetric unit that acts dually as a hydrogen bond donor and a hydrogen bond acceptor (figure 3.18). There is only one unique hydrogen bond in the structure, distance O1…O1$^{\#1}$ 2.809 (4) Å (#1: x-½, -y-½, z). These form hydrogen bonded chains expressed as C(2) in graph set notation – the repeating unit containing one hydrogen bond donor and one acceptor. At a pressure of 1.3 GPa, each molecule occupies 97.2 (1) Å^3, and comparing this to the volume of the low temperature phase gives a 10.3 % reduction in volume with respect to the 100 K structure and an 11.2 % reduction in volume compared to the 220 K structure.

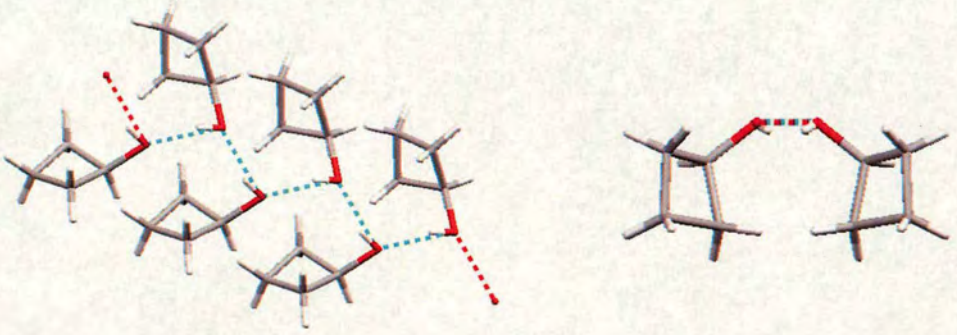

(A) **(B)**

Figure 3.21 (A) The wave-like hydrogen bonded chains of cyclobutanol

Figure 3.21 (B) Projection of the hydrogen bonded chains of the high-pressure phase of cyclobutanol viewed down the crystallographic *a* - axis

Figure 3.21 (A) shows the hydrogen bonded chains of cyclobutanol molecules. The chains involve a repeating unit of two molecules related by the *a*-glide perpendicular to the crystallographic *b*-axis. Unlike the low temperature phase, the packing of the chains shows no intertwining and, instead, the chains are aligned in layers perpendicular to the *b*-axis. There are two distinct layers, as shown in figure 3.21: In layer A the molecules are aligned parallel to the crystallographic *a*-axis; and in layer B they are aligned anti-parallel to the same axis. Layer B is then displaced by half a unit cell with respect to layer A. Each layer is made up of wave-like chains that have six nearest neighbour chains.

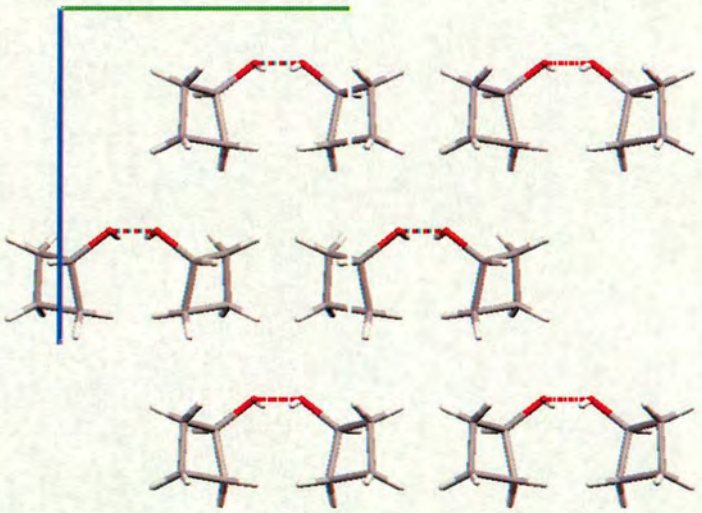

Figure 3.22 Packing plot of the high-pressure phase of cyclobutanol viewed down the crystallographic *a*-axis

The wave-like motif within the hydrogen bonded chains is shown in figure 3.23. This projection down the crystallographic *c*-axis also shows the opposing polarity of the hydrogen bonded chains. Layer A has opposite polarity to layer B therefore the overall polarity is zero.

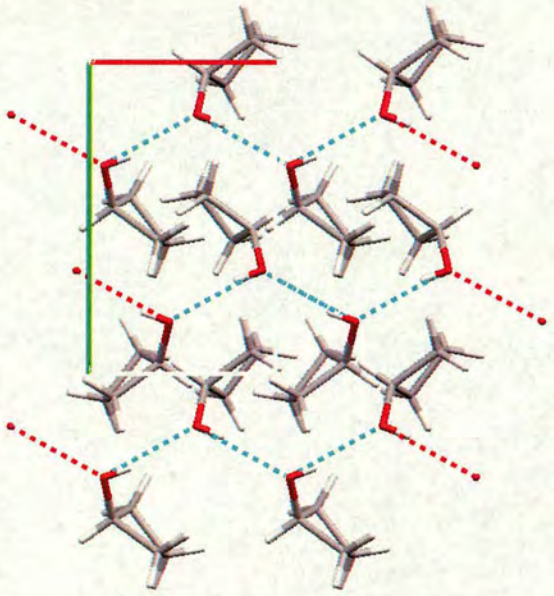

Figure 3.23 The hydrogen bonded chains of phase II of cyclobutanol viewed down the crystallographic *c* – axis.

3.3.3 Discussion and Comparison of Phases

Perhaps the most significant change between the low temperature and the high-pressure polymorphs is the reduction in molecular volume. At ambient pressure and 220 K each molecule occupies 108.4 (1) $Å^3$ compared to 96.8 (1) $Å^3$ at room temperature and 1.27 GPa, a decrease of 10 %. One would assume that the first property that would change would be the intermolecular distances, followed by bond angles and then bond lengths, in order of increasing bond energies. At 1.3 GPa, the unique hydrogen bond has a donor - acceptor distances of O1...O1$^{\#1}$ 2.809 (4) Å [#1 x-½, -y-½, z]. In the low temperature phase there are two unique hydrogen bonds, at 220 K the donor – acceptor distances are O2...O1 2.709 (3) Å and O1...O2$^{\#1}$ 2.742 (2) Å. At 100 K, the distances have donor – acceptor distances of O2...O1 2.703 (3) Å and O1...O2$^{\#1}$ 2.736 (2) Å [#1 x-½, ½-y, z]. In fact the donor – acceptor distance for the low temperature phase is slightly shorter than in the high-pressure phase, which is counter intuitive although this was also found to be the case for phenol

(discussed in section 3.2.3). In the case of phenol, it was suggested that the reason for the increase in the hydrogen bond distance was due to either an electronic or steric effect, the former was ruled out as the intermolecular distances required for either π-π stacking or C-H...π interactions are far shorter than the observed distances. This similar observation for cyclobutanol provides further evidence that this lengthening of hydrogen bond is in fact a steric effect. The hydrogen bonding motifs of both phases consist of hydrogen bonded chains – at low temperatures the chains are helical and at high pressure they are wave like.

The other intermolecular distances that must be considered are the carbon - carbon distances. The change in molecular volume cannot be attributed to the intermolecular hydrogen bonding as they are much the same, if not slightly shorter in the low temperature phase. To compare the intermolecular carbon - carbon distances between the two phases of cyclobutanol, the shortest distances were taken for each and a "cut off" was established to allow a comparison of the two phases. Table 3.5 shows the number of C-C distances for the low temperature and high-pressure phases. The "cut off" for this molecule was 4.0 Å, all contacts between 3.5 and 4.0 Å were considered sufficient for the comparison of the two phases. At 1.27 GPa, the high-pressure phase of cyclobutanol has 18 intermolecular carbon - carbon distances between 3.0 – 4.0 Å, compared to the low temperature phase where there are only 9.

Distance / Å	220 K / 0 GPa	100 K / 0 GPa	293 K / 1.3 GPa
3.0 → 3.6	0	0	0
3.6 → 3.8	3	3	6
3.8 → 4.0	6	6	12
Total	9	9	18

Table 3.5 Number of intermolecular C-C distances between 3 and 4 Å per molecule

Also the intermolecular carbon – oxygen distances can be considered and these are given in table 3.6. In a similar manner to the C-C intermolecular distances, there is an increase in the number of C-O distances between 3 – 4 Å.

Distance / Å	220 K / 0 GPa	100 K / 0 GPa	293 K / 1.3 GPa
3.0 → 3.6	2	4	10
3.6 → 3.8	8	6	6
3.8 → 4.0	3	3	0
Total	13	13	16

Table 3.6 Number of intermolecular C-O distances between 3 and 4 Å per molecule

Ab-initio calculations, carried out by Mr Iain McLeod (Department of Physics, University of Edinburgh), were used to determine accurately the hydrogen atom co-ordinates and calculate the energy difference between the phases. Appendix 1 lists calculated co-ordinates, cell dimensions and relative enthalpies of phase I at 0 GPa and 1.3 GPa, and phase II at 0 GPa and 1.3 GPa. All calculations are carried out at 0 K so to omit thermal effects. The rearrangement of the molecules from the triple helical chain to the wave-like chain results in an energy difference of 4.8 $kJmol^{-1}$ at 1.3 GPa.

It is observed that the intramolecular distances do not change, and also the intermolecular distances remain similar at both low temperature and high pressure. To account for this 10 % reduction in molecular volume, it has been shown that although the intermolecular distances remain similar, in the high-pressure phase there are more of these "contacts" per molecule compared to the structure at low temperature. Therefore, at high pressure the molecules adopt a packing arrangement that is more efficient than at low temperature in order to compensate for the reduction in molecular volume.

3.4 The Crystal Structure of Phase II of Tertiary Butanol at Low Temperature and High Pressure and the Comparison with Phase IV

3.4.1 Introduction

Tertiary butyl alcohol or 2-methyl-2-propanol ($C_4H_{10}O$) is a colourless liquid at just above room temperature with a melting point of 298.5 K and a boiling point of 355.2 K. The molecule is a tetrahedral carbon surrounded by 3 methyl groups and 1 hydroxyl group (figure 3.24).

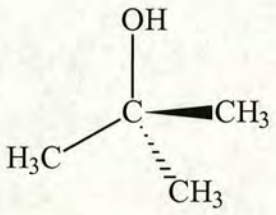

Figure 3.24 Tertiary Butanol

The low temperature phase behaviour of tertiary butanol is very complicated and has been extensively studied using a combination of calorimetric, dilatometric, infra-red and x-ray diffraction techniques. Oetting *et al*[24] identified three phases of tertiary butanol (phases II, III and IV) at low temperature using calorimetric measurements. Phase II is stable below 281 K, and transforms on heating to either phase III at 281.54 K, which is subsequently stable between 282 and 295 K, or phase I at 286.14 K. When crystals of phase I are stored at 298 K, the density of the sample increases with time, forming phase IV (Neu *et al*[25]). The structure of phase IV has been determined by single crystal x-ray diffraction by Steininger *et al*[26], and was found to be triclinic with space group P-1. The structure will be discussed in detail in section 3.3.2. Zone refinement of a distilled sample of tertiary butanol using the technique described in section 2.2 allowed the growth of a single crystal of phase II, which was found to be trigonal in space group P-3. It is also phase II that is found to be stable at high pressure, the crystal was grown at 0.85 GPa using the technique described in chapter 2.1. Attempts to isolate single crystals of phases I and III

proved unsuccessful, as the crystal moved in the capillary, and it was not possible to collect single crystal data successfully. Differential scanning calorimetry was used to confirm the presence of phases I and III.

3.4.2 The Crystal Structure of Phase IV

Phase IV of tertiary butanol which had its structure determined by Steininger *et al* (1989)[26], is stable under ambient conditions. Single crystals are obtained by allowing a pure liquid sample to stand at room temperature where the density of the liquid increases and crystals are formed. Under these conditions, the structure crystallises in the triclinic space group *P*-1 with cell dimensions a = 6.393 (2), b = 9.481 (3), c = 15.126 (4) Å and α = 85.47 (2), β = 79.60 (2), γ = 76.01 (2) °. There are six molecules in the unit cell, leaving three in the asymmetric unit which gives rise to three unique hydrogen bonds (figure 3.25). The donor acceptor distances are as follows: O1…O3 2.714 Å, O3…O2 2.712 Å and O2…O1 [1+x, y, z] 2.741 Å.

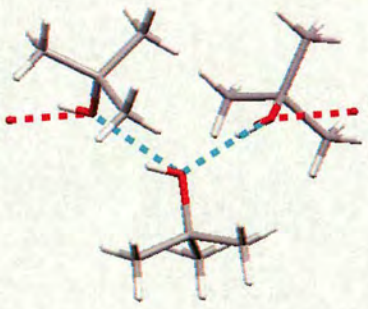

Figure 3.25 The asymmetric unit of phase IV of tertiary butanol

Figure 3.26 shows the chain formation through the hydrogen bonding of the hydroxyl groups of the molecules. In graph set notation, these are $C_3^3(6)$ chains which are aligned parallel to the crystallographic a-axis. Neighbouring chains are aligned anti-parallel to the a-axis, therefore the overall polarity of the structure is zero.

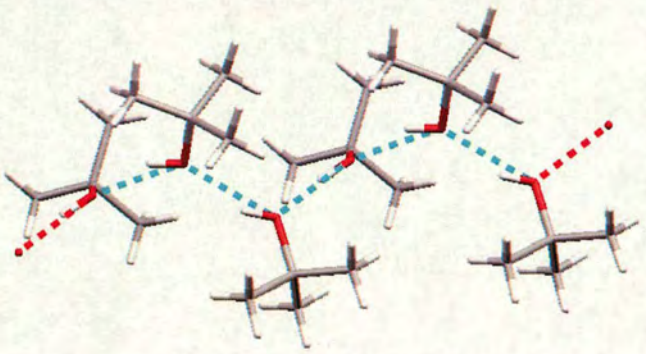

Figure 3.26 Hydrogen bonded chains of tertiary butanol molecules which are aligned parallel to the crystallographic *a*-axis

The pseudo three fold nature of the chains is observed in the projection of the molecules down the crystallographic *a*-axis as shown in figure 3.27. These chains can be described as tubes which are aligned in layers that are displaced by ⅓ of the *b*-axis.

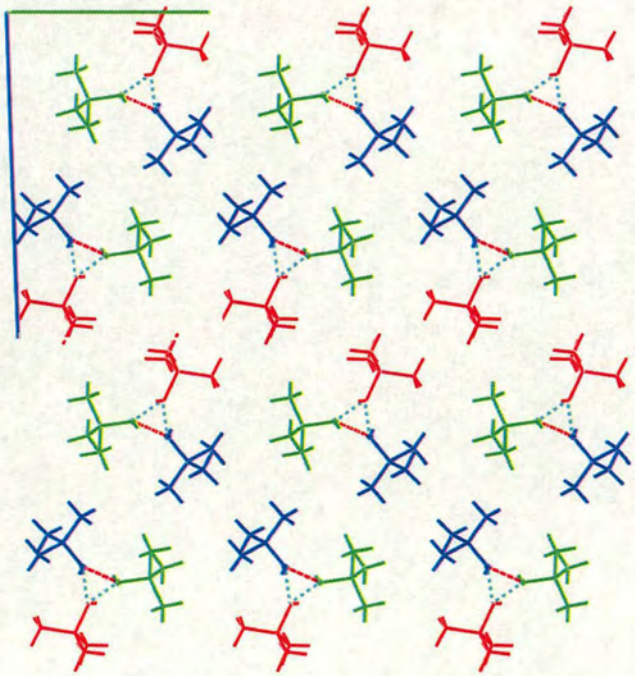

Figure 3.27 Packing plot viewed down the crystallographic *a*-axis showing the pseudo 3-fold nature of the chains aligned parallel to *a* [b-axis in green, c-axis in blue].

In figure 3.28, the alignment of the hydrogen bonds in the chains can be observed. This plot also demonstrates the hydrophobic and hydrophilic parts of the structure. The helical chains of tertiary butanol molecules have a hydrophilic inner core protected by the bulky hydrophobic outer core.

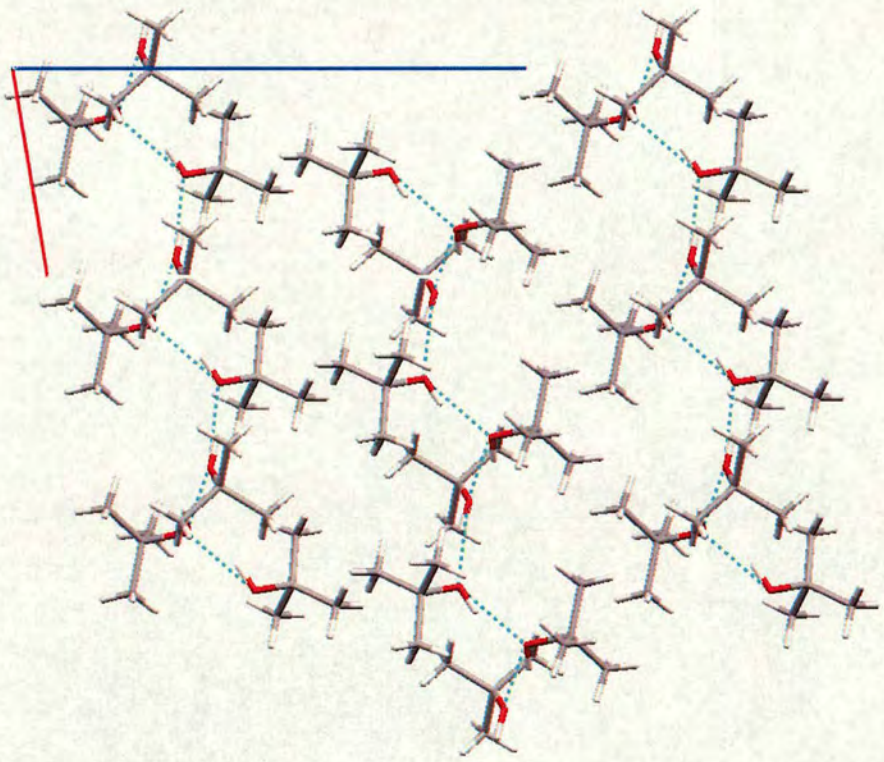

Figure 3.28 View down the crystallographic *b*-axis showing the C_3^3 (8) chains.

3.4.3 Experimental

3.4.3.1 Differential Scanning Calorimetry

The DSC results were obtained using a Perkin Elmer Pyris DSC 1. The sample of tertiary butanol was distilled and dried using the vacuum line and loaded as a liquid into a sealed aluminium pan. The first was carried out at a scan rate of 10 K per minute from 293 K down to 193 K and then back up to room temperature (Figure 3.29).

Crystallisation occurred at 280.6 K and was indicated by the large exothermic peak (event A in figure 3.29). Phase II is stable below 281 K from the study described in section 3.4.1 (Oetting *et al*[24]). In the calorimetric study (figure 3.29), this peak also has a small endothermic shoulder at 276.5 K. This is possibly due to some change within the instrument, but could equally have been produced by the sample which has a very complex phase behaviour. The next event is at 250 K on cooling (event B in figure 3.29), where another exothermic event occurs. This is a phase change, which is followed by another event at 238 K where there is a slight kink in the graph on both cooling and heating (events C and D in figure 3.29). It is postulated that this is due to ordering in the sample, either of the methyl hydrogens or the methyl groups themselves. The data collected are at 220 K, this we have assigned the label phase II, and is also found to be the phase stable at high pressure.

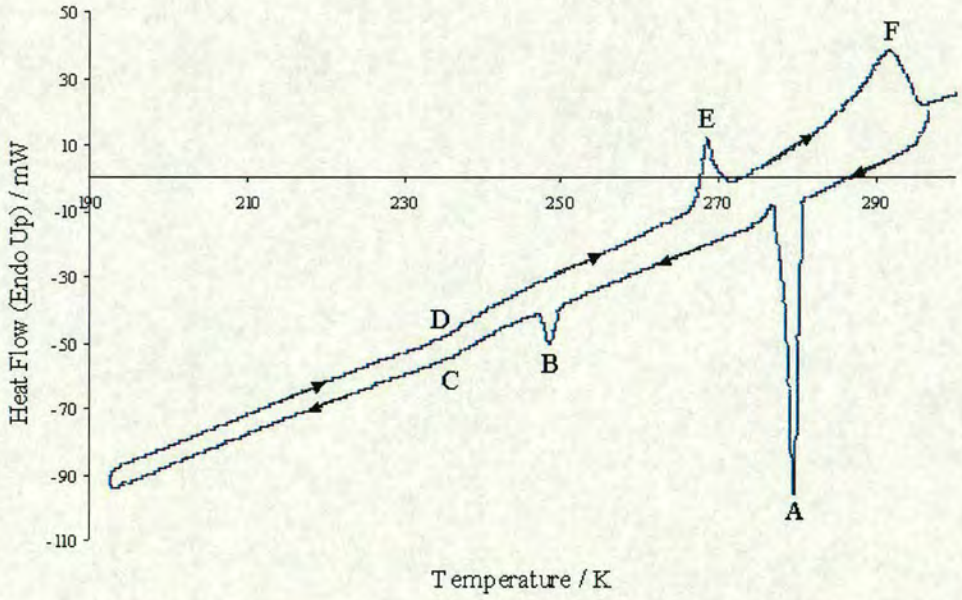

Figure 3.29 Graph of Heat Flow v Temperature for tertiary butanol loaded as a liquid at room temperature, scanning from 298 K to 193 K, then from 193 K to 313 K at 10 K per minute.

On heating from 193 K to room temperature, the kink in the scan at 235 K is observed, then an endothermic event at 267.3 K (event E in figure 3.29). This is the phase change associated with the exothermic peak at 250 K on cooling, although

there is some hysteresis observed in the sample. The melting curve of the sample is very shallow, the onset is just above the phase transition at 270 K and is completed some 20 K later at 290 K (event F in figure 3.29). This is the region where Oetting *et al*[24] identified three further phases in the sample, it is clear from this experiment that there are no further phases above 268 K, although there maybe a mixture of solid and liquid which may have affected their experiments.

3.4.3.2 Low Temperature Crystal Growth of Phase II

A distilled sample of tertiary butanol was loaded into a capillary using a vacuum line in order to prevent exposure to air, and therefore reduce the risk of contamination of water into the hygroscopic sample. The capillary, dimensions 0.5 x 0.1 x 0.1 mm, was mounted and centred onto a BRUKER-SMART[13] diffractometer (graphite monochromated Mo Kα radiation) equipped with a cryogenic cooling system, initially set at 243 K, and a 25 W CO_2 infra-red laser heating system. In an attempt to determine the structure of phase II, stable below 281 K, the laser was used to try to establish a solid - liquid boundary. It was found that at 243 K, the sample was too far below the melting point of 298.2 K to enable melting using the maximum permitted laser power. The temperature was then raised to 268 K, where a single crystal was obtained by zone refinement of the sample over a time span of 20 minutes using the technique described in section 2.3. The sample was indexed using SMART[13], and the crystal system was found to be trigonal. A data set was collected at 268 K as a backup, and then the sample was cooled to 220 K, whilst monitoring the diffraction pattern every 10 K to evaluate crystal quality. A further hemisphere of data were collected using 20 s exposures and 0.3° scans in ω. This data set was indexed, integrated, solved and refined routinely using SMART[13], SAINT[19], SHELXS[16] and SHELXTL[17]. Although the data collected at 268 K could be indexed, a reasonable structure solution could not be obtained. Using the solution obtained from the data at 220 K, a sensible refinement could not be achieved, this is either due to twinning and / or disorder. The unit cell volume shows a 4.1 % reduction in volume between the phases, it is postulated that at 268 K the sample is

highly disordered which would explain the exothermic peak in the temperature scan shown in figure 3.29 – possibly caused by an ordering of either the methyl groups or the methyl hydrogens. Table 3.5 shows the refinement statistics for the 220 K data, the high-pressure data and the unit cell dimensions at 268 K (page 70).

3.4.3.3 High Pressure Crystal Growth of Phase II

A sample of tertiary butanol was warmed above the melting point of 298.5 K and loaded as a liquid into the diamond anvil cell equipped with a tungsten gasket which had been pre-indented and drilled with a 200 μm hole. The cell was then closed, and the pressure slowly increased until nucleation occurred. Heat was applied to the cell using a heat gun until the sample had melted so that only one crystallite remained. This crystal was allowed to grow until it filled the gasket hole. The cell was then mounted on an Enraf-Nonius CAD-4[21] diffractometer and a rotation photo obtained using an image plate, rotating the cell around ϕ over a number of hours. Measuring the sets of spots on the rotation photograph allowed the centering of 19 reflections, which were then indexed using the program DIRAX[22] to give the trigonal unit cell a = 17.55 (2), c = 8.08 (1) Å. The unit cell was indexed from 16 of the 19 reflections where $2 < \theta < 10°$. The data collection was then set up to collect to a theta limit of 30° using an initial 1s scan stepwise over 0.35° in ω. The data were reduced using DECCOR2 and corrected for absorption from the gasket, diamond anvil cell and the sample using ABSORBU2. Refinement statistics are shown in table 3.7.

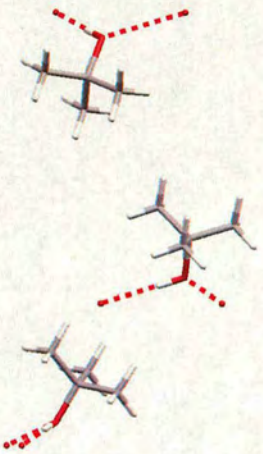

Figure 3.30 The asymmetric unit of phase IV of tertiary butanol

As in phase IV of tertiary butanol, the asymmetric unit of phase II also contains three molecules, which again gives rise to three unique hydrogen bonds within the structure. In the room temperature phase, these are involved in one unique hydrogen bonded chain, whereas in this new phase, the striking difference is that the molecules form six membered rings or hexamers, shown in figure 3.31. In graph set notation, both rings have the notation R^6_6 (12), with six oxygens and six hydrogens involved in the ring.

Temperature / Pressure	220 K / 0 GPa	268 K	293 K / 0.85 GPa
Formula	$C_4H_{10}O$	$C_4H_{10}O$	$C_4H_{10}O$
Weight	74.12	74.12	74.12
Radiation	Mo K-α	Mo K-α	Mo K-α
Crystal System	Trigonal	Trigonal	Trigonal
Space Group	P-3	P-3	P-3
a/Å	18.095(1)	18.313 (3)	17.55(2)
c/Å	8.404(1)	8.08 (1)	8.08(1)
Volume ($Å^3$)	2383.0(4)	2481 (1)	2155(4)
Z	18	-	18
No. reflections for cell	3699	2386	16
2θ range (°)	$5 < 2\theta < 50$	$4 < 2\theta < 40$	$4 < 2\theta < 20$
D_c (Mg/m^3)	0.930	-	1.028
μ mm^{-1}	0.064	-	0.071
Reflections collected	12157	-	1808
Unique data	2818 [R(int) = 0.0260]	-	1203 [R(int) = 0.2110]
No. of data with $I > 2\sigma$	2217	-	550
T_{min}/ T_{max}	0.816 / 1.000	-	0.253 / 0.562
Parameters	143	-	64
R_1	0.0432	-	0.1150
wR_2	0.1136	-	0.2598
S	1.041	-	1.012
$\Delta\rho_{max}$ ($eÅ^3$)	0.113	-	0.329
$\Delta\rho_{min}$ ($eÅ^3$)	-0.131	-	-0.215

Table 3.7 Refinement Statistics for Tertiary Butanol

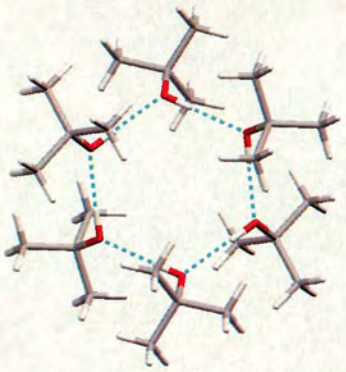

Figure 3.31 View of six tertiary butanol molecules forming a hexamer.

There are two unique hexamers within the structure, referred to as hexamer I and hexamer II. Hexamer I has one unique hydrogen bond, and is centred at (0, 0, ½). Hexamer II has two unique hydrogen bonds and is centred at (⅔, ⅓, 0.961). Hexamer I lies on an three-fold roto-inversion centre, whereas hexamer II lies only a three fold axis. Hydrogen atoms are placed along the donor – acceptor vector, which is along the edge of the hexamer. Figure 3.33 below shows the hexamers in projection down the crystallographic c – axis.

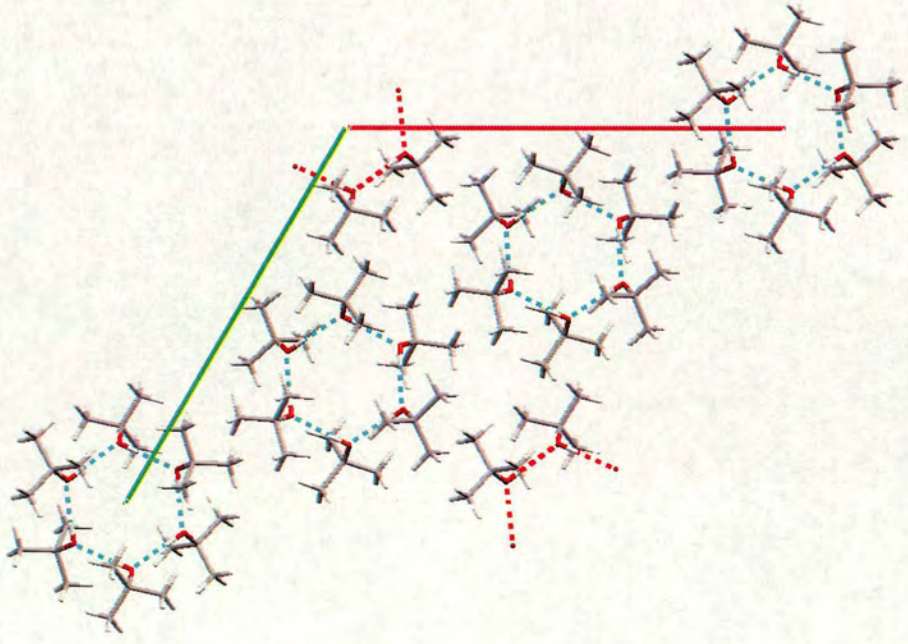

Figure 3.33 Projection down the crystallographic *c*-axis of the high-pressure phase of tertiary butanol showing the hexamer formation.

Table 3.8 shows the magnitude of the donor – acceptor distance of the three hydrogen bonds. Hexamer I contains solely O3-H3…O3 (x-y, x, -z+2) hydrogen bonds, and II contains alternating O1-H1..O2 (x, y, z+1) and O2-H1..O1 (-y+1, x-y, z-1) hydrogen bonds. The magnitudes are given in table 3.8.

	O1-H1…O2	O2-H1…O1	O3-H1…O3
220 K	2.775 (1)	2.779 (1)	2.729 (1)
0.85 GPa	2.786 (9)	2.720 (9)	2.698 (7)

Table 3.8 The donor – acceptor distances (Å) for the hydrogen bonds in phase II of tertiary butanol for the differing conditions.

Both hexamer I and hexamer II are arranged in the "chair" conformation common to cyclohexane and its derivatives. This is the most energetically favourable form of cyclohexane[26]. Figure 3.34 shows the t-butanol molecules arranged in the chair conformation. Neighbouring t-butanol molecules are orientated either above or below the mean plane of the ring.

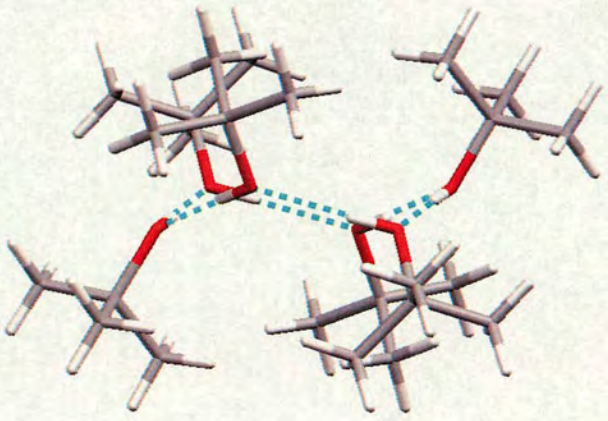

Figure 3.34 A view of a hexamer in tertiary butanol showing the "chair conformation". Neighbouring molecules are orientated either above or below the mean plane of the ring.

A measure of the flatness of the ring can be made by considering the torsion angle between four neighbouring oxygen atoms in the hexamer. Hexamers I (shown in red in figure 3.35) and II (with blue and green molecules in figure 3.35) each have a characteristic torsion angle. In hexamer I, the torsion angle from O3 – O3 (y, y-x, z) – O3 (y-x, -x, z) – O3 (-x, -y, 2-z) and measures 50.1 (1) ° at 220 K which reduces to 42.1 (7) ° at 0.85 GPa. In hexamer II, the torsion angle from O1 – O2 (x, y, 1+z) – O1 (1-y, x-y, z) – O2 (1-y, x-y, 1+z) measures 50.1 (1) ° at 220 K which reduces to 47.8 (5) ° at 0.85 GPa. As the torsion angle would be 0 ° for a perfectly flat hexagon, it can be stated that under pressure there is a slight flattening of the rings.

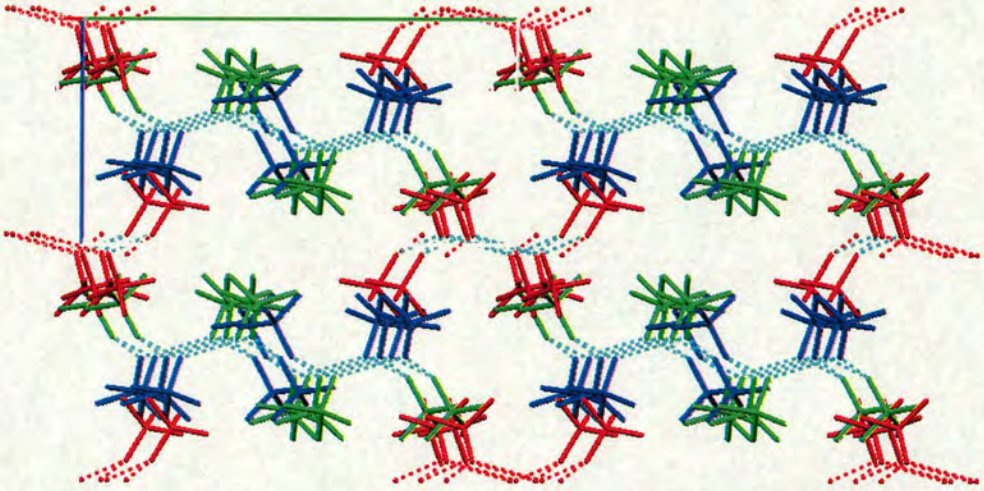

Figure 3.35 Packing plot of phase IV of tertiary butanol. Symmetry equivalent molecules are shown in colour and hydrogen atoms are omitted for clarity

3.4.4 Discussion and Comparison of Phases

In the known crystalline phases of tertiary butanol, phase II and phase IV (Steininger *et al*[26]) described in section 3.4, hydrogen bonded chains are observed in the solid under ambient conditions whereas under lowered temperature or at elevated pressure, 6 membered rings, or hexamers, are formed. In the papers described in the introduction to this chapter on packing of mono- and di-alcohols, it was suggested

that more sterically hindered alcohols will form rings as opposed to less sterically hindered alcohols which tend to form hydrogen bonded chains. The hypothesis in the papers by Taylor[6] and Brock[7] agree with the work carried out here in that the extra hindrance in this system is caused by a change in the conditions as opposed to the increase in size of the alkyl groups in the studies by Taylor[6] and Brock[7]. Reducing the temperature or increasing the pressure forces the molecules to rearrange in a more efficient way.

As for cyclobutanol, the number of C-C and C-O intermolecular distances increases with both a decrease in temperature or an increase in pressure. It is postulated that phase IV of tertiary butanol would be unstable at 0.85 GPa due to the existence of unfavourable intermolecular distances.

Distance / Å	Phase IV - 293 K	Phase II - 220 K	Phase II - 0.85 GPa
3.0 → 3.6	0	0	2
3.6 → 3.8	2	2	11
3.8 → 4.0	4	10	8
Total per asymmetric unit	6	12	21
Total per molecule	2	4	7

Table 3.9 The number of intermolecular C...C distances in tertiary butanol

Table 3.9 shows an increase with both reduction of temperature and application of pressure in the number of intermolecular C...C distances per molecule, under ambient conditions Phase IV has 2 distances per molecule between 3 and 4 Å compared to 4 at 220 K and O GPa and 7 at 293 K and 0.85 GPa in phase II. The distribution of these is similar at low temperature, whereas at high pressure the majority are between 3.6 to 3.8 Å as opposed to 3.8 to 4.0 Å in both phases at ambient pressure.

Distance / Å	Phase IV - 293 K	Phase II - 220 K	Phase II - 0.85 GPa
3.0 → 3.6	6	12	18
3.6 → 3.8	12	12	8
3.8 → 4.0	12	6	8
Total per asymmetric unit	30	30	34
Total per molecule	10	10	11,11,12

Table 3.10 The number of intermolecular C...O distances in tertiary butanol

In the case of the number of C...O distances, there are a similar number of these distances over the 1 Å range, a total of 10 per molecule in both ambient pressure phases and a spread of 11, 11 and 12 per molecule in phase II at 0.85 GPa. The main increase in the distribution is observed between 3.0 and 3.6 Å. This observation is strikingly similar to the results for cyclobutanol shown in table 3.6.

As was the case for cyclobutanol, the intramolecular distances will not change at these relatively low pressures and the intermolecular interactions, specifically the hydrogen bond lengths remain similar for all phases. The change in molecular volume is attributed to the increase in the number of observed C..C and C..O distances per molecule as discussed previously. The molecules are adopting a more efficient packing arrangement in order to compensate for the volume decrease due to the application of pressure. In addition to this, it is observed that a slight flattening of the ring occurs under pressure.

The calculated energy difference (Dr. S. J. Clark, Department of Physics, University of Durham) is very small, at 0.85 GPa the energy required to convert the helical chains of phase IV to the 6 membered rings of phase II is 0.4 $kJmol^{-1}$. This is the small energy difference is expected due to the instability phase IV, crystals of which grow from the neat liquid under ambient conditions (section 3.4.2). Appendix 2 lists the calculated unit cell dimensions, atomic co-ordinates and relative enthalpies.

3.5 Discussion and Comparison of the Different Phases of Mono-Functional Alcohols

There are two major similarities between the different alcohols under differing conditions: Firstly, the type of hydrogen bonding with respect to the steric effects; Secondly the observation that the molecules must rearrange in order to compensate for a reduction in molecular volume. At the relatively low pressures in the study of both cyclobutanol and t-butanol, the parameters affected are not the primary bond lengths or angles of the molecules, but it is the number of intermolecular distances which are altered. This corresponds to more efficient packing at high pressure.

With the exception of the high-pressure γ-phase of methanol, all of the observed hydrogen bonds are of a magnitude greater than 2.65 Å – i.e. they are very similar in energetic terms.

It is expected that the primary bond lengths and angles will not be altered at low pressures due to the high energy compensation, although lower energy intermolecular interactions such as hydrogen bonding may be expected to. A lower compensation of energy would be required to alter the C-C distances and C-O distances between neighbouring molecules. For all of the above parameters, the dimensions remain the same. The change is associated with the molecular packing where the molecules re-arrange into a different packing motif where more of the C-C and C-O intermolecular distances are found.

With a view to the packing motifs investigated by Brock[7] and more recently Taylor[6] all 1° and 2° alcohols in the Cambridge Structural Database are arranged in hydrogen bonded chains or rings. The results presented here are certainly in agreement with this. However, Taylor states, "chains can be zigzag, wave-like or helical, the latter becoming somewhat predominant as steric hinderance increases" and this is certainly not the case for cyclobutanol and also phenol. In cyclobutanol we find that the ambient pressure phase crystallises in pseudo 3-fold helices while

the high-pressure phase contains wave-like chains. This is the reverse of what is expected from Taylor's work. In tertiary butanol, the ambient phase IV forms pseudo 3-fold helical chains, whereas the non-ambient phase II forms hexamers and this certainly agrees with the hypothesis that the formation of rings are favoured by more sterically hindered alcohols.

3.6 References

1. Allan D.R., Clark S.J., Brugmans M.J.P, Ackland G. J. and Vos W.L., *Phys. Rev. B*, **58**, 11809 (1998).
2. Allan D.R. and Clark S.J., *Phys. Rev. B*, **60**, 6328 (1999).
3. Allan D.R., Parsons S. and Teat S.J., *J. Synchrotron. Radiat.*, **8**, 10 (2001).
4. Allan D.R., Clark S.J., Dawson A., McGregor P.A. and Parsons S., *Acta Cryst.*, **B58**, 1018 (2002).
5. Chaplin M., http://www.sbu.ac.uk/water/phase.html
6. Taylor R. and Macrae C. F., *Acta Cryst.*, **B57**, 815 (2001).
7. Brock C.P. and Duncan L.L., *Chem. Mater.*, **6**, 1307 (1994).
8. Tauer K.J. and Lipscomb W.N., *Acta Cryst.*, **5**, 606 (1952).
9. Boese R., private communication.
10. Torrie B.H. and Weng S.-X., *Mol. Phys.*, **67**, 575 (1989).
11. Jonsson P.-G., *Acta Cryst.*, **B32**, 232 (1976).
12. Zadodnik V.E., Bel'skii V.K. and Zorkii P.M., *Zh. Strukt. Khim.*, **28**, 175 (1987).
13. SMART: Area-Detector Software Package. (1993) Siemens Industrial Automation, Inc.: Madison, WI.
14. GEMINI, Sparks R.A.(1999), Bruker AXS, Madison, Wisconsin, USA.
15. SADABS, Sheldrick G.M. (2001), University of Gottingen and Bruker AXS, Madison, Wisconsin, USA.
16. SHELXS86 - Program for Crystal Structure solution. Sheldrick, G. M., Institüt für Anorganische Chemie der Universität, Tammanstrasse 4, D-3400 Göttingen, Germany, 1986.
17. SHELXTL Programs for Crystal Structure Analysis (Release *97-2)*. G. M. Sheldrick, Institüt für Anorganische Chemie der Universität, Tammanstrasse 4, D-3400 Göttingen, Germany, 1998.
18. *PLATON*, A.L.Spek, 2001, *PLATON, A Multipurpose Crystallographic Tool*, Utrecht University, Utrecht, The Netherlands.

19. SAINT: Area-Detector Integration Software. (1995) Siemens Industrial Automation, Inc.: Madison, WI.
20. Merrill L. and Bassett W. A., *Rev. Sci. Instrum.*, **45**, 290 (1974).
21. CAD4 Express Software. Enraf-Nonius, Delft, The Netherlands, 1994.
22. DIRAX: Duisenberg A.J.M, *J. Appl. Cryst.*, **25**, 92 (1992).
23. SHADE, Allan D.R., Clark S.J., Parsons S. and Ruf M., *J. Phys. Condens. Matter.*, **12**, L613 (2000).
24. Oetting F.L., *J. Phys. Chem.*, **67**, 2757 (1963).
25. Neu J.-M., *C.R. Acad. Sci. Paris,* **C267**, 1025 (1968).
26. Steininger R., Bilgram J.H., Gramlich V. and Petter W. , *Zeitschrift für Kristallographie*, **187**, 1 (1989).
27. Leong M.K., Mastryukov V.S. and Boggs J.E., *J. Phys. Chem.*, **98**, 6961 (1994).

Chapter 4

The High Pressure Crystal Structures of α - ω Di-Alcohols

4.1 Introduction

A further extension of the high-pressure study on mono-alcohols was to increase the number of functional groups within a molecule. The next logical series of molecules to study are the α-ω di-alcohols (diols), $HO(CH_2)_nOH$ A low temperature study of these molecules was carried out by Thallidi *et al*[1], which discussed the alternation in melting point between odd and even diols. They also showed that for the diols, $HO(CH_2)_nOH$, where $n \leq 3$, the hydrophilic interactions are dominant within the molecules, whereas for $n \geq 3$, the hydrophobic interactions dominate the packing.

Taylor and Macrae[2] discuss extensively the packing of diols $[C_mH_n(OH)_2]$. They state that the formation of chains is strongly preferred in comparison to the mono-alcohols, especially where the hydroxyl group is on the primary carbon. Of all 101 diol crystal structures in the Cambridge Structural Database[3], only a single structure forms no hydrogen bonds. This indicates that the diols have extensive packing possibilities that are highly likely to contain a hydrogen bonded packing motif. Unlike mono-alcohols, it is also possible for di-alcohols to form internal hydrogen bonds – though this does not happen in either the low temperature or high pressure structures of the molecules studied in this chapter. The chain length for the α-ω diols studied is too short to allow an energetically unfavourable conformation to occur. Also, in the case of the α-ω diols, both hydroxyl groups are chemically equivalent, although in some cases the stereochemistry of the α-ω carbon atoms vary. Hydrogen bonding occurring between diols which have primary hydroxyl groups have a strong preference in forming chains, 16 out of 17 structures in the CSD form chains, the remaining structure forms rings.

As for the mono-alcohols, Taylor and Macrae[2] have defined four categories for hydrogen bonded chain types: planar zigzag; threefold helices; fourfold helices; and wave-like chains. The wave like chains fall into two main groups: the first similar to the mono-alcohols where the chain is generated along a glide plane; and the second is generated by a screw axis.

In graph set terms, there are two possible hydrogen bond chain types that can be formed. The first involves only hydroxyl groups, and is denoted C_i^i (2i) where i is the number of unique hydroxyl groups in the asymmetric unit. For $HO(CH_2)nOH$ where $Z'=1$, this would be a C_2^2 (4) chain, if $Z'=2$, this would be a C_4^4 (8) chain and so on. The second chain type accommodates the alkane chain of the molecule, and is denoted C (n+3) where n=number of carbon atoms in chain and the 3 are the donor, acceptor and hydrogen atom in the bond. There are possibilities of more chains or rings formed by a combination of the above, but the aforementioned rules cover the majority of the packing motifs described in the chapter.

At temperatures below the melting point of 260 K, ethane-1,2-diol ($HO(CH_2)_2OH$) packs in the orthorhombic space group $P2_12_12_1$ and the molecules adopt the low energy *gauche* conformation (Boese *et al*[4]). These conformers pack in what is best described as a three dimensional hydrogen bonded network which is formed by C_2^2 (4) chains running through the structure in 3-dimensions. This polymorph was also found to be stable at 1 GPa, although there is a slight contraction in cell volume. At a pressure of around 2 GPa, a further polymorph exists, again the molecule is in the *gauche* conformation, although this time the molecules pack in the monoclinic space group $P2_1/n$ with layers of chains. At 2.3 GPa, a further new phase exists which is also in the monoclinic space group $P2_1/n$. However, at this pressure the molecules adopt the *trans* conformation and pack in layers. The layers are composed of intertwined hydrogen bonded chains that form 14 membered rings.

This conformational diversity is also present in propane-1,3-diol ($HO(CH_2)_3OH$), although in a different way. At low temperature, below the melting point of 241 K, the conformer is α-*gauche*, ω-*gauche* where the hydrogen bonded chains interlink to form 12 and 20 membered rings (Thallidi *et al*[1]). This polymorph has monoclinic $P2_1/n$ symmetry. At a pressure of 0.95 GPa there are actually two unique conformers in the asymmetric unit: one is α-*trans*, ω-*gauche* and the other α-*trans*, ω-*trans*. The crystal system is also monoclinic, but has the space group *Pc* with four molecules in the unit cell.

For diols with n > 3, even numbered diols (n = 4, 6, 8, 10, 12) are packed in layers (Thallidi *et al*[1]), figure 4.1 (A) shows layers of butane-1,4-diol molecules viewed down the crystallographic *a* – axis. These layers contain hydrogen bonded butane-1,4-diol molecules which adopt a herring bone motif (figure 4.1(B)). In even diols, the conformation adopted by the α and ω carbons are *trans* and *trans* respectively. This conformation gives rise to an absence in hydrogen bonding between the layers.

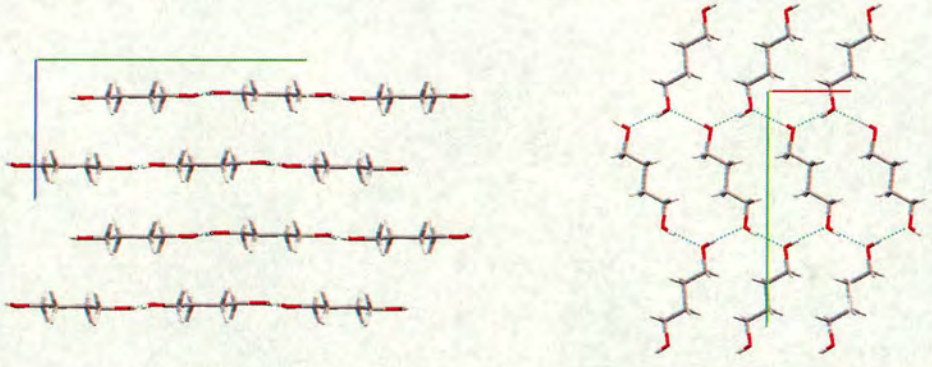

(A) **(B)**

Figure 4.1 The layered structure of butane-1,4-diol (A) viewed down the *a*-axis showing the layers (B) one layer viewed down the *c*-axis showing the hyrodgen bonded molecules which adopt the herring bone motif

The odd diols adopt a three dimensional packing motif where there are layers of chains of hydrogen bonded molecules (Thallidi *et al*[1]), and these chains are subsequently linked by hydrogen bonds (figure 4.2 (A)). These chains run parallel to the crystallographic *c* - axis (figure 4.2 (B)), where the molecules are related by the 2_1 screw axis. The three dimensional nature of these crystal structures is a consequence of the differing conformation about the α and ω carbons and the *trans* and *gauche* conformations are adopted respectively.

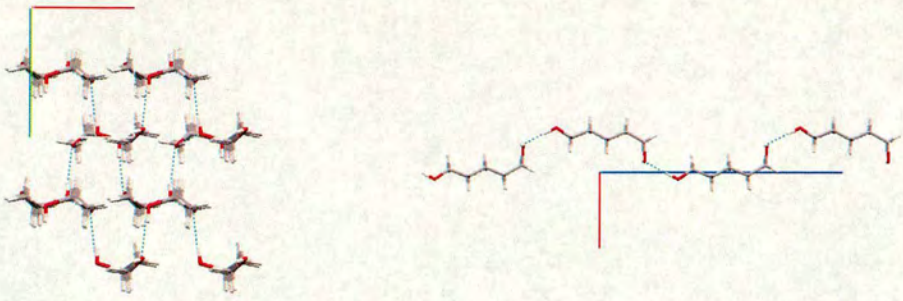

(A) (B)

Figure 4.2 The crystal structure of pentane-1,5-diol. Part A shows the interlinked layers of chains of hydrogen bonded molecules down the *c*-axis and part B shows a chain viewed down the *b*-axis

This work also reports a new high pressure phase of pentane-1,5-diol (n=5), where the conformation at the α and ω carbons is different to that observed in the low temperature phase, where the *trans* and *trans* conformation is adopted. This is the same conformation which would be indicative of an even diol at low temperature and ambient pressure.

The even diols butane-1,4-diol (n=4) and hexane-1,6-diol (n=6) and the odd diol heptane-1,7-diol have the same structure at high-pressure as their low temperature analogues.

4.2 Experimental

Essentially the same crystal growth procedure was undertaken for all diols, except where the melting point is above room temperature when the sample requires melting to enable loading of a liquid rather than a solid. The diol sample (n=2,3,4,5,6,7) is loaded as a liquid into a Merril-Basset[5] diamond-anvil cell that had been prepared with a tungsten gasket. The pressure was increased until the nucleation of several crystallites occurred. The temperature was then cycled close to the melting point until one crystallite remained. Allowing the cell to cool, the crystal eventually filled the 200 μm gasket hole and the final pressure measured using ruby fluorescence spectroscopy.

Data were collected using either a CAD-4[6] or SMART[7] diffractometer (graphite monochromated Mo Kα radiation), and for the following samples, data were collected at the SRS in Daresbury at the Zirconium edge (0.68610 Å): pentanediol, hexanediol and heptanediol.

4.2.1 Ethane-1,2-diol

Of the three different loadings of ethane-1,2-diol in the high pressure cell, three different phases were confirmed. The first, phase III, was crystallised at 2.34 GPa, and a single crystal grown in the diamond anvil cell. A rotation photograph was acquired overnight on the CAD-4[6] diffractometer, and after centering of reflections the unit cell was indexed using DIRAX[8]. After transformation, the unit cell was found to be monoclinic with dimensions a = 6.878(5), b = 8.883(5), c = 4.751(6) Å and β = 109.85(7)°. The unit cell volume was found to be 273.0 (4) Å^3 which implied the presence of 4 molecules in the unit cell. Compared to the low temperature orthorhombic phase I, which has a volume of 321.4 Å^3, this corresponds to a 15% reduction in molecular volume. Data were collected on the CAD-4[6] diffractometer using a theta dependent initial scan width of 1.5° in omega, out to a value of 40° in theta, the limit of the opening angle of the diamond anvil cell. The space group was found to be $P2_1/n$ with 4 molecules in the unit cell, and the structure

was solved using direct methods (SIR92[9]). The solution showed hydrogen bonded rings composed of *trans* ethane-1,2-diol conformers. The structure was refined using shelxtl[10], and the refinement statistics are in table 4.3.

The second, phase II, was isolated at an unknown pressure, later to be determined using *ab-initio* calculations. It was not possible to measure the pressure of this sample as upon loading the liquid, the ruby chip had moved and was obscured by the gasket. From the rotation photograph, the unit cell was indexed using DIRAX[8] using 13 reflections yielding cell dimensions a = 4.139(1), b = 13.825(1), c = 5.302(5) Å and β = 112.97(1)°. At this stage, it was essential to check for relationships to the known phases, and it was found that after halving b in the corresponding orthorhombic supercell gave the orthorhombic cell a = 4.135, b = 6.912 and c = 9.763 Å. These dimensions are very close to the known cell dimensions for phase I. This sample was also collected on the CAD-4[6], with an initial theta dependent scan range of 1.5° in omega. The unit cell volume of 279.3(1) Å^3 again implied 4 molecules in the unit cell, and it was noted at this stage that the volume was close to the unit cell volume of phase III, therefore it was postulated that the pressure was close to 2 GPa. The space group was found to be $P2_1/n$, and the structure was solved using direct methods (SIR92[9]). Phase II is composed of hydrogen bonded chains of *gauche* conformers. The structure was refined using shelxtl[10], refinement statistics are in table 4.3.

On the third loading of the sample, the pressure was measured at 1 GPa, and the sample collected using a ccd-area detector using the scan sequence in table 4.1. This scan sequence was set up to cover the maximum area of reciprocal space possible given the limitations due to the opening angle of the diamond anvil cell. The scan width was 0.3°. After data collection, the unit cell was determined using the twin indexing software GEMINI[11] of which 88/162 reflections fitted the unit cell a = 4.902, b = 6.765, c = 9.125 Å, α = 89.879, β = 89.660 and γ = 89.859°. This was the same cell dimensions as the known ambient pressure phase (Boese *et al*[4]) although the volume of 321.4 Å^3 was reduced by 6% to 302.0 (4) Å^3. The known co-ordinates

of this orthorhombic $P2_12_12_1$ phase were used in the refinement, statistics are shown in table 4.3.

Run	2θ (°)	Ω range (°)	ψ (°)	No. of Frames
1	-28	-8 → -40	90	106
2	28	40 → -40	90	266
3	-28	-140 → -215	90	250
4	28	-140 → -172	90	106
5	-28	-140 → -218	270	260
6	28	-140 → -172	270	106
7	-28	-8 → -40	270	106
8	28	35 → -40	270	250

Table 4.1 Scan sequence for high-pressure data collection on Bruker SMART diffractometer

Run	2θ (°)	Ω range (°)	ψ (°)	No. of Frames
1	27	40 → 320	90	400
2	27	40 → 320	270	400
3	27	220 → 190	270	154
4	27	220 → 190	90	154
5	-27	220 → 140	90	400
6	-27	220 → 140	270	400
7	-27	175 → 140	270	175
8	-27	175 → 140	90	175

Table 4.2 Scan sequence for high-pressure data collection on Bruker SMART diffractometer at the SRS Daresbury

Temperature / Pressure	293 K / 1 GPa	293 K / ~2 GPa	293 K / 2.3 GPa
Phase	I	II	III
Formula	$C_2H_6O_2$	$C_2H_6O_2$	$C_2H_6O_2$
Weight	62.07	62.07	62.07
Diffractometer	SMART[7]	CAD-4[6]	CAD-4[6]
Radiation	Mo K-α	Mo K-α	Mo K-α
Crystal System	Orthorhombic	Monoclinic	Monoclinic
Space Group	$P2_12_12_1$	$P2_1/n$	$P2_1/n$
a/Å	4.893(1)	4.139(1)	6.878(5)
b/Å	6.763(1)	13.825(1)	8.883(5)
c/Å	9.127(2)	5.302(5)	4.751(6)
β / °	90.00	112.97(1)	109.85(7)
Volume (Å^3)	302.0(1)	279.3(1)	273.0(4)
Z	4	4	4
No. reflections for cell	327	13	14
2θ range (°)	$3 < 2\theta < 20$	$5 < 2\theta < 11$	$5 < 2\theta < 14$
D_c (Mg/m^3)	1.365	1.476	1.510
μ mm^{-1}	0.122	0.131	0.134
Reflections collected	578	662	601
Unique data	184 [R(int) = 0.0678]	465 [R(int) = 0.0739]	519 [R(int) = 0.0558]
No. of data with $I > 2\sigma$	165	265	180
Absorption Correction	SADABS[12]	ABSORBU2	ABSORBU2
T_{min}/ T_{max}	0.693 / 1.000	0.244 / 0.557	0.248 / 0.548
Parameters	23	37	37
R_1	0.0668	0.0782	0.1122
wR_2	0.1707	0.1838	0.2006
S	1.050	1.067	1.026
$\Delta\rho_{max}$ (eÅ^3)	0.184	0.216	0.203
$\Delta\rho_{min}$ (eÅ^3)	-0.199	-0.188	-0.202

Table 4.3 Refinement Statistics for Phases I, II and III of Ethane-1,2-diol

4.2.2 Propane-1,3-diol

Several attempts were made to find the high pressure phase of propane-1,3-diol. The sample itself behaved in an odd manner, when the pressure was increased to induce crystallisation the onset of crystallisation occurred after the cell was left over a short period of time (minutes) at a constant pressure. Data were collected using the SMART[7] ccd-area detector using the scan sequence in table 4.1, and a scan width of 0.3° in omega. Initially, it was not possible to solve the structure, and this was later found to be due to ambiguities in space group selection.

The sample was reloaded and an attempt was made to grow a better quality crystal. This time, the sample nucleated at 2.7 GPa. The pressure was then reduced carefully to a pressure of 1 GPa to facilitate melting, and subsequently what appeared to be two crystals were grown from a common nucleation point. Data were collected on the SMART[7] ccd-area detector using the scan sequence in table 4.1 and again a similar problem occurred for the second time. A third crystal was obtained and the final pressure measured at 0.95 GPa. Data were collected using the ccd-area detector using the scan sequence shown in table 4.1, and a scan width of 0.3° in omega. The unit cell was indexed using GEMINI[11], and after subsequent integration using SAINT[14], with a correction for absorption using SHADE[15] and SADABS[12], the correct space group was found to be *Pc*. The structure was solved using direct methods (SHELXS[16]) and surprisingly was found to contain two molecules in the asymmetric unit which had different conformations. After initial refinement, the R-factor stuck relatively high at around 15%. The list file output from SHELXTL[10] showed that the most disagreeable reflections had a value of h=3n (table 4.4). Using the refinement suite CRYSTALS[17] and the twinning tool ROTAX[18], the crystal was found to be twinned about the 1 0 0 direct lattice direction by the matrix 1 0 0, 0 –1 0, –0.34 0 –1. The effect this has on the diffraction pattern is that all reflections where h=3n overlap, causing the high R-factor and the disagreeable reflections. ROTAX[18] indicated that a further twin law with an identical twin matrix for the –6 1 0 reciprocal lattice direction was present. Le Page and Flack's Rule[19] states that where the dot product of parallel direct and reciprocal lattice vectors is greater than 2

there is a higher symmetry supercell. The dot product in this case of (1 0 0).(-6 1 0) is 6. Using the CREDUC program from the XTAL[20] suite, the supercell was found to be orthorhombic with cell dimensions a=5.1269, b=7.4621 and c=60.4645 Å. Coset decomposition of monoclinic (2/m) into orthorhombic (mmm) gives twinning about an extra two-fold axis. The crystal is in fact twinned by a two fold rotation about the c – axis of the supercell. After subsequent refinement of the two domains in CRYSTALS[17] the scale factor of the twin domains was found to be 58 and 42 %, giving a more acceptable R-factor of 9 %.

hkl	F^2(obs)	F^2(calc)
3 1 -4	225.12	22.93
3 -1 -4	201.37	22.93
3 -1 -4	217.14	22.93
-6 0 4	166.67	39.00
3 -1 -9	129.83	22.96
6 0 -4	181.97	39.07
3 1 4	44.29	10.17
0 0 -4	1042.80	372.09
3 1 -7	70.59	7.22
3 -1 -7	61.92	7.22
3 1 -9	108.71	22.96
3 -1 -9	111.84	22.96
3 1 -9	115.74	22.96
6 1 -2	56.91	3.83
3 1 -7	55.49	7.22
3 -1 4	46.91	10.17
6 -1 -2	59.93	3.83

Table 4.4 Selected observed and calculated structure factors for propane-1,3-diol.

4.2.3 Pentane-1,5-diol

As pentane-1,5-diol is a liquid under ambient conditions (melting point –16°C), the sample was loaded in the usual manner (chapter 2.4.1). A single crystal was obtained at 0.38 GPa and a data set was collected at the synchrotron at Daresbury, prior to any indexing attempts. The detector distance was set at 5.5 cm and a 3s exposure time with a scan width of 0.2° in omega was used. Table 4.2 contains details of the scan sequence used on the SMART[7] ccd-area detector at the SRS. The unit cell was indexed using GEMINI[11] where 113/150 reflections were indexed on the orthorhombic unit cell a = 4.790, b = 5.082, c = 24.439 with a volume of 594.9 Å^3. This volume implies the presence of 4 molecules in the unit cell. The cell is clearly different in dimensions to the low temperature phase[1] (a = 5.3234, b = 6.6991, c = 17.0398 Å, orthorhombic $P2_12_12_1$). The structure was solved using Sir92[9] and refined using CRYSTALS[17], refinement statistics are given in table 4.5.

4.2.3 Butane-1,4-diol, Hexane-1,6-diol and Heptane-1,7-diol

The *in-situ* crystallisation of butane-1,4-diol was straight forward, and the ambient pressure phase was found to be stable at 0.35 GPa. Data were collected in the same manner as ethanediol on the SMART[7] ccd area detector, and indexing over all 8 runs (table 4.2) using GEMINI[11] yielded the unit cell a = 5.025, b = 7.444, c = 13.751 Å, α = 89.758, β = 89.759 and γ = 74.454°, indexing on 137/233 reflections. The transformation of the cell gives the monoclinic dimensions a = 5.024 (1), b = 13.733 (2), c = 7.476 (2) Å and β = 105.70 (2), refined over 535 reflections where $4 < \theta < 20$ in SAINT[14]. Refinement details are given in table 4.5.

Hexane-1,6-diol has a melting point of 45 °C therefore the sample had to be melted to load as a liquid in the diamond anvil cell. A single crystal was obtained at 0.3 GPa and as for butanediol, indexing showed that the crystal grown had the same phase as the stable low temperature polymorph[1]. Refinement details are given in table 4.5.

Two data sets were collected for heptane-1,7-diol at the SRS, both with scan widths of 0.2° in omega using the scan sequence in table 4.2 and a detector distance of 5.5 cm, but after the failed attempts to index the first data set collected over 3s exposures, it was decided to collect a second data set over 10s exposures as the sample was weakly diffracting. After manually picking 30 reflections in SMART[7], the sample was indexed using GEMINI[11] where 12 of the 30 reflections fitted the orthorhombic unit cell $a = 5.254$, $b = 6.979$, $c = 22.345$ with a volume of 819.3 Å^3. As was the case for butanediol and hexanediol, this cell is the same as the ambient pressure phase[1]. Due to the quality of the weak data, it was decided not to pursue refinement.

Conditions	293 K / 0.95 GPa	293 K / 0.35 GPa	293 K / 0.38 GPa	293 K / 0.07 GPa
Phase	Propane-1,3-diol	Butane-1,4-diol	Pentane-1,5-diol	Hexane-1,6-diol
Formula	$C_3H_8O_2$	$C_4H_{10}O_2$	$C_5H_{12}O_2$	$C_6H_{14}O_2$
Weight	76.10	90.12	104.15	118.17
Diffractometer	SMART[7]	SMART[7]	SMART[7] (SRS)	SMART[7] (SRS)
Radiation	Mo K-α	Mo K-α	Zr K-α	Zr K-α
λ	0.71073	0.71073	0.68610	0.68610
Crystal System	Monoclinic	Monoclinic	Orthorhombic	Monoclinic
Space Group	Pc	$P2_1/n$	$P2_12_12_1$	$P2_1/n$
a/Å	7.462(1)	5.0238(13)	4.7615(7)	8.0181(18)
b/Å	5.127(1)	13.7331(18)	5.0639(11)	5.0988(11)
c/Å	10.157(1)	7.4757(18)	24.372(6)	17.125(2)
β / °	97.18(1)	105.696(18)	90	94.757(16)
Volume ($Å^3$)	302.0(1)	496.53(19)	587.7(2)	697.7(2)
Z	4	4	4	4
No. refs for cell	466	535	1148	1101
2θ range (°)	$4 < 2\theta < 20$	$4 < 2\theta < 20$	$4 < 2\theta < 20$	$4 < 2\theta < 20$
D_c (Mg/m^3)	1.311	1.206	1.177	1.125
μ mm^{-1}	0.108	0.094	0.088	0.082
Reflections	572	803	931	1127
Unique data	230 [R(int) = 0.03]	Not merged	Not merged	Not merged
Data with $I > 2\sigma$	206	626	874	678
T_{min}/ T_{max} [12]	0.466 / 1.000	0.339 / 1.000	0.225 / 0.928	0.326 / 1.000
Parameters	42	61	65	79
R_1	0.089	0.077	0.0910	0.1096
wR_2	0.112	0.197	0.2425	0.3412
S	0.919	1.010	1.0308	1.147
$\Delta\rho_{max}$ ($eÅ^3$)	0.52	0.163	1.57	0.328
$\Delta\rho_{min}$ ($eÅ^3$)	-0.43	-0.194	-1.15	-0.278

Table 4.5 Refinement Statistics for propane-diol, butane-diol, pentane-diol and hexane-diol.

4.3 The High Pressure Crystal Structures of Ethylene Glycol

4.3.1 Phase I – The Hydrogen Bonded Network of *Gauche* – conformers

Phase I of ethane-1,2-diol is the low-temperature polymorph, which is stable below the melting point of 260 K[4]. In the previous study by Thalladi *et al*[1] on the melting point alternation in the α–ω alkane-diols and alkane-diamines, the differential scanning calorimetry measurements showed that no low-temperature phase changes occur down to the 80 K limit of their study. We also found that this phase was stable at 1 GPa. There is one molecule in the asymmetric unit, which gives rise to two unique hydrogen bonds in the overall structure. The conformation of the molecule is *gauche* (figure 4.3) with the O1-C1-C2-O2 torsion angle measuring –64.4° at 130 K and –63.6° at 1 GPa (see section 4.3.1.1 for further analysis). The torsion angle is defined as the angle between two vectors, in this case the vectors O1-C1 and C2-O2 are used. The sign of the torsion angle is positive if the O1-C1 bond is rotated clockwise onto C2-O2, and is negative if the rotation is anti-clockwise.

Figure 4.3 The *gauche* conformer of ethane-1,2-diol phase I

Phase I of ethane-1,2-diol is characterised by one unique chain of hydrogen bonded molecules. This chain involves the two hydrogen bonds which form a C_2^2 (4) chain in graph set terms. Figure 4.4 depicts one of these chains which is aligned parallel to the crystallographic *a*-axis. As in the chain structures of mono-alcohols discussed in chapter 3, neighbouring chains are aligned in opposite directions, resulting in an overall polarity of zero. The dimensions of the hydrogen bonds involved in this chain are given in table 4.6.

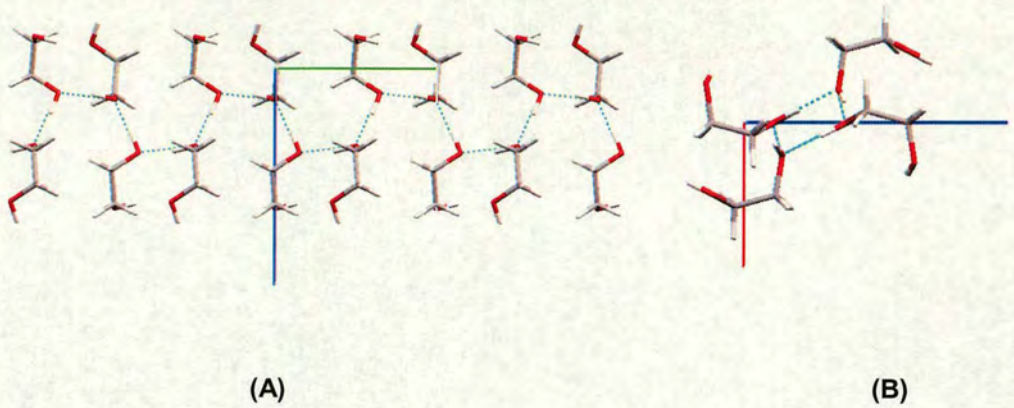

(A) (B)

Figure 4.4 Hydrogen bonded C_2^2 (4) chains of ethane-1,2-diol. Part (A) is viewed down the crystallographic *a*-axis and Part (B) shows the chains in projection down the crystallographic *b*-axis. [*a*-axis in red, *b*-axis in green, *c*-axis in blue]

Using the terms in Macrae and Taylor's paper[2], these chains are termed "zig-zag" like chains as neighbouring molecules are related by the 2-fold screw axis. As with the mono alcohols, this is common in di-alcohol structures. The same chain type is characteristic of the crystal structure of ethanol at low temperature (chapter 3).

Dimension	150 K	1 GPa	Calculated (@ 0 GPa)
Hydrogen bond 1 (O1 donor, O2 acceptor)			
O1(-H1)..O2$^{\#1}$ /Å	2.730	2.709 (7)	2.736
O1-H1 /Å	0.879	0.894	0.998
H1...O2$^{\#1}$ /Å	1.859	1.851	1.750
O1H1O2$^{\#1}$ /°	170.7	159.5	169.3
Hydrogen bond 2 (O2 donor, O1 acceptor)			
O2(-H2)..O1$^{\#2}$ /Å	2.711	2.682 (8)	2.729
O2-H2 /Å	0.834	0.900	0.998
H2...O1$^{\#2}$ /Å	1.879	1.820	1.735
O2H2O1$^{\#2}$ /°	175.4	159.8	174.2

Table 4.6 The dimensions of the hydrogen bonds in Phase I of ethane-1,2-diol at 150 K and 1 GPa. [#1: -½-x, 3/2-y, -z. #2: -½-x, 1-y, ½+z]

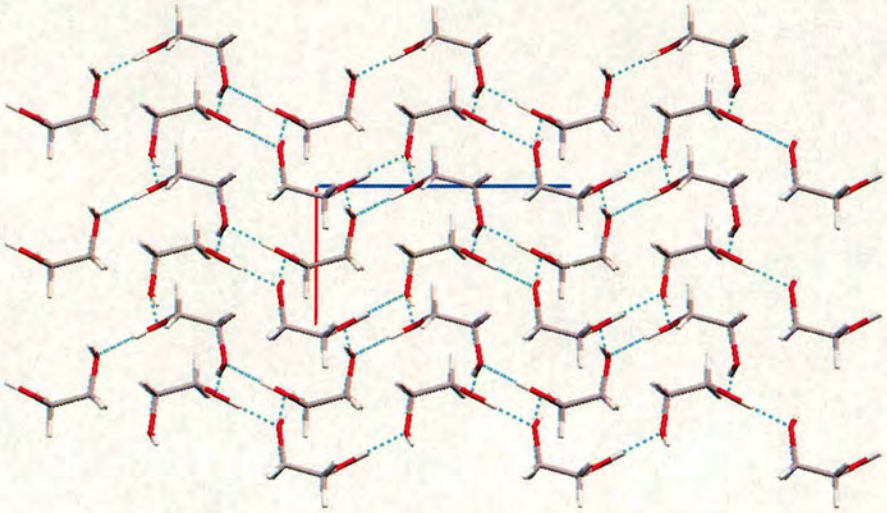

Figure 4.5 The overall crystal structure of phase I of ethane-1,2-diol viewing the hydrogen bonded C_2^2 (4) chains down the crystallographic *b*-axis. [*a*-axis in red, *c*-axis in blue]

The projection shown in figure 4.5 is a view of the complete structure down the crystallographic *b* – axis. The hydrogen bonded chains, coloured cyan, are arranged in a herring bone motif and each ethane-1,2-diol molecule contributes to two neighbouring chains, i.e. the chains are interlinked by ethane-1,2-diol molecules.

4.3.2 Phase II – The Hydrogen Bonded Bilayers of *Gauche* - conformers

Figure 4.6 The *Gauche* conformer of ethane-1,2-diol phase II

As in phase I of ethylene glycol, phase II is also solely composed of *gauche* conformers (figure 4.6). The torsion angle O1-C1-C2-O1 measures 62.7°. Again, there is a solitary molecule in the asymmetric unit, which gives rise to two unique hydrogen bonds in the overall structure. As in phase I, these hydrogen bonds are always between opposing ends of neighbouring molecules. The lengths of these two

hydrogen bonds differ by 0.02 Å: the O1-H1…O2 bond measures 2.733 (3) Å, which is slightly shorter than the 2.754 (3) Å length of the O2-H2…O1 bond. It is interesting to note that the hydrogen bond dimensions of phase II, see table 4.7, compare more closely with those of phase I at low-temperature rather than at high-pressure. This suggests that the shorter, therefore higher in energy, distances observed in phase I at 1 GPa are relaxed at higher pressure by the molecules rearranging into a more efficient packing motif.

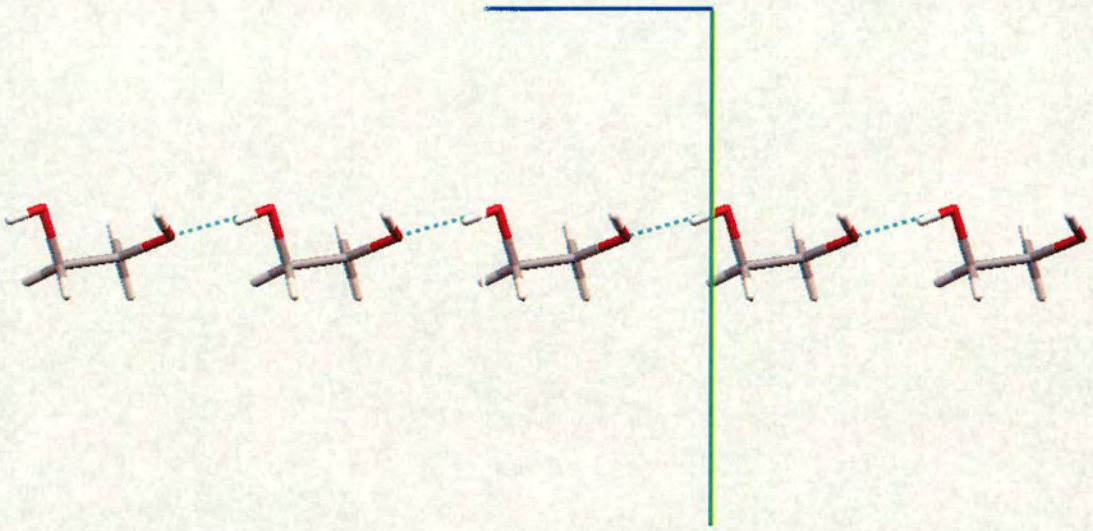

Figure 4.7 Hydrogen bonded C(5) chains of ethane-1,2-diol molecules aligned parallel to the *c* – axis viewed down the crystallographic *a* – axis [*b*-axis in green, *c*-axis in blue]

The O1-H1…O2 hydrogen bond can be described as a C (5) chain that runs parallel to the crystallographic *c* – axis (figure 4.7). In Macrae and Taylor terminology[2], these are "wave-like" chains where the molecules are related by translational symmetry only.

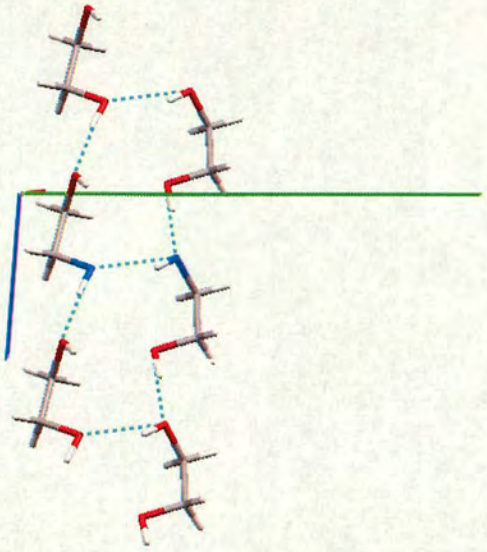

Figure 4.8 The hydrogen bonded chains of ethane-1,2-diol molecules are aligned parallel to the *c* – axis and they are bridged by O2 – H2 …O1 hydrogen bonds – the oxygen atoms in one of the bridging bonds are coloured blue for clarity [*a*-axis in red, *b*-axis in green, *c*-axis in blue]

The slightly longer hydrogen bond, where O2 is the hydrogen bond donor atom and O1 the acceptor, links the neighbouring chains (figure 4.8). As this bond is slightly longer than the hydrogen bond involved in the chain, it is therefore slightly weaker. It is denoted D, a finite hydrogen bond, in graph set terms.

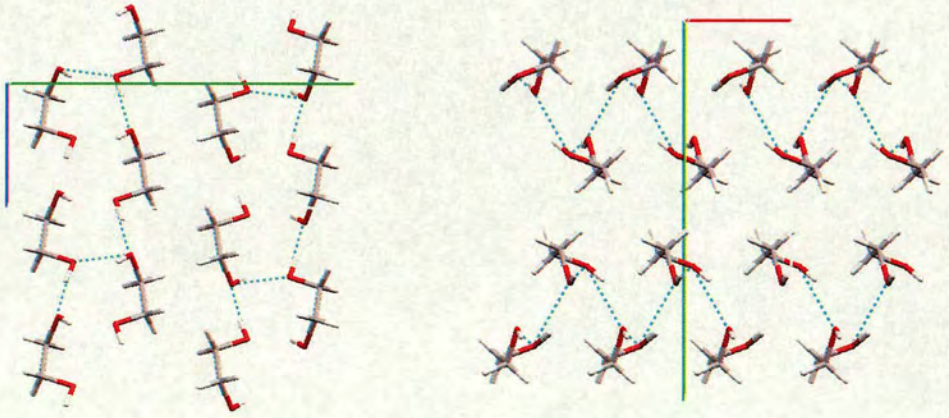

(A) **(B)**

Figure 4.10 The bi-layers shown in projection down the crystallographic *a* and *c*-axis in part (A) and (B) respectively [*a*-axis in red, *b*-axis in green, *c*-axis in blue]

Figure 4.10 depicts how the linked chains pack with respect to the crystallographic *a*- and *c*-axis in part A and B respectively. Both projections show the hydrophilic / hydrophobic nature of the phase. This is the major difference between the structures of phase I and phase II: where phase I is essentially a three dimensional hydrogen bonded network; phase II is composed of bi-layers.

Dimension	~2 GPa	Calculated (@ 2GPa)
Hydrogen bond 1 (O1 donor, O2 acceptor)		
O1(-H1)..O2$^{\#1}$ /Å	2.734 (3)	2.620
O1-H1 /Å	0.859	1.008
H1...O2$^{\#1}$ /Å	1.881	1.615
O1H1O2$^{\#1}$ /°	171.5	173.48
Hydrogen bond 2 (O2 donor, O1 acceptor)		
O2(-H2)..O1$^{\#2}$ /Å	2.754 (6)	2.646
O2-H2 /Å	0.894	1.007
H2...O1$^{\#2}$ /Å	1.982	1.652
O2H2O1$^{\#2}$ /°	143.7	168.06

Table 4.7 The dimensions of the hydrogen bonds in Phase II of ethane-1,2-diol at 2 GPa. [#1: x, y, 1+z; #2: x-½, ½-y, z-½]

4.3.3 Phase III – The Hydrogen Bonded Layers of *Trans* – conformers

Figure 4.11 The *trans* conformer of ethane-1,2-diol phase III

The most striking difference between the third, and highest pressure, phase of ethane-diol compared to phases I and II is the conformation of the molecule. In phase III the molecule adopts the *trans* conformation (figure 4.11) with a torsion angle of -176 ° (O1-C1-C2-O2) whereas phases I and II consist solely of *gauche*

conformers. Similar to phases I and II, there is only one molecule in the asymmetric unit, giving rise to two unique hydrogen bonds. As in phases I and II, the donor and acceptor atoms are at opposing ends of neighbouring molecules.

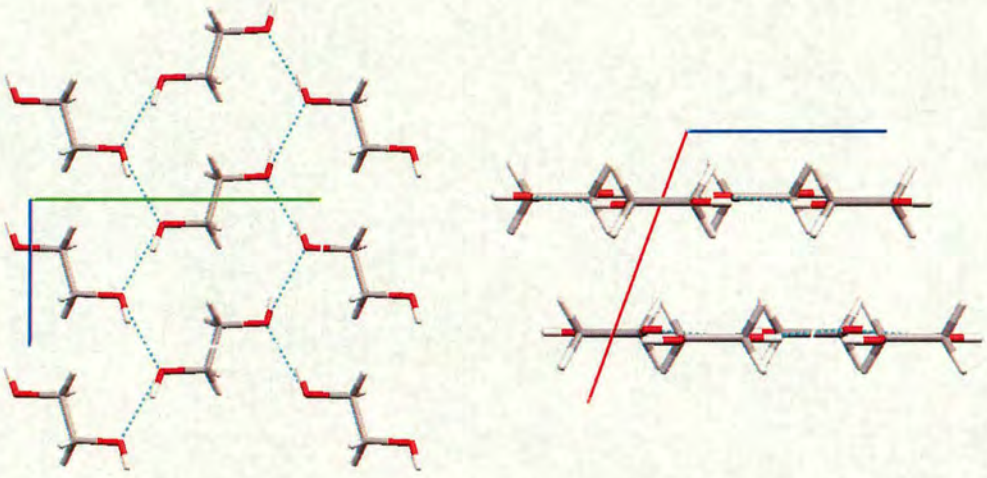

(A) (B)

Figure 4.12 The layered structure of ethane-1,2-diol. Part (A) shows one layer in projection down the crystallographic *a*-axis and (B) shows the skew stacking of the layers, viewed down the crystallographic *b*-axis. [*a*-axis in red, *b*-axis in green, *c*-axis in blue]

Phase III is characterised by hydrogen bonded layers that are primarily composed of hydrogen bonded chains. In graph set terms, the chains are denoted C_2^2 (4), where the 4 atoms involved are the hydrogen and oxygen atoms on the unique hydroxyl groups of neighbouring molecules. A major difference between the characteristic C_2^2 (4) chains of phase I and phase III is determined by the conformation of the molecule itself. In phase I, the *gauche* conformation of the molecules within the chains form a three dimensional box-like arrangement around the central axis of each chain. In contrast, the *trans* conformation of phase III forces the molecules to pack in two-dimensional layers. The C_2^2 (4) chains in phase III are aligned parallel and anti-parallel to each other, forming fourteen membered rings with 4 donor atoms and 4 acceptor atoms, denoted R_4^4 (14). Figure 4.12 (A) shows the chains and rings in projection down the crystallographic *a*-axis. It is also noted that the molecules adopt

a herring bone motif that is common to heavier even diols. The motif could be described as either "zig-zag" chains or rings in Macrae and Taylor notation[2].

The dimensions of the hydrogen bonds are given in table 4.8, both are similar which is due to the fact that they are involved in the same motif.

Dimension	2.3 GPa	Calculated
Hydrogen bond 1 (O1 donor, O2 acceptor)		
O1(-H1)..O2$^{\#1}$ /Å	2.692 (6)	2.712
O1-H1 /Å	0.820	0.994
H1...O2$^{\#1}$ /Å	1.894	1.731
O1H1O2$^{\#1}$ /°	164.2	168.12
Hydrogen bond 2 (O2 donor, O1 acceptor)		
O2(-H2)..O1$^{\#2}$ /Å	2.680 (7)	2.729
O2-H2 /Å	0.820	0.995
H2...O1$^{\#2}$ /Å	1.889	1.749
O2H2O1$^{\#2}$ /°	161.8	167.71

Table 4.8 The dimensions of the hydrogen bonds in Phase II of ethane-1,2-diol at 150 K and 1 GPa. [#1: ½-x, y-½, ½-z; #2: ½-x, y+½, -½-z]

4.3.4 Discussion and Comparison of Phases I, II and III of Ethylene Glycol

4.3.4.1 Molecular Conformation Analysis

In the gas phase, the ethane-1,2-diol molecule has ten stereo-chemically unique conformers (Cramer and Truhlar[21], 1994 and all references cited therin). These are composed of a combination of the three possible torsion angles about the C-C bond and the two C-O bonds. Each has three minima for torsion angles near 180° (*trans*) 60° or 360° (*gauche*), giving 27 (3^3) conformational minima, although many are degenerate by symmetry. The notation used for these conformers is for the torsion about the C-O bond, conformation is denoted t for *trans*, g^+ for *gauche* clockwise and g^- for *gauche* anti-clockwise. Similarly, for the torsion about the C-C bond, T is used

for the *trans* conformer, G^+ and G^- for the *gauche* clockwise and anti-clockwise respectively.

Several experimental studies agree that the tG^+g^- conformer is the most predominant in the gas phase, the *ab-initio* investigations agree that this is the lowest energy conformer, followed by the $g^+G^+g^-$ conformer. In the liquid phase, the molecule is stabilised by the formation of an internal hydrogen bond with the molecule in the *gauche* conformation about the C-C bond. No *trans* conformer can be stabilised by an internal hydrogen bond – only the *gauche* conformers tG^+g^- and $g^+G^+g^-$ can have such a bond.

Torsion	Experimental (150K) /°	Experimental (1 GPa) /°	Calculated /°
O2..O1-C1-C2	86.5	82.7	84.5
H1-O1-C1-C2	80.7	-	78.3
O1-C1-C2-O2	-64.4	-63.6	-66.6
O1..O2-C1-C2	135.3	134.5	133.5
H2-O2-C1-C2	138.6	-	133.8

Table 4.9 The calculated and experimental values for the torsion angles in phase I of ethane-1,2-diol at 150 K and 1 GPa.

In the solid state, the hydrophilic interactions mostly overrule the energetics for the torsion around the C-O bond, the value of which is determined by the intermolecular hydrogen bonding. The *trans* and *gauche* conformers are staggered conformations, in fact some of the observed conformations in the solid state are close to eclipsed, i.e. angles close to 120 or 240°, now denoted e^+ and e^- for eclipsed clockwise or counter clockwise. The eclipsed conformation is higher in energy than the staggered conformation. Tables 4.9 and 4.10 show the experimental and calculated dimensions of the torsion angles in phases I, II and III. The calculated positions for the hydrogens are deemed more reliable than the experimental values as x-ray diffraction data were used. The tables also contain the torsion angle between the hydrogen bond acceptor on the neighbouring molecule, the O..O-C-C torsion. It is observed that in phase I, both the torsion angles about the C-O bond are not in the staggered

conformation, the O2..O1-C1-C2 is closer to staggered with respect to the hydrogen atoms on C1, whereas the O1..O2-C2-C1 is closer to eclipsed (figure 4.13).

Figure 4.13 The conformation of the torsion angle about the O1-C1 bond (left) and the O2-C2 bond (right). The O1-C1 torsion is closer to eclipsed, whereas the O2-C2 torsion is closer to staggered.

The torsion angle in the case of phase I is a direct consequence of the position of the neighbouring molecule and the hydrogen bond between the molecules. The conformation of the molecule in phase I can be denoted $g^-G^-e^+$.

Torsion	Experimental /°	Calculated /°
Phase II		
O2..O1-C1-C2	-174.2	-173.9
H1-O1-C1-C2	-	-176.4
O1-C1-C2-O2	62.6	63.0
O1..O2-C1-C2	-55.1	-52.1
H2-O2-C1-C2	-	-51.6
Phase III		
O2..O1-C1-C2	-174.0	-172.9
H1-O1-C1-C2	-	-179.6
O1-C1-C2-O2	-176.0	-175.6
O1..O2-C1-C2	-175.3	-175.6
H2-O2-C1-C2	-	-176.0

Table 4.10 Experimental and calculated torsion angles in phases II and III of ethane-1,2-diol.

In phase II of ethane-1,2-diol, the conformation can be described as tG^+g^+ and in phase III tTt. It is interesting to note that in the stable higher-pressure phases II and

III, it seems that the hydrogen bonding pattern is now determined by the conformation of the molecule.

4.3.4.2 Hydrogen bonded chains

All three phases are primarily composed of hydrogen bonded chains. There are two possible types of chains – the C_2^2 (4) in which the chain is composed of alternating O1-H1…O2-H2 moieties. The second possible chain is the H1-O1-C1-C2-O2..H1, in graph set terms C (5), of which there are two possibilities, the aforementioned with O1 the donor and O2 the acceptor and the analogue where O2 is the donor and O1 the acceptor. In addition to this there is also the possibility of finite hydrogen bonds that involve one hydrogen bond i.e. only a single hydrogen bond donor and acceptor.

Phases I and III are primarily characterised by C_2^2 (4) chains, and phase II by C (5) chains connected by a finite D hydrogen bond. The conclusion that can be drawn from this is that there is no pressure dependence on the chain type. Similar to the mono-alcohols, it is observed that the C_2^2 (4) chains are pseudo four fold in the low pressure phase I whereas in the higher pressure phase III this chain is flat and the repeating unit of the chain contains 2 molecules. Recalling from chapter 3, this is also the case for the structure of ethanol, and both cyclobutanol and phenol have pseudo three-fold helices at low pressure compared to the "zig-zag" type chains at high pressure which contain two molecules in the repeating unit.

4.3.4.3 Molecular Volume

Table 4.11 shows the average volume occupied by one molecule in each phase of ethanediol, and the percentage reduction compared to the ambient pressure phase at 0 GPa. There is a 15 % reduction in molecular volume between phase I at 0 GPa and phase III, the highest-pressure phase, at 2.3 GPa.

Phase	I	I	II	III
Condition	130 K / 0 GPa	293 K / 1 GPa	293 K / ~2 GPa	293 K / 2.3 GPa
Molecular Volume / Å^3	80.35(8)	75.50 (8)	69.83 (4)	68.3(1)
% reduction cf. Phase I	0	6	13	15
V / V_0	1	0.94	0.87	0.85

Table 4.11 Molecular volume (Å^3) for phases I, II and III of ethanediol

Plotting a graph of V / V_0 against pressure for the three measured pressures shows that there is an approximately linear relationship between the change in volume and pressure. A pressure for phase II can be inferred from this graph to be approximately 2 GPa. The linearity of the relationship appears to be unaffected by presence of different polymorphs.

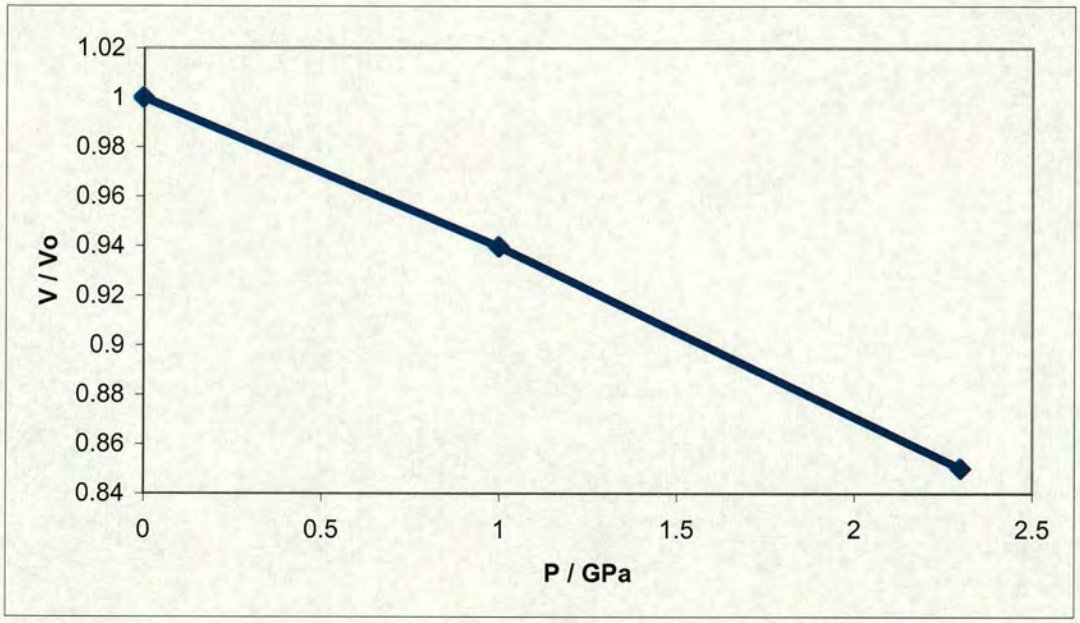

Graph 4.1 Molecular volume (Å^3) v Pressure (GPa) for phases I and III of ethanediol. The pressure for phase II can be inferred from this graph to be around 2 GPa.

As discussed in the previous chapter on the crystal structures of mono-alcohols, the enforced change in molecular volume due to the application of pressure is a major factor in the formation of these new high-pressure polymorphs. It was shown in chapter 3 that the distances between the molecules do not shorten on application of

pressure, the molecules rearrange so that there are more of these distances, i.e. they adopt a more efficient packing arrangement.

Distance / Å	Phase I (130 K)	Phase I (1 GPa)	Phase II	Phase III
3.0 → 3.6	0	0	2	2
3.6 → 3.8	2	2	5	0
3.8 → 4.0	0	4	2	5
Total	2	6	9	7

Table 4.12 Number of intermolecular C-C distances between 3 and 4 Å per molecule

Using the same method described in chapter 3 for cyclobutanol and tertiary butanol, the results for ethane-1,2-diol also fit the trend. Tables 4.12 and 4.13 give the number of distances between atoms on adjacent molecules. As for cyclobutanol and tertiary butanol, the number of these distances increase rather than the distances themselves shortening. This is true for all distances, with the exception of the total number of C-C distances in phase III of ethanediol. This is because this structure is layered, and adjacent layers do not lie directly above one another, they are displaced by ¼ along the *b*-axis.

Distance / Å	Phase I (130 K)	Phase I (1 GPa)	Phase II	Phase III
3.0 → 3.6	10	16	14	20
3.6 → 3.8	8	4	8	10
3.8 → 4.0	2	2	4	2
Total	20	22	26	32

Table 4.13 Number of intermolecular C-C distances between 3 and 4 Å per molecule

4.4 The Crystal Structures of Propylene Glycol

4.4.1 Phase I – the α – *gauche*, ω – *gauche* conformer at 130 K

Figure 4.14 The α – *gauche*, ω – *gauche* conformer or propane-1,3-diol

In the stable low temperature phase of propane – 1,3 – diol, phase I, there is one unique molecule in the asymmetric unit. The molecule exists as the α – *gauche*, ω – *gauche* conformer (figure 4.14 above). There are two characteristic torsion angles, O1 – C1 – C2 – C3 measures 69.45 ° and O2 – C3 – C2 – C1 has a value of 61.54 °.

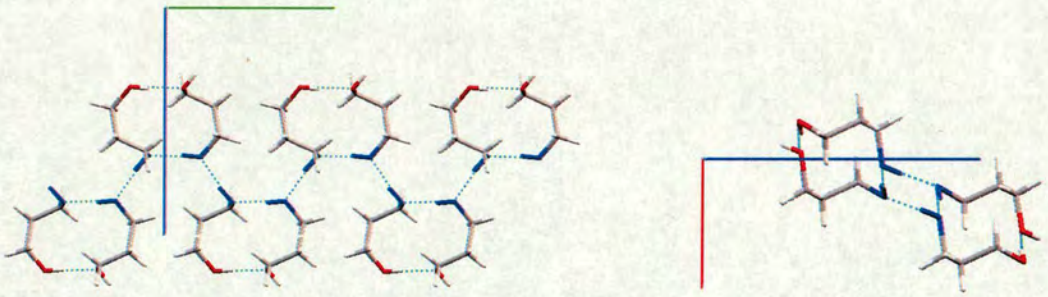

(A) **(B)**

Figure 4.15 Hydrogen bonded chains of propane-1,3-diol shown in projection down the crystallographic *a* – axis [A] and in projection down the crystallographic *b* – axis [B]. The hydroxyl groups in the C_2^2 (4) chains are coloured blue. [*a* – axis in red, *b* - axis in green, *c* - axis in blue]

As in all three phases of ethylene glycol, there are two unique hydrogen bonds in the overall structure. Figure 4.15 shows a hydrogen bonded chain of propane-diol molecules. This chain involves both hydrogen bonds: the first between the donor atom O1 and acceptor O2 with a magnitude of 2.722 Å; the second between the donor atom O2 and acceptor O1 with a magnitude of 2.698 Å. The chain is denoted

C_2^2 (4) in graph set terms. This chain can be used to describe the whole structure, as in phase I and phase III of ethane-1,2-diol.

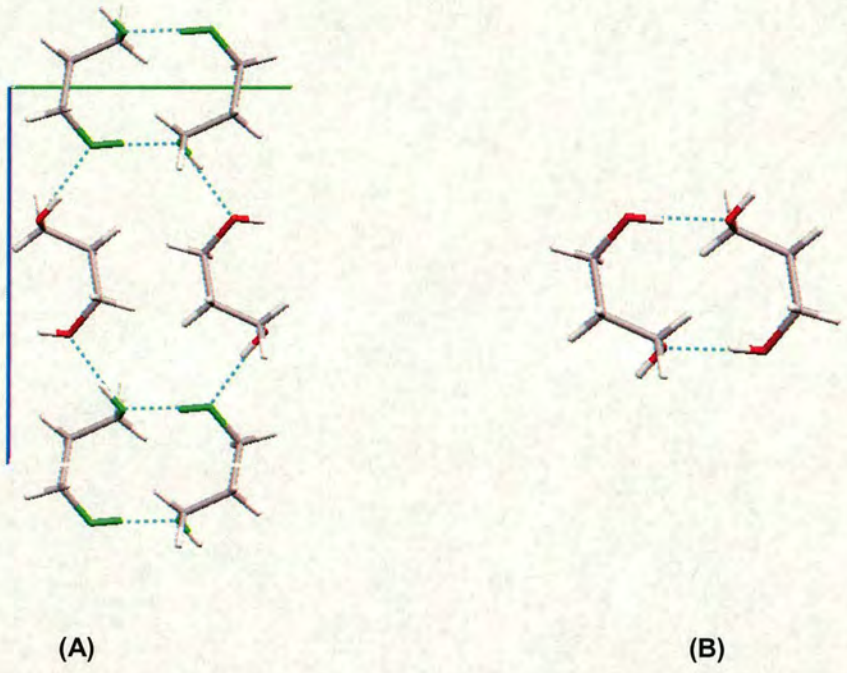

(A) (B)

Figure 4.16 (A) Hydrogen bonded rings of propane-1,3-diol shown in projection down the crystallographic *a* – axis. The $R_2^2(12)$ "dimers", pictured in part (B), contain the slightly shorter O2-H2…O1 hydrogen bond, and the larger R_6^6 (20) rings contain both unique hydrogen bonds. [*a*-axis in red, *b*-axis in green, *c*-axis in blue]

A combination of the C_2^2 (4) chains in the structure results in the formation of hydrogen bonded rings. Two ring types are formed, the first a ring consisting of two hydrogen bond donors and two hydrogen bond acceptors, namely O1-H1…O2 with a magnitude of 2.722 Å, and it's symmetry equivalent. The ring involves 6 atoms from each molecule, and are denoted $R_2^2(12)$. In figure 4.16, the atoms involved in the hydrogen bonding are coloured green. The rings are not planar, as shown in part B of figure 4.16, where the ring is shown in projection down the C4-O2 bond. The second ring involves 6 hydrogen bonds and is denoted R_6^6 (20), 4 of type O2-H2..O1 with a length of 2.698 Å and 2 of type O1-H1..O2, length 2.722 Å. The dimensions of the hydrogen bonds are given in table 4.14.

It is clear that the structure can actually be described in a third manner, involving C (6) chains linked by finite hydrogen bonds as in the structure of phase II of ethane-1,2-diol. The C (6) chains have the repeating unit O2-H2…O1-C1-C2-C3. This actually better describes the structure as the finite hydrogen bond is slightly longer than the hydrogen bond involved in the chain.

Dimension	0 GPa	Calculated
Hydrogen bond 1 (O1 donor, O2 acceptor)		
O1(-H1)..O2$^{\#1}$ /Å	2.722	2.684
O1-H1 /Å	0.883	1.001
H1...O2$^{\#1}$ /Å	1.842	1.684
O1H1O2$^{\#1}$ /°	174.35	176.71
Hydrogen bond 2 (O2 donor, O1 acceptor)		
O2(-H2)..O1$^{\#2}$ /Å	2.698	2.664
O2-H2 /Å	0.889	1.001
H2...O1$^{\#2}$ /Å	1.815	1.669
O2H2O1$^{\#2}$ /°	171.49	172.07

Table 4.14 The dimensions of the hydrogen bonds in Phase I of propane-1,3-diol at 150 K. [#1: 1-x, 1-y, 2-z; #2: ½+x, 3/2-y, ½+z]

As in the structure of phase II of ethane-1,2-diol, the structure of the ambient pressure phase of propane-1,3-diol also forms bi-layers which are parallel to the -h 0 1 lattice plane (figure 4.17). The chains are also termed "wave-like", although in Phase II of ethane-1,2-diol the chain contains only translational symmetry between the conformers, whereas in Phase I of propane-1,3-diol the conformers are related by the *n*-glide.

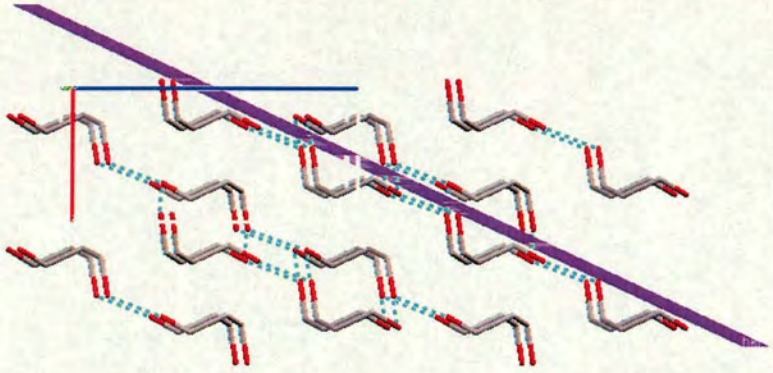

Figure 4.17 The layers of hydrogen bonded propane-1,3-diol molecules parallel to –h 0 l [*a*-axis in red, *b*-axis in green, *c*-axis in blue]

Figure 4.17 shows how these hydrogen bonded chains and dimers are aligned with respect to the unit cell edges. The purple plane shown in the figure is the –2 0 2 plane. The hydrogen bonded chains are in fact aligned parallel to the –h 0 l lattice planes. Neighbouring chains are aligned above and below these lattice planes. The overall structure is shown in figure 4.18. A combination of the hydrogen bonded C (6) chains and finite hydrogen bonds form the two rings described above.

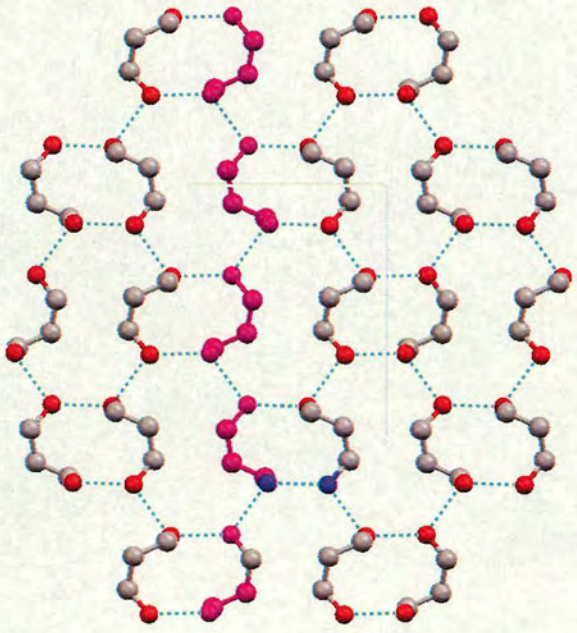

Figure 4.18 The overall structure of propane-1,3-diol. One of the C (6) hydrogen bonded chains is coloured purple and a finite hydrogen bond connecting the chains is shown in navy.

4.4.2 Phase II – The High Pressure Phase with α-*gauche*, ω-*trans* and the α-*trans*, ω-*trans* Conformers

In sharp contrast to the phase I of propane-1,3-diol, the metastable high pressure phase has two conformers in the asymmetric unit, the α-*gauche*, ω-*trans* and the α-*trans*, ω-*trans*. Each molecule has two unique torsion angles and two unique hydrogen bonds.

Figure 4.19 The α-*gauche*, ω-*trans* conformer of propane-1,3-diol, torsion angle dimensions are given in table 4.15

The torsion angles in the α-*gauche*, ω-*trans* conformer (shown in figure 4.19) are 175.6° (O1-C2-C3-C4) and –61.9° (O5-C4-C3-C2). The hydrogen bonds are formed between neighbouring α-*gauche*, ω-*trans* conformers, where O1 donates to O5 (x, -y, z+½) and has a donor-acceptor distance of 2.66 (2) Å. O5 donates a hydrogen to O1 (x, -y, z+½) to form a hydrogen bond with a donor-acceptor distance of 2.67 (2) Å. The torsion angles in the α-*trans*, ω-*trans* conformer (shown in figure 4.20) are 178.9° (O6-C7-C8-C9) and –172.2° (O10-C9-C8-C7). These conformers are also linked by hydrogen bonds that are formed between neighbouring α-*trans*, ω-*trans* conformers, where O6 donates to O10 (x, 1-y, z+½) and has a donor-acceptor distance of 2.67 (2) Å. O10 donates a hydrogen to O6 (x-1, 1-y, z+½) to form a hydrogen bond with a donor-acceptor distance of 2.66 (2) Å.

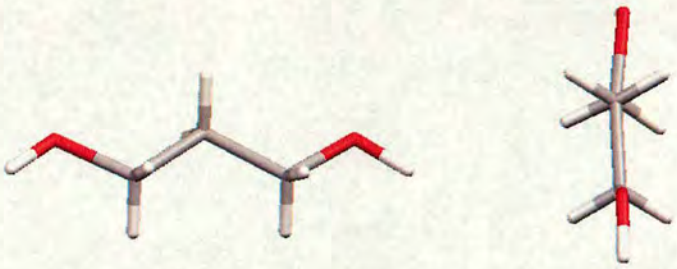

Figure 4.20 The α-*trans*, ω-*trans* conformer of propane-1,3-diol, torsion angle dimensions are given in table 4.15

There are four unique hydrogen bonds in the overall structure and the donor – acceptor distances are given in table 4.15. The overall structure is composed of hydrogen bonded chains of which there are two motifs that can be used to describe the overall structure. In the first motif, one chain is required to fully describe the structure, involving all four unique hydrogen bonds between neighbouring hydroxyl groups: O1 donates to O6; O6 donates to O10; O10 donates to O5; and O5 donates to O1. In graph set terms this is denoted C_4^4 (8), with four hydrogen bond donors, four hydrogen bond acceptors and with all 8 atoms involved together. In figure 4.21, the structure is projected down the axis of the chains and one of the chains is coloured red for clarity. The overall structure is strikingly similar to phase I of ethane-1,2-diol. There are two other chains within the structure forming the second motif that can be used to describe the structure. The first chain contains the hydrogen bond O5-H5…O1 (x, -y, z+½) and is composed of α-*gauche*, ω-*trans* conformers (coloured green in figure 4.21) related by the *c*-glide parallel to the crystallographically unique *b* – axis. In graph set terms, this is a C (6) chain. Aligned approximately parallel to this chain is the second hydrogen bonded chain, solely composed of α-*trans*, ω-*trans* conformers (coloured blue in figure 4.21). In this case, the hydrogen bond donor is O6 and the acceptor O10 (x, -y, z+½), with the conformers also related by the glide plane. These two chains are identical in both graph set terms. In Macrae and Taylor terminology[2] the chains are "wave-like". As the hydrogen bonds in both motifs have similar dimensions, either of the two motifs can be used to describe the structure.

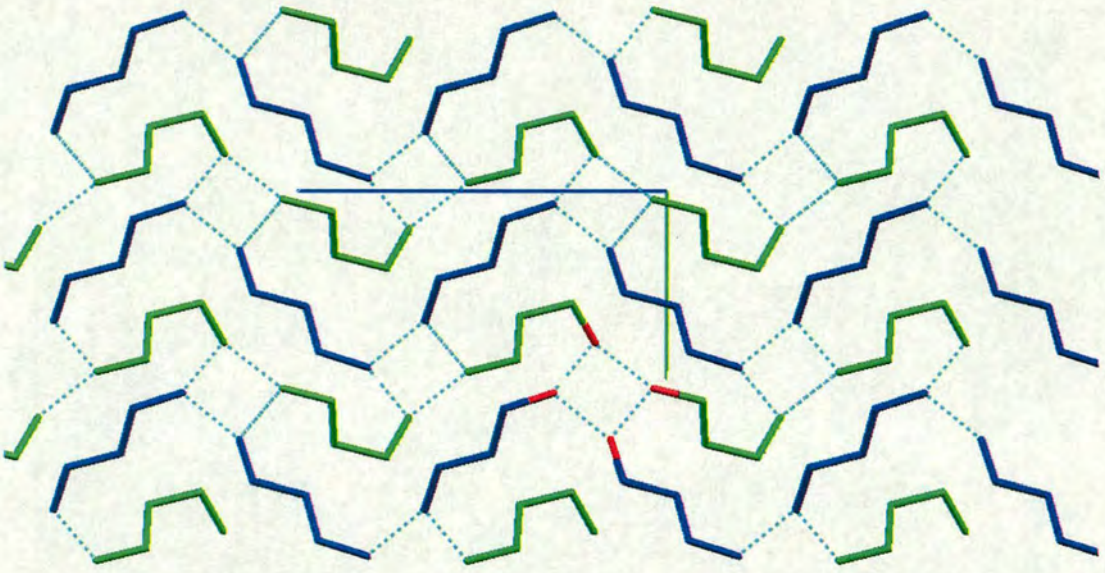

Figure 4.21 The overall crystal structure of phase II of propane-1,3-diol. The hydrogen bonded chains of α-*gauche*, ω-*trans* conformers are shown in green, and the α-*trans*, ω-*trans* in blue. Aligned perpendicular to these chains are the C_4^4 (8) chains, one of which is shown in red.

4.4.3 Discussion and Comparison of Phases I and II of Propylene Glycol

4.4.3.1 Molecular Conformational Analysis

As was the case for the three phases of ethane-1,2-diol, there are four torsion angles that come under consideration when analysing the different conformations of propane-1,3-diol. In the alkyl moiety of the chain, the central carbon is in the *trans* conformation, whereas the conformation differs at the α- and ω-carbons at the extremes of the chain. At each end, the O-C-C-C and the H-O-C-C torsion angles differs between the phases. These dimensions, as was the case for ethane-1,2-diol, are a major factor in the resulting packing motif of the full crystal structure. Table 4.16 contains the dimensions of the experimental and calculated torsion angles for phases I and II of propane-1,3-diol.

Torsion	Experimental /°	Calculated /°
Phase I - α-*gauche*, ω-*gauche*		
O2..O1-C1-C2	-82.90	-81.95
H1-O1-C1-C2	-	-83.43
O1-C1-C2-C3	69.45	69.68
O2-C3-C2-C1	61.54	68.09
O1..O2-C1-C2	73.59	67.46
H2-O2-C1-C2	-	63.42
Phase II - α-*gauche*, ω-*trans*		
O6..O1-C1-C2	84.6	92.45
H1-O1-C1-C2	-	89.78
O1-C2-C3-C4	175.9	176.98
O5-C4-C3-C2	-63.4	-63.67
O1..O5-C4-C3	101.3	103.67
H5-O5-C4-C3	-	100.96
Phase II - α-*trans*, ω-*trans*		
O10..O6-C7-C8	139.1	149.11
H6-O6-C7-C8	-	151.39
O6-C7-C8-C9	178.3	179.77
O10-C9-C8-C7	-174.1	174.81
O5..O10-C9-C8	-154.1	-155.71
H10-O10-C9-C8	-	-157.22

Table 4.16 Experimental and calculated values for the torsion angles in phases I and II of propane-1,3-diol.

To use similar notation to describe the conformation of the molecule as was used for ethane-1,2-diol, G and T will be used to describe the conformation of the C-C bonds and g, t and e the conformation of the C-O bonds. The + and – signs are used for clockwise rotation in the *gauche* form or the eclipsed form. In phase I, the overall conformation of the α-*gauche*, ω-*gauche* molecule is $g^{+}G^{-}G^{-}g^{-}$. The α-*gauche*, ω-*trans* molecule in phase II is denoted $e^{-}TG^{+}e^{-}$ and the α-*trans*, ω-*trans* conformer $e^{+}TTt$. The conformational energy of the propane-1,3-diol molecule in the gas phase was calculated using *ab-initio* calculations (Dr. S. J. Clark, Department of Physics,

University of Durham). Two calculations were carried out, the first rotating the C-C-C-O torsion angle, and the second rotating the C-C-O-H torsion angle, both with a starting geometry of tTTt. The resultant graphs are shown in figures 4.22 and 4.23.

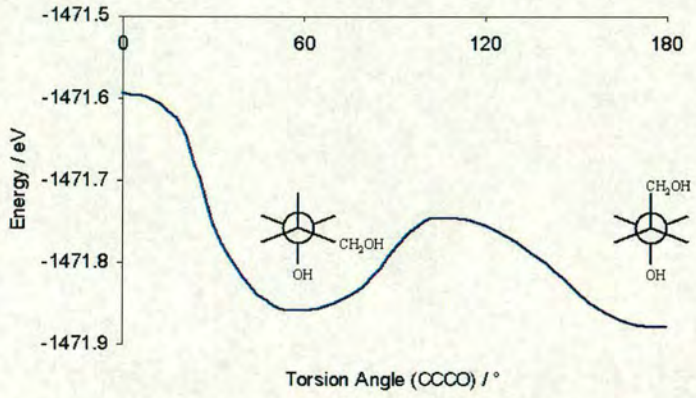

Figure 4.22 Plot of Energy v Torsion Angle for the C-C-C-O torsion in Propane-1,3-diol

The minima in the C-C-C-O torsion are at approximately 60° and 180°, in the *gauche* and *trans* positions. The minima in the C-C-O-H torsion are at approximately are at 90° and 180°. The lone pairs of electrons on the oxgen atom are a heavy influence on the position of the minima as shown in figure 4.23. At 90° and 180°, the lone pairs are positioned such that there is little interaction with the bonded pairs on the neighbouring carbon atom.

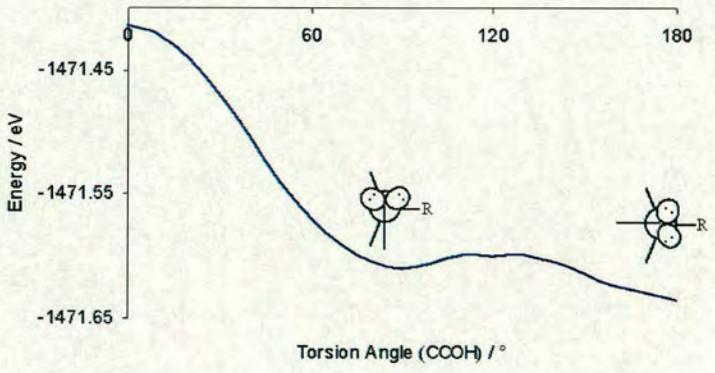

Figure 4.23 Plot of Energy v Torsion Angle for the C-C-O-H torsion in Propane-1,3-diol. [R=CH_2CH_2OH]

The O-C-C-O torsion angle is influenced by the molecular conformation where the molecule always relaxes to an energy minimum. The C-C-O-H torsion angle is not only influenced by the conformational energy, the position of the hydrogen bond

determines this torsion angle, therefore the conformation of the C-O bond is dependant on the crystal packing.

4.4.3.2 Hydrogen bonded chains

Both phases of propane-1,3-diol are primarily composed of hydrogen bonded chains. There are two possible basic chain types. The first involves only hydroxyl groups of the molecule and where $Z'=1$, this can be a C_2^2 (4) chain or where $Z'=2$, a C_4^4 (8) chain. The second chain type also involves the alkyl moiety of the molecule. Where $Z'=1$, this is denoted C (6), and where $Z'=2$ there is the possibility of C_2^2 (12) chains. The latter are not observed in the high pressure phase where $Z'=2$. In addition to this, there is the possibility of finite hydrogen bonds and also hydrogen bonded rings.

Phase I is best described as containing C (6) chains linked by a finite D hydrogen bond. These combine to form hydrogen bonded puckered rings, R_2^2 (12) and R_6^6 (20). These pack in bi-layers. This hydrogen bonded motif is similar to the motif observed in phase II of ethane-1,2-diol. Phase II is characterised by C_2^2 (4) hydrogen bonded chains which are also present in phases I and III of ethane-1,2-diol. The repeating unit of the chain involves four molecules and is most like the structure of phase I of ethane-1,2-diol. Compared to phase III of ethane-1,2-diol, there is more steric hindrance due to the increased number of carbons in the chain, so it may be expected that there is an increase in the number of molecules about the axis of the chain. The two phases of propane-1,3-diol are dramatically different in terms of hydrogen bonded motif.

4.4.3.3 Molecular Volume

The molecular volume of propane-1,3-diol reduces by 7.3 % from 104.0 $Å^3$ at 130 K and 0 GPa to 96.38 (3) $Å^3$ at 293 K and 0.95 GPa. Table 4.17 contains the number of intermolecular distances between carbon atoms on adjacent molecules, table 4.18 the distances between carbon and oxygen atoms on neighbouring molecules.

Distance / Å	Phase I (150 K)	Phase II (0.95 GPa)
3.6 → 3.8	1	2
3.8 → 4.0	3	8
4.0 → 4.2	9	11
Total	13	21

Table 4.17 Number of intermolecular C-C distances between 3.6 and 4.2 Å per molecule

Again, the trend is similar to that of cyclobutanol, tertiary butanol and ethanediol, these distances do not shorten, the new high pressure polymorph has a greater number of them. This is due to the compensation for the 7.3 % reduction in molecular volume, enforced by the application of pressure.

Distance / Å	Phase I (150 K)	Phase II (0.95 GPa)
3.0 → 3.4	0	3
3.4 → 3.6	12	8
3.6 → 4.0	10	18
Total	22	27

Table 4.18 Number of intermolecular C-O distances between 3 and 4 Å per molecule

The energy difference between the phases at 0.95 GPa was calculated using a*b-initio* calculations, carried out by Dr. S. J. Clark (Department of Physics, University of Durham). The energy required to form phase II from phase I is 8.86 $kJmol^{-1}$. Appendix 4 lists the calculated unit cell dimensions, atomic positions and the relative enthalpies, all calculated at O K so to omit thermal effects.

4.5 The Crystal Structures of Even Di-alcohols where n > 3

The crystal structures of the heavier even di-alcohols have been determined at low temperature in the previously mentioned study by Thallidi *et al*[1]. For the di-alcohols $HO(CH_2)_nOH$, where $4 \leq n \leq 10$, differential scanning calorimetry was used to determine the presence of only one phase for each. Each phase is essentially the

same, except the length of the alkane chain. The unit cell dimensions are given in table 4.19, each structure has two short and one long unit cell edge and packs in the space group $P2_1/c$ or $P2_1/n$. The long unit cell dimension increases with the alkyl chain length.

n	Space Group	Z	*a* / Å	*b* / Å	*c* / Å	*β* / Å
4	$P2_1/n$	4	5.0135	13.7880	7.4635	107.275
6	$P2_1/n$	4	7.8676	5.0554	16.9653	93.454
8	$P2_1/n$	2	4.7995	5.0846	17.5408	90.315
10	$P2_1/c$	2	4.799	5.113	21.029	93.37

Table 4.19 Unit cell dimensions for even diols[1] where n > 3

All molecules are in the α-*trans*, ω-*trans* conformation, and the torsion around the C-O bond is also 180° as in phase III of ethane-1,2-diol. The planarity of the molecule causes their structure to be layers of hydrogen bonded chains. Figure 4.24 (A) shows the layers of chains, the separation of the planes between the published structures and the high-pressure phases are given in table 4.20. For butane-1,4-diol and hexane-1,6-diol, the structures were also determined at 0.35 GPa and 0.3 GPa respectively. The cell dimensions and atomic co-ordinates at these pressures are almost identical to the low temperature dimensions.

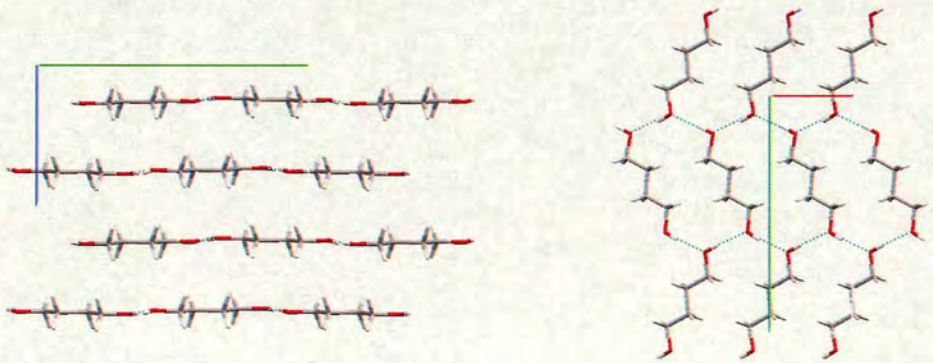

(A) **(B)**

Figure 4.24 The layered structure of butane-1,4-diol (A) viewed down the *a* – axis showing the layers (B) one layer viewed down the *c* – axis showing the hydrogen bonded molecules which adopt the herring bone motif

The hydrogen bonds are involved in a C_2^2 (4) chain in all structures, with the exception of octane-1,8-diol where the molecule lies on an inversion centre, therefore the hydroxyl groups are crystallographically identical. In this case, the chain is denoted C (2) in graph set terms. All structures have essentially the same herring bone arrangement of the molecules within the layers.

N [$HO(CH_2)_NOH$]	Conditions	Layer Separation / Å	H-bond 1 / Å	H-bond 2 / Å
2 (Phase III)	293 K / 2.3 GPa	3.44	2.680 (7)	2.692 (6)
4	130 K / 0 GPa	3.73	2.762	2.772
6	130 K / 0 GPa	3.93	2.776	2.779
8	130 K / 0 GPa	4.80	2.788	2.788

Table 4.21 Layer separation and hydrogen bond lengths in the layered structures of the even diols. (N=4,6,8 from Thallidi *et al*[1])

The displacement of the layers is similar where N=2, 4 and 6, the molecules are displaced in adjacent layers. Where N=8, the molecules lie above one another, hence the layers are slightly further apart.

4.6 The Crystal Structures of Pentane-1,5-diol

4.6.1 Phase I – the *α – trans, ω – gauche* conformer

Figure 4.25 The α–*trans*, ω–*gauche* conformer of pentane-1,5-diol

In the stable low temperature phase of pentane–1,5–diol, phase I (Thallidi *et al*[1]), there is one unique molecule in the asymmetric unit. The molecule exists as the α – *trans*, ω – *gauche* conformer (figure 4.26). There are two characteristic torsion angles, O1 – C1 – C2 – C3 measures 179.9° and O2 – C5 – C4 – C3 has a value of 64.1°. There are two unique hydrogen bonds in the crystal structure (given in table 4.20), one is slightly longer than the other which suggests they are involved in different types of hydrogen bonding motifs in graph set terms. This is similar to phase I of propane-1,3-diol where the structure can be characterised by C_2^2 (4)

chains, but due to the dimensions of the hydrogen bonds, it is better described by C (8) chains connected by a finite hydrogen bond. Indeed, pentane-1,5-diol can be described in both manners also.

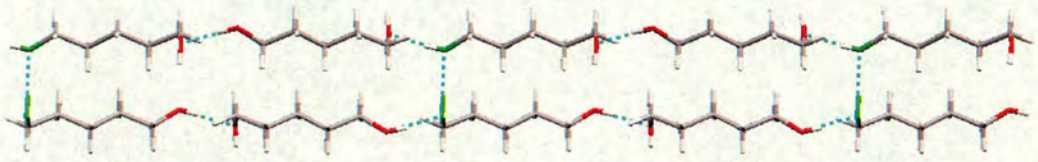

Figure 4. 26 Hydrogen bonded pentane-1,5-diol C (8) chains interconnected by the finite D hydrogen bond coloured green for clarity.

The repeating unit of the C (8) chains is O2..H1-O1-C1-C2-C3-C4-C5-O2, the O1 – O2 donor acceptor distance is slightly shorter than the finite hydrogen bond linking the chains (O2-H2..O1). The dimensions of the hydrogen bonds are given in table 4.21. This is the same for heptane-1,7-diol (O1..O2 2.754 Å, O2...O1 2.702 Å) and nonane-1,9-diol (O1..O2 2.704 Å, O2...O1 2.766 Å), each having one hydrogen bond significantly longer than the other.

Dimension	0 GPa / 150 K	Calculated
Hydrogen bond 1 (O1 donor, O2 acceptor)		
O1(-H1)..O2$^{\#1}$ /Å	2.706	2.671
O1-H1 /Å	0.857	1.005
H1...O2$^{\#1}$ /Å	1.851	1.667
O1H1O2$^{\#1}$ /°	176.0	176.49
Hydrogen bond 2 (O2 donor, O1 acceptor)		
O2(-H2)..O1$^{\#2}$ /Å	2.732	2.724
O2-H2 /Å	0.790	1.001
H2...O1$^{\#2}$ /Å	1.946	1.729
O2H2O1$^{\#2}$ /°	173.2	172.01

Table 4.21 The dimensions of the hydrogen bonds in Phase I of pentane-1,5-diol at 130 K. [$^{\#1}$ -x-½, -y, z-½, $^{\#2}$ x-½, -y-½, 2-z]

Figure 4.27 gives a projection of the full structure, viewed down the crystallographic *b*-axis. The donor / acceptor atoms in a C_2^2 (4) chain are highlighted blue, this can be used to describe the full structure, although the correct notation is the C (8) chain and finite D hydrogen bond.

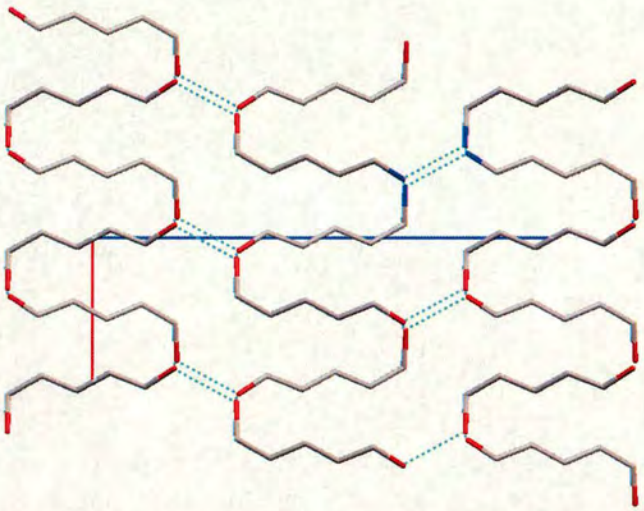

Figure 4.27 The overall structure of pentane-1,5-diol [*a*-axis in red, *c*-axis in blue]. A C_2^2 (4) hydrogen bonded chain is shown in blue. Hydrogen atoms are omitted for clarity.

4.6.2 Phase II – the α – *trans*, ω – *trans* conformer

Similar to the high pressure phase III of ethane-1,2-diol and II of propane-1,3-diol, the high pressure phase II of pentane-1,5-diol contains an α-*trans*, ω-*trans* conformer (figure 4.28). The characteristic torsion angles are -177.1° for O1-C2-C3-C4 and 177.9° for O7-C6-C5-C4.

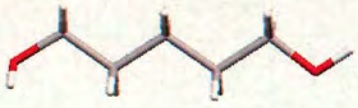

Figure 4.28 The α – *trans*, ω – *trans* conformer of pentane-1,5-diol

A major difference in all structures is the hydrogen bonding. In all cases discussed so far, the donor and acceptor atoms for a unique hydrogen bond have consistently been from α to ω. In this case, the α – hydroxyl group hydrogen bonds to it's

symmetry equivalent, as does the ω – hydroxyl group. The resulting hydrogen bonded motif is characterised by two unique C (2) chains (figure 4.29). This observation is justified by the similarity in the dimensions of the hydrogen bonds (table 4.22). The planes of the chains are parallel or anti-parallel to the 0 1 4 and the –1 0 4 lattice planes.

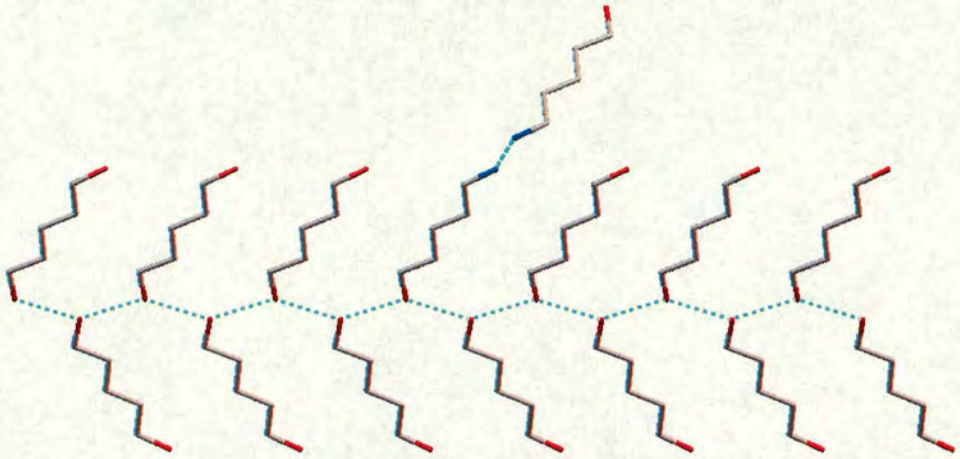

Figure 4.29 The C (2) chains in the full structure of pentane-1.5-diol. The plot is viewed down the crystallographic *a* – axis. The chain involving the ω-hydroxyl group is in the plane of the page, while the chain involving the α-hydroxyl group is perpendicular to the page.

Dimension	0.38 GPa / 293 K	Calculated
Hydrogen bond 1 (O1 donor, O1 acceptor)		
O1(-H1)..O1 /Å	2.781 (3)	2.726
O1-H1 /Å	1.006	0.998
H1...O1 /Å	1.814	1.731
O1H1O1 /°	160.1	174.73
Hydrogen bond 2 (O7 donor, O7 acceptor)		
O7(-H2)..O7 /Å	2.780 (2)	2.800
O7-H2 /Å	1.008	0.992
H2...O7 /Å	1.775	1.811
O7H2O7 /°	175.0	174.23

Table 4.22 The dimensions of the hydrogen bonds in Phase II of pentane-1,5-diol at 130 K. [$^{\#1}$ -x-½, -y, z-½, $^{\#2}$ x-½, -y-½, 2-z]

4.6.3 Discussion and Comparison of Phases I and II of Pentane-1,5-diol

4.6.3.1 Molecular Conformational Analysis

As discussed previously, phase I is composed of α-*trans*, ω-*gauche* conformers and phase II is composed of α-*trans*, ω-*trans* conformers. The α-*trans*, ω-*gauche* conformers have the corresponding hydrogen bonds aligned *trans* and *gauche* respectively. The α-*trans*, ω-*trans* conformer in the high-pressure phase has one hydrogen bond aligned in the *trans* direction and the other in the *gauche* direction. To use the notation discussed previously the low temperature conformer is denoted $g^{-}G^{-}Tt$ and the high pressure conformer $tTTg^{-}$. Experimental and calculated values for the torsion angles are given in table 4.23. The -ve sign symbolises a counter clockwise rotation with respect to the neighbouring C-C bond.

Torsion	Experimental /°	Calculated /°
Phase I - α-*trans*, ω-*gauche*		
O2..O1-C1-C2	169.70	172.58
H1-O1-C1-C2	-	174.19
O1-C1-C2-C3	179.90	-177.27
O2-C5-C4-C3	57.85	67.98
O1..O2-C5-C4	55.90	54.71
H2-O2-C5-C4	-	51.82
Phase II - α-*trans*, ω-*trans*		
O1..O1-C1-C2	70.5	68.44
H11-O1-C1-C2	-	66.91
O1-C2-C3-C4	-177.1	174.24
O7-C6-C5-C4	177.9	179.15
O7..O7-C4-C3	-177.9	-174.12
H71-O7-C4-C3	-	-174.76

Table 4.23 Experimental and calculated values for the torsion angles in phases I and II of pentane-1,5-diol.

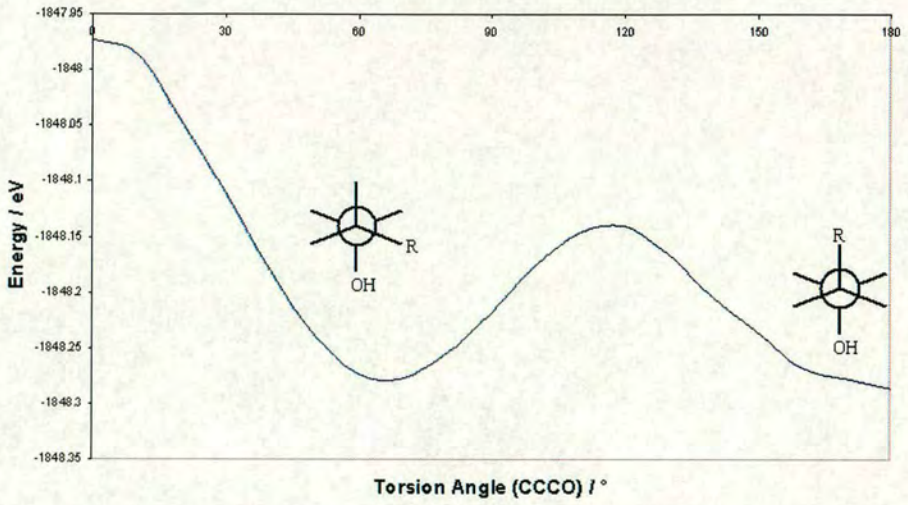

Figure 4.30 Plot of Energy v Torsion Angle for the C-C-C-O torsion in Pentane-1,5-diol. [R=$CH_2CH_2CH_2OH$]

Two *ab-initio* gas phase calculations were performed on the pentane-1,5-diol molecule with a starting geometry of tTTt: the first rotating the C-C-C-O torsion angle; the second rotating the C-C-O-H torsion angle (Dr. S. J. Clark, Department of Physics, University of Durham). The results are shown in figure 4.30 and 4.31 as graphs of relative energy v torsion angle. There are two clear minima shown in figure 4.30, these are the *gauche* and *trans* conformations of the α or ω carbon.

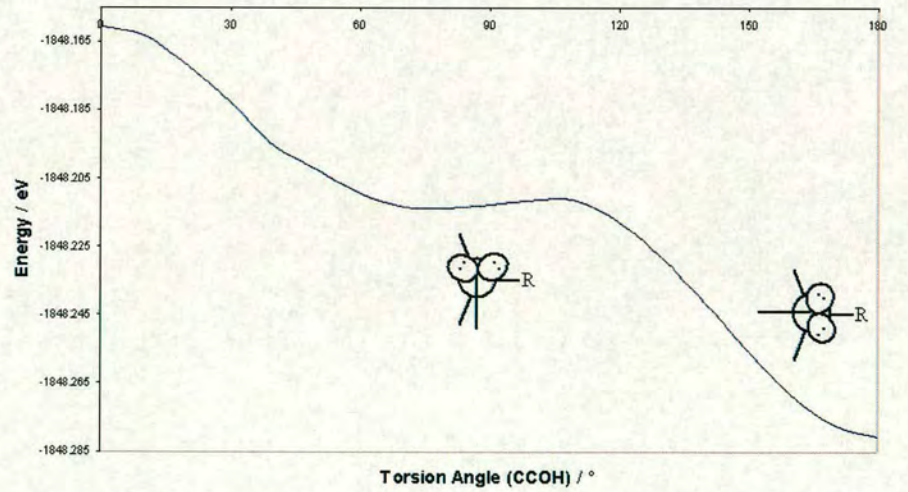

Figure 4.31 Plot of Energy v Torsion Angle for the C-C-O-H torsion in Pentane-1,5-diol. [R=$CH_2CH_2CH_2OH$]

Figure 4.31 contains a clear minimum at 180° and a shallow minimum at 70 – 80°. Experimentally, in phase I the C-C-O-H torsion angles are 170° and 56° and for phase II, 70° and 178°. These conformations are a major factor in the resulting packing motif in the solid state structures.

4.6.3.2 Hydrogen bonded chains

The low temperature and high pressure phases of pentane-1,5-diol are composed of hydrogen bonded chains involving both the α and ω hydroxyl group. Both structures crystallise in the orthorhombic space group $P2_12_12_1$ with Z'=1. Although there is similarity in the crystal system, the structures are quite different. In the low temperature phase, the α hydroxyl group hydrogen bonds to the ω hydroxyl group whereas at high pressure, the α-OH hydrogen bonds to a symmetry equivalent α-OH and the ω-OH to a symmetry equivalent ω-OH. Not only is this a striking difference between the two polymorphs, in the high-pressure phase this is markedly different to the observed hydrogen bonded pattern for other di-alcohols – of the 38 structures in the CSD only 4 have hydrogen bonds between symmetry equivalent hydroxyl groups.

Phase I has a hydrogen bonded motif containing C (8) chains that are interlinked by finite hydrogen bonds. The overall motif is different to the other diol structures with the same type of hydrogen bonds as the structure has hydrogen bonds that link the molecules in three dimensions. In phase I of propane-1,3-diol which has C (6) chains linked by finite D hydrogen bonds, the secondary motif is hydrogen bonded rings which pack in bi-layers. Phase II of ethane-1,2-diol is characterised by C (5) chains linked by finite D hydrogen bonds. These also form bi-layers. In phase I of pentane-1,5-diol, a three dimensional framework is formed.

The high pressure phase of pentane-1,5-diol, phase II, is characterised by C (2) chains. The layers of chains are similar to the herring-bone motif of the even diols, this is distorted due to the conformation of the α C–O bond (figure 4.32). The

overall structure is very different to the low temperature phase, as was the case for ethane-1,2-diol and propane-1,3-diol.

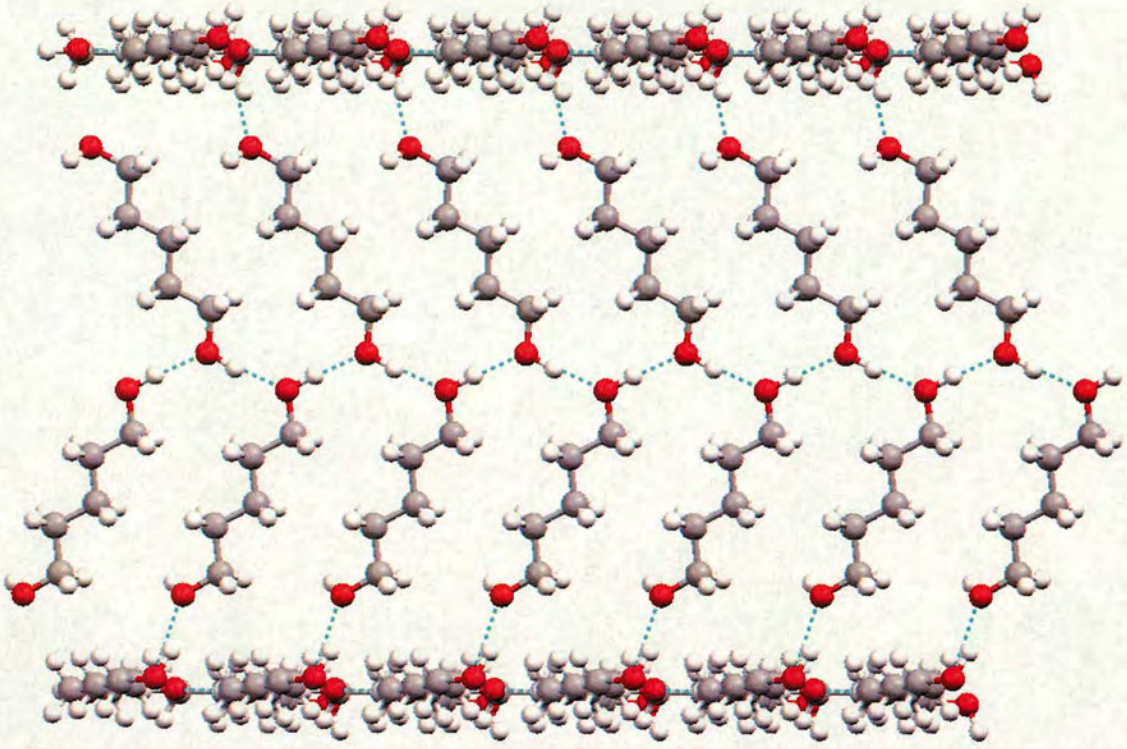

Figure 4.32 The layers of C (2) chains in the full structure of pentane-1,5-diol. Each layer has a similar herring-bone motif to the even diols.

4.6.3.3 Molecular Volume

The decrease in molecular volume from the low temperature phase to the high-pressure phase is only 3.3 %. In the phase I, the average volume occupied by one molecule is 151.9 $Å^3$ compared to 146.9 $Å^3$ in phase II. For the diols, this is the smallest percentage change between low temperature and high-pressure polymorphs, and also the lowest pressure that a different polymorph is observed. To account for this change in molecular volume, the number of intermolecular distances are to be considered.

Distance / Å	Phase I (150 K)	Phase II (0.95 GPa)
3.6 → 3.8	0	4
3.8 → 4.0	14	12
4.0 → 4.2	10	6
Total	24	22

Table 4.24 Number of intermolecular C-C distances between 3.6 and 4.2 Å per molecule

Table 4.24 contains the values for the number of distances between carbon atoms on adjacent molecules from 3.6 – 4.2 Å. Surprisingly, there are slightly fewer of these in the high pressure phase, although this was observed for ethane-1,2-diol where phase III was also layered. The values for the number of distances between carbon and oxygen atoms on adjacent molecules between 3.0 and 4.4 Å show an increase (table 4.25). As before, this shows that these intermolecular distances do not shorten, the molecules rearrange to compensate for the change in molecular volume.

Distance / Å	Phase I (150 K)	Phase II (0.95 GPa)
3.0 → 3.4	0	2
3.4 → 3.6	10	4
3.6 → 4.0	12	16
4.0 → 4.4	4	14
Total	26	36

Table 4.25 Number of intermolecular C-O distances between 3 and 4 Å per molecule

4.7 Discussion and Comparison of the low temperature and high pressure phase behaviour of the α - ω di-alcohols

There are three areas to consider when analysing the structural behaviour of the α – ω diols in the solid state:

The first, and arguably the most interesting, is the molecular conformational analysis. So far, we find that ethane-1,2-diol has two new high pressure phases. The ambient pressure polymorph, phase I, is the *gauche* conformer with one *gauche* hydrogen and one *eclipsed* hydrogen, denoted $g^-G^-e^+$. Phase II at 2 GPa is also a *gauche* conformer, although this time there is one *trans* hydrogen and one *gauche* hydrogen, denoted g^+G^+t. In phase III all conformations about the C-C and C-O bonds are *trans*, denoted tTt. Propane-1,3-diol also has three different conformers present in the solid state contained within 2 different polymorphs. This time there are four torsion angles to consider for each, the extreme C-C and C-O torsions fully describe each molecule. In the ambient pressure phase, the conformer is denoted $g^+G^-G^-g^-$. The high-pressure phase contains 2 conformers, these are denoted $e^-TG^+e^-$ and e^+TTt. Pentane-1,5-diol has two different conformers, again these can be described by the extreme C-C and C-O torsions (the conformation of the middle C-C bonds are all *trans*). At ambient pressure the conformer is g^-G^-Tt and at high pressure, $tTTg^-$. One similarity is that all high-pressure phases contain more *trans* conformations than the ambient pressure phases. This could be a reason why butane-1,4-diol and hexane-1,6-diol do not have different phases at high pressures as they are composed of tTTt conformers.

The second is the type of hydrogen bonding motif, which is highly dependent on the conformation of the molecule. Macrae and Taylor[2] were unable to determine any rules for the packing of diols, and in their work there are similarities between packing motifs determined by the hydrogen bonding and the molecular conformation. The three phases of ethane-1,2-diol show hydrogen bonded motifs that are present in the phases of the heavier diols. The first, in the ambient pressure phase I, is composed of C_2^2 (4) chains that has four molecules in the repeating unit of

the chain, which is similar to the low temperature polymorph of ethanol. This motif is also displayed in the low temperature phases of propane-1,3-diol and pentane-1,5-diol (see figure 4.33).

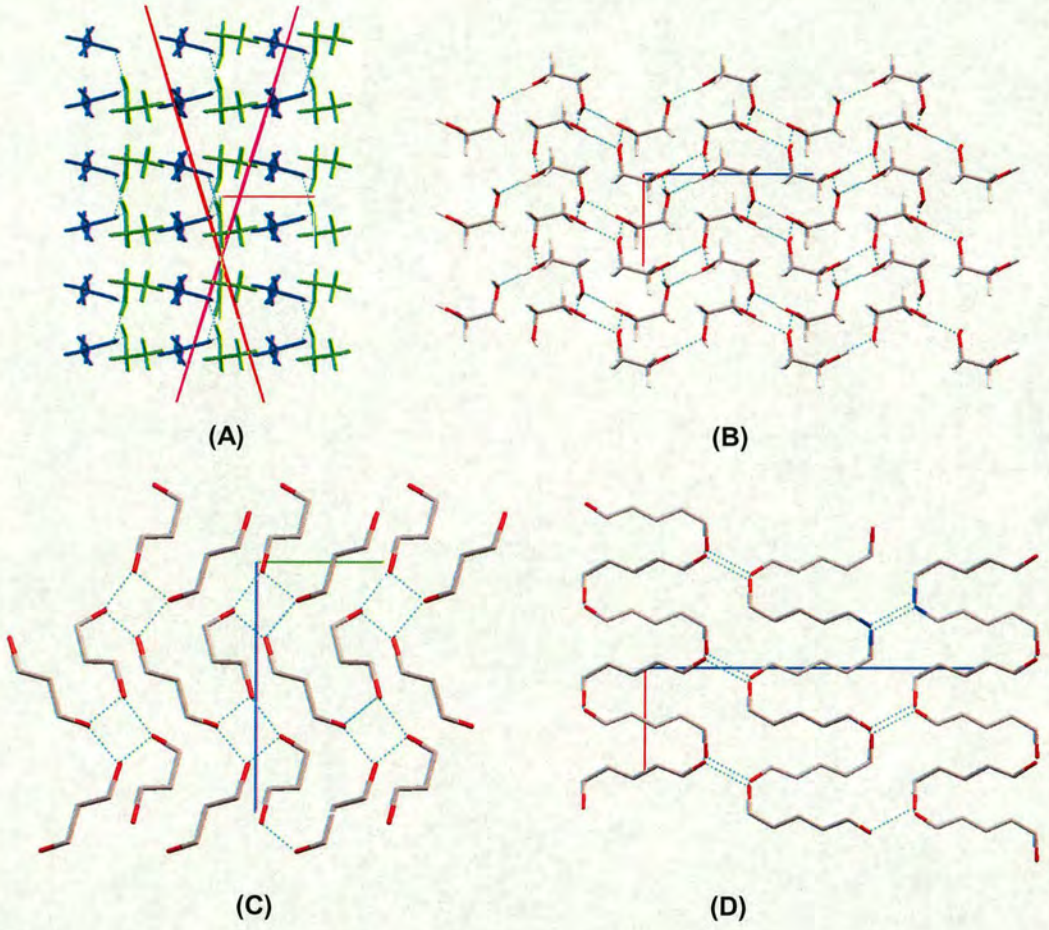

Figure 4.33 The hydrogen bonded chains of (A) ethanol phase I, (B) ethane-1,2-diol phase I, (C) propane-1,3-diol phase II and (D) pentane-1,5-diol phase I. All four structures contain "wave-like" chains with four molecules in the repeating unit.

Phase II of ethane-1,2-diol contains a hydrogen bonded motif that consists of C (5) chains connected by finite D hydrogen bonds. The low temperature polymorphs of both propane-1,3-diol and pentane-1,5-diol can also be described in this way. The structures of phase II of ethane-1,2-diol and phase I of propane-1,3-diol are strikingly similar, both containing bi-layers of hydrogen bonded chains (figure 4.34). Phase I

of pentane-1,5-diol does not have a layered structure and is quite different from the other observed motifs.

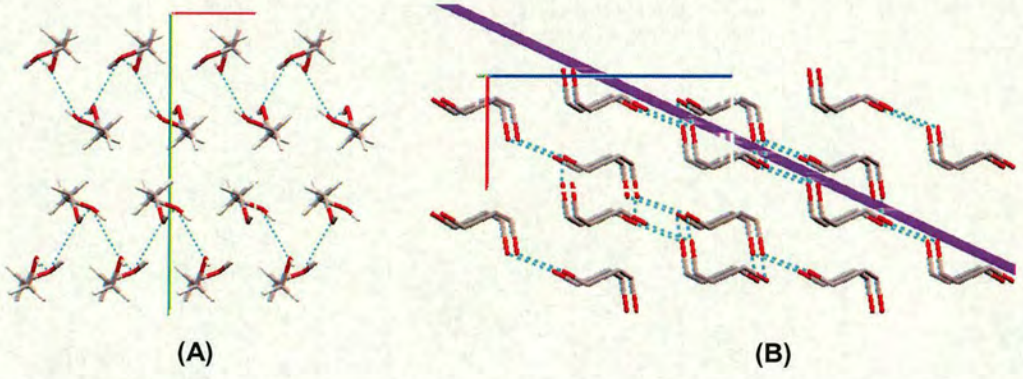

Figure 4.34 The hydrogen bonded chains of (A) ethanol phase II and (B) propane-1,3-diol phase I. Both structures contain bi-layers.

The third and highest pressure phase of ethane-1,2-diol contains layers of hydrogen bonded C_2^2 (4) chains (figure 4.35). This is a similar hydrogen bonded motif to that displayed in the crystal structures of the even diols such as butane-1,4-diol. This motif can only be observed where the conformation of all torsion angles in the molecule are *trans*.

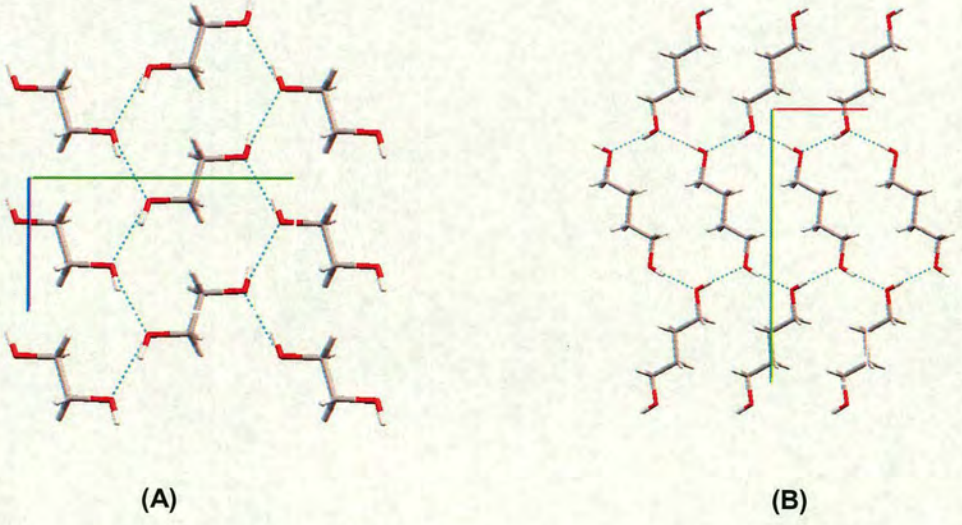

Figure 4.35 The crystal structures of phase III of ethane-1,2-diol (A) and butane-1,4-diol (B). [*a*-axis in red, *b*-axis in green, *c*-axis in blue]

Third and finally is the reduction in molecular volume. As was discussed in the previous chapter, the application of pressure causes a reduction in molecular volume and as a result the molecules rearrange to compensate for this. The primary bond lengths and angles are not affected by these relatively small pressures. It is apparent that there is a slight shortening of intermolecular hydrogen bonds in high pressure structures where the phase is stable at both ambient and high pressure. Mostly, the new high-pressure polymorphs have hydrogen bonds similar in dimensions and therefore energy as the low temperature polymorphs. The major effect when applying pressure is a rearrangement of the molecules so that there are more "contacts" between neighbouring molecules rather than a shortening of intermolecular distances.

4.8 References

1. Thalladi V. R., Boese R., Weiss H. C., *Angew. Chem. Int. Ed.,* **39** (5), 918 (2000).
2. Taylor R. and Macrae C. F., *Acta Cryst.*, **B57**, 815 (2001).
3. Cambridge Structural Database (CSD) Version 5.21, released April 2001, Allen F. H. and Kennard O.
4. Boese R., and Weiss H. C., *Acta Cryst. C.,* **54**, 24, (1998).
5. Merrill L. and Bassett W. A., *Rev. Sci. Instrum.*, **45**, 290 (1974).
6. CAD-4 Express Software. Enraf-Nonius, Delft, The Netherlands, 1994.
7. SMART: Area-Detector Software Package. (1993) Siemens Industrial Automation, Inc.: Madison, WI.
8. DIRAX: Duisenberg A. J. M, *J. Appl. Cryst.,* **25**, 92 (1992).
9. SIR92, Altomare A., Cascarano G., Giacovazzo C. and Gualardi A., *J. Appl. Cryst.*, **26**, 343 (1993).
10. SHELXTL Programs for Crystal Structure Analysis (Release *97-2)*. G. M. Sheldrick, Institüt für Anorganische Chemie der Universität, Tammanstrasse 4, D-3400 Göttingen, Germany, 1998.
11. GEMINI, Sparks R. A.(1999), Bruker AXS, Madison, Wisconsin, USA.
12. SADABS, Sheldrick G. M. (2001), University of Gottingen and Bruker AXS, Madison, Wisconsin, USA.
13. ABSORBU2, Prof. R. J. Angel, Virginia Polytechnic Institute and State University.
14. SAINT: Area-Detector Integration Software. (1995) Siemens Industrial Automation, Inc.: Madison, WI.
15. SHADE, Allan D. R., Clark S. J., Parsons S. and Ruf M., *J. Phys. Condens. Matter.*, **12**, L613 (2000).
16. SHELXS86 - Program for Crystal Structure solution. Sheldrick, G. M., Institüt für Anorganische Chemie der Universität, Tammanstrasse 4, D-3400 Göttingen, Germany, 1986.

17. CRYSTALS, Watkin, D. J., Prout, C. K., Carruthers, J. R., Betteridge, P. W. & Cooper R. I., Issue 11 (2001), Chemical Crystallography Laboratory, OXFORD, UK.
18. ROTAX, Cooper R. I., Gould R. O., Parsons S., Watkin D. J., *J. Appl. Cryst.*, **35**, 168 (2002).
19. Le Page, Y., *J. Appl. Cryst.*, **15**, 255 (1982). Flack, H. D., *Acta Cryst.*, A**43**, 564 (1987).
20. XTAL 3.2, Hall, S. R., Flack, H. & Stewart, R. F. (1992). University of Western Australia.
21. Cramer C. J. and Truhlar G. T., *J. Am. Chem. Soc.*, , **116**, 3892 (1994).

Chapter 5

High Pressure and Low Temperature Structural Studies of Haloforms

5.1 Introduction

Although the trihalogenated derivatives of methane, iodoform (CHI_3), bromoform ($CHBr_3$), and chloroform ($CHCl_3$), have the same tetrahedral molecular geometry, their low-temperature crystalline phases have strikingly different structures. On cooling below the melting temperature of 230 K, Fourme and Renaud[1] found that chloroform crystallises into a centrosymmetric orthorhombic phase, with *Pnma* symmetry, which is stable to at least 185 K — the limit of their single-crystal studies. In contrast to the solitary orthorhombic phase of chloroform, three phases of bromoform have been identified at low temperature. Initial single-crystal x-ray diffraction studies by Kawaguchi *et al*[2] showed that the α-phase, which forms on freezing from the liquid at 281 K, crystallises into a disordered structure with hexagonal $P6_3/m$ symmetry. At 253 K, they found that the molecules are distributed statistically parallel (43%) and anti-parallel (57%) to the *c*-axis of the unit cell. A subsequent Raman study by Burgos *et al*[3] indicated a further two crystalline phases on cooling below the stability region of the α-phase. They found that the α-phase was stable from the melting point at 281 K, to a temperature of 268 K, where the transition to the β-phase occurs. The β-phase was found to be stable to the 98 K limit of the study. However, on rapid cooling of the α-phase to 98 K, the γ-phase was found which can be transformed to the β-phase on subsequent heating. To test the observations found in the Raman work, Myers and Torrie[4] carried out a neutron powder diffraction experiment using deutero-bromoform in order to determine the full structures of both the β and γ phases. Initially a sample of the γ-phase was prepared by quenching liquid bromoform to approximately 90 K where the resulting powder was cryoground to reduce the crystallite size and hence improve the powder averaging. On subsequent cooling to 14 K, the structure was found to be fully ordered with trigonal *P*-3 symmetry. The β-phase was produced by first annealing the sample at 220 K and, on further cooling to 14 K, its structure was determined to be triclinic with *P*-1 symmetry. The structures of the β and γ phases were found to be related by the translation of alternate molecular layers.

The heavier analogue, iodoform (CHI_3), is a solid at ambient conditions and its structure has been determined by Khotsyanova *et al*[5] using single-crystal x-ray diffraction techniques. The structure is also disordered and the molecules pack in the centrosymmetric hexagonal space group $P6_3/m$ with the iodine atoms related by a three-fold axis around the carbon hydrogen bond, and the disorder about the mirror plane. All hydrogen atoms are aligned parallel to the *c*-axis. This structure is essentially the same as α-phase of bromoform.

There is a range of different structures of the haloforms at ambient pressure and low temperature despite their rather similar molecular geometry. However, this chapter reports the high-pressure crystal structures of both chloroform and bromoform, which we have determined using a combination of single-crystal x-ray diffraction techniques and first-principles calculations. It is found that they both adopt the hexagonal $P6_3$ crystal structure. This is structurally similar to the $P6_3/m$ α-phase of bromoform and iodoform, although the molecules are not disordered and so the mirror plane is lost.

5.2 Experimental

The experimental procedures for the determination of the high-pressure phases of chloroform and bromoform were basically identical. For both chloroform and bromoform, the samples were loaded as liquids into Merrill-Bassett[6] diamond-anvil high-pressure cells which had been prepared with tungsten gaskets. The pressure was increased until the nucleation of several crystallites had occurred. For chloroform this initially occurred at 1 GPa while for bromoform crystallisation was initiated at a pressure of 0.6 GPa. For each sample, the temperature was then cycled close to the melting point until only one crystallite had remained. Single crystals were obtained from the remaining nucleation points by allowing the pressure cell to cool. The sample crystals eventually filled the 200 μm gasket holes and the final pressures were measured using ruby fluorescence spectroscopy. All data were measured using a CAD-4[7] diffractometer (graphite monochromated Mo Kα radiation). Intensities were collected using ω-scans at the position of least attenuation of the pressure cell.

For chloroform, the setting angles of 23 strong reflections with $4.00° < \theta < 14.35°$ were determined and indexing using DIRAX[8] gave the hexagonal cell to be a = 5.8610(8) Å and c = 6.5960(13) Å with a volume of 196.23(5) Å^3. Intensities for all accessible reflections, $sin\theta/\lambda < 0.71$ Å were measured, and the structure solved by direct methods using the Sir-92[9] suite, yielding space group $P6_3$ with 2 molecules in the unit cell. The final model was refined against F^2 using Shelxl-97[10]. This gave final residuals of R1 = 4.37 % based on 147 unique data with $F > 4\sigma$ (F) and ωR2 = 10.96 for all 244 data. There were a total of 16 refined parameters, and the goodness of fit was 1.045. The hydrogen atoms were geometrically constrained to ride on the carbon atom, and all other atoms refined with anisotropic displacement parameters.

The sample was re-melted at 1 GPa in order to test the phase stability. A new crystal was formed, and the setting angles for 19 strong reflections with $4.38° < \theta < 12.97°$ determined. Indexing the reflections using DIRAX[8] gave an orthorhombic

cell a=7.324(2) Å, b=9.322(2) Å and c=5.727(1) Å with a volume of 391.0(2) Å^3. This cell is essentially the same as the low temperature phase, but with an average 2.1 (2) % contraction in cell edges and a 6.2 (3) % reduction in volume. An identical data collection and structure solution strategy was adopted to that used for the $P6_3$ phase and this yielded the *Pnma* symmetry with 4 molecules in the unit cell. A least squares refinement was performed against F^2, the hydrogen atoms were placed in calculated positions and all non-H atoms were refined with anisotropic displacement parameters. The final residuals were R1 = 4.44 % based on 184 unique data with F > 4σ (F) and a ωR2 = 11.02 % for refinement of all 23 parameters. The goodness of fit was 0.951.

For bromoform, the setting angles of 25 strong reflections were determined for 3.72° < θ < 15.35°. Indexing using DIRAX[8] gave the hexagonal cell dimensions to be a = 6.300(1) Å and c = 7.150(2) Å with V = 245.76 Å^3. The space group was found to be $P6_3$ with 2 molecules in the unit cell, and the structure was solved by Patterson methods using shelxs[11]. The hydrogen atom was geometrically placed to ride on the carbon atom, and the non-hydrogen atoms refined with anisotropic displacement parameters. A least squares refinement against F^2 gave the residuals R1 = 4.08 % based on 146 unique data with F > 4σ (F) and a ωR2 = 9.47 % for the refinement of all 15 parameters. The goodness of fit was 1.096.

Refinement statistics are given in table 5.1.

Temperature / Pressure	293 K / 0.6 GPa	293 K / 0.6 GPa	293 K / 1.0 GPa
Formula	$CHCl_3$	$CHCl_3$	$CHBr_3$
Weight	119.37	119.37	252.75
Radiation	Mo K-α	Mo K-α	Mo K-α
Crystal System	Orthorhombic	Hexagonal	Hexagonal
Space Group	*Pnma*	$P6_3$	$P6_3$
a/Å	7.324(2)	5.861(1)	6.300(1)
b/Å	9.322(2)	5.861(1)	6.300(1)
c/Å	5.727(1)	6.596(1)	7.150(1)
Volume (Å^3)	391.0(1)	196.23(5)	245.76(7)
Z	4	2	2
No. reflections for cell	25	23	25
2θ range (°)	$8 < 2\theta < 40$	$8 < 2\theta < 30$	$6 < 2\theta < 32$
D_c (Mg/m^3)	2.028	2.020	3.415
μ mm^{-1}	2.093	2.085	24.424
Reflections collected	541	480	600
Unique data	290 [R(int) = 0.0419]	244 [R(int) = 0.0556]	207 [R(int) = 0.0567]
No. of data with $I > 2\sigma$	184	147	146
T_{min}/ T_{max} [ABSORBU]	0.249 / 0.560	0.246 / 0.476	0.247 / 0.526
Parameters	23	16	15
R_1	0.0444	0.0437	0.0408
wR_2	0.1007	0.0993	0.0845
S	0.951	1.043	1.094
$\Delta\rho_{max}$ (eÅ^3)	0.263	0.280	0.399
$\Delta\rho_{min}$ (eÅ^3)	-0.198	-0.322	-0.598

Table 5.1 Refinement Statistics for phases I and II of chloroform at high pressure and the high pressure δ-phase of bromoform.

5.3 The Crystal Structures of Chloroform at Low Temperature and High Pressure

5.3.1 Introduction

Chloroform ($CHCl_3$) is a clear, colourless liquid with a melting point of 209.3 K and a boiling point of 334.7 K. It is a halogenated derivative of methane, characterised by the central sp^3 hybridised carbon atom bonded to three chlorine atoms and one hydrogen atom that are arranged approximately in a tetrahedron around the carbon (figure 5.1).

Figure 5.1 A molecule of chloroform, showing the central carbon atom in grey surrounded by the 3 chlorine atoms (green) and 1 hydrogen atom (white). The atoms bonded to carbon lie approximately on the corners of a tetrahedron.

Two phases of chloroform were found to be stable at a pressure of 1 GPa using a combination of single crystal x-ray diffraction techniques and *ab-initio* density functional calculations. Phase I of chloroform was previously determined by single crystal X-ray diffraction at 185 K by Fourme and Renaud[1]. This phase is metastable at a pressure of 1 GPa, the new high-pressure polymorph, phase II was also determined at a pressure of 1 GPa.

5.3.2 Phase I

Phase I of chloroform, which is stable below the melting point of 209.3 K and at 1 GPa, crystallises in the orthorhombic space group *Pnma*. There are four molecules in the unit cell, the asymmetric unit consists of three half occupied atoms, the H-C-Cl part lies on the mirror plane where b = ¾ and a fully occupied Cl atom on a

general position. The remaining Cl atom in the molecule is generated by the mirror symmetry. The mirror plane symmetry can be used to characterise the structure, figure 5.2 shows that the chloroform molecules have the C-H bond aligned approximately parallel and anti-parallel to the *a*-axis. The molecules on the mirror plane x, 0.25, z are aligned approximately anti-parallel to the *a*-axis and the molecules on the mirror plane x, 0.75, z are aligned approximately parallel to the *a*-axis. The layers are related by inversion.

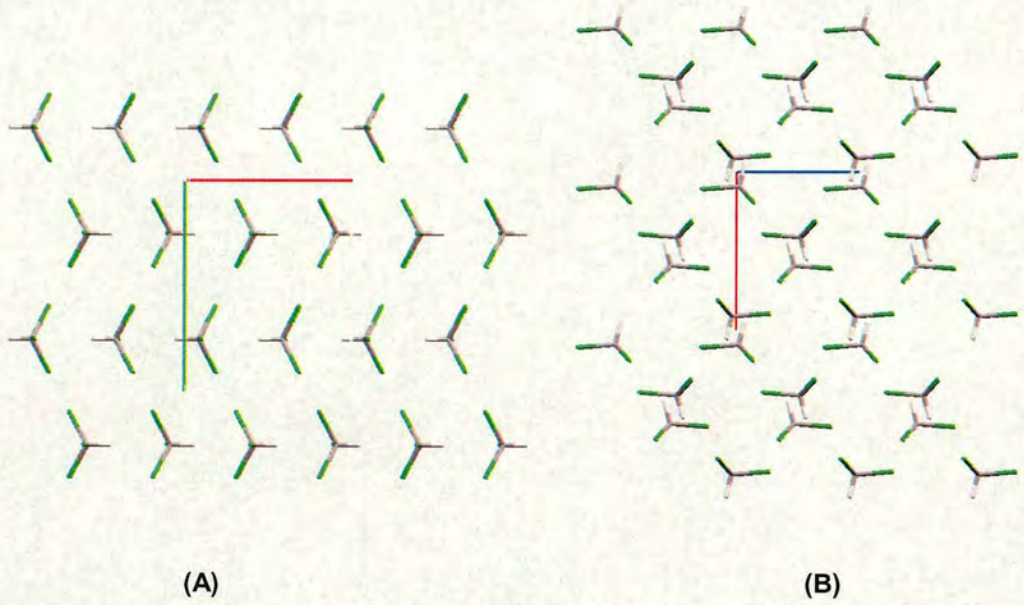

(A) **(B)**

Figure 5.2 The crystal structure of phase I of chloroform. **(A)** Viewed down the crystallographic *c*-axis. **(B)** Viewed down the crystallographic *b*-axis. The molecules are arranged in layers where the C-H bond of each molecule lies on the mirror plane, either at x, 0.25, z or x, 0.75, z. [*a*-axis in red, *b*-axis in green, *c*-axis in blue].

5.3.3 Phase II

Phase II of chloroform was determined at a pressure of 1 GPa, and has a very different structure to that of phase I. In the asymmetric unit, the carbon and hydrogen atoms have an occupancy of 1/3 and lie on the 6_3 axis at 1/3, 2/3, z. The chloroform molecule is completed by a fully occupied chlorine atom on a general position that is replicated by the 3 fold rotation around the C-H bond. The structure packs in layers that are separated by ½ *c* (figure 6.3).

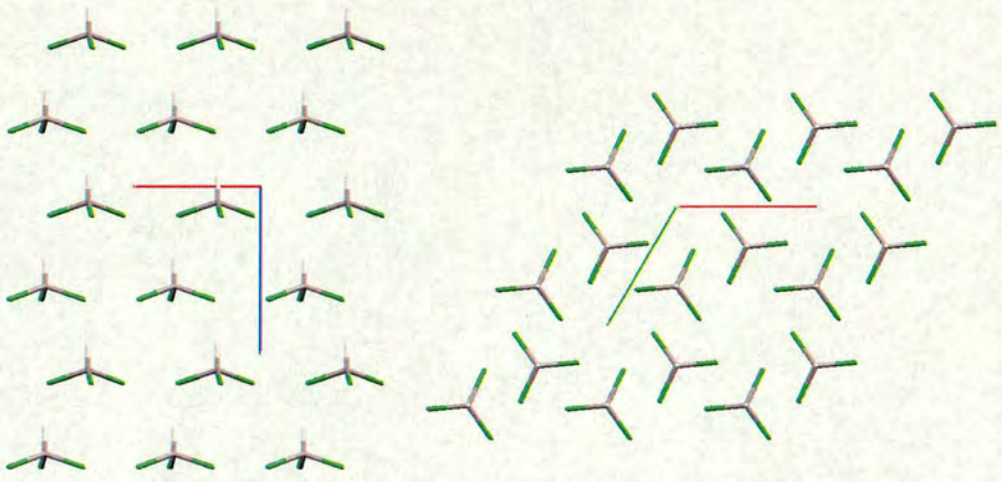

(A) (B)

Figure 5.3 The crystal structure of phase II of chloroform. **(A)** Viewed down the crystallographic *a*-axis. **(B)** Viewed down the polar *c*-axis. [*a*-axis in red, *b*-axis in green, *c*-axis in blue].

5.3.4 Discussion and Comparison of Phases I and II of Chloroform

5.3.4.1 Layer type

Phase I of chloroform is characterised by layers of molecules where the C-H bond lies on the mirror plane at x, ¼, z or x, ¾, z. The C-H bond is aligned parallel to the *a*-axis at x, ¼, z and anti-parallel to the *a*-axis at x, ¾, z. Figure 5.4 (A) shows the two chains, and (B) shows a slice of the crystal structure: i.e. one of the layers in figure 5.4 (A). This layer is split into a further 2 layers where the C-Cl bond that lies on the mirror plane is aligned either parallel or anti-parallel to the *c*-axis. The layers are related by the *a*-glide perpendicular to the *c*-axis.

In phase II, the layer type is quite different. This is a major consequence of the polar nature of the structure, where all C-H bonds are aligned parallel to the *c*-axis. Figure 5.5 (A) shows two layers within the structure that are related by the 6_3 screw axis. An enlargement of one layer shows that the molecules within the layer are related by translational symmetry only.

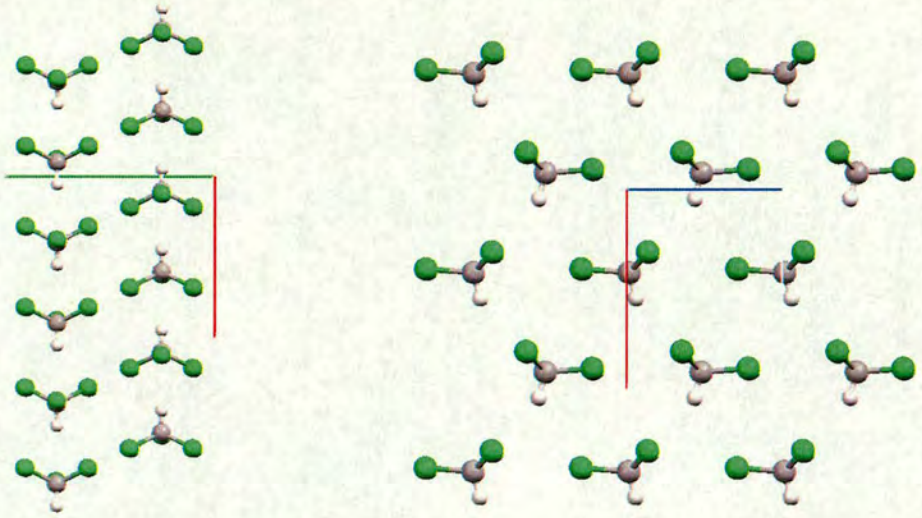

(A) (B)

Figure 5.4 **(A)** Two layers of $CHCl_3$ molecules in phase I showing the alternation of the molecules and the layers with respect to the C-H bond viewed down the *c*-axis **(B)** A layer of $CHCl_3$ molecules viewed down the *b*-axis. [*a*-axis in red, *b*-axis in green, *c*-axis in blue].

A possible mechanism for the phase I to II phase transition is that one layer of molecules in phase I invert, which would leave a polar structure. A rearrangement of alternate layers in the *ab* plane would then be required to complete the transition.

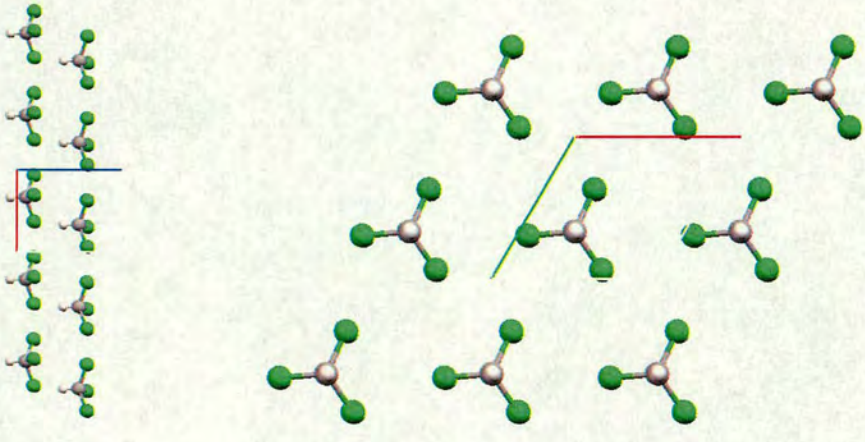

(A) (B)

Figure 5.5 **(A)** Two layers of phase II of chloroform. **(B)** One layer viewed down the polar *c*-axis. [*a*-axis in red, *b*-axis in green, *c*-axis in blue].

The crystal structure of phase I can also be described as having corrugated layers of chloroform molecules, these are aligned approximately parallel to the *c*-axis (figure

5.6). This layer type has the chlorine atoms on the layers. From this comparison of the structures of phase I and phase II it is fairly obvious that the molecular packing in the two polymorphs is very different.

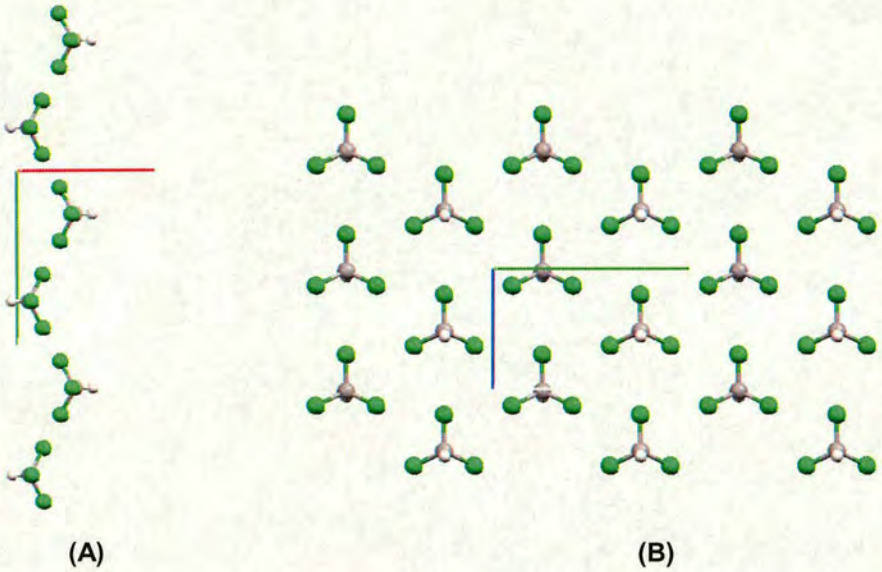

Figure 5.6 **(A)** One corrugated layer of phase I of chloroform. **(B)** The same layer viewed down the *a*-axis. [*a*-axis in red, *b*-axis in green, *c*-axis in blue].

5.3.4.2 Overall packing of molecules and halogen atoms

In the tetra-chlorides of tin and lead, the molecular packing is heavily influenced by the positions of the chlorine atoms, which when considered in isolation adopt a close packed arrangement (Dawson *et al*[12]). In the case of chloroform, the chlorine atoms themselves are not close packed. However, if the carbon atoms are modelled as the centre of the molecule, the carbon atoms and hence the molecules themselves form an arrangement that is very close to being hexagonal close packed. Figure 5.7 (A) shows the packing of the chlorine atoms, these are positioned on either the 2 1 0 or the 2 –1 0 lattice planes. These are both very strong reflections in the data set. Part (B) of figure 5.7 shows the carbon atoms. The nearest neighbours around one carbon atom are highlighted, above and below in green and in the same layer in orange. This shows the ABAB nature of the structure.

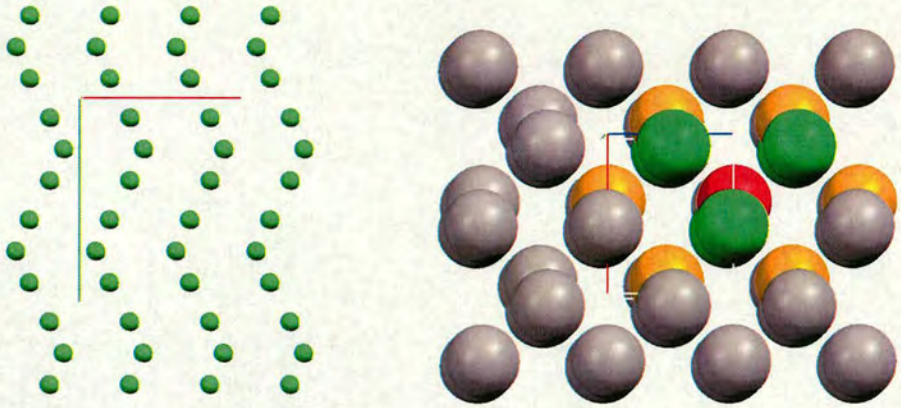

Figure 5.7 **(A)** The chlorine atoms of chloroform phase I. **(B)** The carbon atoms of chloroform phase I. One carbon atom is highlighted red, the nearest neighbours in the A layer are coloured orange, and in the B layer are green. The molecules pack overall in an ABABAB fashion and a small shift in the B layer would result in hexagonal close packing. [*a*-axis in red, *b*-axis in green, *c*-axis in blue].

In phase I it was shown that the chloroform molecules were very close to being close packed. This is not the case for phase II, the packing appears to be simple hexagonal, this is shown in figure 5.8 (B) where the carbon atoms are modelled as the centre of the molecule. Figure 5.8 (A) shows the chlorine atoms, these are also packed in quite a primitive fashion.

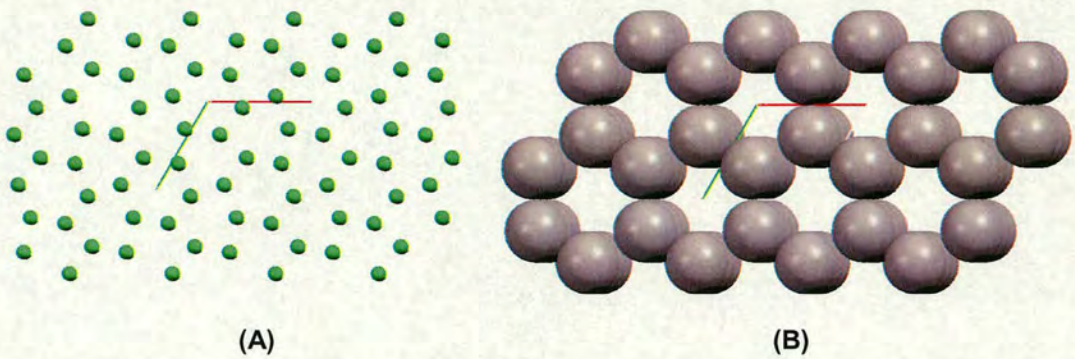

Figure 5.8 **(A)** The chlorine atoms of chloroform phase II. **(B)** The carbon atoms of chloroform phase I. [*a*-axis in red, *b*-axis in green, *c*-axis in blue].

5.3.4.3 Change in molecular volume

At 1 GPa and 295 K, chloroform has two stable phases: the low-temperature *Pnma* phase is observed at this pressure, with the same crystallographic packing structure, and with only a slight contraction in cell edges and unit cell volume; in the $P6_3$ hexagonal phase the molecules are positioned such that the chlorine atoms are related by a three-fold axis around the carbon – hydrogen bond. All the molecules of the $P6_3$ structure are orientated so that the carbon-hydrogen bonds are aligned parallel to the *c*-axis. The molecular packing is more efficient in the high-pressure phases: in the $P6_3$ phase, the molecular volume is 98.12 (3) $Å^3$; and in the *Pnma* high-pressure phase, each molecule occupies 97.75 (3) $Å^3$ compared to a molecular volume of 103.8 $Å^3$ in the low temperature phase. This is the first case discussed in this thesis where two polymorphs are stable at the same pressure. There is a very slight increase in the molecular volume from phase I to the high-pressure phase II. To compare the packing in the structures, the number of distances between the following atoms on neighbouring molecules will be counted (in a manner similar to that used in in chapters 2 and 3): C and Cl; Cl and Cl; C and C. As the hydrogen atoms were placed geometrically in the refinement, it was not possible to compare the intermolecular hydrogen – chlorine distances, although this will be discussed later using results from the *ab-initio* calculations. Unusually chloroform has two different polymorphs that are meta-stable at the same pressure, and this allows us to make pressure independent comparisons between the two structures.

Distance / Å	Phase I (185 K)	Phase I (1 GPa)	Phase II (1 GPa)
3.4 → 3.6	0	0	6
3.6 → 4.0	6	12	0
4.0 → 4.4	12	6	6
4.4 → 4.8	0	0	12
Total	18	18	24

Table 5.2 Number of intermolecular C-Cl distances between 3.4 and 4.8 Å per molecule

The case where the ambient pressure phase is also stable at high pressure has been observed in other molecular systems, for example in the even diols discussed in chapter 4. There are other systems where the ambient phase is found at high pressure, and after increasing the pressure and growing another crystal, a new phase has formed. This is true for ethane-1,2-diol (McGregor *et al*[13]), pyridine (Dawson *et al*[14] and formamide (Dawson *et al*[15]). As was discussed in chapter 4, the intermolecular distances did not shorten with application of pressure, there were more of them. For chloroform, the results are similar. In phase II, there are 6 more C-Cl distances between 3.4 and 4.8 Å than in phase I, even at the pressure where both phases can be observed (table 5.2).

Distance / Å	Phase I (185 K)	Phase I (1 GPa)	Phase II (1 GPa)
3.0 → 3.6	4	4	5
3.6 → 3.8	12	12	0
3.8 → 4.0	4	12	22
Total	20	28	27

Table 5.3 Number of intermolecular Cl-Cl distances between 3.0 and 4.0 Å per molecule

Comparing phase I at 0 GPa (185 K) and phase I at 1 GPa (293 K), there is an increase in the number of intermolecular C-Cl distances between 3 and 4 Å (table 5.3). At 0 GPa (185 K) there are a total of 20 distances, whereas in the same phase at a higher pressure of 1 GPa (293 K), there are 28. Similarly, phase II at 1 GPa (293 K) has 27 observed C-Cl distances. This is an increase with respect to phase I at 0 GPa (185 K), but a slight decrease compared to the same phase at 1 GPa (293 K). This phenomenon was also observed for ethane-1,2-diol (McGregor *et al*[13]), where the difference is due to the different packing motif, as is the case with chloroform.

Distance / Å	Phase I (185 K)	Phase I (1 GPa)	Phase II (1 GPa)
4.4 → 4.8	2	4	6
4.8 → 5.2	4	2	0
5.2 → 5.5	0	0	0
Total	6	6	6

Table 5.4 Number of intermolecular C-C distances between 4.4 and 5.5 Å per molecule

The number of C-C intermolecular distances is the same, there are 6 for each phase between 4.4 and 5.5 Å (table 5.4). These shorten with increasing pressure.

The final distance to be considered is the intermolecular H..Cl distances. All measurements for this section are taken from the *ab-initio* calculations (Dr. S.J. Clark), also used to calculate accurate hydrogen atom co-ordinates.

Distance / Å	Phase I (185 K)	Phase I (0.06 GPa)	Phase II (0.06 GPa)
2.5 → 3.0	0	6	4
3.0 → 3.5	6	0	2
3.5 → 4.0	4	6	6
Total	10	12	12

Table 5.5 Number of intermolecular Cl-H distances between 3.0 and 4.0 Å per molecule

A major difference in the symmetry of the two phases is a consequence of these Cl..H contacts. Figure 5.9 contains a plot of the contacts for phase I (A) and phase II (B). It is observed that in both phases the hydrogen has shared contacts with three neighbouring chlorine atoms. In the orthorhombic phase I there are two short and one long, and in the hexagonal phase II there are three identical contacts. The dimensions of these are given in table 5.6.

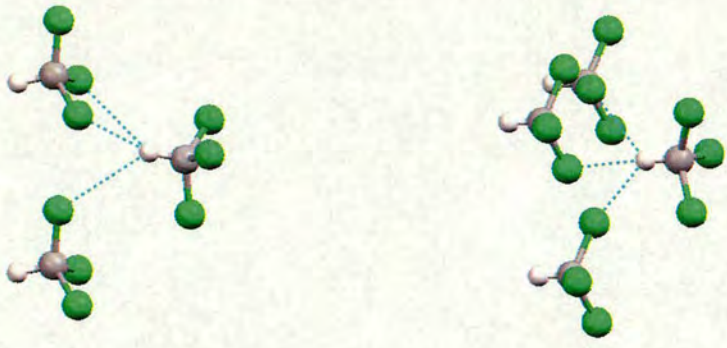

(A) (B)

Figure 5.9 **(A)** The C-H..Cl contacts in Phase I. The short contacts are to the top molecule, and the long contact to the bottom molecule. **(B)** The C-H..Cl contacts in phase II. The contacts have the same dimensions, and are to chlorine atoms on different molecules.

A striking difference shown in figure 5.9 is that the contacts are to chlorine atoms in two different molecules in phase I, whereas in phase II the contacts are to chlorine atoms on three different molecules. The experimental values are in parenthesis; these are in good agreement with the calculated values (table 5.6).

Dimension	185 K	0.6 GPa	0.6 GPa
Short contacts – x2 for Phase I and x3 for phase II			
C…Cl / Å	3.887 (3.845)	3.848 (3.789)	3.597 (3.563)
H..Cl / Å	3.000 (2.954)	2.966 (2.974)	2.871 (2.867)
C-H / Å	1.057 (1.060)	1.055 (0.980)	1.054 (0.979)
CHCl / °	141.86 (141.93)	141.45 (141.36)	126.34 (128.34)
Long contacts – x1 for Phase I			
C…Cl / Å	3.953 (3.909)	3.878 (3.778)	-
H..Cl / Å	3.161 (3.124)	3.069 (3.027)	-
C-H / Å	1.057 (1.060)	1.055 (0.980)	-
CHCl / °	132.50 (131.53)	134.10 (134.40)	-

Table 5.6 The calculated dimensions of the Cl..H-C contacts for Phases I of chloroform at 185 K and 0.6 GPa, and Phase II at 0.6 GPa. The experimental values are in brackets.

These dimensions can be considered as very weak hydrogen bonds[17]. The carbon donor is shared by three chlorine acceptors, this is known as a chelated hydrogen

bond. The bond energy of these weak interactions is less than 4 kcal/mol, other examples of hydrogen bonds of this strength are C-H…O/N or O/N-H…π bonds[17].

Ab-initio calculations (Dr. S. J. Clark, Department of Physics, University of Durham) were used to determine accurately the hydrogen atom positions and the relative enthalpies of the phases. Calculated co-ordinates and unit cell dimensions are given in Appendix 6. The calculated energy difference between the orthorhombic phase I and the hexagonal phase II is 3.6 $kJmol^{-1}$.

5.4 The Crystal Structures of Bromoform at Low Temperature and High Pressure

5.4.1 Introduction

Bromoform is a halogenated derivative of methane, the central sp^3 hybridised carbon is surrounded approximately tetrahedrally by three bromine atoms and one hydrogen atom (figure 5.10). The compound exists as a colourless or slightly yellow liquid with a melting point of 281.3 K.

Figure 5.10 A molecule of bromoform, showing the central carbon atom in grey surrounded by the 3 bromine atoms (red) and 1 hydrogen atom (white). The atoms bonded to carbon lie approximately on the corners of a tetrahedron.

There are four known phases of bromoform, the α-phase which is stable under ambient conditions, the β and γ-phases that are low temperature meta-stable phases and the new high pressure polymorph, the δ-phase. All three ambient pressure phases are centro-symmetric, the disordered α-phase packs in $P6_3/m$ and the data were measured under ambient conditions at 293 K and 0 GPa[2], the β-phase in P-1 obtained at 14 K and 0 GPa, and the γ-phase in P-3 obtained under the same conditions as the β-phase. The α, β and γ-phase were characterised using neutron diffraction with the deuterated form[4]. The high pressure δ-phase packs in the polar

space group $P6_3$, this has the same structure as the high pressure phase of chloroform, phase II. The data were obtained at 293 K and 0.1 GPa.

5.4.2 The α – phase

The α-phase of bromoform is stable just below the melting point of 281 K. Initial single-crystal x-ray diffraction studies by Kawaguchi *et al*[2] showed that the α-phase, which forms on freezing from the liquid at 281 K, crystallises into a disordered structure with hexagonal $P6_3/m$ symmetry. The asymmetric unit consists of one fully occupied bromine atom that is bonded to a ⅓ occupied C-H group which sits on the three fold axis at ⅔, ⅓, z. The molecule is completed by generating the remaining bromine atoms around the three-fold axis, and the disordered molecule is created by the mirror plane. At 253 K, Kawaguchi *et al*[2] found that the molecules are distributed statistically parallel (43%) and anti-parallel (57%) to the *c*-axis of the unit cell, about the mirror plane. Each of the two parts of the disorder model have essentially the same structure as the high pressure phase II of chloroform (figure 5.11).

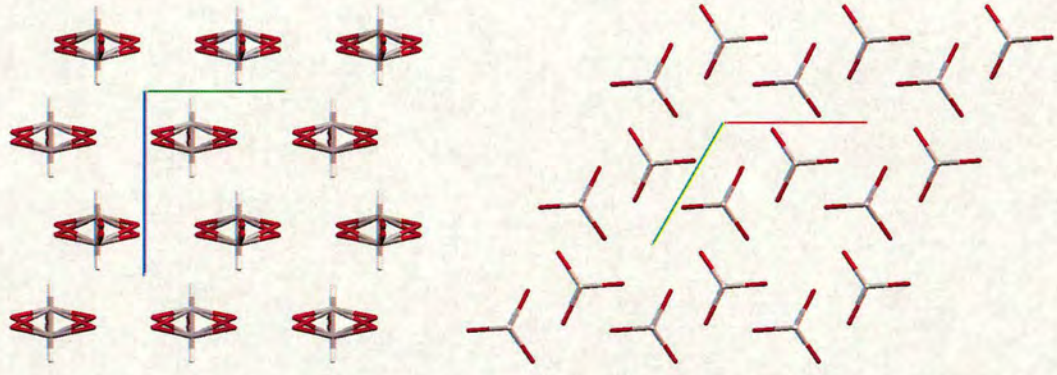

Figure 5.11 The crystal structure of the α-phase of bromoform. **(A)** Viewed down the crystallographic *a*-axis. The molecules are distributed parallel (43%) and anti-parallel (57%) to the *c*-axis. **(B)** Viewed down the crystallographic *c*-axis. [*a*-axis in red, *b*-axis in green, *c*-axis in blue].

5.4.3 The β – phase

The transition from the α-phase of bromoform to the β-phase occurs at 268 K and was found to be stable to the 98 K limit of the Raman study by Burgos *et al*[3]. In the neutron study by Myers and Torrie[4], annealing the γ-phase at 220 K produces the β-phase. Structural data were collected at 14 K and the molecules were found to pack in the triclinic space group *P*-1. The low symmetry of the crystal structure results in the absence of local symmetry in the molecule and the asymmetric unit consists of a fully occupied deutero-bromoform molecule. The layered structure is shown in figure 5.12.

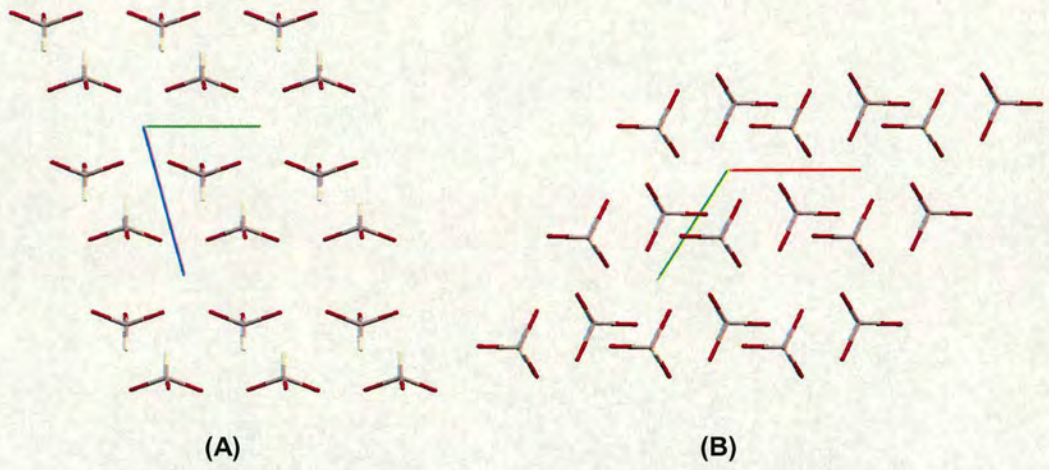

Figure 5.12 The crystal structure of the β-phase of bromoform. **(A)** Viewed down the crystallographic *a*-axis. **(B)** Viewed down the crystallographic *c*-axis. [*a*-axis in red, *b*-axis in green, *c*-axis in blue].

5.4.4 The γ – phase

The γ-phase of bromoform can be formed by rapid quenching of the α-phase to temperatures below 100 K[3,4]. On heating, this phase transforms to the β-phase. The γ-phase crystallises in the trigonal space group *P*-3. As for the α-phase, the asymmetric unit consists of a fully occupied bromine atom on a general position bonded to the third occupied C-D group. The C-D group lies on the 3-fold axis at ⅔, ⅓, z and the bromine atoms generated by this symmetry operator complete the

molecule. The structure of the γ-phase also consists of layers of bromoform molecules (figure 5.13).

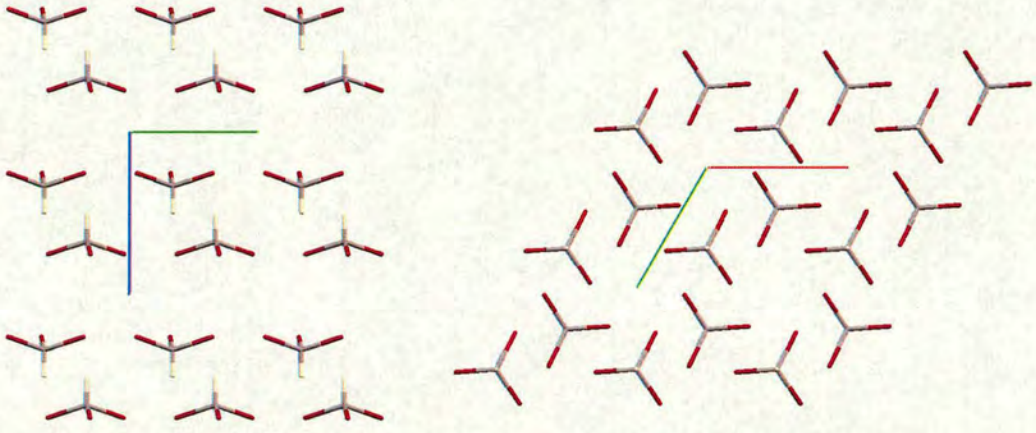

Figure 5.13 The crystal structure of the γ-phase of bromoform. **(A)** Viewed down the crystallographic *a*-axis. **(B)** Viewed down the crystallographic *c*-axis. [*a*-axis in red, *b*-axis in green, *c*-axis in blue].

5.4.5 The δ - phase

The δ-phase is a meta-stable high-pressure polymorph, the single crystal was obtained at a pressure of 0.1 GPa. This phase crystallises in the hexagonal space group $P6_3$, and is iso-structural to the high-pressure polymorph of chloroform (phase II). A fully occupied bromine atom on a general position is bonded to a third occupied C-H group in the asymmetric unit. The C-H group lies on the 3-fold axis at $-\frac{1}{3}$, $\frac{1}{3}$, z and the remaining bromine atoms in the molecule are generated by the symmetry operator. As was the case for the α, β and γ-phases, the final structure also consists of layers (figure 5.14). In contrast to the three ambient pressure phases, the high-pressure δ-phase is polar.

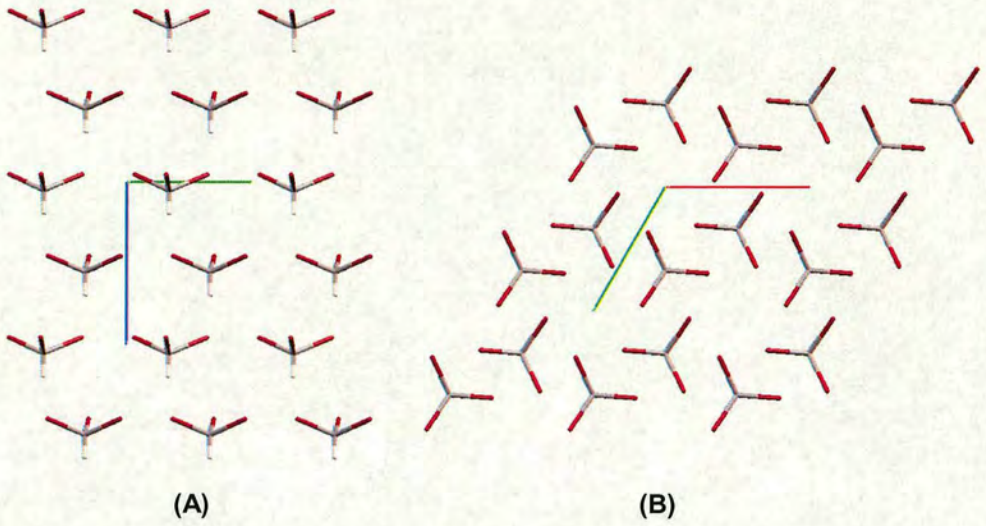

Figure 5.14 The crystal structure of the γ-phase of bromoform. **(A)** Viewed down the crystallographic *a*-axis. **(B)** Viewed down the crystallographic *c*-axis. [*a*-axis in red, *b*-axis in green, *c*-axis in blue].

5.4.6 Discussion and Comparison of the α, β, γ and δ Phases of Bromoform

5.4.6.1 Layer type

Each of the four different phases of bromoform have structures that are composed of layers of bromoform molecules. Within these layers, the bromine atoms are positioned in layers in a lattice plane.

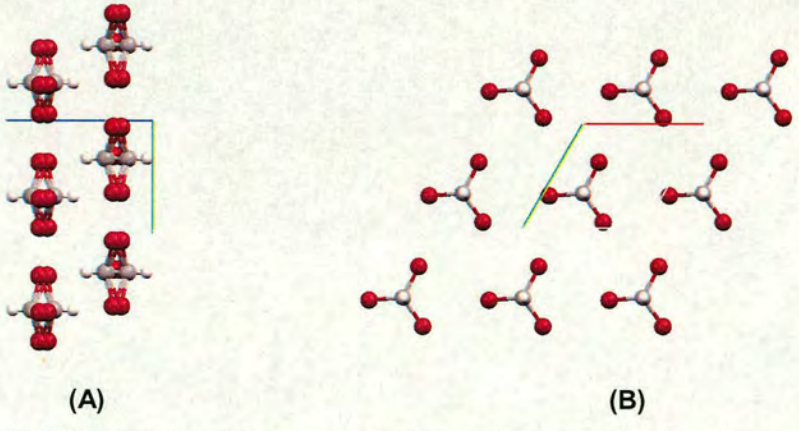

Figure 5.15 **(A)** Two layers of the α-phase of bromoform viewed down the *a*-axis. **(B)** One layer viewed down the polar *c*-axis. [*a*-axis in red, *b*-axis in green, *c*-axis in blue].

The α-phase is composed of layers of molecules that are disordered about the mirror planes at x, y, 1/4 and x, y, 3/4 (figure 5.15 (A)). The bromine atoms are disordered about these planes, Br1 in the repeating unit has a z co-ordinate of 0.277. Part (B) of figure 5.15 shows one of these layers in projection down the *c*-axis. The three-fold symmetry can be observed around the central molecule.

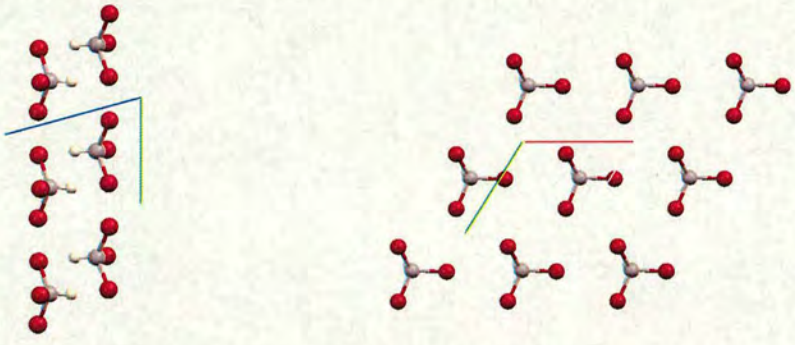

(A) (B)

Figure 5.16 **(A)** Two layers of the β-phase of bromoform viewed down the *a*-axis. **(B)** One layer viewed down the *c*-axis. [*a*-axis in red, *b*-axis in green, *c*-axis in blue].

The β-phase is also composed of layers that are related by inversion (figure 5.16). As the bromine atoms in this phase are not related by symmetry (unlike the α, γ and δ-phases) the layers of molecules are only approximately perpendicular to the *c*-axis. The z co-ordinates of Br1, Br2 and Br3 are 0.25620, 0.24410 and 0.23940 respectively, in the α, γ and δ-phases the bromine atoms have the same z co-ordinate by symmetry. The molecules in the layers of the β-phase are only related by the translational symmetry.

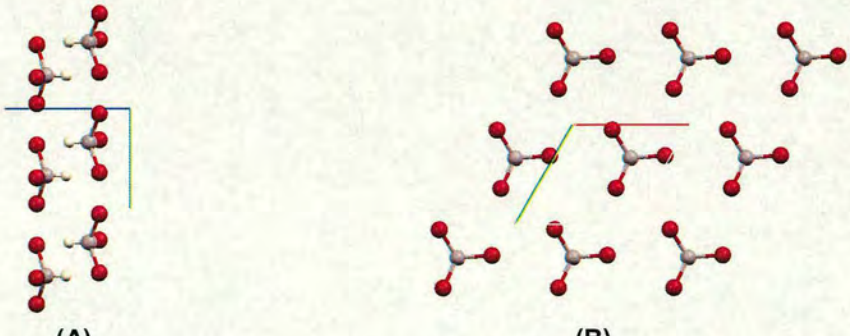

(A) (B)

Figure 5.17 **(A)** Two layers of the γ-phase of bromoform viewed down the *a*-axis. **(B)** One layer viewed down the *c*-axis. [*a*-axis in red, *b*-axis in green, *c*-axis in blue].

Like the β-phase, the γ-phase is also composed of layers that are related by inversion (figure 5.17). The C-H groups are aligned in an opposite sense with respect to the *c*-axis for alternate layers. The difference in the overall structures is shown in figure 5.18. Both structures have one repeating pair of layers where the hydrogen atoms are situated between the layers, and the bromine atoms are at the layer "surfaces". The difference between the structures is the positioning of these bi-layers with respect to one another. In the γ-phase (B), the bi-layers are related by translation with respect to the *c*-axis and lie directly on top of one another. In contrast, the β-phase has the bi-layers related by inversion so that the bromoform molecules are directly above and below in the neighbouring layers.

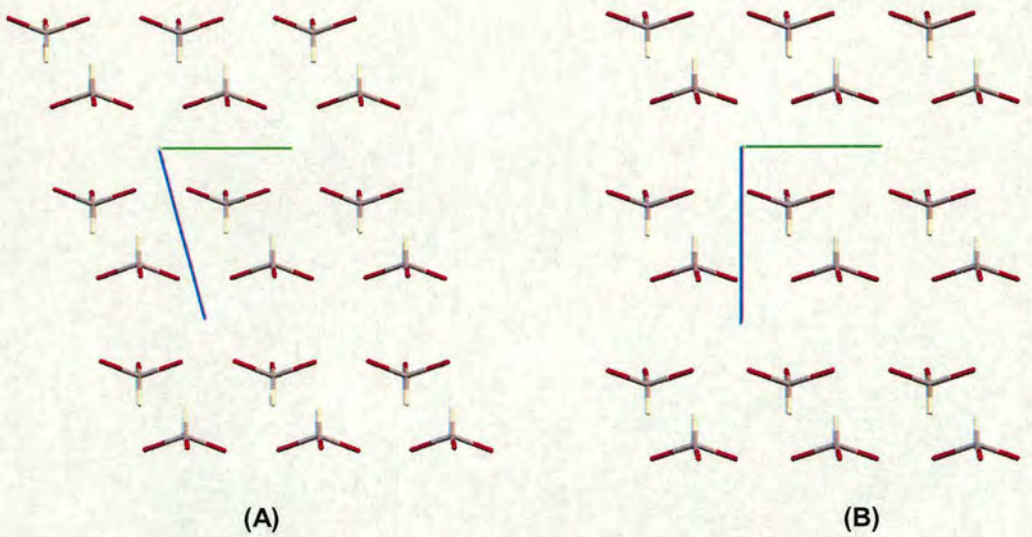

Figure 5.18 **(A)** The β-phase of bromoform viewed down the *a*-axis. **(B)** The γ-phase of bromoform viewed down the *a*-axis. [*b*-axis in green, *c*-axis in blue].

The δ-phase is also composed of the same layer type observed in the α, β, and γ-phases, although the layers are not arranged in bi-layers and structure is polar. A consequence of this is that all of the C-H groups are aligned parallel. As for the α and γ-phases, the bromine atoms in the layer lie on the same *ab* plane. The planes in this phase are separated by ½ of the *c*-axis.

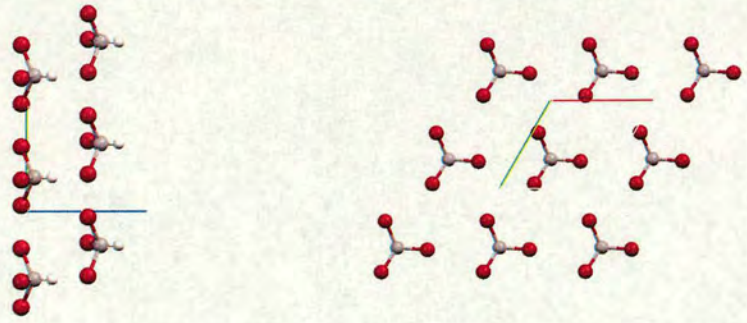

(A) (B)

Figure 5.19 **(A)** Two layers of the γ-phase of bromoform viewed down the *a*-axis. **(B)** One layer viewed down the *c*-axis. [*a*-axis in red, *b*-axis in green, *c*-axis in blue].

To compare the four phases, there are two common aspects of these layers that can be discussed: Firstly, the separation of the layers of bromine atoms; and secondly the distance between the bromine atoms within the layers themselves. Although the structure determinations for the β and γ-phases were conducted using the deutero-form of the bromoform molecule the discrepancies with the hydrogenous form are not expected to be significant and the intralayer distances between the bromine atoms will be unaffected.

Within the layer, each bromine atom has a short contact to four other bromine atoms. There are 12 distances in total from the central molecule, shown in figure 5.20. For the α, γ and δ-phases, the three-fold axis reduces the number of distances unrelated by the space group symmetry to 2. In the triclinic β-phase there are 6 different distances as the only symmetry is the inversion symmetry. The distances are given in table 5.7.

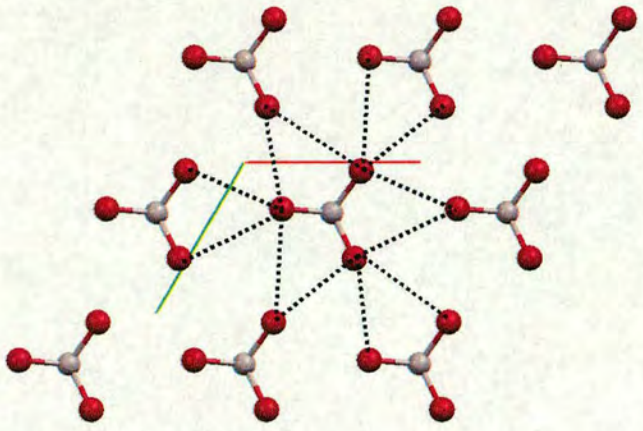

Figure 5.20 The Br..Br distances in bromoform

The dimensions shown here are very similar. In the four structures the layer type is strikingly similar and hence the difference between the four polymorphs is mainly in the way the layers are packed. The calculated models (Dr. S.J. Clark) can be used to compare the separation between the layers as all calculations use hydrogen over deuterium. This enables a fair comparison between the structures. There are three different types of separation to be considered (figure 5.21): Type 1 – the distance between of layers of bromine atoms separated by C-H groups donated by both layers; Type 2 – the direct separation between layers of bromine atoms; and Type 3 – the distance between layers of bromine atoms separated by C-H groups donated by one layer between them. The β and γ-phases contain type 1 and type 2 layers, the δ-phase type 3 layers, and the disordered α-phase contains type 3 as the disorder is modelled about the mirror plane.

Br..Br / Å	α – phase	β - phase	γ - phase	δ - phase
1	3.760	3.737	3.678	3.714
2	4.117	3.923	4.017	4.098
3	-	3.888	-	-
4	-	3.707	-	-
5	-	3.710	-	-
6	-	3.918	-	-

Table 5.7 Distances between bromine atoms in the layers of the α, β, γ and δ - phases of bromoform.

Type 1 Type 2 Type 3

Figure 5.21 Layer Type in the packing of haloforms

In the α-phase, the type 3 layers are separated by 3.775 Å. The β-phase contains type 1 and type 2 layers, the average separations (taking the average plane in z for the three inequivalent bromine atoms) are 3.789 and 3.599 Å respectively. In the γ-phase, the separation between the type 1 layers is 3.420 Å and for type 2 is 3.466 Å. In the δ-phase, the type 3 layers are separated by 3.572 Å.

A final area to discuss with reference to the layers is how the layers pack together. In figure 5.18, it can be seen that the packing of the layers is different when viewed in projection down the crystallographic *a*-axis, hence the different crystal system. Figure 5.22 shows the layers in the β and γ-phases in projection down the *c*-axis. Part (A) contains vectors, a layer shift along which would transform the β-phase to the γ-phase.

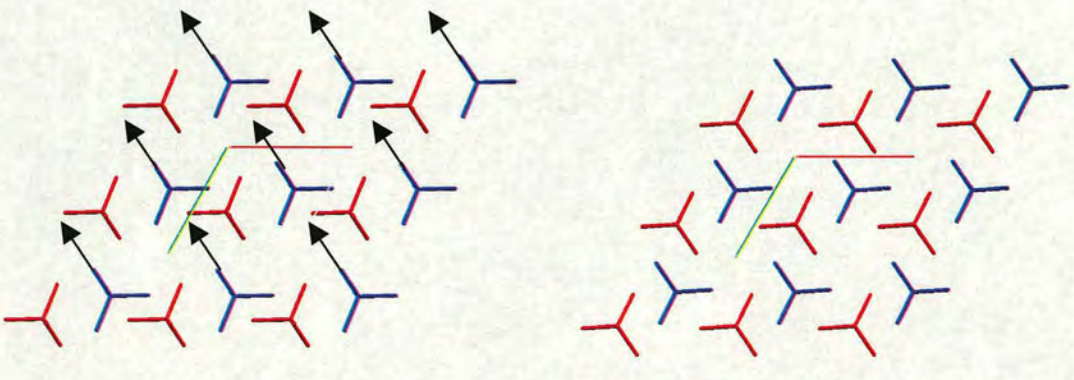

(A) **(B)**

Figure 5.22 **(A)** Two layers of the β-phase of bromoform viewed down the *c*-axis. The vectors show the direction of the layer shift required to transform to the γ-phase. **(B)** Two layers of the γ-phase of bromoform viewed down the *c*-axis. The repeating layers have molecules coloured red or blue – with the lower layer of molecules inverted with respect to the upper layer. [*a*-axis in red, *b*-axis in green].

In conclusion, all four phases of bromoform are composed of the same layer type. The layers are packed in different fashions to form the four different structural phases.

5.4.5.2 Change in Molecular Volume

To determine the molecular volume for each phase, independent of whether or not the molecules were deuterated, the structures calculated using the *ab-initio* technique will be used. The α, β, γ-phases had their volumes calculated at 0 GPa while the calculations for the δ-phase were conducted at 0.1 GPa. As standard, the calculations did not take into account thermal effects and can be considered to be at 0 K for all four structures. Table 5.6 contains the unit cell dimensions and volume for all four phases. Z = 2 for each phase.

Phase	a / Å	b / Å	c / Å	α / °	β / °	γ / °	V / Å^3
α	6.752	6.752	7.550	90.00	90.00	120.00	298.11
β	6.299	6.269	7.388	82.10	83.07	117.22	255.09
γ	6.254	6.254	6.887	90.00	90.00	120.00	233.28
δ	6.200	6.200	7.144	90.00	90.00	120.00	237.80

Table 5.6 Calculated unit cells and volumes for the four phases of bromoform. All calculations are for HCX_3, for the α, β and γ-phases the conditions are 0 K / 0 GPa, and for the δ-phase 0 K / 0.6 GPa. Z=2 for all phases.

The most efficient packing for this system is in the low temperature γ-polymorph. Compared to this phase, the δ-polymorph has the next most efficient packing with an increase of just 1 % per molecule. The molecules in the β-phase occupy 4.3 % more space than the γ-phase, and in the α-phase, the molecules occupy 10.9 % more volume than the γ-phase. The α-phase is disordered and would therefore be expected to have the largest molecular volume. The difference in molecular volume between the phases is a consequence of the way in which the layers are stacked. The

most efficient way of stacking the layers is observed in the γ-phase and this is closely followed by the δ-phase.

5.4.5.3 C-H...Br Interactions

Using the convention we have already adopted to describe the three different layer types present in the α, β, γ and δ-phases of bromoform, section 5.5.4.1, it is clear that the type 2 layer will not involve hydrogen bonding as the C-H groups on neighbouring layers are directed away from one another and the molecules are effectively back-to-back. The two possible ways of interaction between the bromine and hydrogen atoms will be named type A (interaction due to layer type 1 stacking) and type B (interaction due to type 3 stacking).

The α-bromoform polymorph is modelled in space group $P6_3/m$, with the molecules disordered about the mirror plane. Figure 5.23 shows the close contacts between H and Br in α – bromoform. The disorder model implies that only type 3 layers are present, so only type B interactions are permitted. Table 5.9 contains the dimensions of the interactions.

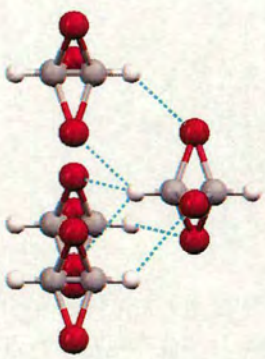

Figure 5.23 The close contacts between H and Br in α-phase of bromoform.

In the β and γ-phases, type A interactions are permitted. The β-phase has three unique contacts and the γ-phase has a single contact that is replicated twice by the three fold symmetry. In the high-pressure δ-phase, one type B interaction is present, and as for the γ-phase there are another two symmetry equivalent contacts generated by the three fold axis.

H....Br / Å	H-C-Br / °	C....Br / Å
α-phase, $P6_3/m$		
3.188	127.92	4.117
β-phase, P-1		
3.051	127.13	3.794
3.151	135.68	3.987
3.228	129.79	3.998
γ-phase, P-3		
2.924	127.46	3.683
δ-phase, $P6_3$		
3.027	129.55	3.810

Table 5.9 Calculated dimensions for the H..Br short contacts in bromoform. Results are taken from the *ab-initio* calculations.

All four phases of bromoform have the same type of chelating hydrogen bond as phase II of chloroform i.e. the hydrogen has a weak interaction with three bromine atoms from different neighbouring molecules.

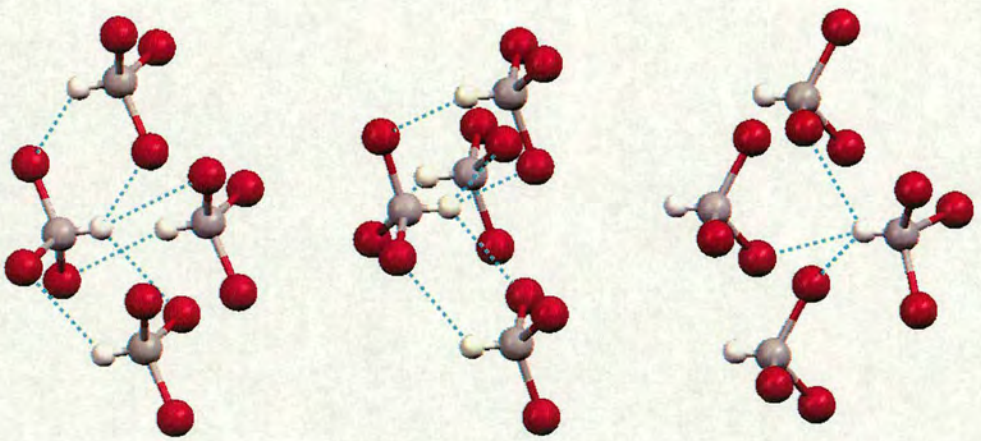

(A) **(B)** **(C)**

Figure 5.24 The close contacts between H and Br in **(A)** the β-phase, **(B)** the γ-phase and **(C)** the δ-phase of bromoform.

Relative to the β-phase, the γ-phase is 4.3 $kJmol^{-1}$ higher in energy at 0 GPa, whereas at 0.1 GPa, the δ-phase is 0.3 $kJmol^{-1}$ lower in energy. As the relative

enthalpies are so close at 0.1 GPa, the phases may be expected to form metastably at high pressure as was the case for chloroform.

5.5 The Crystal Structure of Iodoform

Iodoform is the next in the haloform series, another tri-halogenated derivative of methane with the central sp^3 carbon atom bonded to one hydrogen and three iodine atoms in a tetrahedral arrangement (figure 5.25). The substance is a yellow crystalline material with a melting point of 393 K.

Figure 5.25 A molecule of iodoform, showing the central carbon atom in grey surrounded by the 3 iodine atoms (purple) and 1 hydrogen atom (white). The atoms bonded to carbon lie approximately on the corners of a tetrahedron.

There is one known phase of iodoform and the substance crystallises in the hexagonal crystal system $P6_3/m$, with essentially the same structure as that of α-bromoform. The full structure is shown in figure 5.26.

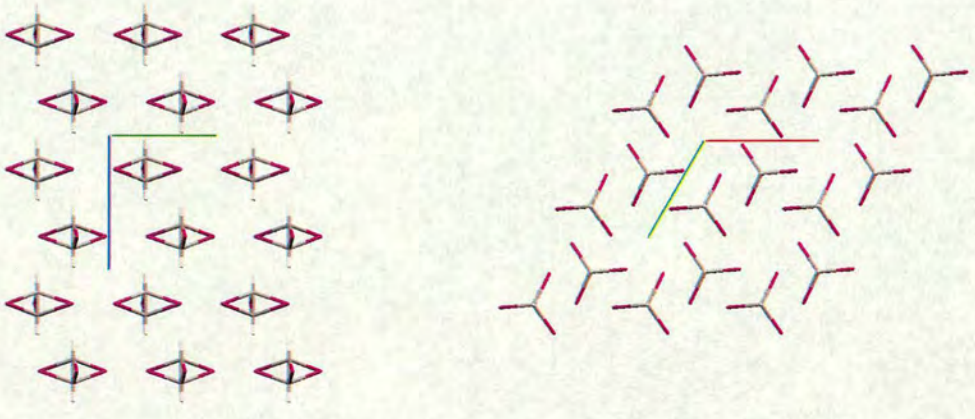

(A) **(B)**

Figure 5.26 The crystal structure of iodoform viewed: **(A)** in projection down the *a*-axis and **(B)** the *c*-axis. [*a*-axis in red, *b*-axis in green, *c*-axis in blue].

The close contacts in the solid state structure of iodoform are the same type that are observed in the α-phase of bromoform. Figure 5.27 shows the contacts, in the disorder model both types A and B as discussed in section 5.4.5.3 are present,

although only type B interactions are permitted as the molecule is disordered about the mirror plane.

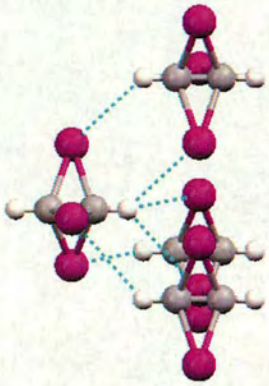

Figure 5.27 The close H..I contacts in the crystal structure of iodoform

Although iodoform has not been studied experimentally at high pressure, *ab initio* calculations on iodoform were undertaken assuming that it will have a comparable phase diagram to that of bromoform due to its rather similar molecular geometry. Relative to its known low-temperature $P6_3$ phase, the P-3 phase is 77 $kJmol^{-1}$ higher in energy. This is much higher than the energy difference calculated for bromoform and is likely to preclude the metastable formation of a P-3 phase of iodoform. However at 0.1 GPa, iodoform in the P-1 phase is lower in enthalpy by 4.34 $kJmol^{-1}$, it is therefore postulated that this phase may exist at high pressures.

5.6 Discussion and Comparison of the Low Temperature and High Pressure Phase Behaviour of the Haloforms

With the exception of phase I of chloroform which has orthorhombic *Pnma* symmetry, all other known phases of the haloform series are composed of layers that are strikingly similar. Within these layers, the halogen atoms lie on the same lattice plane. There are then three types of bi-layer depending on the direction of the C-H groups between neighbouring layers. Type 1 has the C-H groups from neighbouring layers in between the layers, in type two there are no C-H groups between the layers, and finally in type 3, the C-H groups from one layer only are between the layers. The low temperature phase of chloroform is different to the other structures as the chlorine atoms do not lie on the same lattice plane, the layers of chlorine atoms are corrugated, and the C-H groups alternate with respect to these corrugated layers.

There is an indication of interactions between the C-H groups and the halogen atoms in all known structures. The C-H bond in all of the discussed polymorphs have short contacts with more than one halogen atom on neighbouring molecules. As a result, the hydrogen atom can be considered to be almost four co-ordinate, with the bonded carbon atom at one corner, and the non-bonded halogen atoms occupying the remaining three corners. The lone-pairs on the halogen atoms provide the basis for these interactions which are present in all the layered structures.

There appears to be a trend with increasing pressure towards the polar hexagonal $P6_3$ structure, with both chloroform and bromoform adopting this structure at elevated pressures. Only chloroform packs in the orthorhombic *Pnma* phase which unlike all other phases has no recognisable three fold symmetry outwith the molecule itself. This is likely to be a consequence of the increasing molecular weight of the halogen atom, where in bromoform and iodoform, the halogen atoms dominate the packing.

5.7 References

1. Fourme R. and Renuad M., *C.R.Acad. Sci.*, Ser. C, **263**, 69 (1966).

2. Kawaguchi T., Takashina K., Tanaka T., and Watanabé T., *Acta Cryst.*, **B28**, 967 (1972).

3. Burgos E., Halac E. and Bonddeo H., *J.Chem.Phys.*, **74**, 1546 (1981).

4. Myers R. and Torrie B.H., *J.Chem.Phys.*, **79**, 1495 (1983).

5. Khotsyanova T.L., Kitaigorodski A.I., and Struchov Yu.T., *Zh. Fiz. Khim.*, **27**, 647 (1953).

6. Merrill L. and Bassett W. A., *Rev. Sci. Instrum.*, **45**, 290 (1974).

7. CAD4 Express Software. Enraf-Nonius, Delft, The Netherlands, 1994.

8. DIRAX: Duisenberg A. J. M, *J. Appl. Cryst.* **25**, 92 (1992).

9. SIR92, Altomare A., Cascarano G., Giacovazzo C. and Gualardi A., *J. Appl. Cryst.*, **26**, 343 (1993).

10. SHELXTL Programs for Crystal Structure Analysis (Release *97-2)*. G. M. Sheldrick, Institüt für Anorganische Chemie der Universität, Tammanstrasse 4, D-3400 Göttingen, Germany, 1998.

11. SHELXS86 - Program for Crystal Structure solution. Sheldrick, G. M., Institüt für Anorganische Chemie der Universität, Tammanstrasse 4, D-3400 Göttingen, Germany, 1986.

12. Dawson A., Parkin A., Parsons S., Pulham C.R. and Young A.L.C., *Acta Cryst. E.*, **58**, Part 10, i95 (2002).

14. McGregor P. A., Allan D. R., Parsons S., and Pulham C.R., in preparation (2003).

15. Dawson A., Allan D. R., and Parsons S., in preparation (2003).

16. Dawson A., Allan D. R., and Parsons S., in preparation (2003).

17. Jeffrey G.A., An Introduction to Hydrogen Bonding, Oxford University Press (1997).

Chapter 6

Summary and Conclusions

The principal aim of this thesis was to crystallise small organic molecules with one or more functional groups using *in-situ* single crystal growth techniques at elevated pressures or lowered temperatures in order to study the solid state structures of these materials using X-ray diffraction techniques. New polymorphs of cyclobutanol, tertiary butanol, ethane-1,2-diol, propane-1,3-diol, pentane-1,5-diol, chloroform and bromoform are presented. For each of the systems studied, the low temperature / ambient pressure crystal structures were compared to the corresponding ambient temperature / high-pressure crystal structures.

Two phases of cyclobutanol were found. The low temperature polymorph is stable below the melting point of 221 K and is characterised by triple helical chains with a central hydrogen bonded core. The second polymorph, found at 1.3 GPa, is characterised by wave-like hydrogen bonded chains. This system is strikingly similar to that of phenol, which also has a low temperature polymorph with triple helical chains with a central hydrogen bonded core (stable below the melting point of 313 K); at a relatively low pressure of 0.16 GPa, the molecules pack into wave-like hydrogen bonded chains. Both phenol and cyclobutanol have slightly longer hydrogen bonds in their crystal structures at high pressure compared to their low temperature analogues, which is counter intuitive as it would be expected that if the length of the hydrogen bond was to change, it would shorten.

Crystals of tertiary butanol can be grown under ambient conditions. This structure is characterised by pseudo triple helical chains. At a pressure of 0.85 GPa, hydrogen bonded rings containing six tertiary butanol molecules were found. This phase was also found to be stable below 268 K. Studies by Brock and Macrae on the packing of mono-alcohols found that more sterically hindered alcohols would form rings rather than chains, in this case the steric hindrance is a direct result of loss of volume due to the lowering of the temperature or application of pressure.

Increasing the number of hydroxyl groups to two led to the study of the α-ω di-alcohols. These molecules allow the effects of pressure on molecular conformation to be studied in addition to changes in hydrogen bonding. The extreme ends of the molecules have torsion angles associated with the rotation of the α (or ω) C-C bond

and the α (or ω) C-O bond. In ethane-1,2-diol, two new phases were found at elevated pressures in addition to the known low temperature phase. Each of the phases were found to be characterised by hydrogen bonded chains, although the conformation of the molecule within each phase is different. In phase I, the O-C-C-O torsion is *gauche*, the α-C-C-O-H torsion is *gauche* and the ω-C-C-O-H torsion is *eclipsed*. The O-C-C-O torsion in phase II is also *gauche*, as is the α-C-C-O-H torsion, but the ω-C-C-O-H torsion is *trans*. In phase III, all three torsion angles are in the *trans* conformation.

Similar to ethane-1,2-diol, three different conformations of propane-1,3-diol were found in the solid state. There are four characteristic torsion angles, the α-(C-C-C-O), the ω-(C-C-C-O), the α-(C-C-O-H) and the ω-(C-C-O-H). In the low temperature polymorph, all four characteristic torsion angles are *gauche*. In the high-pressure polymorph, two different molecules co-exist in the same crystal structure. One has both C-C-O-H torsions *eclipsed*, the α-(C-C-C-O) in the *gauche* conformation and the ω-(C-C-O-H) in the *trans* conformation. In the other conformer, both C-C-O-H torsions are *eclipsed* and both C-C-C-O torsions are in the *trans* conformation. Pentane-1,5-diol has two different conformers; in the low temperature phase, the α-torsions are both *gauche* and the ω-torsions are both *trans*; while in the high pressure phase the α-torsions and the ω-(C-C-C-O) are *trans* but the ω-(C-C-O-H) torsion is *gauche*. Interestingly, no new high-pressure phases of the even diols of butane and hexane have been found. The conformations of the α and ω torsion angles discussed above are all *trans* for these molecules. All of the new high pressure phases discussed above contain more *trans* conformations than their corresponding low temperature analogues; this is a possible explanation why butane- and hexane-diol do not form new polymorphs at elevated pressures.

It would be interesting to study these transformations using both variable pressure and variable temperature infra-red techniques. This study will give insights into the behaviour of the molecules in the liquid state, and possibly an understanding of why the specific conformations occur under different conditions. As the temperature is lowered, or the pressure is increased, toward the freezing point, is there a mixture of conformers until the melting point is reached? Or, for example in ethane-1,2-diol,

does the ratio of the *trans* conformer to the *gauche* conformer increase with an increase of pressure? Variable pressure powder diffraction could also be used to map the phase boundaries. The exploration of the phase diagram is limited in this study, only three points have been utilised. Like ice, the diols could have many more phases that lie undiscovered.

For both the mono-alcohols and the di-alcohols, it was found that to compensate for the change in molecular volume associated with the application of pressure the molecules rearrange to form a more efficient packing motif. It is expected that the primary bond lengths and angles will not be altered at low pressures due to the high energy compensation, although lower energy intermolecular interactions such as hydrogen bonding may be expected to. A lower compensation of energy would be required to alter the C-C distances and C-O distances between neighbouring molecules. For all of the above parameters in the mono-alcohols and di-alcohols the dimensions remain the same. The reduction in volume is instead associated with changes in the molecular packing where the molecules re-arrange into a different packing motif where more of the C-C and C-O intermolecular distances are found.

The new high-pressure phases of chloroform and bromoform were both found to be isostructural, crystallising in the polar hexagonal space group, $P6_3$. This structure is characterised by layers of haloform molecules with the C-H groups aligned parallel, similar to the low temperature phases of bromoform and iodoform. These structures are also composed of layers, however with an alternating parallel and anti-parallel alignment of C-H groups. All of these structures have three-fold symmetry associated with both the crystal structure and the molecule. In contrast the low temperature phase of chloroform has no recognisable three-fold symmetry within the crystal structure, only in the molecule itself. The results suggest that the halogen atoms dominate the packing in the structures of the heavier analogues bromoform and iodoform, and also in the high-pressure phase of chloroform. It could be argued that pressure is forcing the chloroform molecule to behave in a manner similar to that of its heavier analogues.

All of the small organic molecules studied in this work have biological implications, namely the hydrogen bonding, intermolecular interactions and the changes in

molecular configuration. This is an exciting time in high-pressure molecular science with the development of high-pressure single crystal techniques for the study of macromolecules. To help understand the functions of the larger molecules at high pressures, an understanding of the simple molecules is vital. The results described in thesis show that even these simple systems exhibit complex behaviour on the application of pressure.

Appendices

Appendix 1 - Experimental and Calculated Atomic Co-ordinates of Phases I and II of Cyclobutanol

Phase I

	Experimental (100 K and 0 GPa)			Calculated (0 K and 0 GPa)		
Relative Enthalpy	-			-72.0609 eV/molecule		
Space Group	*Aba*2			*Aba*2		
a / Å	9.3312(15)			9.203069		
b / Å	13.642(2)			13.892111		
c / Å	13.619(2)			14.078993		
Atom	x	y	z	x	y	z
C11	0.0545(3)	0.22494(19)	0.79351(17)	0.055701	0.225808	0.794552
H11	0.1477	0.2006	0.7666	0.163212	0.200688	0.771497
O1	0.06638(17)	0.23508(13)	0.89729(12)	0.064121	0.236291	0.894703
H1	-0.0037	0.2673	0.9186	0.971487	0.264318	0.920318
C12	-0.0687(3)	0.16276(19)	0.75094(17)	0.935349	0.162954	0.749829
H122	-0.1562	0.1620	0.7920	0.835811	0.166273	0.792505
H121	-0.0401	0.0956	0.7316	0.960589	0.087408	0.734670
C13	-0.0742(3)	0.23692(18)	0.66429(17)	0.931336	0.235795	0.666527
H131	-0.0174	0.2167	0.6063	1.003611	0.214675	0.608400
H132	-0.1724	0.2566	0.6452	0.825041	0.253988	0.636842
C14	0.0032(3)	0.31201(18)	0.73171(18)	0.004983	0.310933	0.732148
H141	0.0813	0.3485	0.6989	0.088072	0.358442	0.702053
H142	-0.0624	0.3570	0.7669	0.924302	0.354472	0.770115
C21	0.3245(2)	0.08065(18)	0.99115(17)	0.325212	0.084652	0.986890
H21	0.4234	0.0614	1.0118	0.437406	0.069019	0.008316

O2	0.32292(16)	0.18252(11)	0.97302(12)	0.321360	0.185194	0.967713
H2	0.2400	0.1998	0.9563	0.222022	0.204711	0.945670
C22	0.2170(3)	0.03517(18)	1.06350(18)	0.217099	0.040012	0.058251
H221	0.1237	0.0695	1.0664	0.112351	0.077436	0.055370
H222	0.2563	0.0239	1.1301	0.250965	0.033388	0.132553
C23	0.2171(3)	-0.05692(19)	0.9973(2)	0.216326	0.948824	0.994818
H231	0.2854	-0.1083	1.0183	0.296658	0.895699	0.017924
H232	0.1206	-0.0848	0.9855	0.112765	0.911897	0.984367
C24	0.2725(3)	0.00793(18)	0.9131(2)	0.273522	0.011190	0.911629
H241	0.3506	-0.0222	0.8743	0.354469	0.980318	0.863446
H242	0.1962	0.0340	0.8700	0.183332	0.040954	0.870083
	Experimental (220 K and 0 GPa)			Calculated (0 K and 1.3 GPa)		
Relative Enthalpy	-			-71.5629 eV/molecule		
Space Group	*Aba*2			*Aba*2		
a / Å	9.3789(16)			8.956019		
b / Å	13.658(2)			13.476153		
c / Å	13.661(2)			13.671092		
Atom	x	y	z	x	y	z
C11	0.0552(2)	0.22614(18)	0.79482(17)	0.058299	0.225054	0.793989
H11	0.1480	0.2031	0.7692	0.168669	0.199454	0.769947
O1	0.06454(17)	0.23641(13)	0.89748(12)	0.066869	0.235612	0.896917
H1	-0.0049	0.2682	0.9177	0.970974	0.263838	0.924335
C12	-0.0639(3)	0.16372(19)	0.75122(18)	0.934376	0.160282	0.748208
H122	-0.1509	0.1619	0.7909	0.832781	0.163963	0.792593
H121	-0.0339	0.0977	0.7322	0.959663	0.082525	0.731971

C13	-0.0696(3)	0.23728(19)	0.66552(17)	0.928931	0.235754	0.662861
H131	-0.0121	0.2181	0.6088	0.003396	0.214648	0.602862
H132	-0.1665	0.2556	0.6458	0.819429	0.254247	0.632640
C14	0.0032(3)	0.31213(17)	0.73273(19)	0.005094	0.312933	0.730288
H141	0.0799	0.3492	0.7011	0.089783	0.362039	0.698784
H142	-0.0632	0.3558	0.7668	0.922638	0.357465	0.770109
C21	0.3225(2)	0.08035(17)	0.98968(17)	0.327444	0.084776	0.989083
H21	0.4209	0.0613	1.0079	0.442757	0.067936	0.010406
O2	0.32034(15)	0.18196(10)	0.97174(12)	0.323261	0.188713	0.971997
H2	0.2387	0.1988	0.9553	0.221440	0.208968	0.947194
C22	0.2203(4)	0.03520(19)	1.0629(2)	0.216366	0.037736	0.061730
H221	0.1285	0.0691	1.0678	0.108988	0.076412	0.058162
H222	0.2619	0.0240	1.1278	0.250102	0.030073	0.138403
C23	0.2176(3)	-0.05606(19)	0.9972(2)	0.215425	0.944844	0.995173
H231	0.2861	-0.1068	1.0164	0.297644	0.889435	0.018324
H232	0.1222	-0.0838	0.9876	0.108702	0.907272	0.984023
C24	0.2680(3)	0.00845(19)	0.9134(2)	0.273979	0.010490	0.910361
H241	0.1907	0.0342	0.8726	0.180899	0.041312	0.868233
H242	0.3432	-0.0211	0.8733	0.357254	0.979354	0.859869

Phase II

	Experimental (293 K and 1.3 GPa)			Calculated (0 K and 1.3 GPa)		
Relative Enthalpy	-			-71.5131 eV/molecule		
Space Group	$Pna2_1$			$Pna2_1$		
a / Å	4.9208(4)			4.829732		
b / Å	8.2302(10)			8.379915		
c / Å	9.5980(16)			9.883195		
Atom	x	y	z	x	y	z
C1	0.3773(15)	-0.0358(8)	0.2542(11)	0.383375	0.960790	0.254582
H1A	0.5411	0.0316	0.2603	0.576823	0.029263	0.254810
O1	0.4261(10)	-0.1676(6)	0.1630(12)	0.428384	0.827959	0.167123
H1	0.3066	-0.2361	0.1729	0.251737	0.766169	0.163717
C2	0.1304(14)	0.0731(8)	0.2301(13)	0.131445	0.069976	0.228142
H2A	0.1747	0.1777	0.1893	0.167607	0.181027	0.172238
H2B	-0.0154	0.0205	0.1792	0.965327	0.003205	0.178086
C3	0.0851(17)	0.0791(10)	0.3853(14)	0.088602	0.079250	0.383569
H3A	-0.1015	0.0591	0.4129	0.876162	0.068558	0.421137
H3B	0.1557	0.1764	0.4293	0.179949	0.186750	0.427365
C4	0.272(2)	-0.0706(9)	0.4002(15)	0.277816	0.931111	0.400495
H4A	0.4090	-0.0597	0.4725	0.431711	0.933243	0.481898
H4B	0.1756	-0.1728	0.4085	0.157885	0.820246	0.406179

Appendix 2 - Experimental and Calculated Atomic Co-ordinates of Phases II and IV of Tertiary Butanol

Phase II

	Experimental (293 K and 0 GPa)			Calculated (0 K and 0 GPa)		
Relative Enthalpy	-			-7.35009476x10^3 eV/molecule		
Space Group	*P*-1					
a / Å	6.393(2)			6.202696		
b / Å	9.481(3)			9.143128		
c / Å	15.126(4)			14.755383		
α / °	85.47(2)			86.372950		
β / °	79.60(2)			78.776361		
γ / °	76.01(2)			76.362746		
Atom	x	y	z	x	y	z
O1	-0.077(1)	0.5508(8)	0.2538(4)	-0.104297	0.550492	0.267295
H1	-	-	-	0.003122	0.606747	0.230239
C1	0.0092(25)	0.3925(14)	0.2679(12)	0.010243	0.393833	0.272181
C2	-0.193(3)	0.3265(17)	0.2976(13)	-0.170374	0.303902	0.295366
H21	-	-	-	-0.291877	0.336446	0.249273
H22	-	-	-	-0.094200	0.183739	0.288086
H23	-	-	-	-0.262118	0.323676	0.366059
C3	0.1761(31)	0.3335(16)	0.1806(13)	0.154585	0.351569	0.177984
H31	-	-	-	0.047656	0.353406	0.127146
H32	-	-	-	0.262387	0.430208	0.154834
H33	-	-	-	0.263505	0.239573	0.178708
C4	0.1435(32)	0.3829(19)	0.3488(13)	0.150352	0.372988	0.347589

H41	-	-	-	0.043125	0.379978	0.416208
H42	-	-	-	0.270725	0.264083	0.342933
H43	-	-	-	0.244809	0.460560	0.343279
O2	0.510(1)	0.7208(8)	0.3008(5)	0.468016	0.717279	0.311150
H2	-	-	-	0.621775	0.650268	0.293810
C5	0.4791(25)	0.8152(18)	0.376(1)	0.475881	0.820840	0.379581
C6	0.2357(20)	0.8900(18)	0.4002(9)	0.232860	0.907509	0.412440
H61	-	-	-	0.154559	0.863394	0.478150
H62	-	-	-	0.222491	1.027290	0.420492
H63	-	-	-	0.131288	0.897745	0.361516
C7	0.5805(31)	0.7205(21)	0.4548(10)	0.573522	0.730179	0.457604
H71	-	-	-	0.474639	0.647955	0.486233
H72	-	-	-	0.745736	0.667053	0.433401
H73	-	-	-	0.574190	0.802876	0.513208
C8	0.6257(26)	0.9342(18)	0.3370(12)	0.621266	0.927973	0.334488
H81	-	-	-	0.545990	0.997477	0.280774
H82	-	-	-	0.638802	1.003290	0.385653
H83	-	-	-	0.789710	0.866998	0.303038
O3	0.2298(11)	0.7036(8)	0.1893(5)	0.201078	0.702484	0.191714
H3	-	-	-	0.296697	0.716336	0.236684
C9	0.2731(27)	0.7768(19)	0.0994(10)	0.266046	0.774895	0.105100
C10	0.1144(28)	0.7362(21)	0.0415(10)	0.119196	0.742282	0.040979
H101	-	-	-	0.194310	0.636520	0.005100
H102	-	-	-	-0.046052	0.735215	0.080306
H103	-	-	-	0.094236	0.832766	-0.010723
C11	0.5199(28)	0.7201(22)	0.0626(10)	0.517489	0.714022	0.067520
H111	-	-	-	0.601044	0.805404	0.043533

H112	-	-	-	0.542924	0.641560	0.008821
H113	-	-	-	0.605573	0.649579	0.119470
C12	0.2310(38)	0.9434(19)	0.1152(11)	0.214585	0.943695	0.119617
H121	-	-	-	0.286855	0.968318	0.177242
H122	-	-	-	0.284631	1.003170	0.058522
H123	-	-	-	0.032105	0.988663	0.134894

Phase IV

	Experimental (293 K and 0.85 GPa)			Calculated (0 K and 0.85 GPa)		
Relative Enthalpy	-			-2.20497778×10^4 ev/molecule		
Space Group	*P*-3			*P*-3		
a / Å	17.55(2)			17.438890		
c / Å	8.080(10)			8.021036		
Atom	x	y	z	x	y	z
O1	0.8388(4)	0.4113(4)	0.9176(7)			
H1	-	-	-	0.190876	0.047996	0.047996
C1	0.8820(5)	0.4415(5)	0.7612(10)	0.118206	0.559728	0.237242
C11	0.9089(6)	0.3763(6)	0.7103(11)	0.037916	0.468581	0.214414
H11A	-	-	-	0.058844	0.421703	0.177962
H11B	-	-	-	-0.004667	0.471097	0.118038
H11C	-	-	-	-0.000011	0.445328	0.330174
C12	0.8180(6)	0.4446(6)	0.6379(11)	0.091167	0.625615	0.289751
H12A	-	-	-	0.149492	0.690443	0.308280
H12B	-	-	-	0.054163	0.604575	0.405747

H12C	-	-	-	0.049707	0.630864	0.194497
C13	0.9619(6)	0.5326(6)	0.7828(10)	0.181719	0.556923	0.362410
H13A	-	-	-	0.239019	0.622887	0.376447
H13B	-	-	-	0.203808	0.511659	0.320489
H13C	-	-	-	0.149320	0.534611	0.483162
O2	0.7615(5)	0.5109(4)	0.0047(7)			
H2	-	-	-	0.220093	0.700017	0.030001
C2	0.7067(6)	0.4834(6)	0.2844(11)	0.228318	0.776819	-0.163298
C21	0.8671(5)	0.5694(6)	0.2160(10)	0.224025	0.707292	-0.280966
H21A	-	-	-	0.288949	0.713121	-0.291305
H21B	-	-	-	0.203113	0.716086	-0.404186
H21C	-	-	-	0.176441	0.641570	-0.235119
C22	0.7702(6)	0.6307(6)	0.1550(11)	0.138525	0.770066	-0.152078
H22A	-	-	-	0.088778	0.702988	-0.116825
H22B	-	-	-	0.119627	0.786522	-0.271041
H22C	-	-	-	0.141268	0.816213	-0.057886
C23	0.7702(6)	0.6307(6)	0.1550(11)	0.298615	0.868058	-0.214398
H23A	-	-	-	0.362303	0.870966	-0.223702
H23B	-	-	-	0.303388	0.915309	-0.120412
H23C	-	-	-	0.282662	0.885911	-0.333817
O3	0.9243(4)	0.0970(4)	0.5368(7)			
H3	-	-	-	0.107793	0.965150	-0.510575
C3				0.100196	0.884058	-0.694804
C31	0.9243(4)	0.0970(4)	0.5368(7)	0.029421	0.792490	-0.743949
H31A	-	-	-	-0.032797	0.791318	-0.765391
H31B	-	-	-	0.048444	0.771801	-0.856562
H31C	-	-	-	0.019756	0.746082	-0.644458

C32	0.8909(6)	0.0469(6)	0.8215(12)	0.188737	0.888629	-0.669234
H32A	-	-	-	0.239665	0.955868	-0.636911
H32B	-	-	-	0.209481	0.867592	-0.780594
H32C	-	-	-	0.182050	0.844645	-0.566862
C33	0.8112(6)	0.1111(6)	0.6714(11)	0.108997	0.951394	-0.823389
H33A	-	-	-	0.044868	0.946460	-0.842501
H33B	-	-	-	0.131254	0.937892	-0.941147
H33C	-	-	-	0.156732	1.018329	-0.782845

Appendix 3 - Experimental and Calculated Atomic Co-ordinates of Phases I, II and III of Ethane-1,2-diol

Phase I

	Experimental (130 K and 0 GPa)			Calculated (0 K and 0 GPa)		
Space Group	$P2_12_12_1$			$P2_12_12_1$		
a / Å	5.013(3)			5.105488		
b / Å	6.915(3)			6.967720		
c / Å	9.217(4)			9.330529		
Atom	x	y	z	x	y	z
O1	-0.27350	0.50075	-0.14225	-0.27428	0.49781	-0.14477
H1	-0.34080	0.61530	-0.12340	-0.34853	0.62653	-0.12155
O2	-0.00510	0.64400	0.11378	-0.00065	0.64871	0.11358
H2	-0.06480	0.59940	0.19090	-0.08404	0.60370	0.20423
C1	0.00890	0.50020	-0.12257	0.00126	0.50103	-0.12144
H3	0.08610	0.62450	-0.16090	0.08631	0.63167	-0.16683
H4	0.07760	0.38840	-0.17210	0.08530	0.38001	-0.18006
C2	0.08560	0.47890	0.03459	0.07815	0.48490	0.03299
H5	0.26300	0.46700	0.03950	0.29147	0.46824	0.03800
H6	0.00540	0.36940	0.07590	-0.00872	0.35578	0.07949

Relative Enthalpies at 0 K

Final Enthalpy = -5.14436205 x10^3 eV at 0 GPa
Final Enthalpy = -5.14256220 x10^3 eV at 1 GPa
Final Enthalpy = -5.14080412 x10^3 eV at 2 GPa

Phase II

	Experimental (293 K and ~2 GPa)			Calculated (0 K and 2 GPa)		
Space Group	*P*21/*n*			*P*21/*n*		
a / Å	4.1385			4.033240		
b / Å	13.8247			13.597377		
c / Å	5.3021			5.230183		
β / °	112.967			112.895697		
Atom	x	y	z	x	y	z
O1	0.084993	0.310075	0.940227	0.081653	0.308440	0.942787
H1	0.048066	0.328815	1.080748	0.025247	0.319901	1.112079
C1	0.173963	0.399873	0.860581	0.161849	0.399801	0.851290
H11	0.385434	0.424786	1.003428	0.406553	0.430891	1.008369
H12	-0.013942	0.445993	0.831153	-0.059282	0.451380	0.816293
O2	-0.077001	0.354415	0.379663	-0.086157	0.349859	0.366836
H2	-0.224603	0.320874	0.432539	-0.189638	0.289835	0.421464
C2	0.232574	0.386303	0.601049	0.222542	0.385202	0.591004
H21	0.309412	0.447049	0.551424	0.293196	0.455712	0.526877
H22	-0.224603	0.320874	0.432539	0.450204	0.335821	0.631626

Relative Enthalpies at 0 K

Final Enthalpy = -5.14049892 x10^3 eV at 2GPa
Final Enthalpy = -5.14216452 x10^3 eV at 1 GPa
Final Enthalpy = -5.14386568 x10^3 eV at 0 GPa

Phase III

	Experimental (293 K and 2.3 GPa)			Calculated (0 K and 2.3 GPa)		
Space Group	*P*21/*n*			*P*21/*n*		
a / Å	6.878(5)			6.950462		
b / Å	8.883(5)			8.947441		
c / Å	4.751(6)			4.836812		
β / °	109.85(7)			108.931884		
Atom	x	y	z	x	y	z
O1	0.260076	0.450127	0.172150	0.26085	0.44979	0.16490
H1	0.261422	0.422342	0.337406	0.25727	0.41145	0.35613
O2	0.270542	0.810673	-0.158530	0.27267	0.81270	-0.14726
H2	0.269237	0.835192	-0.325571	0.26598	0.84928	-0.34438
C1	0.258340	0.608436	0.161224	0.25673	0.60823	0.15607
H1A	0.379122	0.648743	0.315245	0.39120	0.65375	0.32207
H1B	0.135696	0.647285	0.193237	0.11990	0.65107	0.19524
C2	0.259415	0.652686	-0.142690	0.26089	0.65429	-0.14006
H2A	0.377219	0.607508	-0.178685	0.39273	0.60404	-0.18130
H2B	0.134556	0.616690	-0.294905	0.12078	0.61530	-0.30406

Relative Enthalpies at 0 K

Final Enthalpy = -5.14369556×10^3 eV at 0 GPa
Final Enthalpy = -5.14199805×10^3 eV at 1 GPa
Final Enthalpy = -5.14033073×10^3 eV at 2 GPa

Appendix 4 - Experimental and Calculated Atomic Co-ordinates of Phases I and II of Propane-1,3-diol

Phase I

	Experimental (130 K and 0 GPa)			Calculated (0 K and 0 GPa)		
Space Group	*P*21/*n*			*P*21/*n*		
a / Å	4.940(2)			5.007309		
b / Å	7.944(3)			7.989296		
c / Å	10.601(3)			10.728685		
β / °	90.10(3)			89.946037		
Atom	x	y	z	x	y	z
O1	0.2103(3)	0.7093(2)	0.84586(12)	0.215342	0.712015	0.841160
H1	0.2927(61)	0.611(4)	0.8524(29)	0.300824	0.598789	0.839313
O2	0.5542(2)	0.6004(2)	1.14792(12)	0.556020	0.591741	1.154777
H2	0.6056(57)	0.6718(39)	1.2079(29)	0.608750	0.673779	1.220832
C1	0.3266(4)	0.8157(2)	0.9408(2)	0.334643	0.812245	0.936529
H3	0.2994(47)	0.9329(32)	0.9158(24)	0.299565	0.942789	0.909916
H4	0.5240(49)	0.7935(29)	0.9457(22)	0.551686	0.792843	0.937515
C2	0.1985(4)	0.7871(2)	1.0695(2)	0.216860	0.781030	1.064280
H5	0.2629(52)	0.8798(34)	1.1257(25)	0.280753	0.881271	1.127564
H6	0.0003(55)	0.7968(33)	1.0616(25)	-0.001123	0.790145	1.057261
C3	0.2688(3)	0.6172(2)	1.1273(2)	0.280950	0.612523	1.121714
H7	0.2116(49)	0.5237(34)	1.0723(25)	0.233988	0.511339	1.056791
H8	0.1674(51)	0.5985(32)	1.2113(25)	0.153784	0.593971	1.203838

Relative Enthalpies at 0 K

Final Enthalpy = -5.88845700x10^3 eV at 0 GPa
Final Enthalpy = -5.88744290 x10^3 eV at 0.95 GPa

Phase II

	Experimental (293 K and 0.95 GPa)			Calculated (0 K and 0.95 GPa)		
Space Group	*Pc*			*Pc*		
a / Å	7.4621(7)			7.530908		
b / Å	5.1269(11)			5.192991		
c / Å	10.1571(9)			10.294767		
β / °	97.183(9)			97.255463		
Atom	x	y	z	x	y	z
O1	0.3287(12)	0.039(4)	1.0364(8)	-0.310936	0.079677	1.047867
H1	-0.3759	0.1880	1.0837	-0.407451	0.186729	1.079334
C2	-0.3142(17)	0.105(4)	0.902(1)	-0.292350	0.132099	0.914307
H21	-0.4287	0.1759	0.8606	-0.423718	0.179000	0.860760
H22	-0.2546	-0.0170	0.8601	-0.248484	-0.046655	0.872036
C3	-0.186(2)	0.332(5)	0.8976(12)	-0.161265	0.344916	0.896190
H31	-0.2456	0.5294	0.9206	-0.207178	0.525379	0.935815
H32	-0.0673	0.3441	0.9511	-0.031811	0.299748	0.952666
C4	-0.153(2)	0.402(5)	0.757(1)	-0.137596	0.385838	0.753525
H41	-0.0902	0.5341	0.7322	-0.266482	0.434324	0.697075
H42	-0.2828	0.3838	0.6952	-0.048728	0.550036	0.744804
O5	0.0668(12)	0.193(4)	0.6957(7)	-0.061821	0.166931	0.696404

H5	-0.1486	0.0193	0.6949	-0.157813	0.065350	0.642228
O6	0.4303(14)	0.682(4)	0.6529(8)	0.430048	0.669802	0.644452
H6	0.4237	0.7205	0.7483	0.367977	0.775809	0.706292
C7	0.320(2)	0.463(5)	0.6160(11)	0.314179	0.456797	0.605655
H71	0.3763	0.2581	0.6679	0.175411	0.516941	0.608567
H72	0.1931	0.4353	0.6474	0.340743	0.300857	0.677433
C8	0.3171(17)	0.386(5)	0.472(1)	0.338147	0.361626	0.471180
H81	0.4492	0.3949	0.4530	0.309477	0.518540	0.400419
H82	0.2677	0.5758	0.4327	0.477177	0.302614	0.469093
C9	0.2020(15)	0.147(5)	0.439(1)	0.217126	0.137050	0.430284
H91	0.2539	0.0322	0.4998	0.253637	-0.028413	0.494374
H92	0.0820	0.2184	0.4477	0.077773	0.187100	0.439043
O10	0.2190(14)	0.068(4)	0.3066(9)	0.234116	0.070218	0.297613
H10	0.1392	-0.0865	0.2872	0.123606	-0.024306	0.258602

Relative Enthalpies at 0 K

Final Enthalpy = -5.88805879×10^3 eV at 0 GPa
Final Enthalpy = -5.88707567×10^3 eV at 0.95 GPa

Appendix 5 - Experimental and Calculated Atomic Co-ordinates of Phases I and II of Pentane-1,5-diol

Phase I

	Experimental (130 K and 0 GPa)			Calculated (0 K and 0 GPa)		
Space Group	$P2_12_12_1$			$P2_12_12_1$		
a / Å	5.3234(12)			5.435652		
b / Å	6.6991(11)			6.844740		
c / Å	17.040(3)			17.073639		
Atom	x	y	z	x	y	z
O1	0.08893(13)	-0.06689(10)	0.32080(4)	0.080649	-0.066781	0.320890
H1	0.0140(28)	-0.0427(25)	0.2773(9)	0.005048	-0.026561	0.269649
O2	-0.35440(11)	-0.02812(11)	0.68492(3)	-0.362773	-0.038250	0.687165
H2	-0.3595(28)	-0.1456(28)	0.6816(8)	-0.370834	-0.183574	0.680981
C1	-0.0406(2)	0.03084(14)	0.38359(5)	-0.046188	0.030318	0.383080
H3	-0.0155(24)	0.1712(18)	0.3801(6)	-0.017747	0.188573	0.378275
H4	-0.2205(22)	0.0107(20)	0.3806(7)	-0.245222	0.003596	0.378330
C2	0.0572(2)	-0.05019(13)	0.46058(5)	0.047188	-0.043996	0.460444
H5	0.2358(23)	-0.0296(19)	0.4642(8)	0.245158	-0.015199	0.464415
H6	0.0319(26)	-0.1899(20)	0.4612(6)	0.026098	-0.203116	0.461110
C3	-0.06723(15)	0.04351(12)	0.53247(5)	-0.082334	0.041581	0.530829
H7	-0.0418(25)	0.1842(19)	0.5319(7)	-0.060481	0.200673	0.531029
H8	-0.2435(23)	0.0211(19)	0.5300(8)	-0.280388	0.013758	0.526690
C4	0.0373(2)	-0.04037(14)	0.60902(5)	0.015004	-0.039359	0.607433
H9	0.2103(22)	-0.0134(20)	0.6143(7)	0.210323	-0.002587	0.613642
H10	0.0227(27)	-0.1798(20)	0.6075(6)	0.007714	-0.199233	0.606605
C5	-0.0964(2)	0.03418(15)	0.68219(5)	-0.114989	0.031226	0.680474

H11	-0.0948(23)	0.1738(22)	0.6850(7)	-0.126824	0.190793	0.680505
H12	-0.0129(24)	-0.0146(21)	0.7320(7)	-0.008352	-0.011530	0.732292

Relative Enthalpies at 0 K

BFGS: Final Enthalpy = -7.39622353×10^3 eV at 0 GPa
BFGS: Final Enthalpy = -7.39472629×10^3 eV at 0.38 GPa

Phase II

	Experimental (293 K and 0.38 GPa)			Calculated (0 K and 0.38 GPa)		
Space Group	$P2_12_12_1$			$P2_12_12_1$		
a / Å	4.7615(7)			4.778149		
b / Å	5.0639(11)			5.094323		
c / Å	24.372(6)			25.164746		
Atom	x	y	z	x	y	z
O1	0.0649(6)	0.1767(7)	0.52524(17)	0.124682	0.178030	0.521633
H11	0.2388	0.2679	0.5115	0.303977	0.241591	0.505868
C2	0.1432(8)	-0.0672(9)	0.5491(2)	0.178788	-0.063404	0.548293
H21	-0.0326	-0.1499	0.5640	-0.024108	-0.143985	0.560110
H22	0.2307	-0.1791	0.5215	0.272684	-0.205227	0.520723
C3	0.3437(9)	-0.0413(9)	0.5970(2)	0.364366	-0.031536	0.596325
H31	0.2498	0.0588	0.6271	0.258998	0.093261	0.625592
H32	0.5129	0.0570	0.5841	0.553868	0.074799	0.584514
C4	0.4342(8)	-0.3068(8)	0.6196(2)	0.444455	-0.291260	0.621137
H41	0.2656	-0.4070	0.6297	0.255138	-0.400246	0.631963

H42	0.5397	-0.3998	0.5895	0.550959	-0.413088	0.591397
C5	0.6269(9)	-0.2836(9)	0.6684(2)	0.628614	-0.260860	0.669621
H51	0.5205	-0.1963	0.6990	0.514666	-0.153124	0.700449
H52	0.7936	-0.1753	0.6587	0.812269	-0.141692	0.659625
C6	0.7248(9)	-0.5513(9)	0.6897(2)	0.725382	-0.519479	0.691566
H61	0.5655	-0.6595	0.7017	0.544350	-0.640263	0.702853
H62	0.8300	-0.6455	0.6592	0.840753	-0.628964	0.660932
O7	0.9117(7)	-0.5141(6)	0.73399(14)	0.900845	-0.477194	0.736584
H7	0.9835	-0.6905	0.7470	0.976144	-0.649303	0.748241

Relative Enthalpies at 0 K

Final Enthalpy = -7.39572789 x10^3 eV at 0 GPa
Final Enthalpy = -7.39426056 x10^3 eV at 0.38 GPa

Appendix 6 - Experimental and Calculated Atomic Co-ordinates of Phases I and II of Chloroform

Phase I

	Experimental (185 K and 0 GPa)			Calculated (0 K and 0 GPa)		
Space Group	*Pnma*			*Pnma*		
a / Å	7.485			7.544		
b / Å	9.497			9.476		
c / Å	5.841			5.879		
Atom	x	y	z	x	y	z
H1	-0.04720	0.25000	0.07200	-0.04338	0.25000	0.06746
C1	0.09000	0.25000	0.02700	0.09342	0.25000	0.02829
Cl1	0.18920	0.09950	0.14200	0.18597	0.10098	0.14597
Cl2	0.10720	0.25000	-0.27200	0.11310	0.25000	-0.25971

Phase II

	Experimental (130 K and 0.6 GPa)			Calculated (0 K and 0.6 GPa)		
Space Group	$P6_3$			$P6_3$		
a / Å	5.8610(8)			5.902		
c / Å	6.5960(13)			6.538		
Atom	x	y	z	x	y	z
H1	0.3333	0.6667	0.9426	0.33333	0.66667	0.93435
C1	0.3333	0.6667	1.091(2)	0.33333	0.66667	1.09552
Cl1	0.06443(18)	0.69504(17)	1.170(2)	0.07800	0.70204	1.17416

Appendix 7 - Experimental and Calculated Atomic Co-ordinates of the α, β, γ and δ-phases of Bromoform

The α-phase

	Experimental (273 K and 0 GPa)			Calculated (0 K and 0 GPa)		
Space Group	$P6_3/m$			$P6_3/m$		
a / Å	6.3350			6.752253		
c / Å	7.2140			7.550041		
Atom	x	y	z	x	y	z
H1	0.667	0.333	0.455	0.667	0.333	0.49013
C1	0.667	0.333	0.325	0.667	0.333	0.33301
Br1	0.690	0.632	0.277	0.68945	0.63838	0.2516

The β-phase (Experimental $CDCl_3$, Calculated $CHCl_3$)

	Experimental (14 K and 0 GPa)			Calculated (0 K and 0 GPa)		
Space Group	*P*-1			*P*-1		
a / Å	6.226			6.299		
b / Å	6.211			6.269		
c / Å	7.263			7.388		
α / °	81.25			82.10		
β / °	81.50			83.07		
γ / °	119.71			117.22		
Atom	x	y	z	x	y	z
D(H)1	0.66260	0.33150	0.48710	0.67479	0.34988	0.46936
C1	0.66260	0.33150	0.48710	0.72603	0.39255	0.32021
Br1	1.04270	0.40120	0.25620	1.02294	0.38375	0.26082
Br2	0.76960	0.72210	0.24410	0.76583	0.71173	0.23560
Br3	0.45800	0.13160	0.23940	0.46949	0.14835	0.23428

The γ-phase (Experimental $CDCl_3$, Calculated $CHCl_3$)

	Experimental (14 K and 0 GPa)			Calculated (0 K and 0 GPa)		
Space Group	*P*-3			*P*-3		
a / Å	6.253			6.254		
c / Å	6.886			6.887		
Atom	x	y	z	x	y	z
D(H)1	0.66670	0.33330	0.48890	0.66667	0.33333	0.33301
C1	0.66670	0.33330	0.33150	0.66667	0.33333	0.49013
Br1	0.68890	0.63770	0.25290	0.68945	0.63838	0.25166

The δ-phase

	Experimental (293 K and 1 GPa)			Calculated (293 K and 1 GPa)		
Space Group	$P6_3$			$P6_3$		
a / Å	6.3000(9)			6.200		
c / Å	7.1500(14)			7.144		
Atom	x	y	z	x	y	z
H1	-0.3333	0.3333	0.1889	-0.33333	0.33333	0.18940
C1	-0.3333	0.3333	0.052(5)	-0.33333	0.33333	0.03770
Br1	-0.05714(16)	0.63472(13)	-0.045(5)	-0.05590	0.63960	-0.04077

Published Work

DALTON
FULL PAPER

Comparison of the high-pressure and low-temperature structures of sulfuric acid

David R. Allan,[a] Stewart J. Clark,[b] Alice Dawson,[c] Pamela A. McGregor[a] and Simon Parsons[c]

[a] *Department of Physics and Astronomy, The University of Edinburgh, Mayfield Road, Edinburgh, UK EH9 3JZ*
[b] *Department of Physics, Durham University, Science Laboratories, South Road, Durham, UK DH1 3LE*
[c] *Department of Chemistry, The University of Edinburgh, West Mains Road, Edinburgh, UK EH9 3JJ*

Received 16th October 2001, Accepted 6th February 2002
First published as an Advance Article on the web 13th March 2002

We have determined the high-pressure crystal-structure of sulfuric acid, including the positions of the hydrogen atoms, using a combination of single-crystal X-ray diffraction techniques and *ab initio* density functional calculations. Just above the onset of crystallization, at 0.7 GPa, we find that a previously unobserved monoclinic structure, with $P2_1/c$ symmetry, is formed which is characterised by $SO_2(OH)_2$ tetrahedra interconnected by hydrogen bonds. In contrast to the low-temperature $C2/c$ phase, the tetrahedra in the high-pressure crystal structure are no longer arranged in $R_4^4(16)$ hydrogen-bonded layers but, instead, they form chains where the hydrogen bonding adopts a $R_3^3(12)$ arrangement. A series of *ab initio* calculations indicates that this rearrangement of the molecules results in a relatively small reduction in the enthalpy (13.603 kJ mol^{-1}) for the $P2_1/c$ structure at 0.7 GPa.

Introduction

Sulfuric acid (H_2SO_4) is a ubiquitous chemical reagent and is used for a very wide range of synthetic processes within both the academic and industrial disciplines. It is the largest volume chemical commodity and it can be used in the production of phosphate fertilizers, inorganic pigments, as a leaching agent in metal extraction and a variety of other economically important applications. Sulfuric acid can be readily co-crystallized with other molecular species: for example, the H_2SO_4–H_2O system has six intermediate compounds, $H_2SO_4 \cdot nH_2O$ with n = 1, 2, 3, 4, 6.5, 8;[1] and simple salts can be produced with other acids, such as acetic acid (forming $CH_3C(OH)_2^+ \cdot HSO_4^-$).[2,3] Anhydrous sulfuric acid crystallizes into a monoclinic crystal structure, with $C2/c$ symmetry, at approximately 10 °C. The structure is composed of layers of $SO_2(OH)_2$ tetrahedra connected *via* hydrogen bonds which, in turn, form four-fold, $R_4^4(16)$, nets as a result of the pairs of acceptor and donor oxygen atoms of the H_2SO_4 molecule.[4] Due to the nature of the hydrogen-bond network in the layers, the $C2/c$ crystal structure of H_2SO_4 has been regarded as a two-dimensional version of the well known KH_2PO_4 (KDP) structure, and it was considered possible that hydrogen-bond ordering transitions could occur at low temperature. However, neutron powder-diffraction studies of the structure revealed that the hydrogen-bond networks were ordered over a range of temperatures from near to the melting point down to the 10 K limit of the studies.[5] In KDP the hydrogen-ordering transition temperature (T_c) can be altered with the application of high-pressure as the hydrogen–hydrogen site separation (δ) is directly coupled to the distance between the acceptor and donor oxygens ($2R$). With increasing pressure $2R$ decreases with an accompanying decrease in both δ and T_c.[6,7] Although it would be anticipated that H_2SO_4 would adopt a similar behaviour and high-pressure would induce disorder, no high-pressure study of sulfuric acid appears to have been conducted to date.

We have recently determined the high-pressure crystal structures of the first three members of the monocarboxylic series—formic acid, acetic acid and propionic acid—and we have found that they all exhibit new structural phases at pressures just in excess of that required for crystallization.[8–10] All three of the organic acid systems investigated so far, therefore, have shown that profound structural modification can be induced by the application of fairly modest pressures (*i.e.* pressures in the 0.2 to 1.0 GPa regime) and it can be expected that the mineral acids, for example nitric acid, hydrochloric acid and sulfuric acid should exhibit equally rich high-pressure structural behaviour. We have selected sulfuric acid for this initial study and we find that just above the onset of crystallization, at 0.7 GPa, a previously unobserved monoclinic structure, with $P2_1/c$ symmetry, is formed. As for the low-temperature $C2/c$ phase, the high-pressure crystal structure is also characterised by $SO_2(OH)_2$ tetrahedra interconnected by hydrogen bonds. However, in the high-pressure structure the tetrahedra are no longer arranged in layers but, instead, they form hydrogen-bonded ribbons where the molecules adopt a $R_3^3(12)$ arrangement. A series of *ab initio* calculations indicates that this rearrangement of the molecules results in a relatively small reduction in the enthalpy (13.603 kJ mol^{-1}) for the $P2_1/c$ structure at 0.7 GPa.

Experimental

Crystallography

Liquid sulfuric acid was loaded and pressurised in a Merrill–Bassett diamond-anvil cell[11] that had been equipped with 600 μm culet diamonds and a tungsten gasket. After the nucleation of several crystallites the temperature was cycled close to the melting curve, in order to reduce the number of crystallites, in a manner similar to the methods used by Vos *et al.*[12] Finally, a single crystal was obtained at approximately 0.7 GPa that entirely filled the 200 μm gasket hole.

The diamond-anvil cell was mounted and centred on a Bruker APEX diffractometer (equipped with a monochromated Mo X-ray tube (μ(Mo-Kα) = 0.946 mm^{-1})) and a sequence

DOI: 10.1039/b109395a

Table 1 High-pressure data collection scan sequence for the Bruker APEX CCD diffractometer

Run	2θ/°	ω range/°	ϕ/°	Frames
1	−28.00	−8, −40	90.00	106
2	28.00	40, −40	90.00	266
3	−28.00	−140, −215	90.00	250
4	28.00	−140, −172	90.00	106
5	−28.00	−140, −218	270.00	260
6	28.00	−140, −172	270.00	106
7	−28.00	−8, −40	270.00	106
8	28.00	35, −40	270.00	250

of eight data collection scans was initiated, as detailed in Table 1. The SMART[13] program was used for data collection control and, with a detector distance of 70 mm, 2θ was set at either +28° or −28° to provide maximum coverage while ensuring that the detector surface did not intercept the primary beam. The eight scans were conducted as a sequence of frames that each had a range of 0.3° in ω and had an exposure time of 30 s. The ϕ-axis was fixed at either 90° or 270°, to ensure that the axis of the diamond-anvil cell was held parallel to the $\omega/2\theta$-plane so that absorption from the pressure cell components was minimised and the maximum possible access of reciprocal space could be achieved. As the APEX diffractometer has a three-circle goniometer the χ-axis is permanently fixed at a value of 54.74°. The overall data collection time was 15 h. With the SMART[13] code the sample reflections were identified by hand and an orientation matrix was determined using the GEMINI program.[13] Data integration and global cell refinement were performed with the program SAINT.[13] The monoclinic cell dimensions produced by SAINT for H_2SO_4 were found to be a = 7.695(13), b = 4.559(7), c = 8.378(3) Å, β = 107.42(8)°, V = 280.4(9) Å^3 (T = 293 K) which gives a total of four molecules in the unit cell, on comparison of the unit cell volume of the low-temperature phase.

The program SHADE[10] was used to reject reflections for which either the incident or diffracted beam was completely absorbed by the cell and resulted in the shading of the detector. The data completeness was 36.4%; this low value is a result of the unavoidable shading of reciprocal space by the pressure cell. Although the completeness is substantially lower than would normally be accepted for a typical ambient-pressure study, it is very close to the expected coverage for the design of pressure cell used in the experiment, as will be discussed later. Reflections with very poorly fitting profiles were also rejected. The surviving reflections were corrected for absorption by the pressure cell components with the program SADABS[14] and the transmission ranged from 0.494 to 1.000. The low minimum transmission factor arises due to partial shadowing by the highly absorbing tungsten gasket, which is difficult to model analytically. The structure was solved by direct methods in *Pc* (SHELXS-97[14]) and subsequently refined against F in $P2_1/c$ symmetry following identification of the crystallographic inversion centres (CRYSTALS[15]). H-atoms were placed on O1 and O2 on the basis of their longer bonds to the sulfur atom and their short intermolecular contacts to O-atoms in neighboring molecules. Chemically equivalent S–O and OSO distances and angles were restrained to be equal. Following refinement of the H-positions in which the OH and SOH distances and angles were restrained to 0.85(1) Å and 109(1)° the H-atom positions were fixed. The S-atom was refined with anisotropic displacement parameters, but the O-atoms were modeled isotropically. A common isotropic thermal parameter was also modeled for the H-atoms. The structure refined to R = 5.99%, R_w = 3.81% for 27 parameters and 178 data with $F > 4\sigma(F)$ and 8 restraints. The final difference map extremes were −0.34 and +0.48 e Å^{-3} and the goodness-of-fit was 1.037. The structural parameters are presented in Table 2 and selected bond lengths and bond angles are listed in Table 3.

CCDC reference number 172536.

See http://www.rsc.org/suppdata/dt/b1/b109395a/ for crystallographic data in CIF or other electronic format.

Theoretical calculations

We have performed *ab initio* calculations that were carried out using the CASTEP code.[16] The calculations were performed within the density functional formalism using a plane wave basis set and also using the generalized gradient approximation[17] that gives an accurate description of the many-body effects of electron exchange and correlation in hydrogen-bonded materials. Vanderbilt ultrasoft pseudopotentials[18] are used to describe the valence electron–ionic core interactions. This is necessary to reduce the size of the basis set in order to make the calculations tractable. The electronic wavefunction is expanded in a plane-wave basis set up to a kinetic energy of 380 eV which we find converges the total energy differences of the system to better than 1 meV atom^{-1}. This required the use of approximately 4 × 10^6 basis functions. Brillouin zone integrations are performed using a Monkhorst–Pack[19] k-point set. In each of the calculations, a k-point density is chosen such that the total energy of the system is converged to better than 1 meV atom^{-1} in line with the cut-off convergence criteria. The electronic structure is optimised by use of a pre-conditioned conjugate gradients energy minimization scheme. In all cases, the initial geometric configuration was taken from the experimental results, but both the lattice parameters and internal positions have been optimised self-consistently.

We have chosen this *ab initio* method for a number of reasons; a large enough plane wave basis set is guaranteed to be both converged and complete. This is necessary in calculating properties of such complex materials where many different bonding configurations are possible, since *a priori* knowledge of the likely electronic configuration is not available in this case which would be useful in the choice of a localized atomic/molecular orbital basis set. Also, since the basis set is complete, we can make use of the Hellmann–Feynman theorem to calculate forces on the atoms for use in geometric optimization. The positions of the atoms within the unit cell are optimised also using a conjugate gradients method and the *ab initio* forces. Using the *ab initio* methods we find that the lattice parameters are a = 7.905, b = 4.591, c = 8.749 Å and β = 108.17° and the atomic coordinates along with the calculated bond lengths and bond angles are presented in Tables 2 and 3 respectively. We have also performed *ab initio* calculations on the low-temperature structure to make a comparison between the geometries. We find that the relaxed ambient pressure lattice parameters are a = 8.087, b = 5.007, c = 8.899 Å, β = 110.47° and V = 337.58 Å^3, and these compare favorably with the reported experimental values of a = 8.181(2), b = 4.6960(10), c = 8.563(2) Å, β = 110.47° and V = 306.31(12) Å^3. We report the atomic positions in Table 4 and the bond lengths and bond angles in Table 5, where the experimental results of Kemnitz *et al.*[4] have been given for comparison.

For both the high-pressure $P2_1/c$ structure and the low-temperature $C2/c$ structure, the experimentally and theoretically derived bond lengths and bond angles involving the H atoms differ considerably. This is mainly due to the difficulty in obtaining accurate hydrogen positions from X-ray diffraction data. However, the DFT calculations can more accurately determine the hydrogen positions, and consequently the structural parameters involving the hydrogen atoms, and, therefore, it is expected that the results obtained by theory will be more reliable. Furthermore, the PW91 exchange-correlation functional used here is fully *ab initio* (unlike many commonly used functionals in quantum chemistry) and it has been demonstrated that its use in DFT calculations reproduces known hydrogen-bonded structures very accurately (for example references 8, 9 and 10).

Table 2 Fractional coordinates for the high-pressure monoclinic, $P2_1/c$, sulfuric acid structure obtained from the *ab initio* calculations (second set of coordinates) and, for comparison, the coordinates obtained from the Bruker APEX CCD single-crystal X-ray diffraction results. The standard deviations obtained from the single-crystal refinements are shown in parentheses

	Experimental			Theoretical		
Species	*x*	*y*	*z*	*x*	*y*	*z*
S	0.2639(8)	0.0672(9)	0.1787(4)	0.2679	0.0680	0.1840
O(1)	0.0994(17)	−0.111(3)	0.1901(16)	0.1196	−0.1354	0.1958
O(2)	0.316(2)	−0.065(2)	0.0318(12)	0.3348	−0.0625	0.0524
O(3)	0.4062(15)	0.034(2)	0.3289(11)	0.4105	0.0677	0.3344
O(4)	0.199(2)	0.3538(19)	0.1292(13)	0.1861	0.3410	0.1272
H(1)	0.131	−0.289	0.209	0.1432	−0.3500	0.1806
H(2)	0.38	−0.22	0.064	0.4371	−0.2090	0.0952

Table 3 Selected bond lengths (Å) and bond angles (°) for the high-pressure monoclinic, $P2_1/c$, sulfuric acid structure obtained from the single-crystal X-ray diffraction results (first set of numbers) and the *ab initio* calculations. The standard deviations obtained from the single-crystal refinements are shown in parentheses. The symmetry equivalent atomic positions are obtained from: #1 $x, y - 1, z$; #2 $-x + 1, y - 1/2, -z + 1/2$; #3 $-x + 1, y + 1/2, -z + 1/2$; #4 $x, y + 1, z$

	Experimental	Theoretical
S(1)–O(1)	1.537(7)	1.531
S(1)–O(2)	1.537(5)	1.527
S(1)–O(3)	1.416(6)	1.441
S(1)–O(4)	1.407(6)	1.427
O(1)–H(1)	0.85	1.019
O(2)–H(2)	0.85	1.028
O(1)–O(4)#1	2.668(9)	2.571
O(2)–O(3)#2	2.765(11)	2.583
O(3)–H(2)#3	2.05	1.555
O(4)–H(1)#4	1.89	1.564
O(1)–S(1)–O(2)	105.0(4)	105.3
O(1)–S(1)–O(3)	109.3(4)	109.3
O(2)–S(1)–O(3)	110.5(5)	107.9
O(1)–S(1)–O(4)	106.1(5)	106.7
O(2)–S(1)–O(4)	106.8(4)	109.3
O(3)–S(1)–O(4)	118.3(4)	117.3
S(1)–O(1)–H(1)	109	113.5
S(1)–O(2)–H(2)	109	114.0
O(1)–H(1)–O(4)#1	151	177.8
O(2)–H(2)–O(3)#2	142	169.0

Discussion

In the low-temperature phase of sulfuric acid the crystal structure is characterised by layers of $SO_2(OH)_2$ tetrahedra interconnected by hydrogen bonds to form $R_4^4(16)$ nets of molecules. However, the arrangement of the molecules in the $P2_1/c$ phase is strikingly different. At high-pressure the molecules arrange themselves into isolated chains so that the hydrogen-bonding scheme adopts an $R_3^3(12)$ form, see Fig. 1. There are two ribbons running parallel to the *b*-axis, within each unit cell, and the chains are related to one another by the *c*-glide symmetry. The molecules within each ribbon are related by a 2_1 screw axis and they, consequently, form an alternating sequence about the axis. The molecules on either side of the central axis form a pair of strands that are linked together by O1–H ··· O4 hydrogen bonds. This arrangement forms a double back-bone of hydrogen bonds which runs along the length of the ribbon. The pair of strands are cross-linked together by O2–H ··· O3 hydrogen bonds to complete the box-like form of the full molecular ribbon. The molecular chains are stacked within the crystal so that the edges of the box, as defined by the cross-linking O2–H ··· O3 hydrogen bonds, are coplanar and as a consequence layers of ribbons parallel to (1 0 $\bar{2}$) are produced. Inter-layer contacts are formed between O1–O2 (3.08 Å, 3.21 Å), O2–O3 (2.94 Å, 3.15 Å), O3–O3 (2.81 Å) and O2–O2 (3.09) Å while intra-layer contacts are formed between O1–O1 (3.08 Å, 3.25 Å), O1–O2 (3.28 Å) and O1–O4 (3.16 Å).

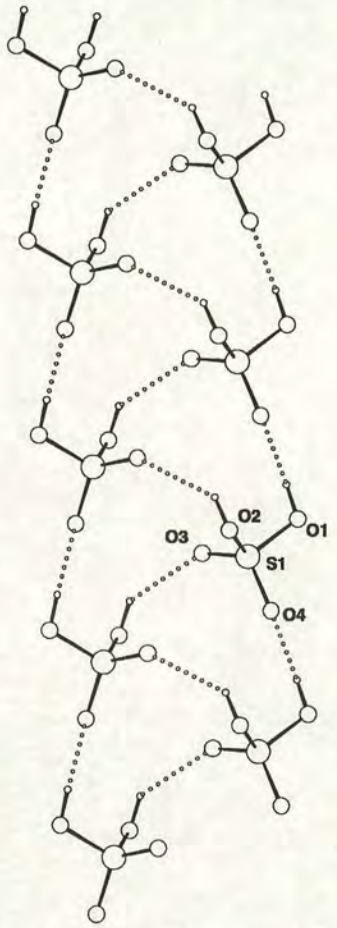

Fig. 1 A view of the molecular chains within the high-pressure monoclinic, $P2_1/c$, crystal structure of sulfuric acid detailing the $R_3^3(12)$ configuration of the hydrogen bonding. The orientation of the figure is approximately along the [0 0 1] direction, with [0 1 0] along the chain direction.

From the *ab initio* pseudo-potential calculations, we find that this arrangement of the molecules in the $P2_1/c$ structure at 0.7 GPa results in a relatively small, 13.603 kJ mol^{-1}, reduction in enthalpy when compared to the arrangement of the molecules in the low-temperature *C*2/*c* structure at the same pressure. This reduction in enthalpy is similar in magnitude to our previous calculations on acetic acid (CH_3COOH) and propionic acid (CH_3CH_2COOH) where enthalpy differences of 5.403 kJ mol^{-1} and 5.981 kJ mol^{-1} respectively were found between the low-temperature and high-pressure phases.[9,10] The rearrangement of the H_2SO_4 molecules from the $R_4^4(16)$ hydrogen-bonded layers that characterize the low-temperature structure to the

Table 4 Fractional coordinates for the low-temperature monoclinic, *C2/c*, sulfuric acid structure obtained from the *ab initio* calculations (second set of coordinates) and, for comparison, the coordinates obtained from the experimental study of Kemnitz *et al.*[4] The standard deviations obtained from the experimental work are shown in parentheses

	Experimental[4]			Theoretical		
Species	*x*	*y*	*z*	*x*	*y*	*z*
S(1)	0.0000	0.07450(9)	0.2500	0.0000	0.0761	0.2500
O(1)	−0.15928(13)	−0.0822(2)	0.17792(13)	−0.1584	−0.0664	0.1744
O(2)	0.00920(13)	0.2733(2)	0.11080(12)	0.0212	0.2661	0.1203
H(1)	0.088(4)	0.328(5)	0.128(3)	0.1444	0.3411	0.1461

Table 5 Selected bond lengths (Å) and angles (°) for the low-temperature monoclinic, *C2/c*, sulfuric acid structure obtained from the experimental studies of Kemnitz *et al.*[4] (first set of values) and, for comparison, the numbers obtained from the *ab initio* calculations. The standard deviations obtained from the single crystal refinements are shown in parentheses. The symmetry equivalent atomic postions are obtained from: #1 $-x, y, -z + 1/2$, #2 $x + 1/2, y + 1/2, z$

	Experimental[4]	Theoretical
S(1)–O(1)	1.426(1)	1.427
S(1)–O(2)	1.537(1)	1.533
O(2)–H(1)	0.66(3)	1.018
O(1)#2–H(1)	1.99(3)	1.570
O(1)#2–O(2)	2.648(2)	2.367
O(1)#2–H(1)–O(2)	170.0(3)	155.7
O(1)–S(1)–O(1)#1	117.87	116.9
O(2)–S(1)–O(2)#1	105.22	105.8
O(1)#1–S(1)–O(2)	110.70	110.7
O(1)–S(1)–O(2)	105.85	106.1

$R_3^3(12)$ form of the chains found in the high-pressure structure is accompanied by a more efficient molecular packing: in the low-temperature structure, at 113 K, each molecule occupies a volume of 76.58 Å^3 while at high-pressure the molecular volume is 69.85 Å^3. This 9% reduction in molecular volume is significantly greater than those observed in either acetic acid or propionic acid where the volume decrease between the low-temperature and high-pressure phases was only 3% and 2% respectively.

Finally, we have performed a Mulliken population analysis on the systems, which allows us to examine the nature of the charge transfer between the various species in the structures which gives a qualitative description of the relative strengths of the hydrogen bonds. The methods described in references 20 and 21 were used to calculate the Mulliken charges on each of the atoms, but it is worth noting that several other methods exist and therefore the actual values of the charges can vary from method to method. They should not, therefore, be taken as the actual atomic charge, which in any case, is rather ambiguously defined. However it is generally thought that the direction of charge transfer will be correct. We find that in both the *C2/c* phase and the $P2_1/c$ phase at ambient pressure and at 0.74 GPa the atomic charges are the same in each case; the charge on S atoms is 2.55 e, O is −0.91 e and H is 0.54 e. It therefore appears that the molecular charge distribution is relatively insensitive to the environment of the molecules (at least at these relatively low pressures). As pressure is increased from ambient to 0.74 GPa the intra-molecular bond lengths and angles remain relatively unchanged and, as is expected, it is mainly the inter-molecular separations that decrease. A comparison of the intra-molecular S–O bond lengths and O–S–O bond angles in Tables 3 and 5 indicates that they are essentially the same between the *C2/c* and $P2_1/c$ phases, with a retention of the long ($P2_1/c$: S(1)–O(1), S(1)–O(2); *C2/c*: S(1)–O(2)) and short ($P2_1/c$: S(1)–O(3), S(1)–O(4); *C2/c*: S(1)–O(1)) bonds. Hence, the molecular properties remain similar over the pressure range investigated. Therefore, the charge on the atoms forming the hydrogen bond remains the same for the low-temperature and high-pressure structures indicating that they have very similar strengths. This is also indicated by the low enthalpy difference between the two structures given that the molecular shapes are very similar.

In conclusion, we have solved the high-pressure monoclinic $P2_1/c$ structure of sulfuric acid and find that this previously unobserved phase has a radically different hydrogen bonding topology to that observed in the low-temperature *C2/c* phase. The high-pressure structure is composed of molecular ribbons adopting an $R_3^3(12)$ hydrogen bond scheme whereas the low-temperature phase is formed from $R_4^4(16)$ layers of molecules. This rearrangement not only offers a marked improvement in molecular packing efficiency but also results in a modest reduction of the enthalpy.

The present study is a further development in the use of area detectors for high-pressure single-crystal X-ray diffraction that we implemented in our recent work on the high-pressure phase of propionic acid. In this initial study, we used a conventional four-circle Eulerian goniometer (Bruker P4) equipped with the Bruker SMART 1000 CCD detector and sets of ω-scans were performed at 30° intervals in χ. The completeness of the resulting data set was 29%. The combination of the Bruker P4 and a CCD detector is somewhat non-standard and, conventionally, Bruker CCD detectors are used in conjunction with three-circle goniometers. Although the scan range is much more limited than in the four-circle instrument, we find that the use of a three-circle machine does not reduce the completeness of the resulting high-pressure data sets and a completeness of 36.4% is produced—which is somewhat better than that obtained with the four-circle goniometer and is close to the maximum 40% volume of reciprocal space that it is possible to access with a diamond-anvil cell of the Merrill–Bassett design. This is a significant consideration as our results indicate that it is possible to collect an almost ideal high-pressure data set from a CCD diffractometer that has neither its mechanical design nor its data collection control software modified for the purpose. Apart from the application of the SHADE program after data integration and the use of a short collimator, high-pressure data collection and refinement follow a relatively standard procedure that can be easily implemented at any X-ray laboratory equipped with a CCD machine. As CCD goniometers are now in wide use and are increasingly supplanting point-detector diffractometers, it can be anticipated that high-pressure studies will be performed by a greater number of workers at non-specialized laboratories.

Acknowledgements

This work is supported by a grant from the Engineering and Physical Sciences Research Council (EPSRC) of the United Kingdom. P. A. McGregor and A. Dawson also express gratitude to the EPSRC for their Ph.D. studentships.

References

1 W. F. Giaque, E. W. Hornung, J. E. Kunzler and T. R. Rubin, *J. Am. Chem. Soc.*, 1960, **82**, 62.
2 J. Kendall and E. Brakeley, *J. Am. Chem. Soc.*, 1921, **43**, 1826.

3 B. P.-G. Jönsson and I. Olovsson, *Acta Crystallogr., Sect. B*, 1968, **24**, 559.
4 E. Kemnitz, C. Werner and S. Trojanov, *Acta Crystallogr., Sect. C*, 1996, **52**, 2665.
5 A. R. Moodenbaugh, J. E. Hartt, J. J. Hurst, R. W. Youngblood, D. E. Cox and B. C. Frazer, *Phys. Rev. B*, 1983, **28**, 3501.
6 R. J. Nelmes, *Ferroelectrics*, 1987, **71**, 87.
7 R. J. Nelmes, Z. Tun and W. F. Kuhs, *Ferroelectrics*, 1987, **71**, 125.
8 D. R. Allan and S. J. Clark, *Phys. Rev. Lett.*, 1999, **82**, 3464.
9 D. R. Allan and S. J. Clark, *Phys. Rev. B*, 1999, **60**, 6328.
10 D. R. Allan, S. J. Clark, S. Parsons and M. Ruf, *J. Phys.: Condens. Matter*, 2000, **12**, L613.
11 L. Merrill and W. A. Bassett, *Rev. Sci. Instrum.*, 1974, **45**, 290.
12 (*a*) W. L. Vos, L. W. Finger and R. J. Hemley, *Nature*, 1992, **358**, 46; (*b*) W. L. Vos, L. W. Finger and R. J. Hemley, *Phys. Rev. Lett.*, 1993, **71**, 3150.
13 R. A. Sparks, GEMINI, Bruker AXS, Madison, Wisconsin, 1999; R. A. Sparks, SMART, Area-Detector Software Package, Bruker AXS, Madison, Wisconsin, 1993; R. A. Sparks, SAINT, Area-Detector Software Package, Bruker AXS, Madison, Wisconsin, 1995.
14 G. M. Sheldrick, SADABS, A Program for Empirical Absorption Correction of Area Detector Data, University of Göttingen, Germany, 1996; G. M. Sheldrick, SHELXS-97, University of Göttingen, Germany, 1997.
15 D. J. Watkin, C. K. Prout, J. R. Carruthers, P. W. Betteridge and R. I. Cooper, CRYSTALS, Issue 11, Chemical Crystallography Laboratory, Oxford, UK, 2001.
16 M. C. Payne, M. P. Teter, D. C. Allen, T. A. Arias and J. D. Joannopolous, *Rev. Mod. Phys.*, 1992, **64**, 1045.
17 J. P. Perdew and Y. Wang, *Phys. Rev. B*, 1992, **46**, 6671.
18 D. Vanderbilt, *Phys. Rev. B*, 1990, **41**, 7892.
19 H. J. Monkhorst and J. D. Pack, *Phys. Rev. B*, 1976, **13**, 5188.
20 M. D. Segal, R. Shah, C. J. Pickard and M. C. Payne, *Phys. Rev. B*, 1996, **54**, 16317.
21 M. D. Segal, R. Shah, C. J. Pickard and M. C. Payne, *Mol. Phys.*, 1996, **89**, 571.

s6.m1.p5 **Under Pressure: Hydroxylamine**, P.A. McGregor[1], D.R. Allan[1], D.J. Francis[2], W.G. Marshall[2], S. Parsons[3], C.R. Pulham[3], *1. Department of Physics and Astronomy, The University of Edinburgh, King's Buildings, Mayfield Road, Edinburgh, EH9 3JZ, 2. ISIS Neutron Facility, Rutherford Appleton Laboratory, Chilton, Didcot, Oxon, OX110QX, 3. Department of Chemistry, The University of Edinburgh, King's Buildings, West Mains Road, Edinburgh, EH9 3JJ.*
Keywords: hydroxylamine, neutron diffraction, pressure.

The hydrogen-bonded systems of water, ammonia and water-ammonia mixtures have been extensively studied under a variety of conditions, and show a rich diversity of structural motifs involving hydrogen bonding. Hydroxylamine (NH_2OH) contains both amine and hydroxy functional groups in the same molecule, and so should also be expected to give rise to a range of interesting structures that are dependent on the relative magnitude of intermolecular interactions. Pressure is a powerful tool for tuning these interactions.

Unlike its fully substituted analogues, eg Me_3N^+-O^-, hydroxylamine exists under ambient conditions as the N-OH bonded tautomer rather than the N^+-O^- bonded tautomer.

Preliminary investigations at the University of Edinburgh using Raman spectroscopy showed a substantial increase in the N-O stretching mode that is consistent with the formation of the amine-oxide tautomer.

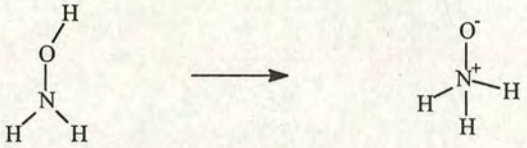

A fully deuterated sample was prepared for neutron diffraction on PEARL/HiPr at ISIS. With a limited pressure and temperature range, 260-300K and 0-9Gpa, these initial neutron diffraction studies produced convincing evidence of the existence of two high- pressure phases. A third phase was also observed, but we have yet to rule out the possibility that this pattern is due to decomposition of the sample.

Acta Cryst. (2002). A58 (Supplement), C60

HIGH-PRESSURE CRYSTAL STRUCTURES OF HYDROGEN BONDED SMALL MOLECULES

P. A. McGregor[1] D. R. Allan[1] S. Parsons[2] A. Dawson[2] C. R. Pulham[2] S. J. Clark[3]

[1]University of Edinburgh Department of Physics And Astronomy James Clerk Maxwell Building The King's Buildings, Mayfield Road EDINBURGH EH9 3JZ UK [2]Department of Chemistry, University of Edinburgh, UK [3]Department of Physics, Durham University, UK

The application of moderate pressure (0-15 GPa) can cause significant changes in the structures of small molecules. Differences between low temperature and the corresponding high pressure phases have shown a great diversity in molecular packing arrangements, new structural motifs through variance in hydrogen bonding and even molecular conformational changes.

Previous structural analysis of small organic molecules has provided a range of new high pressure phases of hydrogen bonded systems: low molecular weight mono-alcohols (methanol and ethanol); acetone; and the small carboxylic acids (formic acid and acetic acid). The results provide an insight towards the differences between the low temperature and high-pressure phases arising from the range of hydrogen bonding, which can cause differences in molecular packing.

These studies have been extended to include the quaternary alcohols, cyclobutanol and tertiary butanol, and molecules with more than one functional group, for example the alpha-omega di-alchohols [$HO(CH_2)_nOH$] ethane-diol (n = 2) and propane-diol (n = 3). These small molecules have high-pressure phases that are different from their corresponding low-temperature phases. In the case of ethane-diol, not only do we observe major changes in the packing arrangement of the molecules, there is also a conformational change - this is the first example of such a difference between the phases under these conditions. For propane-diol, the high-pressure phase has two conformers in the asymmetric unit, one planar molecule and the other non-planar, compared to one conformer in the low-temperature analogue.

Keywords: HYDROGEN BONDING, HIGH PRESSURE, SMALL MOLECULES

Acta Crystallographica Section E
Structure Reports Online
ISSN 1600-5368

Treatment of 'twinning' in isopropylcyclohexane

David R. Allan,[a] Pamela A. McGregor,[a] Lorna J. McLachlan,[b] Simon Parsons[b]* and Colin R. Pulham[b]

[a]Department of Physics and Astronomy, The University of Edinburgh, King's Buildings, West Mains Road, Edinburgh EH9 3JZ, Scotland, and [b]Department of Chemistry, The University of Edinburgh, King's Buildings, West Mains Road, Edinburgh EH9 3JJ, Scotland

Correspondence e-mail: s.parsons@ed.ac.uk

Key indicators

Single-crystal X-ray study
T = 150 K
Mean σ(C–C) = 0.003 Å
R factor = 0.061
wR factor = 0.237
Data-to-parameter ratio = 13.7

For details of how these key indicators were automatically derived from the article, see http://journals.iucr.org/e.

Received 25 February 2002
Accepted 22 April 2002
Online 17 May 2002

Isopropylcyclohexane, C_9H_{18}, which is a liquid under ambient conditions, tends to form a glass on cooling. Laser-assisted zone refinement of the frozen solid yielded a crystalline solid, although the sample was not single. The crystal was not really a twin in the usual sense of the term, but the consequences of the multiplicity of the sample could be modelled with a combination of domains generated by twofold rotations about the reciprocal lattice [1k0] directions, where k = 9–12.

Comment

There is active current interest in obtaining crystal structures from compounds which are liquids or gases under ambient conditions (Bond & Davies, 2002*a*,*b*; Downs *et al.*, 2001; Romano *et al.*, 2001; Tang *et al.*, 2001; Thalladi & Boese, 2000; Thalladi, Nuesse & Boese, 2000; Thalladi, Boese & Weiss, 2000). Such structure determinations can be frustrated if a compound tends to form a glass, a particular problem if the molecules under study are conformationally flexible.

Our interest in isopropylcyclohexane, (I), lay in its possible use as a model for traction fluids (Hentschel, 1985), and we wished to compare its structure after crystallization at low temperature with that obtained on application of high pressure. In the event, crystallization of the compound at high pressure was frustrated by glass formation. However, a crystalline sample was obtained at low temperature by means of Boese's laser-assisted zone-refinement technique (Boese & Nussbaumer, 1994). The X-ray diffraction pattern clearly showed that the sample was not single, but, given the difficulty with which it had been obtained, we were reluctant to attempt to regrow it without collecting a data set.

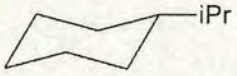

(I)

A suitable indexing of the pattern was achieved by the use of the program *GEMINI* (Sparks, 1999) for 48 out of 132 reflections selected from images taken during data collection. A second matrix indexed a further 29 reflections with a similar unit cell. These two matrices indexed the majority of the strong reflections, and the relationship between them (a possible twin law) could be expressed by the matrix

$$\begin{pmatrix} -0.92 & 1.26 & 0.09 \\ 0.15 & 0.90 & 0.06 \\ 0.09 & 0.06 & -1.01 \end{pmatrix}$$

DOI: 10.1107/S1600536802007274

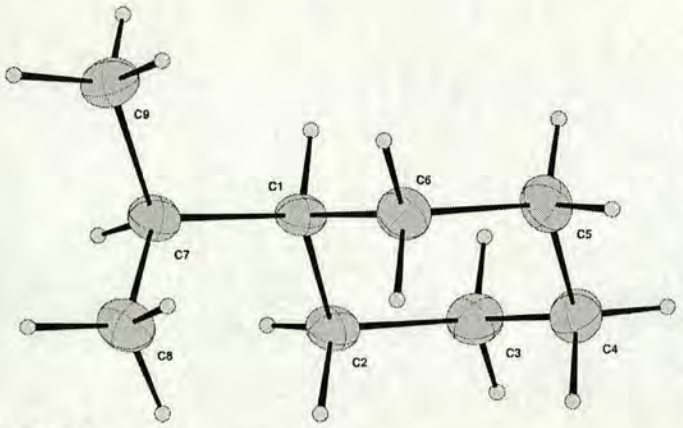

Figure 1
The molecular structure of (I) in the crystal. Ellipsoids are drawn at the 50% probability level.

The combination of terms in this matrix means that overlap between the reflections from the components that it relates is unlikely to affect refinement.

Of the remaining 55 reflections, 22 could be indexed (using the program *DIRAX*; Duisenberg, 1992) with a third orientation matrix. Attempts made to index the remaining reflections were not successful. The relationship between the first and third matrices can be expressed as

$$\begin{pmatrix} -1.00 & 0.25 & 0.00 \\ 0.03 & 0.98 & 0.01 \\ 0.11 & 0.02 & -0.98 \end{pmatrix}$$

The trace of this matrix is −1 and the determinant approximately 1 (0.96), so that it can be considered to be a twofold rotation. The eigenvector of this matrix corresponding to the eigenvalue near 1 (actually 0.98) is [0.13,1.04,0.01], and the twofold axis can be interpreted as being roughly parallel to the reciprocal lattice [180] direction (referred to from now on as [180]*) (Sands, 1982). The figures quoted here deviate from ideal values, and their accuracy may be compromised by the relatively small number of rather weak reflections used to determine them, and the difficulty of extracting accurate peak positions for reflections which overlap with reflections from a different domain of the sample.

The data set was integrated using the first orientation matrix derived above. The structure was solved by direct methods (*SIR*92; Altomare *et al.*, 1994), and refined by full-matrix least-squares against $|F|$ using data with $I > 2\sigma(I)$ (*CRYSTALS*; Watkin *et al.*, 2002). This strategy was adopted because it is useful to be able to compare weighted and unweighted R factors directly. This means that the data-to-parameter ratio is *ca* 7.5:1.

Only about half the reflections in the data set had $I > 2\sigma(I)$, and it is usual to treat the H atoms with a riding model during refinement under these circumstances. However, H atoms contribute almost 15% by weight and 25% of $F(000)$ for this compound and so the H-atom parameters have a significant effect on data-fitting. H-atom positional parameters were therefore refined subject to a similarity restraint on the C—H bond lengths; two common isotropic displacement parameters were refined, one for the methyl groups and the other for the remaining H atoms.

The R factor for this model converged to 6.93% with unit weights. An attempt was made to model the twinning by incorporating a twofold axis about the [180]* direction as a possible twin law. The R factor dropped only slightly to 6.91%.

At this stage, the *ROTAX* procedure was used to identify possible twin laws using trends in the indices of the poorly agreeing data with $|F_o| > |F_c|$ (Cooper *et al.*, 2002). The program identified as possible twin laws six twofold axes along the [190]*, [1,10,0]*, [1,11,0]*, [1,12,0]*, [12,1,3] and [$\bar{1}$04]* directions. An eight-domain twinning model consisting of these domains, plus a domain for a twofold rotation about [180]*, was set up using a recently implemented routine in *CRYSTALS* which facilitates this. (Detailed instructions are given under _refine_special_details in the CIF.) A reflection from the primary domain was considered to be overlapped with a reflection from another domain if the original and transformed reciprocal lattice points lay within 0.07 Å^{-1} of each other, this value being optimized by trial-and-error. The sum of the domain scale factors was tightly restrained to unity. We have found in the past that refinements of multi-domain twins sometimes need to be stabilized with shift-limiting restraints; these were applied here, although the refinement was quite stable without them. The R factor dropped to 5.89% on refinement, but four twin scale factors (for the twofold rotations about [190]*, [180]*, [1,11,0]* and [$\bar{1}$04]*) fell to less than 2%. These were fixed at zero in subsequent cycles of refinement, and so the final model was a four domain twin. The R factor at this stage, with unit weights, was 5.96%. We have previously discussed the use of the Watkin–Carruthers weighting scheme (Carruthers & Watkin, 1979; Cooper *et al.*, 2002) in the analysis of twinned crystal structures. Incorporation of this scheme into the refinement led R to drop to 5.66%.

The final cycles of least squares were performed against $|F|^2$ using all data. The differences between the refined structural parameters on making this change were negligibly small, but some effect on the scale factor was anticipated (Hirshfeld & Rabinovich, 1973). The scale factor after the initial stages of F refinement [$F > 4\sigma(F)$] was 1.282 (15), and 1.224 (15) after F^2 refinement against all data. The correlation between the scale factor and the element scale for the primary domain of the twin meant that this change in scale had a knock-on effect on the twin element scale factors. The largest changes were from 0.631 (14) to 0.721 (14) (domain 1) and from 0.185 (17) to 0.118 (15) ([1,12,0]*). The correlation coefficient between the scale and the primary domain scale factor was −0.909 if weak data were omitted, but −0.823 if they were included. This is a much more compelling argument for including all data in this refinement than, say, the increase in the data-to-parameter ratio. Normal probability plots can be used to assess the

agreement between $|F_o|$ and $|F_c|$ (Abrahams & Keve, 1971). After F refinement with a cut-off of $4\sigma(F)$, a normal probability plot using the statistic $(F_o-F_c)/\sigma(F_o)$ had a gradient of 1.710, an intercept of −0.001 and a correlation coefficient of 0.924. After $|F|^2$ refinement using all data, the corresponding quantities were 1.343, −0.136 and 0.915, and this shift towards a more ideal gradient is perhaps another reason for using all data in the final stages of this refinement. The R factor based on F and $F > 4\sigma(F)$ was 6.08%.

A full list of twin laws and scale factors is given in the supplementary data. Other refinement parameters are listed in the *Experimental* table. The bond lengths and angles are normal (these have been deposited in the CIF), and the displacement parameters show no unusual features. A view of the molecule is shown in Fig. 1; the isopropyl group is in an equatorial position on the cyclohexane ring, which adopts the expected chair conformation.

A separate integration was performed using the second orientation matrix described above. The diffraction from this domain was rather weaker [mean $I/\sigma(I) = 1.78$ against 6.62 for the data set obtained with the first matrix]. Although no twin modelling appeared to be necessary, the standard uncertainties on the C—C bond lengths were some three times higher.

The crystal used for the determination of this structure was not really a twin in the usual sense of the term, which is usually taken to be associated with the geometrical properties of the unit cell or a supercell. It is more accurate to describe the sample as a 'multiple crystal'. Nevertheless, the refinement strategy used was rather similar to that employed for a twinned structure. In attempting to model the diffraction pattern from this multiple crystal, it was necessary to use several twin matrices in order to model the contribution of the minor component(s) of the sample. In general, it is preferable to determine a twin law *via* the relationship between the orientation matrices of the different domains. If the orientation matrix so-derived suffers from errors due to poor profile, weak diffraction, overlapped data, *etc.*, this procedure can be subject to systematic errors. In this case, it suggested that a twofold axis about the [180]* direction could be used to model twinning, whereas analysis of the poorly fitting data during refinement suggested that it could potentially be described as twofold axes about [1k0]*, where k had values in the range 9–12. The matrices for these operations are not very different, but in a competitive refinement it was found that a combination of these twin laws formed a successful model. An additional twin domain generated by a twofold axis about the [2,1,3] direct lattice direction was also included in the model, although its refined domain scale factor is small.

Experimental

The sample of (I) was obtained from Aldrich and used as received. Crystallization of the material at low temperature was achieved with a sample held in a 0.4 mm outside-diameter capillary held at 150 K using the laser-assisted zone-refinement technique of Boese & Nussbaumer (1994).

Crystal data

C_9H_{18}
$M_r = 126.24$
Monoclinic, $P2_1/c$
$a = 15.689\ (8)$ Å
$b = 5.298\ (3)$ Å
$c = 10.641\ (6)$ Å
$\beta = 101.79\ (1)°$
$V = 865.9\ (14)$ Å^3
$Z = 4$
$D_x = 0.968$ Mg m^{-3}
Mo $K\alpha$ radiation
Cell parameters from 1016 reflections
$\theta = 2$–$27°$
$\mu = 0.05$ mm^{-1}
$T = 150$ K
Cylinder, colourless
1.0 × 0.4 × 0.4 mm

Data collection

Bruker SMART APEX diffractometer equipped with an Oxford Cryosystems low-temperature device and an OHCD laser-assisted crystallization device (Scientific Consulting, Essen, Germany)
φ and ω scans
Absorption correction: multi-scan (*SADABS*; Sheldrick, 2001)
$T_{min} = 0.554$, $T_{max} = 1$
5107 measured reflections
1950 independent reflections
1069 reflections with $I > 2\sigma(I)$
$R_{int} = 0.04$
$\theta_{max} = 28.3°$
$h = -20 \rightarrow 19$
$k = 0 \rightarrow 6$
$l = 0 \rightarrow 14$

Refinement

Refinement on F^2
$R[F^2 > 2\sigma(F^2)] = 0.061$
$wR(F^2) = 0.237$
$S = 1.04$
1950 reflections
142 parameters
All H-atom parameters refined
Weights: Tukey & Prince method (Carruthers & Watkin, 1979); w= [weight][1 − [$\Delta F/6*\sigma(F)^2$]]^2 using a four-term Chebychev polynomial, with parameters 69.3, 109, 54.8, 14.3
$(\Delta/\sigma)_{max} = 0.003$
$\Delta\rho_{max} = 0.28$ e Å^{-3}
$\Delta\rho_{min} = -0.16$ e Å^{-3}

The refinement strategy is described in the text. A detailed instruction list for building a multi-domain twin model in *CRYSTALS* is given in the CIF under _refine_special_details.

Data collection: *SMART* (Siemens, 1993); cell refinement: *SAINT* (Siemens, 1995); data reduction: *SAINT*; program(s) used to solve structure: *SIR*92 (Altomare *et al.*, 1994); program(s) used to refine structure: *CRYSTALS* (Watkin *et al.*, 2002); molecular graphics: *CAMERON* (Watkin *et al.*, 1996); software used to prepare material for publication: *CRYSTALS*.

The authors thank the EPSRC for funding.

References

Abrahams, S. C. & Keve, E. T. (1971). *Acta Cryst.* A**27**, 157–165.
Altomare, A., Cascarano, G., Giacovazzo, C., Guagliardi, A., Burla, M. C., Polidori, G. & Camalli, M. (1994). *J. Appl. Cryst.* **27**, 435.
Boese, R. & Nussbaumer, M. (1994). In *Correlations, Transformations, and Interactions in Organic Crystal Chemistry*, IUCr Crystallographic Symposia, Vol. 7, edited by D. W. Jones & A. Katrusiak, pp. 20–37. Oxford University Press.
Bond, A. D. & Davies, J. E. (2002*a*). *Acta Cryst.* E**58**, o5–o7.
Bond, A. D. & Davies, J. E. (2002*b*). *Acta Cryst.* E**58**, o196–o197.
Carruthers, J. R. & Watkin, D. J. (1979). *Acta Cryst*, A**35**, 698–699.
Cooper, R. I., Gould, R. O., Parsons, S. & Watkin, D. J. (2002). *J. Appl. Cryst.* **35**, 168–174.
Downs, A. J., Greene, T. M., Johnsen, E., Brain, P. T., Morrison, C. A., Parsons, S., Pulham, C. R., Aarset, K., Mills, I. M., Page, E. M. & Rice, D. A. (2001). *Inorg. Chem.* **40**, 3484–3497.
Duisenberg, A. J. M. (1992). *J. Appl. Cryst.* **25**, 92–96.
Hentschel, K. H. (1985). *J. Synth. Lubr.* **2**, 143–65.
Hirshfeld, F. L. & Rabinovich, D. (1973). *Acta Cryst.* A**29**, 510–513.
Romano, R. M., Della Vedova, C. O., Downs, A. J., Oberhammer, H. & Parsons, S. (2001). *J. Am. Chem. Soc.* **123**, 12623–12631.
Sands, D. E. (1982). *Vectors and Tensors in Crystallography*. New York: Dover Publications Inc.

Sheldrick, G. M. (2001). *XPREP*, *SHELXL* and *SADABS* (Version 2.06). University of Göttingen, Germany, and Bruker–Nonius, Madison, Wisconsin, USA.
Siemens (1993). *SMART*. Siemens Analytical X-ray Instruments Inc., Madison, Wisconsin, USA.
Siemens (1995). *SAINT*. Siemens Analytical X-ray Instruments Inc., Madison, Wisconsin, USA.
Sparks, R. A. (1999). *GEMINI*. Bruker AXS Inc., Madison, Wisconsin, USA.
Tang, C. Y., Coxall, R. A., Downs, A. J., Greene, T. M. & Parsons, S. (2001). *J. Chem. Soc. Dalton Trans.* pp. 2141–2147.
Thalladi, V. R. & Boese, R. (2000). *New J. Chem.* **24**, 579–581.
Thalladi, V. R., Boese, R. & Weiss, H.-C. (2000). *Angew. Chem. Int. Ed.* **39**, 918–922.
Thalladi, V. R., Nuesse, M. & Boese, R. (2000). *J. Am. Chem. Soc.* **122**, 9227–9236.
Watkin, D. J., Prout, C. K., Carruthers, J. R., Betteridge, P. W. & Cooper, R. I. (2002). *CRYSTALS*. Issue 11.80. Chemical Crystallography Laboratory, Oxford, England.
Watkin, D. J., Prout, C. K. & Pearce, L. J. (1996). *CAMERON*. Chemical Crystallography Laboratory, University of Oxford, England.

Selective Recognition of Configurational Substates of Zinc Cyclam by Carboxylates: Implications for the Design and Mechanism of Action of Anti-HIV Agents

Xiangyang Liang, Michael Weishäupl, John A. Parkinson, Simon Parsons, Pamela A. McGregor, and Peter J. Sadler*[a]

Abstract: The interaction of metal cyclams with carboxylate groups is thought to play an important role in their binding to the CXCR4 chemokine receptor and in their anti-HIV activity. Here we report the synthesis of acetate, phthalate, perchlorate and chloride complexes of Zn^{II} cyclam (1,4,8,11-tetraazacyclotetradecane). The X-ray crystal structures of $[Zn(cyclam)(phthalate)]_n(CH_3OH)_{2n}$ and $[Zn(cyclam)(H_2O)_2](OAc)_2$ contain octahedral Zn^{II} centres. Phthalate acts as a bridging ligand in the former complex, binding through monodentate carboxylate groups, and giving rise to infinite chains in the lattice together with extensive hydrogen bonding between carboxylate donor oxygen atoms and amine and methanol acceptor atoms. The uncoordinated acetate groups and the aqua ligand in the acetate complex are also involved in a rich network of hydrogen bonds and this may account for the unusually long Zn–O distance (2.27 Å). In both crystalline complexes, the macrocycle adopts the *trans*-III (*S,S,R,R*) configuration. 1D ^1H NMR spectra of all four complexes have been fully assigned by a combination of 2D [^1H, ^1H] COSY and TOCSY, and [^1H, ^{13}C] and [^1H, ^{15}N] HSQC NMR data. In aqueous solution, the stable *trans*-III configuration found in the solid-state equilibrates slowly (hours at 298 K) with *trans*-I (*R,S,R,S*) and *cis*-V (*R,R,R,R*) configurations. The *trans*-III configuration is predominant in aqueous solution for both the chloride and perchlorate complexes, but for the acetate and phthalate complexes, the *cis*-V configuration dominates. Carboxylate groups appear to stabilize the *cis*-V configuration in solution through Zn^{II} coordination and hydrogen bonding. Titration of the chloride Zn^{II}–cyclam complex with acetate confirmed that carboxylates strongly induce formation of the *cis*-V configuration. This implies that carboxylates can exert a strong influence over configurational selectivity. Cyclam NH hydrogen bonding is prevalent both in the solid state and in solution, and is relevant to the anti-HIV activity of Zn^{II} and other metal cyclam complexes and to their ability to recognize the CXCR4 transmembrane co-receptor.

Keywords: anti-HIV activity · cyclam · NMR spectroscopy · X-ray diffraction · zinc

Introduction

The bicyclam AMD3100 ([1,1′-(1,4-phenylenebismethylene)-bis-1,4,8,11-tetraazacyclotetradecane octahydrochloride dihydrate]) is a highly potent and selective CXCR4 antagonist with strong antiviral activity against replication of the human immunodeficiency virus HIV-1 and HIV-2 at nanomolar concentrations,[1] whilst not being toxic to host cells at millimolar concentrations.[2] AMD3100 has been on phase II clinical trials for the treatment of AIDS[3] and is also of clinical interest in relation to stem cell transplantation. Cyclam itself, although much less potent, also exhibits significant anti-HIV activity.[4]

Metal complexation has a significant influence on the antiviral activity of cyclam and bicyclams.[5] In particular, Zn^{II}–cyclam and -bicyclam complexes can exhibit lower toxicity and greater anti-HIV activity than the free ligands.[3, 6] Zn^{II} is readily available in the body and binds strongly to cyclam ($\log K = 15.0 \sim 15.5$).[7] Therefore Zn^{II} could play a key role in the biological activity of cyclam derivatives.

AMD3100 is a highly specific antagonist of the 7-transmembrane helical co-receptor CXCR4, and mutagenesis studies have suggested that aspartate residues 171 and 262 in transmembrane helices 4 and 6, which have carboxylate groups on their side chains, play key roles in the recognition of cyclams.[8, 9] We have therefore studied the interaction of carboxylate ligands with zinc cyclam both in the solid-state by X-ray crystallography and in solution by NMR spectroscopy.

[a] Prof. Dr. P. J. Sadler, X. Liang, Dr. M. Weishäupl, Dr. J. A. Parkinson, Dr. S. Parsons, P. A. McGregor
School of Chemistry, The University of Edinburgh
West Mains Road, Edinburgh, EH9 3JJ (UK)
Fax: (+44) 131-650 6452
E-mail: P.J.Sadler@ed.ac.uk

Supporting information for this article is available on the WWW under http://www.wiley-vch.de/home/chemeurj.org/ or from the author.

 DOI: 10.1002/chem.200304808

Our work suggests that interactions of zinc cyclam complexes with the CXCR4 co-receptor may involve the selective recognition of configurational substates of the metallomacrocycle and such knowledge may aid the design of more effective anti-HIV agents.

Results

Solution NMR studies of $[Zn(cyclam)(H_2O)_2](OAc)_2$ (1): As can be seen in Figure 1a, the ^1H NMR spectrum of **1** in 10% D_2O/90% H_2O at pH 6.8, consists of two distinct regions. Two

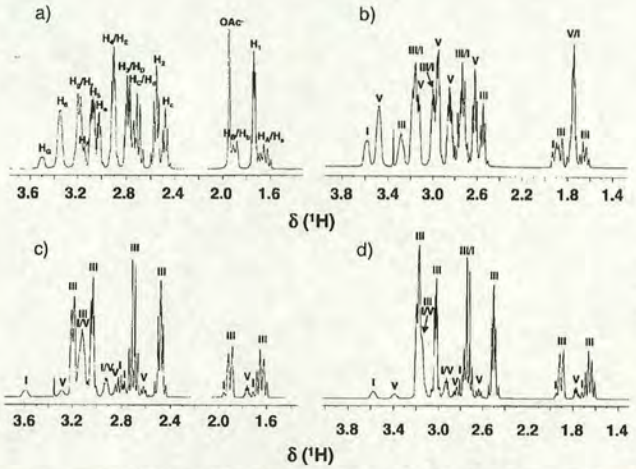

Figure 1. ^1H NMR spectra of a) acetate complex **1**, b) phthalate complex **2**, c) perchlorate complex **3** and d) chloride complex **4** in 10% D_2O/90% H_2O at equilibrium (298 K). In a) resonances for the *trans*-I, *trans*-III and *cis*-V configurations of complex **1** are designated H_A-H_G, H_a-H_g and H_1-H_6, respectively. Resonances for the *trans*-I, *trans*-II and *cis*-V configurations of complexes **2**–**4** are designated I, III, and V, respectively.

sets of multiplets and a strong singlet appear between $\delta = 1.5$ and 2.1 ppm. The second region of signals lies between $\delta = 2.4$ and 3.6 ppm. To fully assign the complicated ^1H NMR spectrum, 2D homonuclear [^1H, ^1H] TOCSY and DQF-COSY NMR data sets and natural abundance 2D heteronuclear [^1H, ^{13}C] and [^1H, ^{15}N] HSQC NMR data were acquired.

Three spin-systems were found in the 2D [^1H, ^1H] TOCSY spectrum (see Figure S1 in the Supporting Information). 2D [^1H, ^1H] DQF-COSY NMR data (see Figure S2 in the Supporting Information) revealed couplings in the first spin-system (labelled **III**) as follows: H_a ($\delta = 1.64$ ppm) is coupled to H_b ($\delta = 1.90$ ppm), to H_d ($\delta = 2.70$ ppm) and to H_g ($\delta = 3.20$ ppm), and H_b is also coupled to H_f ($\delta = 3.18$ ppm); H_c ($\delta = 2.48$ ppm) and H_e ($\delta = 3.03$ ppm) couple to one another and both also couple to H_g. The second spin-system (labelled **V**) is composed of five signals: H_1 ($\delta = 1.74$ ppm) is coupled to H_3 ($\delta = 2.79$ ppm), H_5 ($\delta = 3.08$ ppm), and weakly to a broad signal H_6 ($\delta = 3.35$ ppm); H_2 ($\delta = 2.56$ ppm) and H_4 ($\delta = 2.91$ ppm) couple to each other. Both H_2 and H_4 also couple to the broad signal H_6. The third spin-system (labelled **I**) consists of seven signals: H_A ($\delta = 1.69$ ppm), H_B ($\delta = 1.92$ ppm), H_C ($\delta = 2.73$ ppm), H_D ($\delta = 2.76$ ppm), H_E ($\delta = 2.91$ ppm), H_F ($\delta = 3.16$ ppm) and a broad signal H_G ($\delta = 3.50$ ppm) through TOCSY NMR data. The last spin-system could not be observed easily in the DQF-COSY NMR data due to extensive overlap and low signal intensity. The strong singlet ($\delta = 1.93$ ppm) can be assigned to OAc^- since it does not couple to any other resonances.

Three NH signals were detected in the 2D [^1H, ^{15}N] HSQC NMR spectrum (Figure 2). The spin system H_a-H_f

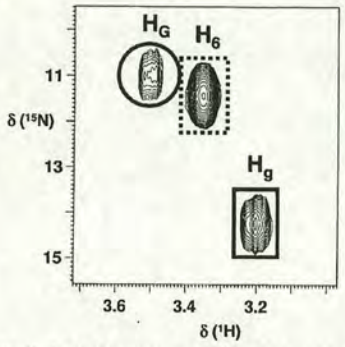

Figure 2. 2D [^1H, ^{15}N] HSQC NMR spectrum of complex **1** in 10% D_2O/90% H_2O. NH resonances for the *trans*-I (H_G), *trans*-III (H_g) and *cis*-V (H_6) configurations are designated by circles, solid and dashed boxes, respectively.

showed correlations to the NH signal H_g; the spin system H_1-H_5 relates to the broad NH signal H_6; the third spin-system H_A-H_B relates to the broad NH signal H_G. The three identified spin systems arise from three different configurations (**I**, **III** and **V**) of complex **1**. Time- and pH-dependent experiments also support this conclusion.

The 2D [^1H, ^{13}C] HSQC NMR spectrum (Figure 3) revealed the presence of 17 proton signals corresponding to those described above, which were correlated to a total of nine

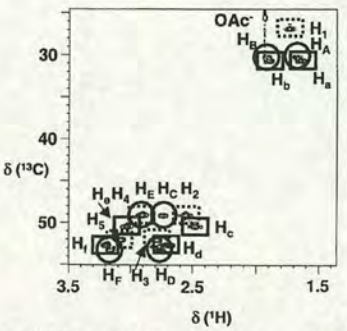

Figure 3. 2D [^1H, ^{13}C] HSQC NMR spectrum of complex **1** in 10% D_2O/90% H_2O. Resonances for the *trans*-I (H_A to H_G), *trans*-III (H_a to H_g) and *cis*-V (H_1 to H_6) configurations are designated by circles, solid and dashed boxes, respectively.

^{13}C NMR signals (Table 1). Geminal pairs of protons were identified as follows: H_a/H_b ($\delta(^{13}C) = 30.77$); H_c/H_e ($\delta(^{13}C) = 50.59$); H_d/H_f ($\delta(^{13}C) = 52.82$); H_A/H_B ($\delta(^{13}C) = 30.32$); H_C/H_E ($\delta(^{13}C) = 49.22$), H_D/H_F ($\delta(^{13}C) = 53.34$); H_2/H_4 ($\delta(^{13}C) = 49.28$); H_3/H_5 ($\delta(^{13}C) = 52.19$). Since all proton resonances

Table 1. Assignment of the ^1H, ^{13}C and ^{15}N NMR resonances of complexes **1**–**4**.[a]

Complex	Solvent	Config.		$\delta(^1H)$, (^{13}C) and (^{15}N) and assignment								
				NCH_2CH_2N		$NCH_2CH_2CH_2N$		$NCH_2CH_2CH_2N$				NH
1	D_2O/H_2O	*trans*-I	^1H	2.91	2.73	3.16	2.76	1.92	1.69			3.50
	(pH 6.8)		^{13}C	49.22		53.34		30.32				
			^{15}N						11.00			
		trans-III	^1H	3.03	2.48	3.18	2.70	1.90	1.64			3.20
			^{13}C	50.59		52.82		30.77				
			^{15}N									14.22
		cis-V	^1H	2.91	2.56	3.08	2.79		1.74			3.35
			^{13}C	49.28		52.19			27.68			
			^{15}N									11.46
2	D_2O/H_2O	*trans*-I	^1H	2.99	2.74	3.20	2.78	1.93	1.78			3.59
	(pH 7.4)		^{13}C	49.29		53.39		30.34				
			^{15}N									10.84
		trans-III	^1H	3.02	2.55	3.18	2.74	1.88	1.66			3.28
			^{13}C	50.58		52.95		30.70				
			^{15}N									14.01
		cis-V	^1H	2.97	2.63	3.14	2.86		1.76			3.48
			^{13}C	49.27		52.20			27.08			
			^{15}N									11.01
3	D_2O/H_2O	*trans*-I	^1H	2.92	2.76	3.16	2.81	1.96	1.71			3.59
	(pH 7.2)		^{13}C	49.17		53.24		30.17				
			^{15}N									10.24
		trans-III	^1H	3.04	2.48	3.20	2.70	1.90	1.64			3.12
			^{13}C	50.52		52.75		30.71				
			^{15}N									14.25
		cis-V	^1H	2.92	2.61	3.12	2.84		1.76			3.29
			^{13}C	48.77		51.85			26.39			
			^{15}N									11.16
4	D_2O/H_2O	*trans*-I	^1H	2.93	2.76	3.16	2.80	1.95	1.72			3.58
	(pH 6.7)		^{13}C	49.10		53.34		30.20				
			^{15}N						11.39			
		trans-III	^1H	3.03	2.50	3.19	2.73	1.90	1.65			3.15
			^{13}C	50.53		52.76		30.75				
			^{15}N				14.90					
		cis-V	^1H	2.93	2.63	3.13	2.84		1.77			3.39
			^{13}C	48.81		51.81			26.47			
			^{15}N				11.56					

[a] $\delta = 1.93$ ppm for OAc^- in **1**; $\delta = 7.52$ and 7.46 ppm for aromatic protons in **2**.

except three N*H* signals belong to geminal pairs in this complex, the remaining signal, H_1 ($\delta(^{13}C) = 27.68$) corresponds to two equivalent protons.

Solution NMR studies of [Zn(cyclam)(phthalate)]$_n$(-$CH_3OH)_{2n}$ (2), Zn(cyclam)$(ClO_4)_2$ (3) and Zn(cyclam)Cl_2 (4): ^1H, ^{13}C and ^{15}N NMR data for complexes **2**, **3** and **4** in 10% D_2O/90% H_2O (Figure 1b, c and d) are summarised in Table 1.

Time dependence: The time dependence of the 1D ^1H NMR spectrum of [Zn(cyclam)$(H_2O)_2$](OAc)$_2$ (**1**) in water was monitored. In the first spectrum, acquired immediately after dissolving the crystalline complex, only one major form (**III**) was observed (Figure 4). Then resonances for two other forms (**I** and **V**) appeared and increased in intensity with time. Over a period of 10 h, resonances for form **V** increased strongly and form **I** increased slightly as those for form **III** decreased giving ratios of **III**:**V**:**I** of 43:42:15 at equilibrium. The rate constants for these conversions, assuming they occur by parallel first-order processes, are given in the caption for Figure 4.

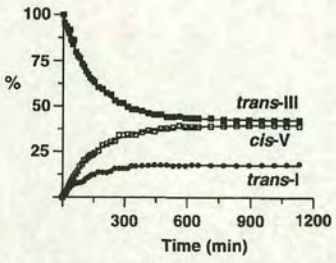

Figure 4. Time-dependent configurational changes for [Zn(cyclam)-$H_2O)_2$](OAc)$_2$ (1) in water as determined by integration of ^1H NMR peaks (see Figure 1a). The solid lines represent best fits to the data and the following rate constants: k_1, 2.54×10^{-3} min^{-1}; k_{-1}, 2.70×10^{-3} min^{-1} for *cis*-V and k_2, 1.33×10^{-3} min^{-1}; k_{-2}, 3.24×10^{-3} min^{-1} for *trans*-I.

pH dependence: The NMR spectra of [Zn(cyclam)(-$H_2O)_2$](OAc)$_2$ (**1**) and Zn(cyclam)$(ClO_4)_2$ (**3**) were highly pH dependent. For [Zn(cyclam)$(H_2O)_2$](OAc)$_2$, as the pH was increased, peaks for **V** decreased and for form **I** increased, whereas those for form **III** were almost constant (Figure 5a). For Zn(cyclam)$(ClO_4)_2$, peaks for form **III** decreased and for

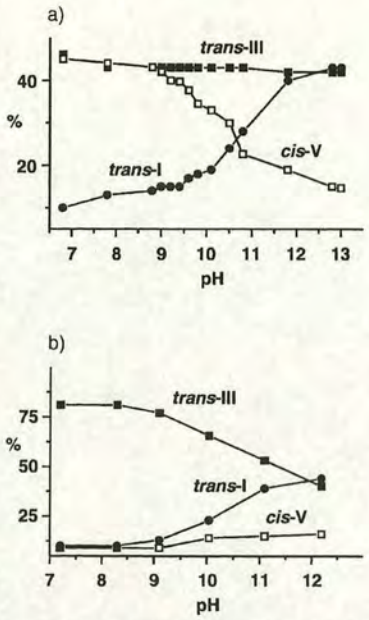

Figure 5. pH-dependent configurational changes of a) the acetate complex **1**, and b) the perchlorate complex **3** in water. *trans*-I, *trans*-III and *cis*-V configurations are designated by filled circles, filled squares and open squares, respectively.

form **I** increased as the pH was raised, whereas the amount of form **V** present was almost constant (Figure 5b).

Temperature dependence: The temperature dependence of the NH ^{1}H NMR resonances of all four complexes **1**–**4** was studied (Table 2). Over the range 278 to 323 K, the NH resonances of all four complexes exhibited temperature dependences of -1.9 to -4.4 ppbK^{-1}, except for form **V** of complexes **3** and **4** which underwent even smaller changes in shift of -0.5 and -0.8 ppbK^{-1}, respectively.

Table 2. Temperature dependence of the NH ^{1}H NMR chemical shifts for various configurations of Zn^{II} cyclam complexes **1**–**4**.

Complex	$\Delta\delta$/ppb K^{-1}		
	trans-I	*trans*-III	*cis*-V
1	−3.2	−1.9	−3.3
2	−3.0	−2.1	−3.4
3	−2.8	−2.2	−0.5
4	−4.4	−2.6	−0.8

Effect of acetate on the configurational distribution of Zn(cyclam)Cl$_2$: The four Zn cyclam complexes can be grouped according to the distribution of three different configurations present in aqueous solution at equilibrium (Table 3). Form **V** is predominant for [Zn(cyclam)-(H$_2$O)$_2$](OAc)$_2$ (**1**) and [Zn(cyclam)(phthalate)]$_n$(CH$_3$OH)$_{2n}$ (**2**). In contrast, form **III** is predominant and form **V** is minor for Zn(cyclam)(ClO$_4$)$_2$ (**3**) and Zn(cyclam)Cl$_2$ (**4**). These results show that the anions affect the distribution of three configurations of Zn–cyclam complexes and that carboxylates increase the amount of form **V** present.

Table 3. Distribution of configurations of complexes **1**–**4** (40 mM) in 10% D$_2$O/90% H$_2$O at equilibrium.

Complex	Configuration [%]		
	trans-I	*trans*-III	*cis*-V
1	11.9	45.3	42.8
2	22.7	31.9	45.4
3	8.2	83.2	8.6
4	11.2	79.6	9.2

The ^{1}H NMR spectrum of Zn(cyclam)Cl$_2$ in aqueous solution was then acquired in the presence of increasing amounts of NaOAc at molar ratios of **4**:NaOAc of 1:0.5 to 1:9 at equilibrium. The ^{1}H NMR spectra showed that form **III** decreases and form **V** increases, whereas the amount of form **I** present was almost constant on addition of NaOAc (Figure 6).

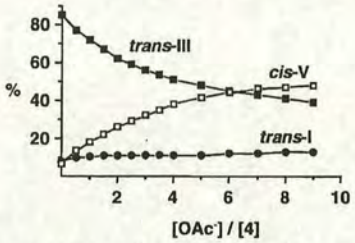

Figure 6. Effect of acetate on the configuration of complex **4** in water as determined by integration of the ^{1}H NMR resonances. *trans*-I, *trans*-III and *cis*-V configurations are designated by filled circles, filled squares and open squares, respectively.

X-ray crystallography: Complexes **1** and **2** were characterised by X-ray crystallography. The crystal structure of complex **1** consists of [Zn(cyclam)(H$_2$O)$_2$]$^{2+}$ ions, and uncoordinated OAc$^-$ ions, which are linked by a network of hydrogen bonds. The Zn^{II} ion sits at a centre of symmetry and is surrounded octahedrally by four nitrogen atoms of the macrocyclic ligand in a plane with distances of 2.08 and 2.12 Å, and by two water molecules occupying the axial positions with Zn–O distances of 2.27 Å (Figure 7). The overall configuration of the cation is

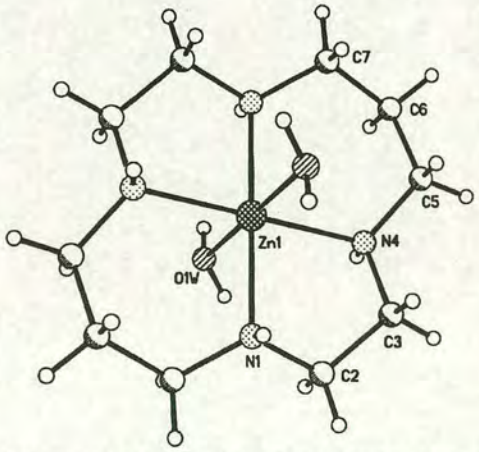

Figure 7. X-ray crystal structure of the cation of complex **1** together with the atom numbering scheme. Selected bond lengths [Å] and angles [°]: Zn1–N1 2.1198(15), Zn1–N4 2.0809(15), Zn1–O1W 2.2719(14); N1-Zn1-N1#1 180.00, N4-Zn1-N1 84.94(6), N4-Zn1-N1#1 95.06(6); #1: $-x, -y, -z$.

trans-III, with two adjacent N–H hydrogen atoms directed toward one side of the cyclam plane and the other two directed toward the opposite side of the plane. *trans*-III is the most stable configuration for cyclam complexes. The two six-membered chelate rings adopt chair conformations and the two five-membered rings are in *gauche* conformations, as found in a number of Zn^{II}–cyclam complexes.[10, 11]

The crystal packing and hydrogen-bonding scheme for complex **1** are shown in Figure 8. Eight intermolecular interactions link a complex cation to eight neighbouring complex cations through six acetate anions to form a rich three-dimensional network of hydrogen bonds. There are two types of hydrogen bonds: O–H···O with H···O distances ranging from 1.84 to 1.95 Å and O–H···O angles ranging from 169 to 176°, and N–H···O with H···O distances ranging from 1.99 to 2.24 Å and N–H···O angles ranging from 158 to 164°. Both carboxylate oxygen atoms of acetate act as acceptors, with one of them participating in three intermolecular hydrogen bonds. All four H atoms of the secondary amine groups of each complex cation and all four H atoms of the two water molecules coordinated to the Zn^{II} centre act as hydrogen-bond donors. The details of hydrogen bonds are listed in Table 4.

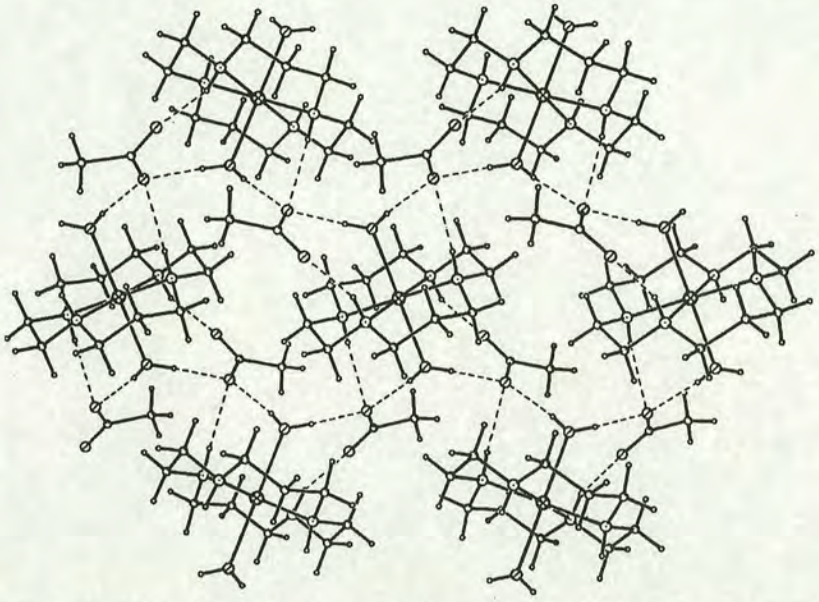

Figure 8. Crystal packing of complex **1**. Hydrogen bonds involving axial H_2O molecules, acetate anions and cyclam NH groups are shown by dotted lines.

The crystal structure of complex **2** consists of infinite chains of [Zn(cyclam)(phthalate)] units linked to methanol molecules from the solvent by hydrogen bonds (Figure 9). The unique phthalate ligand is bridged between two Zn^{II} ions occupying crystallographic inversion centres, Zn1 and Zn2. Each Zn^{II} ion has octahedral geometry with four nitrogen atoms of the macrocycle bound in the equatorial plane, and axially bound oxygen atoms from the phthalate anion.

The carboxylate group of the phthalate anion at C9 is bound to Zn1 through O2 with a distance of 2.22 Å. The second oxygen atom in the group, O1 acts as a hydrogen-bond acceptor to both the secondary amine hydrogens, H6 and H21 on neighbouring cyclam rings with donor–acceptor distances of 2.87 Å for N6–O1 and 2.88 Å for N21–O1. The phthalate carboxylate group at C14, is bound to Zn2 through O3 with a distance of 2.19 Å. O4 of the same carboxylate group is hydrogen-bonded to two methanol solvent molecules, O1M and O2M, with hydrogen-bond donor–acceptor distances of 2.77 and 2.72 Å, respectively. O2M also acts as a weak hydrogen-bond acceptor, hydrogen bonding to the secondary amine N3 with a donor–acceptor distance of 2.98 Å. The details of the hydrogen bonds are given in Table 4.

Discussion

The three 2D [^{1}H, ^{15}N] HSQC NMR cross-peaks from separate spin systems of the acetate complex **1** revealed that there are three configurations (**I**, **III** and **V**) present in aqueous solution. The signals between $\delta = 1.6$ and 2.0 ppm can readily be assigned by their chemical shifts to the central methylene group in the six-membered rings. Hence in the first spin system (form **III**), H_a and H_b are assigned to $NCH_2CH_2CH_2N$ in the six-membered rings. 2D [^{1}H, ^{1}H] COSY data showed that H_d and H_f correlate to H_a and H_b, and therefore H_d and H_f are assignable to $NCH_2CH_2CH_2N$ methylene groups in the six-membered rings. The remaining two signals H_e and H_e for form **III**, are therefore assignable to NCH_2CH_2N methylene groups in the five-membered rings. The NH resonance H_g can be clearly distinguished in the 2D

Table 4. Hydrogen bond lengths [Å] and angles [°] for complexes **1** and **2**.

Complex	D–H···A	d(H···A)	∢DHA	d(D···A)
1	O1W–H1W···O1A[a]	1.95(3)	169(6)	2.736(2)
	O1W–H2W···O1A[b]	1.85(3)	176(3)	2.727(2)
	N1–H1···O1A[c]	2.24	164	3.135(2)
	N4–H4···O2A[d]	1.99	158	2.869(2)
2	N3–H3···O2M[e]	2.08	162	2.976(4)
	N6–H6···O1	2.01	153	2.870(3)
	N17–H17···O4	2.31	147	3.132(4)
	N21–H21···O1	1.96	169	2.882(3)
	O1M–H1M···O4	1.94(7)	169(7)	2.770(5)
	O2M–H2M···O4	1.89(4)	174(3)	2.715(4)

[a] O1A $[-x+1, -y, -z]$. [b] O1A $[-x+1, y-1/2, -z+1/2]$. [c] O1A $[x-1, y, z]$. [d] O2A $[-x+1, y-1/2, -z+1/2]$. [e] O2M $[-x, 1-y, 1-z]$.

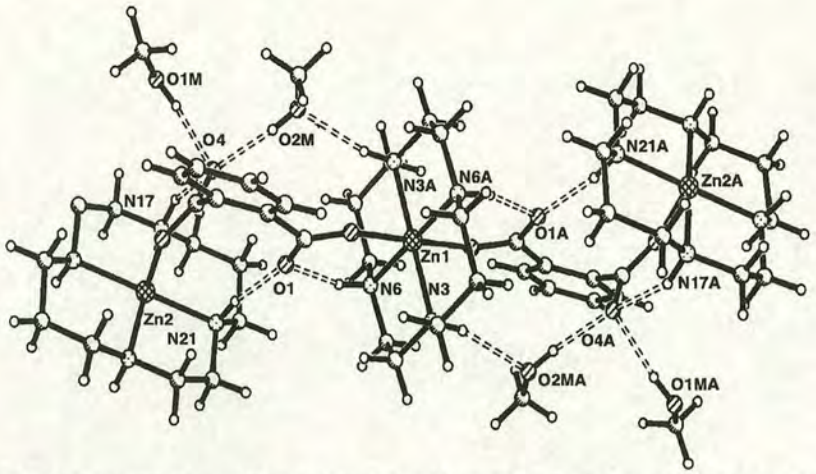

Figure 9. X-ray crystal structure of complex **2** together with the atom numbering scheme. The phthalate groups form bridges between Zn cyclam units. Selected bond lengths [Å] and angles [°]: Zn1–N3 2.097(2), Zn1–N6 2.100(2), Zn2–N21 2.100(2), Zn2–N17 2.108(3), Zn1–O2 2.220(2), Zn2–O3 2.190(2); N3-Zn1-N3#1 180.0, N3-Zn1-N6#1 95.75(9), N3-Zn1-N6 84.25(9); #1: $-x, -y+1, -z+1$.

[^{1}H, ^{15}N] HSQC NMR spectrum, whereas it overlaps with H_f in the 1D ^{1}H NMR spectrum. For the second spin-system (form **V**), we similarly conclude that H_1 is from $NCH_2CH_2CH_2N$, H_3 and H_5 are from the $NCH_2CH_2CH_2N$ methylene groups in the six-membered rings, and H_2 and H_4 are from NCH_2CH_2N in the five-membered rings. For the third spin-system (form **I**), seven weak signals were observed including one broad NH peak, and H_A and H_B can be assigned to $NCH_2CH_2CH_2N$ in the six-membered rings.

Cyclam complexes can adopt five different configurations depending on the spatial alignment of the NH protons (Figure 10). From these, it can be seen that only the *trans*-I and *trans*-III configurations can produce six -CH_2- proton signals, including two for the central methylene group of the six-membered rings. These resonances for form **III** of complex **1** can be assigned to the *trans*-III configuration since complex **1** adopts the most stable configuration *trans*-III in crystals and it is reasonable to assume that this configuration is predominant during the initial stages after dissolution in water. Therefore, the resonances for form **I** are assigned to the *trans*-I configuration.

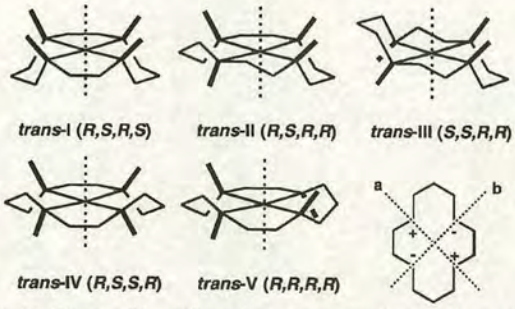

Figure 10. Five possible configurations of metal cyclam complexes, showing different alignments of the NH protons and chirality at the N atoms. The folding of the *trans*-V configuration along axes a or b to give the *cis*-V configuration is shown in the bottom right (+ indicates NH proton above the cyclam plane, – below).

Configurational analysis also indicates that only the *trans*-IV and *trans*-V configurations have five non-equivalent -CH_2- protons and can give rise to five -CH_2- proton signals including one for the central methylene group of the six-membered rings. However, both the *trans*-IV and *trans*-V configurations are usually considered to be unstable because they contain two six-membered rings of high energy in the twist-boat conformation. In contrast, the *cis*-V configuration is strain-free and the *trans*-V configuration can easily fold along diagonal a or b (Figure 10) to form the more common *cis*-V configuration with the two six-membered rings in the chair conformation. Rapid exchange on the NMR time scale between the two enantiomeric folded *cis*-V configurations could give rise to NMR features which appear to be assignable to the *trans*-V configuration. Therefore, we propose that form **V** corresponds to a *cis*-V configuration.

Conversion of the *trans*-III configuration of [Zn(cyclam)-$(H_2O)_2$]$(OAc)_2$ to *cis*-V and *trans*-I configurations in aqueous solution requires the successive inversion of two amine nitrogen atoms via an intermediate *trans*-II configuration (see Figure 10). However, the *trans*-II configuration was not detected. It therefore appears that the formation of the *trans*-II configuration is a slow step that determines the rate of isomerization, and that the *trans*-II configuration rapidly converts to the other configurations.

In aqueous solution, the distribution of the three configurations (Scheme 1) of these Zn^{II}–cyclam complexes is strongly dependent on the counterion (Table 3). Aqueous solutions of the perchlorate and chloride complexes **3** and **4**, respectively, consist mainly of the *trans*-III configuration, whereas for the carboxylato complexes **1** and **2**, the *cis*-V form is predominant. Titration of the chloride complex **4** with acetate also led to an increase in the proportion of the *cis*-V configuration at the expense of *trans*-III (Figure 6). It appears that the carboxylate group of acetate can act as a bidentate ligand for Zn^{II} and also form hydrogen bonds to the two amine NH protons on the opposite face of the macrocycle, thus stabilising the *cis*-V configuration in aqueous solution. We have recently found that the acetate salt of a Zn^{II}–bicyclam,

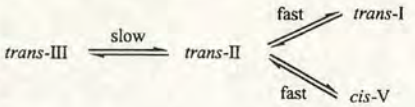

Scheme 1.

$[Zn^{II}(xylyl\text{-}bicyclam)(OAc)_2](OAc)_2$, crystallises in such a *cis*-V configuration.[12] In aqueous solution, some of the latter complex converts to *trans*-I and *trans*-III configurations.

On increasing the pH of aqueous solutions of complex **1**, the proportion of the *cis*-V form decreased and *trans*-I form increased, whereas the proportion of the *trans*-III form remained almost constant. For complex **3**, the proportion of the *trans*-III form decreased, and of *trans*-I increased, whereas *cis*-V was almost constant (Figure 5). Thus the *trans*-I configuration is more favoured at high pH for both complexes. Normally, at alkaline pH, Zn^{II} macrocycles can form hydroxo complexes. These have a high affinity for atmospheric CO_2 giving rise to a hydrogen carbonate complex, which can react further to form a trinuclear complex.[13] We have recently isolated such a trinuclear carbonate complex of Cd^{II} cyclam.[14] In such carbonate complexes, all NH protons are situated on the same side of the ring as CO_3^{2-} with the macrocycle in the *trans*-I configuration and hydrogen bonds can form readily between CO_3^{2-} and the NH protons of cyclam. However, axial binding of carboxylates such as acetate, which has increased steric bulk compared to carbonate, cannot be readily accommodated when the four NH protons are also oriented towards this side of the ring, and hence the *cis*-V configuration is favoured.

The temperature dependences of the NH proton resonances of all the Zn^{II} cyclam complexes studied here are small ($\Delta\delta/\Delta T$ values more positive than -4.5 ppb K^{-1}, Table 2). It seems likely therefore that the NH protons in all the observed configurations are involved in strong hydrogen bonds. The temperature coefficients of amide NH ^1H NMR resonances have been widely used for studying intramolecular hydrogen bonding in peptides,[15–17] and for aqueous solutions, temperature coefficients of amide protons which are more positive than -4.5[16] or -5 ppb K^{-1}[17] have usually been interpreted as being indicative of intramolecular hydrogen bonding. However we have been unable to find other reports of the temperature dependences of amine NH resonances.

Comparison with the Zn–O bond lengths for bound water in the other Zn^{II} complexes in the Cambridge Structural Database, shows that the Zn–O distance (2.27 Å) in complex **1** is longer than normal (ca. 2.10 Å). The elongation of the Zn–O bond may be due to competitive hydrogen bonding of the coordinated water by lattice acetate ions. The Zn–N bond lengths of 2.08 Å and 2.12 Å are comparable with those in reported Zn–cyclam complexes.[10, 11] The average value of the Zn–N bond length (2.10 Å) is very close to the "ideal" metal–nitrogen bond length (2.07 Å)[18] in *trans*-cyclam complexes, and close to the Zn–N bond lengths in complexes containing 1,2-ethanediamine and 1,3-propanediamine.[19]

The Zn–O distance of 2.22 Å for the phthalate complex **2** is slightly longer than that observed for Zn^{II}–carbonate complexes,[11] and intermediate in value between the Zn–O bond lengths observed[12] for the chelated acetate in $[Zn^{II}(xylylbicyclam)(OAc)_2](OAc)_2$ (2.09 and 2.41 Å). The two cyclam planes associated with the bridging phthalate ligand are not parallel, probably due to the steric constraints between the neighboring cyclam rings. The structural features of the Zn^{II} cyclam in **2** are similar to those of complex **1**. It contains the most stable configuration, *trans*-III, and has the same average value of Zn–N bond lengths as complex **1**. Bond lengths and angles within the chelate rings also correspond closely to those of complex **1**.

The secondary amine NH groups of the cyclam rings and hydroxyl groups of water and methanol act as proton donors for hydrogen bonding in crystals of complexes **1** and **2**. The hydrogen-bond acceptors are the carbonyl groups of the carboxylates and hydroxyl group of methanol. The OH group of methanol displays dual hydrogen bond functionality and therefore gives rise to hydrogen-bond cooperativity and forms multicentre hydrogen bonds. Through hydrogen bonding, complexes **1** and **2** form infinite network and infinite chain structures, respectively. The hydrogen bonds O1W–H2W···O1A (H···O 1.85 Å) in complex **1** and O2M–H2M···O4 (H···O 1.89 Å) in complex **2** are strong with near linear geometry (176 and 168°, respectively).

After coordination to Zn^{II}, monocyclam adopts the most stable configuration *trans*-III in the solid state. In Zn–xylyl-bicyclam complexes, in which the two cyclam rings are connected through a 1,4-phenylenebis(methylene) linker, the aromatic ring is close to the two flat monocyclam rings if they are in *trans* configurations, which can result in the folding of each monocyclam and adoption of the *cis*-V configuration. Acetate can further stabilize the *cis*-V configuration by bidentate coordination and formation of hydrogen bonds.[12] Therefore, the Zn–bicyclam complex with acetate, in contrast to the Zn–cyclam complex with acetate, adopts the *cis*-V configuration in the solid state. Such a configurational change may contribute to the increased anti-HIV activity of Zn^{II} bicyclam complexes and the aromatic linker can play an important role in the anti-HIV activity.

Conclusion

The X-ray structures indicate that, in the solid state, the acetate and phthalate Zn^{II} cyclam complexes studied here adopt the most stable configuration *trans*-III, in which the six-membered rings are in the chair conformation and five-membered rings in the gauche conformation. Three configurations, *trans*-I, *trans*-III, and *cis*-V, of each of the acetate, phthalate, perchlorate and chloride complexes were detected in aqueous solution by 1D and 2D ^1H, ^{13}C and ^{15}N NMR spectroscopy. ^1H NMR spectra were fully assigned by 2D NMR methods. Both time dependent experiments and titration of the chloride Zn^{II} cyclam complex indicated that carboxylates induce a large increase in the proportion of the *cis*-V configuration and a slight increase in *trans*-I at the expense of *trans*-III, the configuration observed in the solid state. This suggests that carboxylates can exert a strong influence over the selection of Zn^{II}–cyclam configurations which exist in solution. Extensive hydrogen bonding between the amine NH groups of the Zn^{II} macromacrocycle and oxygen atoms of the carboxylate and solvent molecules is present in both aqueous solution and in the solid state. These hydrogen bonds could also play an important role in the anti-HIV activity of cyclam complexes, which is known to correlate with affinity for the CXCR4 co-receptor. This in turn is

dependent on the presence of carboxylate side chains of specific aspartate residues in the co-receptor protein.[8, 9]

Experimental Section

$[Zn(cyclam)(H_2O)_2](OAc)_2$ (1): Cyclam (100.2 mg, 0.5 mmol) and $Zn(OAc)_2 \cdot 2H_2O$ (109.6 mg, 0.5 mmol) were heated under reflux in methanol (15 mL) for 2 h. The solution was reduced in volume to about 4 mL by rotary evaporation, and crystals were obtained by diffusion of Et_2O into the solution at ambient temperature. The crystals were filtered off and dried. Yield 133.3 mg (63.5%). Elemental analysis calcd (%) for $C_{14}H_{34}N_4ZnO_6$: C 40.05, H 8.16, N 13.35; found: C 40.21, H 8.30, N 13.51; selected IR (KBr): $\tilde{\nu}$ = 3225 s, (NH), 3213 s (NH), 3156 s, (NH), 2928 m (CH), 2862 m (CH), 1577 s (CO) cm^{-1}.

$[Zn(cyclam)(phthalate)]_n(CH_3OH)_{2n}$ (2): Cyclam (150.3 mg, 0.75 mmol), ZnO (60.9 mg, 0.75 mmol) and phthalic acid (124.4 mg, 0.75 mmol) were stirred in water (15 mL) for 6 h. The solvent was removed by rotary evaporation and the residue was dissolved in methanol (ca. 4 mL). Crystals were grown by diffusion of Et_2O into the solution at ambient temperature. The crystals were filtered off and dried. Yield 258.2 mg (69.7%). Elemental analysis calcd (%) for $C_{20}H_{36}N_4ZnO_6$: C 48.64, H 7.35, N 11.34; found: C 49.03, H 7.50, N 11.52; selected IR (KBr): $\tilde{\nu}$ = 3418 m, br (OH), 3254 s (NH), 3211 s, (NH), 2906 s (CH), 2838 s (CH), 1594 s (CO), 1577 s (CO), 1377 s (CO), 1364 s (CO) cm^{-1}.

$Zn(cyclam)(ClO_4)_2$ (3): Cyclam (100.2 mg, 0.5 mmol) and $Zn(ClO_4)_2 \cdot 6H_2O$ (185.9 mg, 0.5 mmol) were heated under reflux in methanol (15 mL) for 2 h. The solution was kept in a refrigerator overnight and the precipitate was then filtered off and dried. Yield 162.2 mg (69.8%). Elemental analysis calcd (%) for $C_{10}H_{24}N_4ZnCl_2O_8$: C 25.85, H 5.21, N 12.06; found: C 25.60, H 5.47, N 12.20; selected IR (KBr): $\tilde{\nu}$ = 3271 s, (NH), 3214 w (NH), 2935 m (CH), 2876 m (CH) cm^{-1}.

$Zn(cyclam)Cl_2$ (4): Cyclam (240 mg, 1.2 mmol) and $ZnCl_2$ (163.3 mg, 1.2 mmol) were heated under reflux in methanol (15 mL) for 2 h. The solution was then kept in a refrigerator overnight and the crystals which formed were filtered off and dried. The solution was reduced to about 5 mL by rotary evaporation. After storage in a refrigerator for two days, further crystals were obtained. Yield 257.4 mg (63.7%). Elemental analysis calcd (%) for $C_{10}H_{24}N_4ZnCl_2$: C 35.68, H 7.19, N 16.64; found: C 35.64, H 6.56, N 16.16; selected IR (KBr): $\tilde{\nu}$ = 3223 s, (NH), 3161 m (NH), 2927 s (CH), 2862 s (CH), 1647 w (NH) cm^{-1}.

Spectroscopic measurements: Infrared spectra were recorded as KBr pellets in the range 4000–400 cm^{-1} on a Perkin-Elmer Paragon 1000 Fourier-transform IR spectrometer. ^1H NMR spectra were acquired on either Bruker DMX 500 (^1H = 500 MHz) or Varian ^{Unity}INOVA (^1H = 600 MHz) NMR spectrometers using TBI [^1H, ^{13}C, X] or triple resonance [^1H, ^{13}C, ^{15}N] probeheads, respectively, and equipped with z-field gradients. All data were acquired at a probe temperature of 298 K. ^1H chemical shifts were internally referenced to the methyl singlet of TSP ([D_6]-3-trimethylsilylpropionate) at 0 ppm; ^{13}C chemical shifts were referenced externally also using TSP. All NMR experiments on complexes **1**–**4** were performed in 10% D_2O/90% H_2O at concentrations of 120 mM, at pH values of 6.8, 7.4, 7.2, and 6.7, respectively, unless otherwise stated.

^1H NMR data were acquired over a ^1H frequency width of 6 kHz into 32 *k* data points (acquisition time = 2.73 s). The water resonance was suppressed by presaturation or by the WATERGATE pulsed-field-gradient sequence.[20]

2D [^1H, ^{13}C] HSQC NMR data were typically acquired over a ^1H frequency width of 5 kHz and a ^{13}C frequency width of 5 kHz (40 ppm) centred at 43 ppm. Data were acquired with 64 transients into 2 *k* complex data points (acquisition time 205 ms) for each of 128 t_1 increments (acquisition time 12.7 ms).

2D [^1H, ^{15}N] HSQC NMR data were acquired over a ^1H frequency width of 3.5 kHz and a ^{15}N frequency width of 2.5 kHz (50 ppm) centred at 10 ppm. Data were acquired with 240 transients into 2 *k* complex data points for each of 128 t_1 increments.

All NMR data were processed using Xwin-nmr (version 2.0, Bruker UK Ltd.).

Time dependence: $[Zn(cyclam)(H_2O)_2](OAc)_2$ (40 mM, pH 6.8) was dissolved in 10% D_2O/90% H_2O and ^1H NMR spectra were recorded. Rate constants were obtained by fitting the appropriate rate equations using the program Scientist (MicroMath, Inc, Version 2.0). The configurational changes were assumed to occur by parallel first-order reactions.

pH dependence: ^1H NMR spectroscopy was employed to study the effects of pH on complexes **1** and **3** over the range 6.8 to 12.8 and 7.2 to 12.2, respectively. Values of pH were measured with a Corning 145 pH-meter equipped with a microcombination electrode (Aldrich) calibrated with Aldrich standard buffers (pH 4, 7, and 10). pH values were adjusted with 0.1M NaOH in the NMR tube. No correction has been applied for deuterium isotope effects.

Temperature dependence: Spectra of each complex (40 mM) were acquired at 5 K intervals over the temperature range of 278 to 323 K in 10% D_2O/90% H_2O. Temperature gradients are expressed in units of ppb K^{-1} with a negative sign indicating a shift to lower ppm upon warming.

Effect of acetate on the configuration of complex 4: Complex **4** (27 mM) was dissolved in 10% D_2O/90% H_2O in the presence of TSP. Aliquots of a stock aqueous solution of CH_3COONa (1M) were made to this solution in nine separate NMR tubes to give **4**: acetate molar ratios of 1:0.5 to 1:9. The pH value of each solution was readjusted to pH 7.4 (0.1M NaOH, HCl). ^1H NMR spectra were acquired on these samples after standing overnight as well as on **4** itself in 10% D_2O/90% H_2O.

X-ray crystallography: Diffraction data were collected on a Stoë Stadi-4 diffractometer with $Cu_{K\alpha}$ radiation. Crystal data and details of data collection for complexes **1** and **2** are given in Table 5. An absorption correction was performed by Gaussian integration following refinement of the crystal face-indices and dimensions against a set of Ψ scans (Stoë X-shape[21]). Data were collected to $2\theta_{max} = 140°$ and the structures solved by direct methods (Shelx-97)[22] and refined by full-matrix least-squares against F^2. Methyl groups were treated as rotating rigid groups. Hydrogen atoms attached to coordinated water in complex **1** were located in a difference map and refined freely; other hydrogen atoms were placed in calculated positions and allowed to ride on their parent atoms. Hydroxyl groups in complex **2** were refined freely, and hydrogen atoms were placed in calculated positions and allowed to ride on their parent atoms. All non-hydrogen atoms were refined with anisotropic displacement parameters, to give convergence *R*1 and w*R*2 values as indicated in Table 5. The final difference map extremes were max 0.867, min −1.121 eÅ^{-3}. Geometry calculations were performed by using PLATON.[23]

Table 5. Crystal data and data collection for complexes **1** and **2**.

Complex	**1**	**2**
formula	$C_{14}H_{34}ZnN_4O_6$	$C_{20}H_{36}ZnN_4O_6$
FW	419.82	493.90
crystal system	monoclinic	triclinic
space group	$P2_1/c$	$P\bar{1}$
V [Å^3]	963.68 (19)	1182.6(3)
Z	2	2
a [Å]	9.1377(10)	8.6255(11)
b [Å]	12.1643(16)	10.2268(17)
c [Å]	8.7265(8)	15.110(2)
α [°]	90	94.596(9)
β [°]	96.537(10)	100.913(8)
γ [°]	90	113.450(7)
T [K]	220(2)	150(2)
ρ_{calcd} [g cm^{-3}]	1.447	1.387
μ [mm^{-1}]	2.093	1.797
unique reflections	1720	4188
observed reflections	1633	3837
R1 (obs reflections)	0.0336	0.0508
w*R*2 (all reflections)	0.0933	0.1408

CCDC-202455 (**1**) and CCDC-202456 (**2**) contain the supplementary crystallographic data for this paper. These data can be obtained free of charge via www.ccdc.cam.ac.uk/conts/retrieving.html (or from the Cam-

bridge Crystallographic Data Centre, 12 Union Road, Cambridge CB2 1EZ, UK; fax: (+44) 1223-336-033; or email: deposit@ccdc.cam.ac.uk).

Acknowledgement

We thank the Committee of Vice-Chancellors and Principals of the Universities of the United Kingdom for an Overseas Research Student Award (for X.L.), the DFG for a fellowship (for M.W.), EPSRC, Wellcome Trust (Edinburgh Protein Interaction Centre), Royal Society, Wolfson Foundation, and EC COST D8/D20 for their support for this work.

[1] E. De Clercq, N. Yamamoto, R. Pauwels, J. Balzarini, M. Witvrouw, K. De Vreese, Z. Debyser, B. Rosenwirth, P. Peichl, R. Datema, D. Thornton, R. Skerlj, F. Gaul, S. Padmanabhan, G. Bridger, G. Henson, M. Abrams, *Antimicrob. Agents Chemother.* **1994**, *38*, 668.
[2] E. De Clercq, *Metal-Based Drugs* **1997**, *4*, 173.
[3] E. De Clercq, D. Schols, *Antiviral Chem. Chemother.* **2001**, *12 (Suppl. 1)*, 19.
[4] Y. Inouye, T. Kanamori, T. Yoshida, X. Bu, M. Shionoya, T. Koike, E. Kimura, *Antiviral Chem. Chemother.* **1995**, *6*, 337.
[5] G. J. Bridger, R. T. Skerlj, *Adv. Antiviral Drug Res.* **1999**, *3*, 161.
[6] G. J. Bridger, R. T. Skerlj, D. Thornton, S. Padmanabhan, S. A. Martellucci, G. W. Henson, M. J. Abrams, N. Yamamoto, K. De Vreese, R. Pauwels, E. De Clercq, *Biol. Pharm. Bull.* **1994**, *17*, 243.
[7] M. Kodama, E. Kimura, *J. Chem. Soc. Dalton Trans.* **1978**, 1081.
[8] a) S. Hatse, K. Princen, L.-O. Gerlach, G. J. Bridger, G. Henson, E. De Clercq, T. W. Schwartz, D. Schols, *Mol. Pharmacol.* **2001**, *60*, 164; b) L. O. Gerlach, R. T. Skerlj, G. J. Bridger, T. W. Schwartz, *J. Biol. Chem.* **2001**, *276*, 14153.
[9] L. O. Gerlach, J. S. Jakobsen, K. P. Jensen, M. R. Rosenkilde, R. T. Skerlj, U. Ryde, G. J. Bridger, T. W. Schwartz, *Biochemistry* **2003**, *42*, 710.
[10] a) T. Ito, M. Kato, H. Ito, *Bull. Chem. Soc. Jpn.* **1984**, *57*, 2634; b) N. W. Alcock, A. Berry, P. Moore, *Acta Crystallogr. C* **1992**, *48*, 16; c) T. A. Tyson, K. O. Hodgson, *Acta Crystallogr. C* **1990**, *46*, 1638.
[11] M. Kato, T. Ito, *Inorg. Chem.* **1985**, *24*, 509.
[12] X. Liang, J. A. Parkinson, M. Weishäupl, R. O. Gould, S. J. Paisey, H. Park, T. M. Hunter, C. A. Blindauer, S. Parsons, P. J. Sadler, *J. Am. Chem. Soc.* **2002**, *124*, 9105.
[13] C. Bazzicalupi, A. Bencini, A. Bianchi, V. Fusi, P. Paoletti, B. Valtancoli, *J. Chem. Soc. Chem. Commun.* **1995**, 1555.
[14] X. Liang, J. A. Parkinson, S. Parsons, M. Weishäupl, P. J. Sadler, *Inorg. Chem.* **2002**, *41*, 4539.
[15] a) J. J. Skalicky, M. E. Selsted, A. Pardi, *Proteins* **1994**, *20*, 52; b) N. H. Andersen, C. Chen, T. M. Marschner, S. R. Krystek Jr., D. A. Bassolino, *Biochemistry* **1992**, *31*, 1280; c) I. Ségalas, Y. Prigent, D. Davoust, B. Bodo, S. Rebuffat, *Biopolymers*, **1999**, *50*, 71; d) S. Tauro, E. Coutinho, S. Srivastava, *Magn. Reson. Chem.* **2002**, *40*, 211; e) P. A. Raj, T. Karunakaran, D. K. Sukumaran, *Biopolymers*, **2000**, *53*, 281.
[16] N. J. Baxter, M. P. Williamson, *J. Biomol. NMR* **1997**, *9*, 359.
[17] E. Condamine, S. Rebuffat, Y. Prigent, I. Ségalas, B. Bodo, D. Davoust, *Biopolymers*, **1998**, *46*, 75.
[18] L. Y. Martin, L. J. Dehayes, L. J. Zompa, D. H. Busch, *J. Am. Chem. Soc.* **1974**, *96*, 4046.
[19] a) D. Neill, M. J. Riley, C. H. L. Kennard, *Acta Crystallogr. C* **1997**, *53*, 701; b) C. Muralikrishna, C. Mahadevan, S. Sastry, M. Seshasayee, S. Subramanian, *Acta Crystallogr. C* **1983**, *39*, 1630; c) J. H. Welch, R. D. Bereman, P. Singh, C. Moreland, *Inorg. Chim. Acta* **1989**, *158*, 9.
[20] M. Piotto, V. Saudek, V. Sklenar, *J. Biomol. NMR* **1992**, *2*, 661.
[21] X-Shape, Stoë and Cie, Darmstadt, Germany, **1995**.
[22] G. M. Sheldrick, SHELX-97, Program for Crystal Structure Refinement, University of Göttingen, Göttingen, Germany, **1997**.
[23] A. L. Spek, *Acta Crystallogr. A* **1990**, 46, C34 (PC version by L. Farrugia).

Received: February 6, 2003
Revised: May 5, 2003 [F4808]

Acta Crystallographica Section B
Structural Science
ISSN 0108-7681

Pressure-induced polymorphism in phenol

David R. Allan,[a]* Stewart J. Clark,[b] Alice Dawson,[c] Pamela A. McGregor[a] and Simon Parsons[c]

[a]School of Physics, The University of Edinburgh, Mayfield Road, Edinburgh EH9 3JZ, UK, [b]Department of Physics, Durham University, Science Laboratories, South Road, Durham DH1 3LE, UK, and [c]School of Chemistry, The University of Edinburgh, West Mains Road, Edinburgh EH9 3JJ, UK

Correspondence e-mail: dra@ph.ed.ac.uk

Received 20 March 2002
Accepted 11 October 2002

The high-pressure crystal structure of phenol (C_6H_5OH), including the positions of the H atoms, has been determined using a combination of single-crystal X-ray diffraction techniques and *ab initio* density-functional calculations. It is found that at a pressure of 0.16 GPa, which is just sufficient to cause crystallization of a sample held at a temperature just above its ambient-pressure melting point (313 K), a previously unobserved monoclinic structure with $P2_1$ symmetry is formed. The structure is characterized by the formation of hydrogen-bonded molecular chains, and the molecules within each chain adopt a coplanar arrangement so that they are ordered in an alternating 1-1-1 sequence. Although the crystal structure of the ambient-pressure $P112_1$ phase is also characterized by the formation of molecular chains, the molecules adopt an approximate threefold arrangement. A series of *ab initio* calculations indicates that the rearrangement of the molecules from helical to coplanar results in an energy difference of only 0.162 eV molecule^{-1} (15.6 kJ mole^{-1}) at 0.16 GPa. The calculations also indicate that there is a slight increase in the dipole moment of the molecules, but, as the high-pressure phase has longer hydrogen-bond distances, it is found that, on average, the hydrogen bonds in the ambient-pressure phase are stronger.

1. Introduction

Phenol (C_6H_5OH, monohydroxybenzene) is an economically important chemical reagent and is used in a wide variety of synthetic processes. It is a member of the monoalcohol series and, as its hydroxyl group is slightly acidic (pK_a at 298 K is 9.99 in aqueous solution), it is often referred to as carbolic acid. Below its melting point of 313 K, phenol crystallizes in a monoclinic structure with $P2_1$ symmetry (which is often reported in the non-conventional $P112_1$ setting) (Zavodnik *et al.*, 1987). The crystal structure is characterized by infinite hydrogen-bonded chains of molecules, which are aligned parallel to the crystallographic *b* axis of the unit cell, where the molecules are arranged in approximate threefold helices. This threefold helical arrangement is also observed in phase IV of tertiary-butanol [$(CH_3)_3COH$ (Steininger *et al.*, 1989)]. However, the other preceding members of the monoalcohol series that can crystallize rather than vitrify on cooling, methanol (CH_3OH; Torrie *et al.*, 1989; Boese, 2002), ethanol (CH_3CH_2OH; Jönsson, 1976) and cyclobutanol (C_4H_6OH; McGregor *et al.*, 2003), form structures that, although they are also characterized by infinite hydrogen-bonded chains, have molecular arrangements that are essentially planar. Steric effects dominate the adoption of either a helical or a planar conformation of the molecules along the hydrogen-bonded

Table 1
High-pressure data collection scan sequence for the Bruker APEX CCD diffractometer.

Run	2θ (°)	ω range (°)	φ (°)	Frames
1	−28.00	−8, −40	90.00	106
2	28.00	40, −40	90.00	266
3	−28.00	−140, −215	90.00	250
4	28.00	−140, −172	90.00	106
5	−28.00	−140, −218	270.00	260
6	28.00	−140, −172	270.00	106
7	−28.00	−8, −40	270.00	106
8	28.00	35, −40	270.00	250

chains; therefore, the relatively bulky R—OH tails in tertiary-butanol and phenol promote the formation of helical chains.

Intermolecular interactions, such as steric effects and hydrogen bonding, depend strongly on intermolecular distances; consequently, high pressure provides an excellent probe for the investigation of the structure and dynamics of molecular solids. A systematic study of molecular systems at high pressure is fruitful as competition between the various interactions causes phase transitions, including vitrification, as well as effecting crystal nucleation. Moreover, it is expected that this competition will lead to an alteration in the hierarchy of interaction strengths, and, for example, it has been proposed that with increasing pressure hydrogen bonding diminishes relative to repulsive forces (Angell, 1991; Cook *et al.*, 1992, 1994). In our previous high-pressure crystal structure studies of methanol (Allan *et al.*, 1998) and ethanol (Allan & Clark, 1999) we found that the molecular chains of both the high-pressure and the ambient-pressure phases are essentially flat and each crystalline phase is characterized by the sequence of parallel or antiparallel molecules along the chains. In Etter's graph-set notation (Bernstein *et al.*, 1995) these structures can all be designated as $C(2)$ (or variants thereof, depending on local symmetry conditions). However, this designation conveys little conformational information, and so in this analysis we have adopted an alternative formalism. For methanol, the high-pressure phase has a pair of molecules aligned parallel with one another and a third set antiparallel so that a 2-1-2-1 (two molecules parallel, one molecule antiparallel *etc.*) sequence is formed, while both of the ambient-pressure phases have an alternating 1-1-1 sequence of molecules (*i.e.* individual molecules are aligned antiparallel with one another in an alternating sequence). The ambient-pressure phase of ethanol has pairs of *trans* and *gauche* conformers linked in parallel so that these molecular pairs alternate in a 2-2-2 sequence along the chain. In the high-pressure structure the molecules are aligned in a very simple alternating 1-1-1 sequence, which is reminiscent of both of the ambient-pressure phases of methanol. For all of these phases, the molecules are small enough to be packed in a ribbon-like arrangement along the chains, and the variation of the steric effects with pressure only changes the parallel and antiparallel ordering of the molecules along the chains. Conversely, for phenol the steric factors between the comparatively large C_6H_5 groups are such that a ribbon-like arrangement of the molecules within the chains is no longer possible, and helical hydrogen-bonded chains of molecules are formed in the crystal structure under ambient conditions.

In this article, we report the high-pressure crystal structure of phenol, which has been obtained using single-crystal X-ray diffraction techniques. We find that the high-pressure structure shares the same monoclinic $P2_1$ symmetry as the ambient-pressure phase and is also characterized by the formation of infinite hydrogen-bonded molecular chains. However, the molecules within the chains of the high-pressure phase are coplanar and they adopt an alternating 1-1-1 sequence. Although the high-pressure structure is distinct from that of the ambient-pressure phase, a series of *ab initio* density-functional calculations indicates that the alteration of the arrangement of the molecules within the chains, from helical to ribbon-like, results in a relatively small reduction in the enthalpy (0.162 eV molecule^{-1} or 15.6 kJ mole^{-1}) for the high-pressure structure.

2. Experimental

2.1. Crystallography

The sample was prepared by heating crystalline phenol above its melting temperature of 313 K and then loading it, as a liquid, into a preheated Merrill–Bassett diamond-anvil cell (Merrill & Bassett, 1974) that had been equipped with 600 μm culet diamonds and a tungsten gasket. The sample was pressurized, while maintaining the cell's initial temperature, until the nucleation of several crystallites was observed. The temperature was then increased, so that the polycrystalline sample was partially remelted, and subsequently cycled close to this elevated melting temperature, in order to reduce the number of crystallites [in a manner similar to the method of Vos *et al.* (1992, 1993)]. Finally, on cooling to ambient temperature, at approximately 0.16 GPa, we obtained a single crystal that entirely filled the 200 μm gasket hole.

The diamond-anvil cell was mounted and centred on a Bruker SMART APEX diffractometer (graphite monochromated Mo $K\alpha$ radiation) and a sequence of eight data collection scans was initiated, as detailed in Table 1. The *SMART* program (Bruker, 2001) was used for data collection control, and, with a detector distance of 70 mm, 2θ was set at either +28° or −28° to provide maximum coverage while ensuring that the detector surface did not intercept the primary beam. (No beam stop is used, and with this selection of detector distance and 2θ the primary beam does not impinge on the detector aperture.) The eight scans were conducted as a sequence of frames that each had a range of 0.3° in ω and an exposure time of 30 s. The φ axis was fixed at either 90° or 270°, to ensure that the axis of the diamond-anvil cell was held parallel to the $\omega/2\theta$ plane so that absorption from the pressure-cell components was minimized and the maximum possible access of reciprocal space was achieved. As the APEX diffractometer has a three-circle goniometer the χ axis is permanently fixed at a value of 54.74°. The overall data collection time was 15 h. The sample reflections were identified by hand with the aid of the *SMART* code, and an orien-

Table 2
Experimental details.

Crystal data	
Chemical formula	C_6H_5OH
Chemical formula weight	94.11
Cell setting, space group	Monoclinic, $P2_1$
a, b, c (Å)	11.610 (4), 5.4416 (11), 12.217 (5)
β (°)	101.47 (3)
V (Å^3)	756.4 (4)
Z	6
D_x (Mg m^{-3})	1.240
Radiation type	Mo $K\alpha$
No. of reflections for cell parameters	331
θ range (°)	2.5–25.5
μ (mm^{-1})	0.083
Crystal form, colour	Cylindrical, colourless
Radius (mm)	0.1
Temperature (K)	293 (2)
Data collection	
Diffractometer	CCD area detector
Data collection method	ω scans
Absorption correction	*SADABS*
T_{min}	0.213
T_{max}	1.000
No. of measured, independent and observed parameters	1129, 455, 269
Criterion for observed reflections	$I > 2\sigma(I)$
R_{int}	0.0567
θ_{max} (°)	24.88
Range of h, k, l	$-12 \rightarrow h \rightarrow 12$ $-6 \rightarrow k \rightarrow 6$ $-7 \rightarrow l \rightarrow 7$
Refinement	
Refinement on	F^2
$R[F^2 > 2\sigma(F^2)]$, $wR(F^2)$, S	0.0863, 0.2777, 0.975
No. of reflections and parameters used in refinement	455, 29
H-atom treatment	Riding
Weighting scheme	$w = 1/[\sigma^2(F_o^2) + (0.1876P)^2]$ where $P = (F_o^2 + 2F_c^2)/3$
$(\Delta/\sigma)_{max}$	0.002
$\Delta\rho_{max}$, $\Delta\rho_{min}$ (e Å^{-3})	0.321, −0.199
No. of restraints	14

Computer programs used: *SMART* (Bruker, 2001), *SHELXTL* (Sheldrick, 1997), *SHELXS97* (Sheldrick, 1990), *SHELXL97* (Sheldrick, 1997).

tation matrix was determined using the *GEMINI* program (Sparks, 1999). Data integration and global-cell refinement were performed with the program *SAINT* (Bruker, 2001). The program *SHADE* (Allan *et al.*, 2000) was used to reject reflections for which either the incident or the diffracted beam was completely absorbed by the cell and resulted in the shading of the detector. Reflections with very poorly fitting profiles [*i.e.* those reflections with poor correlations (< 0.3) between their measured and calculated profiles] were also rejected. The surviving reflections were corrected for absorption by the pressure-cell components with the program *SADABS* (Sheldrick, 2001) and the transmission ranged from 0.494 to 1.000. The low minimum transmission factor arises because of partial shadowing by the highly absorbing tungsten gasket; this shadowing is difficult to model analytically.

One of the most serious difficulties encountered in high-pressure crystallography is the limited volume of reciprocal space that can be sampled because of shading by the body of the pressure cell. In molecular systems, where low-symmetry space groups are usual, data completeness may be only 20% or 30% depending on the orientation of the sample. The completeness of the data set collected here is only 20% to $2\theta = 50°$, and this lack of completeness presented difficulties during solution and refinement. The structure was solved in $P2_1$ using direct methods (*SHELXTL*; Sheldrick, 1997); two highly distorted phenol molecules were just recognizable from the initial maps. The third phenol molecule was located by iterative cycles of least-squares refinement (in which the phenyl rings were constrained to be perfect hexagons) and difference-Fourier syntheses. Solution recognition is difficult because Fourier peaks are broadened along directions that are related to poorly sampled regions of reciprocal space; Gilmore & Stewart (2001) have recently shown that map interpretation can be facilitated by the use of maximum entropy methods.

Owing to the poor completeness, a full anisotropic refinement with independent positional parameters for each atom was not possible. Instead the hexagon constraints on the phenyl rings were retained in the final model, while the geometries about the three independent hydroxyl moieties were restrained to be similar. A common overall isotropic displacement parameter was also refined. This model, which comprises 29 parameters and 14 restraints, converged to a conventional R factor ($R1$) of 8.63% (see Table 2). H atoms were placed in calculated positions, those related to O atoms being placed so as to optimize hydrogen bonding. An alternative model, in which the three phenol molecules were restrained to be geometrically similar and have C_{2v} symmetry, converged to $R1 = 7.67\%$ for 65 parameters and 104 restraints. We report the first of these models here since the Hamilton (1965) R-ratio test implies that this improvement in R factor is not statistically significant. A summary of the crystal, data collection and final refinement details are listed in Table 2. The refined fractional coordinates of the high-pressure structures are deposited.[1]

2.2. Theoretical calculations

Because the atomic positions are difficult to refine, we have also determined the full set of structural parameters for the various phases of phenol by performing a series of *ab initio* calculations using the *CASTEP* code (Payne *et al.*, 1992; Segall *et al.*, 2002). This has enabled us to obtain the positions of the H atoms that were only inferred from the data collected using the X-ray diffraction techniques.

The density-functional formalism was used to solve the electronic structure of the materials with the generalized gradient approximation (GGA) (Perdew & Wang, 1992) applied for the many-electron exchange and correlation interactions. GGAs are known to provide a very accurate description of the structural and electronic properties of hydrogen-bonded systems compared with the often-used local density approximation (Perdew & Zunger, 1981). Non-local ultrasoft pseudopotentials generated by the method of

[1] Supplementary data for this paper are available from the IUCr electronic archives (Reference: BM0050). Services for accessing these data are described at the back of the journal.

Vanderbilt (1990) are used to describe electron–ion interactions. The valence electron wavefunctions are expanded in a plane-wave basis set with a kinetic energy cut-off of 380 eV. This converges the total energy differences of the system to better than 0.001 eV molecule^{-1}. Brillouin zone integrations are performed on a Monkhorst–Pack (Monkhorst & Pack, 1976) grid that is taken large enough to reach a similar level of convergence in total energy as the wavefunction cut-off. The electronic structure calculation proceeds *via* a preconditioned conjugate gradients energy-minimization scheme (Perdew & Wang, 1992) and density-mixing algorithm using the plane-wave coefficients as variational parameters. We have also optimized the structural parameters, both internal coordinates and lattice parameters, using a conjugate-gradients scheme. We report the relaxed high-pressure and ambient-pressure structural parameters with the deposited experimental values. The lattice parameters from these calculations are found to be $a = 6.236$, $b = 9.071$, $c = 14.756$ Å, $\gamma = 90.136°$ with $V = 834.70$ Å^3 for the ambient-pressure phase in the $P112_1$ setting and $a = 11.728$, $b = 5.560$, $c = 12.332$ Å, $\beta = 100.496°$ with $V = 790.69$ Å^3 for the high-pressure phase in the $P12_11$ setting.

We have also performed a Mulliken population analysis on the systems, which has allowed us to examine the nature of the charge transfer between the various species in each of the structures. We have used the method described by Segall *et al.* (1996*a*,*b*) to calculate the Mulliken charges on the atoms. However, it is worth noting that several other methods exist, and the actual values of the charges change from method to method. Therefore, these values should not be taken as the actual atomic charge, which, in any case, is rather ambiguously defined. However, it is generally thought that the direction of charge transfer will be correct. The results of the analysis are illustrated in Fig. 1. We find that the charge distribution is fairly insensitive to the surroundings of the molecule, in that for the ambient-pressure and high-pressure structures considered here the atomic charges are relatively similar. However, we note that the most significant change is in the O—H bond and the C atom opposite, and this change indicates a slight increase in the strength of the hydrogen-bond within the high-pressure system compared with that in the ambient-pressure structure. We have used the distribution of atomic charges to calculate the dipole moment of the phenol molecule in each structure. We find that in the ambient-pressure structure there is a molecular dipole moment of 3.51 Debye, which increases slightly to 3.86 Debye in the high-pressure structure.

3. Discussion

The general features of packing motifs adopted by mono-alcohols, *R*OH, have been described by Brock & Duncan (1994). There is a conflict between the packing requirements of the *R* groups and the need to bring the small OH groups into close enough proximity to form a hydrogen bond. If the hydroxyl-containing molecules are relatively 'thin' (Brock's terminology) they can be related by a 2_1 screw axis or a glide plane. Steric hindrance between *R* groups prohibits this for bulkier molecules, and these systems often form helices about three-, four- or sixfold screw axes or contain more than one molecule in the asymmetric unit. To quote Brock directly: 'C_nH_mOH molecules with fully elaborated hydrogen-bond networks are much more likely to crystallize with $Z' > 1$ or in high-symmetry space groups than would be expected based on statistics determined for the Cambridge Structural Database as a whole'.

Viewed in this light the ambient- and high-pressure polymorphs of phenol exhibit quite typical packing motifs, with the phenyl group behaving as though it is 'borderline thin'. At ambient pressure, phenol behaves like a bulky molecule, with a structure with $Z' = 3$ that forms a pseudo-threefold helical chain (Fig. 2). The three molecules that compose the repeat-unit of the helix are not related to one another by symmetry, and it is only the neighbouring hydrogen-bonded chains that are related by a 2_1 screw axis. At 0.16 GPa, phenol behaves like a typical small alcohol (Fig. 3). The structure, which also has $Z' = 3$, consists of one crystallographically unique molecule that is disposed along a chain that is generated by a 2_1 axis (labelled '*C*' in the tables and supplemental data). A second very similar chain is built of two crystallographically independent molecules (labelled *A* and *B*). The molecules within each chain adopt a ribbon-like arrangement and they are ordered in an alternating 1-1-1 sequence.

When the high-pressure phase is viewed along the **c** direction, consecutive molecules in each chain appear to be arranged so that the phenyl groups adopt a herringbone arrangement (Fig. 4). The angles made between the planes of the phenol molecules labelled *A* and *B* and the plane containing the OH···OH hydrogen bonds are 36.9 (5)° and 31.6 (7)°, respectively; the angle between the planes of the *A* and *B* phenyl rings is 66.0 (3)°. The corresponding values for the molecule labelled 'C' are similar: 33.6 (8)° and 63.5 (4)°.

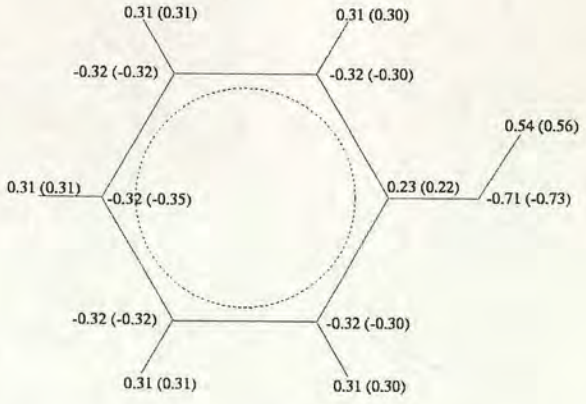

Figure 1
The results of the Mulliken analyses derived from plane-wave density-functional-theory calculations on the ambient- and high-pressure polymorphs of phenol. The numbers represent the nominal atomic charge in electrons and numbers given in parentheses are for the high-pressure phase.

This arrangement avoids close contacts between neighbouring CH groups along a chain.

As regards the packing of the chains, an analogy can be drawn between the high-pressure phase of phenol and the high-pressure, $P2_1/c$, structure of ethanol, in which alternating 1-1-1 molecular hydrogen-bonded chains of molecules are arranged so that they are coplanar and, consequently, layers of chains parallel to $(\bar{1}01)$ are produced. Within these layers, the chains are staggered so that the CH_3CH_2 tail groups interlock with one another. Analogously, for the high-pressure structure of phenol, layers of hydrogen-bonded chains are produced that are parallel to (100) and a very similar interlocking motif is adopted (Fig. 4). The layers appear to occupy the (300) planes, and the 300 reflection is the most intense in the data set. For ethanol, the rearrangement of the chains between the ambient-pressure and high-pressure phases is accompanied by a more efficient molecular packing: in the ambient-pressure structure, at 87 K, each molecule occupies a volume of 78.51 Å^3, while at high pressure the molecular volume is 75.99 Å^3. A comparable effect is also observed in phenol where each molecule occupies 131.33 Å^3 in the ambient-pressure structure while for the high-pressure phase there is an appreciable improvement in packing efficiency with each molecule occupying 126.07 Å^3.

In the ambient-pressure crystal structure the phenyl groups have a rather more complex interaction motif, though this motif is generally of the form expected from a herringbone arrangement. Neighbouring helical chains have two classes of phenyl contacts: the first comprises phenyl contacts where the axes of the molecules, as defined by the C—O vector, are arranged antiparallel to one another so that only pairs of molecules interact (B and C'); and in the second, the axes of the molecules (of type A) are directed towards the centre of the neighbouring chain so that they interact with a pair of molecules (type B' and C') on that adjacent chain (see Fig. 2).

It is interesting to note that the crystallographic screw axis is perpendicular to the axes of the helical chains themselves, and, consequently, the hydrogen bonding can be thought of as antiferroelectric in character: *i.e.* if we define the hydrogen bonds to be dipolar units, then the 2_1 screw axis ensures that half of the dipoles are arranged parallel to the a axis (along the length of the molecular chains) while half are arranged antiparallel. This means of describing a structure, while common in the physics literature, is rarely employed in chemistry. The

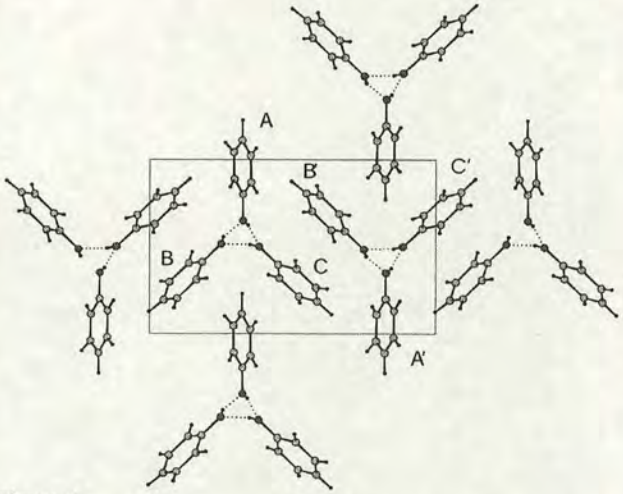

Figure 2
An a axis projection of the ambient-pressure, $P112_1$, structure of phenol, from Zavodnik *et al.* (1987). The crystallographic b axis is vertical while the c axis is horizontal. The helical hydrogen-bonded molecular chains are viewed along their lengths.

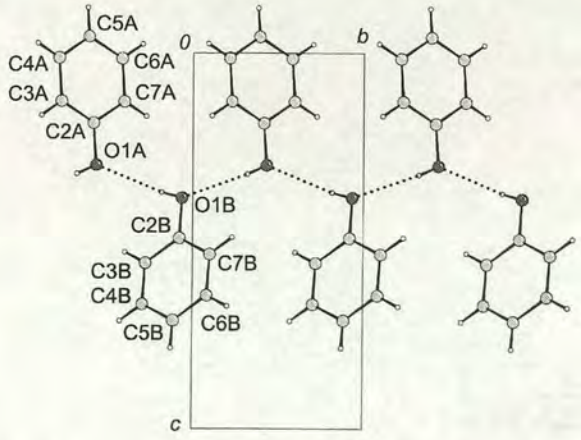

Figure 3
One of the crystallographically unique hydrogen-bonded chains in the high-pressure polymorph of phenol. The chain is viewed along the a axis. The molecules adopt an alternating 1-1-1 sequence.

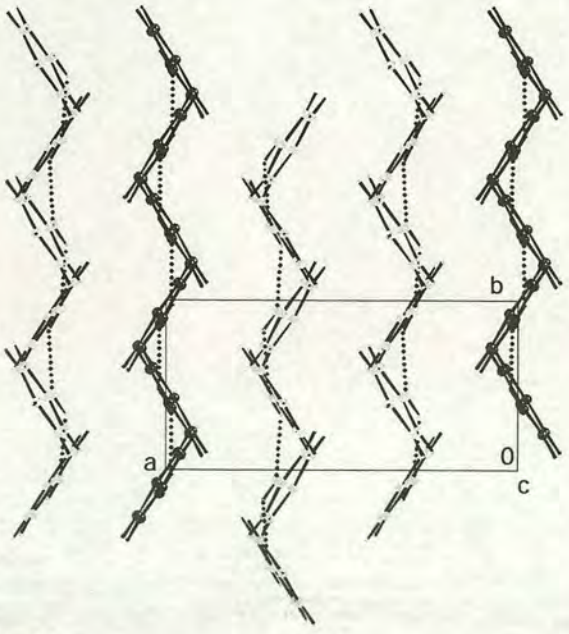

Figure 4
The high pressure phase of phenol viewed along the **c** direction. The chains generated by lattice repeat of the A and B molecules are shown in grey; the chains formed by the action of the 2_1 axis on the molecules labelled 'C' are shown in black.

antiparallel arrangement of the hydrogen bonds does not necessarily mean that the ambient-pressure phase of phenol is antiferroelectric; a measurement of the dielectric properties would be required to establish antiferroelectricity. In the high-pressure phase both types of molecular chain are parallel to the polar 2_1 screw axis, and, consequently, the dipoles in the high-pressure phase have ferroelectric-like characteristics: *i.e.* the dipoles, as defined by the hydrogen bonds, can be arranged parallel to one another without altering the crystal symmetry – though it is possible for the H atoms in each chain type to order in a different sense with respect to the polar *b* axis (as is the case with the structure reported here).

In Table 3 we compare the experimental and *ab initio* bond lengths and bond angles for selected hydrogen bonds in both the high-pressure and the ambient-pressure structures. The values derived from the theoretical calculations are in good overall agreement with the values determined by experiment, although the experimental values tend to consistently underestimate the lengths of the bonds and generally give smaller O—H···O bond angles (*i.e.* hydrogen bonds that are less straight). The discrepancies are largest for dimensions that depend on the H-atom positions, which are difficult to determine accurately with X-ray diffraction techniques and have been treated during refinement with geometrical constraints. (For molecules closely related to phenol in the Cambridge Structural Database, O—H distances, as defined by internuclear separations, are generally found to be 1.000 Å, and this value gives a correction ratio of 1.217, on average, for the tabulated values of both the ambient-pressure and the high-pressure phases.) However, the distances that involve only the O atoms, which can be determined accurately both experimentally and theoretically, are in excellent agreement and differ by less than 2%. It is significant, though, that both the experimental and theoretical studies show that, on average, the O—O distances are 10% larger for the high-pressure structure than for the ambient-pressure phase.

We have also examined the hydrogen-bond strength in the ambient-pressure and high-pressure phases of phenol using a simple electrostatic model. We have used the charge-density analysis (Mulliken charges given in Fig. 1) and the hydrogen-bond distances to calculate values of Q_1Q_2/r (from Coulomb's law), which can be considered as a measure of the hydrogen-bond strength. Although the charge increases slightly on the O—H atoms in the high-pressure phase relative to the ambient-pressure phase, the H···O distances also increase. In addition, when we use this measure of the hydrogen-bond strength we find that the ambient-pressure hydrogen-bond strength is approximately 8% greater, on average, than that in the high-pressure phase. Despite the difference in hydrogen-bond strength we find that the two structures are energetically similar (they have an enthalpy difference of only 0.162 eV molecule^{-1} or 15.6 kJ mole^{-1}) at 0.16 GPa, and the energy is thus lowered in the high-pressure phase with an accompanying increase in packing efficiency.

The ambient-pressure structure has a pseudosymmetry with the orthorhombic $P222_1$ (Gillier-Pandraud, 1967) and $P2_122_1$ (Scheringer, 1963) space groups, and this is partly reflected in the small deviation of the monoclinic unit-cell axes from orthogonality ($\gamma = 90.360°$). Indeed, the ambient-pressure crystal structure of phenol was originally identified as having $P222_1$ symmetry, although the same, and subsequent, workers established that the monoclinic $P112_1$ symmetry (an alternative setting of the conventional $P12_11$) is correct and allows for sensible hydrogen bonding. To test the stability of the $P112_1$ structure relative to either of the orthorhombic $P222_1$ or $P2_122_1$ symmetries we have performed calculations in which the symmetry of the ambient-pressure phase is reduced to $P1$ but the cell parameters and heavy-atom positions are taken from the $P222_1$ structure. Full structural relaxation results in a model that closely reproduces the ambient-pressure $P112_1$ phase and which has only a weak pseudosymmetry for either $P222_1$ or $P2_122_1$, at least for the C and O atoms. This result indicates that the $P112_1$ structure is the stable phase.

Table 3
Selected hydrogen-bond lengths and bond angles for the high-pressure and ambient-pressure phases of phenol from the experimental studies and the *ab initio* calculations.

The experimental values for the ambient-pressure phase are taken from Zavodnik *et al.* (1987). We have denoted the acceptor and donor atoms that are involved in the bonds as *A* and *D*, respectively. Note that the *D*—H distances for the high-pressure refinement were restrained.

High-pressure phase

	D—H (Å)		H···*A* (Å)		<*DHA* (°)		*D*···*A* (Å)		
D—H	Expt.	Theor.	Expt.	Theor.	Expt.	Theor.	Expt.	Theor.	*A*
O1*A*—H1*A*	0.82	0.98	2.23	2.05	147.6	167.2	2.957	3.019	O1*B*
O1*B*—H1*B*	0.82	0.98	2.24	2.06	143.0	165.6	2.940	3.021	O1*A*
O1*C*—H1*C*	0.82	0.98	2.26	2.07	148.8	166.9	2.996	3.035	O1*C*

Ambient-pressure phase (Zavodnik *et al.*, 1987)

	D—H (Å)		H···*A* (Å)		<*DHA* (°)		*D*···*A* (Å)		
D—H	Expt.	Theor.	Expt.	Theor.	Expt.	Theor.	Expt.	Theor.	*A*
O1*A*—H1*A*	0.74	1.00	1.98	1.76	164.7	174.3	2.693	2.757	O1*C*
O1*B*—H1*B*	0.82	1.00	1.89	1.67	156.0	177.1	2.655	2.673	O1*A*
O1*C*—H1*C*	0.91	1.00	1.81	1.70	157.2	167.2	2.664	2.687	O1*B*

In conclusion, we have solved the high-pressure monoclinic, $P2_1$, crystal structure of phenol and find that at the modest pressure of 0.16 GPa a very different molecular-packing arrangement is adopted from that of the ambient-pressure phase. The high-pressure structure is characterized by hydrogen-bonded molecular chains that adopt an alternating 1-1-1 sequence, whereas the ambient-pressure phase is composed of chains where the molecules are arranged in approximate threefold helices. This rearrangement of the molecular chains not only offers a marked improvement in molecular packing efficiency for the overall crystal structure but also results in a small reduction of the calculated enthalpy.

We would like to express our thanks to Dr J. S. Loveday and Professor R. J. Nelmes for a number of fruitful discussions. This work is supported by a grant from the Engineering and Physical Sciences Research Council (EPSRC) of the United Kingdom. The EPSRC also funds the PhD studentships for PAM and AD, and an EPSRC Advanced Fellowship currently

supports DRA. *CASTEP* version 4.2 is licensed under the UKCP/MSI agreement.

References

Allan, D. R. & Clark, S. J. (1999). *Phys. Rev. B*, **60**, 6328–6334.

Allan, D. R., Clark, S. J., Brugmans, M. J. P., Ackland, G. J. & Vos, W. L. (1998). *Phys. Rev. B*, **58**, R11809–R11812.

Allan, D. R., Clark, S. J., Parsons, S. & Ruf, M. (2000). *J. Phys. Condens. Matter*, **12**, L613–L618.

Angell, C. A. (1991). *J. Non-Cryst. Solids*, **13**, 133.

Bernstein, J., Davis, R. E., Shimoni, L. & Chang, N-L. (1995). *Angew. Chem. Int. Ed. Engl.* **34**, 1555–1573.

Boese, R. (2002). Private communication.

Brock, C. P. & Duncan, L. L. (1994). *Chem. Mater.* **6**, 1307–1312.

Bruker (2001). *SMART Data Collection and SAINT Integration Programs for Area Detector Data.* Bruker AXS, Madison, Wisconsin, USA.

Cook, R. L., King H. E., Herbst, C. A. & Herschbach, D. R. (1994). *J. Chem. Phys.* **100**, 5178–5189.

Cook, R. L., King, H. E. & Pfeiffer, D. G. (1992). *Phys. Rev. Lett.* **69**, 3072–3075.

Gillier-Pandraud, H. (1967). *Bull. Soc. Chim. Fr.* **6**, 1988.

Gilmore, C. J. (2001). Plenary lecture delivered at the European Crystallography Meeting ECM20, Krakow, Poland, 25–31 August 2001.

Gilmore, C. J. & Stewart, A. (2001). Personal communication.

Hamilton, W. L. (1965). *Acta Cryst.* **18**, 502–510.

Jönsson, P. G. (1976). *Acta Cryst.* B**32**, 232–235.

McGregor, P. A., Allan, D. R., Clark, S. J. & Parsons, S. (2003). In preparation.

Merrill, L. & Bassett, W. A. (1974). *Rev. Sci. Instrum.* **45**, 290–294.

Monkhorst, H. J. & Pack, J. D. (1976). *Phys. Rev. B*, **13**, 5188.

Payne, M. C., Teter, M. P., Allan, D. C., Arias, T. A. & Joannopolous, J. D. (1992). *Rev. Mod. Phys.* **64**, 1045–1097.

Perdew, J. P. & Wang, Y. (1992). *Phys. Rev. B*, **45**, 13244–13249.

Perdew, J. P. & Zunger, A. (1981). *Phys. Rev. B*, **23**, 5048–5079.

Scheringer, C. (1963). *Z. Kristallogr.* **119**, 273.

Segall, M. D., Lindan, P. L. D., Probert, M. J., Pickard, C. J., Hasnip, P. J., Clark, S. J. & Payne, M. C. (2002). *J. Phys. Condens. Matter*, **14**, 2717–2744.

Segall, M. D., Shah, R., Pickard, C. J. & Payne, M. C. (1996*a*). *Phys. Rev. B*, **54**, 16317–16320.

Segall, M. D., Shah, R., Pickard, C. J. & Payne, M. C. (1996*b*). *Mol. Phys.* **89**, 571–577.

Sheldrick, G. M. (1990). *Acta Cryst.* A**46**, 467–473.

Sheldrick, G. M. (1997). *SHELXTL. SHELXL*97. University of Göttingen, Germany, and Bruker AXS, Madison, Wisconsin, USA.

Sheldrick, G. M. (2001). *SADABS.* University of Göttingen, Germany, and Bruker AXS, Madison, Wisconsin, USA.

Sparks, R. A. (1999). *GEMINI.* Bruker AXS, Madison, Wisconsin, USA.

Steininger, R., Bilgram, J. H., Gramlich, V. & Petter, W. (1989). *Z. Kristallogr.* **187**, 1–13.

Torrie, B. H., Weng, S.-X. & Powell, B. M. (1989). *Mol. Phys.* **67**, 575–581.

Vanderbilt, D. (1990). *Phys. Rev. B*, **41**, 7892–7995.

Vos, W. L., Finger, L. W. & Hemley, R. J. (1992). *Nature* (*London*), **358**, 46–48.

Vos, W. L., Finger, L. W. & Hemley, R. J. (1993). *Phys. Rev. Lett.* **71**, 3150–3153.

Zavodnik, V. E., Bel'skii, V. K. & Zorkii, P. M. (1987). *Zh. Strukt. Khim.* **28**, 175.

Acta Crystallographica Section B
Structural Science
ISSN 0108-7681

The formation of paracetamol (acetaminophen) adducts with hydrogen-bond acceptors

Iain D. H. Oswald,[a] David R. Allan,[b] Pamela A. McGregor,[b] W. D. Samuel Motherwell,[c] Simon Parsons[a]* and Colin R. Pulham[a]

[a]School of Chemistry, The University of Edinburgh, King's Buildings, West Mains Road, Edinburgh EH9 3JJ, UK, [b]School of Physics and Astronomy, The University of Edinburgh, King's Buildings, West Mains Road, Edinburgh EH9 3JZ, UK, and [c]Cambridge Crystallographic Data Centre, 12 Union Road, Cambridge CB2 1EZ, UK

Correspondence e-mail: s.parsons@ed.ac.uk

Received 29 July 2002
Accepted 4 September 2002

The crystal structures of five hemiadducts of paracetamol with 1,4-dioxane, *N*-methylmorpholine, morpholine, *N*,*N*-dimethylpiperazine and piperazine and a related 1:1 adduct of paracetamol with 4,4′-bipyridine are described. All structures are characterized by the formation of chains of paracetamol molecules, which are linked *via* either OH···O=C interactions [*C*(9) chains in graph-set notation] or NH···O=C interactions [*C*(4) chains], depending on the presence or absence of substituent groups on the guest molecule. In all cases except for the morpholine and bipyridine adducts these chains are connected by hydrogen-bond interactions with the guest molecules, which reside on crystallographic inversion centres. In the bipyridine adduct this linkage also involves a π-stacking interaction; in the morpholine adduct it is formed between the OH groups of two opposed paracetamol molecules. Most adducts (that with 4,4′-bipyridine is an exception) decompose on heating to give monoclinic paracetamol. This is the first systematic study of a series of co-crystals containing paracetamol.

1. Introduction

There have been a number of detailed studies on the polymorphic behaviour of paracetamol (acetaminophen, *p*-hydroxylacetanilide or Tylenol). Form I, which is monoclinic, was first characterized by Haisa *et al.* (1976), and has since been shown to be the thermodynamically more stable form. Form II is orthorhombic and was also described by Haisa *et al.* in 1974 (Haisa *et al.*, 1974). The orthorhombic form can be grown using a single orthorhombic crystal as a seed from a super-saturated aqueous solution of paracetamol. This method, however, can result in the crystals changing to the monoclinic form if left in contact with the solution for any length of time (Nichols & Frampton, 1998). The same authors showed that the only method that gives the orthorhombic polymorph reproducibly is growth from the melt. They also showed that this form is stable if dried and stored in a stoppered vial and that neither grinding nor compression induces a transition to the monoclinic form. In a very careful study, Boldyreva *et al.* (2000) have shown that application of hydrostatic pressures up to 4.2 GPa does not induce a transition from the monoclinic to the orthorhombic form. The behaviour of the orthorhombic form is of interest for its ability to undergo plastic deformation when compressed, thereby facilitating the production of tablets of paracetamol.

With the exception of our own recent report of paracetamol trihydrate (McGregor *et al.*, 2002), little structural work appears to have been carried out on solvates or other co-crystals of paracetamol, although a thermochemical study showed the existence of a hemisolvate of paracetamol with

1,4-dioxane (Fachaux *et al.*, 1995). In this report, we describe the preparation and characterization of six new adducts of paracetamol with 1,4-dioxane, 4,4′-bipyridine, *N*-methylmorpholine, *N*,*N*-dimethylpiperazine, morpholine and piperazine (these are referred to as *guest molecules* below; see Schemes). All these molecules, except for morpholine, can be considered to be at least pseudo-centrosymmetric with respect to their hydrogen-bonding properties.

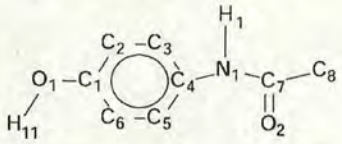

Paracetamol, with atomic numbering scheme.

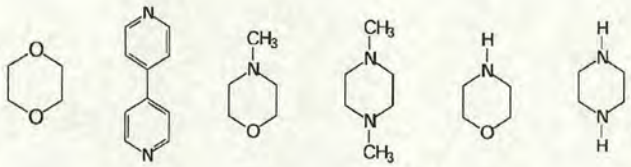

Guest molecules used to form adducts with paracetamol. Left to right: dioxane, bipyridine, *N*-methylmorpholine, *N*,*N*-dimethylpiperazine, morpholine and piperazine.

2. Experimental

2.1. Synthesis

All starting materials were obtained from Sigma-Aldrich except for 1,4-dioxane (May & Baker) and were used as received.

Paracetamol:0.5 1,4-dioxane. A saturated solution of paracetamol (1.51 g, 10 mmol) in 1,4-dioxane (2 cm^3, 23 mmol) was refluxed and allowed to cool. Colourless crystals were formed overnight at 293 K according to the published procedure (Fachaux *et al.*, 1995).

Paracetamol:4,4′-bipyridine. Paracetamol (0.51 g, 3.40 mmol) was refluxed with an equimolar amount of 4,4′-bipyridine (0.52 g, 3.33 mmol) in ethanol (1 cm^3). Pale-yellow needle-like crystals were formed on standing overnight at room temperature.

Paracetamol:0.5 N-methylmorpholine. Paracetamol (0.43 g, 2.85 mmol) and *N*-methylmorpholine (1 cm^3, 9.11 mmol) were refluxed and allowed to cool. The flask was maintained at 277 K, leading to the formation of colourless rod-shaped crystals.

Paracetamol:0.5 N,N-dimethylpiperazine. Paracetamol (0.55 g, 3.64 mmol) and *N*,*N*-dimethylpiperazine (3 cm^3, 22.2 mmol) were refluxed together and allowed to cool. A large excess of dimethylpiperazine was required to dissolve the paracetamol completely. The flask was maintained at 277 K leading to the formation of colourless rod-shaped crystals.

Paracetamol: 0.5 piperazine. Paracetamol (0.62 g, 4.1 mmol) was refluxed together with piperazine (0.35 g, 4.1 mmol) in ethanol (1 cm^3). Colourless crystals formed on cooling to 293 K.

Paracetamol:0.5 morpholine. Paracetamol (0.57 g, 3.8 mmol) was refluxed with morpholine (0.37 g, 4.3 mmol). Colourless crystals formed directly from the reaction mixture after a week at 277 K.

Ethanol was required in the reactions of paracetamol with piperazine and 4,4′-bipyridine because these compounds are both solids at room temperature.

2.2. Differential scanning calorimetry (DSC)

DSC traces were recorded using a Perkin Elmer Pyris DSC 1. Samples were contained in open aluminium pans and purged with helium during the temperature scans to facilitate the removal of any volatile products of thermal decomposition. Samples were heated from 298 K to 453 K at a rate of 10 K min^{-1}.

2.3. Crystallography

X-ray diffraction intensities were collected on either a Stoe Stadi-4 diffractometer with Cu $K\alpha$ radiation or a Bruker SMART APEX CCD diffractometer with Mo $K\alpha$ radiation. Both instruments were equipped with Oxford Cryosystems low-temperature devices. An absorption correction for the four-circle data was applied using ψ scans [*SHELXTL* (Sheldrick, 1997*a*), based on the procedure described by North *et al.* (1968)]; the multiscan procedure *SADABS* [(Sheldrick, 1997*b*), based on the procedure described by Blessing (1995)] was applied to the CCD data sets. All structures were in space group $P2_1/c$, except the morpholine adduct, which formed in $P2_12_12_1$. All structures were solved by direct methods and refined by full-matrix least squares against F^2 using all data (*SHELXTL*). H atoms were placed in calculated positions and allowed to ride on their parent atoms; methyl groups were treated with the Sheldrick (1997) rotating rigid group model. H atoms involved in hydrogen bonding were located in difference maps and refined freely. All non-H atoms were modelled with anisotropic displacement parameters.

One of the two crystallographically independent dioxane molecules in the 1,4-dioxane adduct was disordered over two orientations about a crystallographic inversion centre. The occupancies of the two components were fixed at 0.75 and 0.25 after competitive refinement. Similarity restraints were applied to the geometries and displacement parameters of the two components. The program *ROTAX* (Cooper *et al.*, 2002) suggested that the crystal may have been twinned by a twofold rotation about the [100] direct lattice direction. Incorporation of this into the model reduced *R*1 slightly from 7.02% to 6.86%, with a twin scale factor of 2.6 (3)%. This is barely significant, and the twinning is omitted in the model presented here.

In the *N*-methylmorpholine adduct, the *N*-methylmorpholine is disordered over a crystallographic inversion centre with

Table 1
Experimental details.

All data were collected at 150 K.

	1,4-Dioxane adduct	Dimethylpiperazine adduct	*N*-methylmorpholine adduct
Crystal data			
Chemical formula	$2[C_8H_9O_2N][C_4H_8O_2]$	$2[C_8H_9NO_2][C_6H_{14}N_2]$	$2[C_8H_9NO_2][C_5H_{11}NO]$
Chemical formula weight	390.43	416.52	403.47
Cell setting, space group	Monoclinic, $P2_1/c$	Monoclinic, $P2_1/c$	Monoclinic, $P2_1/c$
a, b, c (Å)	12.421 (5), 12.056 (4), 13.396 (3)	10.6970 (9), 11.0240 (9), 9.4896 (8)	10.5749 (8), 11.0221 (8), 9.3894 (7)
β (°)	91.51 (3)	100.684 (2)	101.145 (2)
V (Å^3)	2005.4 (11)	1099.65 (16)	1073.77 (14)
Z	4	2	2
D_x (Mg m^{-3})	1.293	1.258	1.248
D_m (Mg m^{-3})	Not measured	Not measured	Not measured
Radiation type	Cu $K\alpha$	Mo $K\alpha$	Mo $K\alpha$
No. of reflections for cell parameters	80	3488	2729
θ range (°)	20–22	2.5–29	2.5–27.5
μ (mm^{-1})	0.795	0.088	0.090
Temperature (K)	220 (2)	150 (2)	150 (2)
Crystal form, colour	Lath, colourless	Plate, colourless	Rod, colourless
Crystal size (mm)	0.78 × 0.19 × 0.16	0.56 × 0.18 × 0.08	0.34 × 0.09 × 0.07
Data collection			
Diffractometer	Stoe Stadi-4	Bruker SMART APEX CCD	Bruker SMART APEX CCD
Data collection method	ω–θ scans	φ and ω scans	φ and ω scans
Absorption correction	Empirical	Multiscan	Multiscan
T_{min}	0.602	0.833	0.792
T_{max}	0.826	1	0.962
No. of measured, independent and observed reflections	4865, 3499, 2508	7034, 2724, 2512	6517, 2444, 1890
Criterion for observed reflections	$I > 2\sigma(I)$	$I > 2\sigma(I)$	$I > 2\sigma(I)$
R_{int}	0.0532	0.0164	0.0221
θ_{max} (°)	69.79	29.08	27.49
Range of h, k, l	$-15 \rightarrow h \rightarrow 15$ $0 \rightarrow k \rightarrow 14$ $0 \rightarrow l \rightarrow 15$	$-8 \rightarrow h \rightarrow 14$ $-15 \rightarrow k \rightarrow 14$ $-12 \rightarrow l \rightarrow 12$	$-13 \rightarrow h \rightarrow 13$ $-14 \rightarrow k \rightarrow 14$ $-11 \rightarrow l \rightarrow 12$
No. and frequency of standard reflections	3 every 60 min	Not measured	Not measured
Intensity decay (%)	10.9	0	0
Refinement			
Refinement on	F^2	F^2	F^2
$R[F^2 > 2\sigma(F^2)]$, $wR(F^2)$, S	0.0702, 0.2243, 1.078	0.0525, 0.1339, 1.059	0.0408, 0.1082, 0.973
No. of reflections and parameters used in refinement	3499, 285	2724, 146	2444, 147
H-atom treatment	Riding	Riding/All H-atom parameters refined	Riding/All H-atom parameters refined
Weighting scheme	$w = 1/[\sigma^2(F_o^2) + (0.125P)^2 + 1.1494P]$ where $P = (F_o^2 + 2F_c^2)/3$	$w = 1/[\sigma^2(F_o^2) + (0.069P)^2 + 0.4625P]$ where $P = (F_o^2 + 2F_c^2)/3$	$w = 1/[\sigma^2(F_o^2) + (0.0658P)^2]$ where $P = (F_o^2 + 2F_c^2)/3$
$(\Delta/\sigma)_{max}$	0.002	0.009	0.000
$\Delta\rho_{max}$, $\Delta\rho_{min}$ (e Å^{-3})	0.503, −0.260	0.401, −0.193	0.216, −0.220
Extinction method	*SHELXL*	None	*SHELXL*
Extinction coefficient	0.0019 (6)	0	0.008 (3)

	Piperazine adduct	4,4′-Bipyridine adduct	Morpholine adduct
Crystal data			
Chemical formula	$2[C_8H_9NO_2][C_4H_{10}N_2]$	$[C_8H_9NO_2][C_{10}H_8N_2]$	$2[C_8H_9NO_2][C_4H_9O]$
Chemical formula weight	388.46	307.35	389.45
Cell setting, space group	Monoclinic, $P2_1/c$	Monoclinic, $P2_1/c$	Orthorhombic, $P2_12_12_1$
a, b, c (Å)	15.893 (5), 5.1664 (17), 12.993 (4)	11.2906 (10), 24.103 (2), 11.5526 (10)	7.2791 (9), 14.6277 (18), 18.303 (2)

the N and O atoms sharing an equivalent site. A composite scattering factor $[0.5f(N) + 0.5f(O)]$ was used for this site; the occupancy of the methyl group was fixed at 0.5.

A consistent numbering scheme was used for the paracetamol molecules in all structures and this is shown in the schemes above. Where there is more than one paracetamol molecule in the asymmetric unit the labels in the schemes are augmented with the letters *A* and *B*. Labels for atoms forming part of the guest molecules carry the letters *S*, *T etc.* A full listing of crystal, data collection and refinement parameters is given in Table 1; a set of hydrogen-bonding parameters is given in Table 2.[1] The figures were produced using *CAMERON* (Watkin *et al.*, 1993). Other analyses utilized the PC version of the program *PLATON* (Spek, 2002; Farrugia, 1999).

3. Results

3.1. Paracetamol

Crystal structures of the monoclinic and orthorhombic polymorphs of paracetamol have been reported several times, but here we have used the structures reported by Nichols & Frampton (1998) [Cambridge Structural Database (CSD; Allen *et al.*, 1983) reference codes HXACAN07 and HXACAN08]. Our motive for discussing them here is to highlight certain features of their graph sets that enable structural relationships to be drawn between them and the adducts that form the subject of the rest of this paper.

Packing in both polymorphs is dominated by the formation of NH···OH and OH···O=C hydrogen bonds (Fig. 1) giving rise to layered two-dimensional networks. Both polymorphs of paracetamol have identical graph sets (Bernstein *et al.*, 1995), in which the

[1] Supplementary data for this paper are available from the IUCr electronic archives (Reference: AN0622). Services for accessing these data are described at the back of the journal.

Table 1 (continued)

	Piperazine adduct	4,4′-Bipyridine adduct	Morpholine adduct
β (°)	113.633 (5)	96.1484 (16)	90
V (Å^3)	977.4 (6)	3125.8 (5)	1948.9 (4)
Z	2	8	4
D_x (Mg m^{-3})	1.320	1.306	1.327
D_m (Mg m^{-3})	Not measured	Not measured	Not measured
Radiation type	Mo $K\alpha$	Mo $K\alpha$	Mo $K\alpha$
No. of reflections for cell parameters	1227	5375	3801
θ range (°)	2.5–29	2–28.5	2.5–24.5
μ (mm^{-1})	0.093	0.087	0.096
Temperature (K)	150 (2)	150 (2)	150 (2)
Crystal form, colour	Plate, colourless	Block, colourless	Block, colourless
Crystal size (mm)	0.77 × 0.28 × 0.11	0.46 × 0.28 × 0.18	0.54 × 0.52 × 0.28
Data collection			
Diffractometer	Bruker Smart Apex CCD	Bruker SMART APEX CCD	Bruker SMART APEX CCD
Data collection method	ω and φ scans	ω and φ scans	φ and ω scans
Absorption correction	Multiscan	Multiscan	Multiscan
T_{min}	0.690	0.830	0.868
T_{max}	1	1	1
No. of measured, independent and observed reflections	5628, 2309, 1778	20270, 7766, 6044	12312, 4733, 4265
Criterion for observed reflections	$I > 2\sigma(I)$	$I > 2\sigma(I)$	$I > 2\sigma(I)$
R_{int}	0.0458	0.0220	0.0308
θ_{max} (°)	28.55	29.18	28.97
Range of h, k, l	$-17 \rightarrow h \rightarrow 21$ $-6 \rightarrow k \rightarrow 6$ $-17 \rightarrow l \rightarrow 16$	$-14 \rightarrow h \rightarrow 14$ $-19 \rightarrow k \rightarrow 31$ $-15 \rightarrow l \rightarrow 15$	$-9 \rightarrow h \rightarrow 7$ $-19 \rightarrow k \rightarrow 18$ $-24 \rightarrow l \rightarrow 22$
No. and frequency of standard reflections	Not measured	Not measured	Not measured
Intensity decay (%)	0	0	0
Refinement			
Refinement on	F^2	F^2	F^2
$R[F^2 > 2\sigma(F^2)]$, $wR(F^2)$, S	0.0779, 0.1652, 1.179	0.0471, 0.128, 1.038	0.0462, 0.1028, 1.066
No. of reflections and parameters used in refinement	2309, 140	7766, 433	4733, 276
H-atom treatment	Riding/All H-atom parameters refined	Riding/All H-atom parameters refined	Riding/All H-atom parameters refined
Weighting scheme	$w = 1/[\sigma^2(F_o^2) + (0.052P)^2 + 0.5663P]$ where $P = (F_o^2 + 2F_c^2)/3$	$w = 1/[\sigma^2(F_o^2) + (0.0676P)^2 + 0.569P]$ where $P = (F_o^2 + 2F_c^2)/3$	$w = 1/[\sigma^2(F_o^2) + (0.049P)^2 + 0.2716P]$ where $P = (F_o^2 + 2F_c^2)/3$
$(\Delta/\sigma)_{max}$	0.002	0.001	0.001
$\Delta\rho_{max}$, $\Delta\rho_{min}$ (e Å^{-3})	0.336, −0.447	0.357, −0.246	0.256, −0.270
Extinction method	None	None	*SHELXL*
Extinction coefficient	0	0	0.0031 (7)

Computer programs used: Stoe *DIF4* (Stoe & Cie, 1990*a*), Stoe *REDU4* (Stoe & Cie, 1990*b*), Bruker *SMART* (Bruker, 2001), Bruker *SAINT* (Bruker, 2002), *SHELXTL* (Sheldrick, 1997*a*).

OH···O=C and NH···OH hydrogen bonds, respectively, form $C(9)$ and $C(7)$ motifs at the unitary level.[2] In both polymorphs, these are disposed about crystallographic glide planes. In the monoclinic form, the hydrogen-bonded layers are arranged parallel to the (010) planes, which means that the layers are polar: in Fig. 1(*a*) all the molecules have the methyl group on the left. This polarity is reversed in neighbouring layers by crystallographic inversion centres. In the orthorhombic form, glide planes run perpendicular to the layers, so that the layers are non-polar: in Fig. 1(*b*) the methyl groups lie on the left- and right-hand sides of the molecules in alternate $C(9)$ chains.

The angles between mean planes of the amide and phenyl groups in orthorhombic and monoclinic paracetamol are 17.7° and 20.5°, respectively. Analogous angles observed in this work are given in the figure captions and range from 3.03° to 41.72°. pπ-pπ bonding between the phenyl ring and the amide group favours a dihedral angle of zero, and some correlation between this angle and the N—C(phenyl) bond length might have been expected, though none is evident at the precision of these structure determinations. This angle is evidently a rather easily deformed structural parameter, and is presumably at the mercy of crystal-packing forces. As we show in the following sections, hydrogen bonding is the dominant feature in these structures, and the torsion observed is presumably a consequence of the optimization of these interactions.

3.2. The paracetamol:1,4-dioxane adduct

The asymmetric unit in the crystal structure of the dioxane adduct of paracetamol consists of two paracetamol molecules and two half molecules of dioxane. The latter both reside on crystallographic inversion centres. One of the dioxane molecules (labelled *T*/*U* in the tables and supplemental data) is disordered, although both components participate in hydrogen bonding. The occupancy ratio is 0.75:0.25 and in the discussion that follows we have ignored the minor component (*U*). There is some evidence from electron-density difference maps that the other dioxane molecule (labelled *S*) is disordered as well, although, if present, the distinction between the components is at the limit of the resolution of our data set. An ordered model for this part of the structure is therefore presented here. The structure is depicted in Fig. 2. Primary bond lengths and angles are normal and have been deposited; hydrogen-bonding parameters are listed in Table 2.

[2] Note that where no sub- and superscripts appear in the graph-set descriptor, one donor and one acceptor are implied.

The $C(9)$ chains formed by hydrogen bonding between OH···O=C moieties of neighbouring molecules described above with regard to the crystal structures of paracetamol are also observed in the structure of the 1,4-dioxane adduct. In order to accommodate the dioxane molecules these chains are sinusoidal, with the two crystallographically independent paracetamol molecules alternating along the chain. The NH groups point towards the O atoms of dioxane molecules forming NH···O hydrogen bonds. Since both dioxane molecules reside on inversion centres, the space-group symmetry builds up two-dimensional sheets in which chains of paracetamol are linked by dioxane bridges (Fig. 2). In graph-set notation, the bridges can be described as $D_2^2(6)$. The two-dimensional sheets are parallel to the (210) lattice planes, and the rather open structure depicted in Fig. 2 is 'filled in' by symmetry-equivalent sheets parallel to $(2\bar{1}0)$.

Table 2
Hydrogen-bonding parameters.

Standard uncertainties are omitted in the case of the dioxane adduct because the H-atom positions were calculated and not refined. N—H and O—H distances were normalized to 1.009 Å and 0.983 Å, respectively, to aid comparison with Cambridge Structural Database search results (Fig. 7).

Adduct	Donor	Acceptor	Observed distance (Å)	Normalized distance (Å)	Typical normalized distance (Å)
1,4-Dioxane	N1*A*—H1*A*	O1*S*	2.03	1.90	1.96
	O1*A*—H11*A*	O2*B*	1.82	1.67	1.78
	O1*B*—H11*B*	O2*A*^{i}	1.86	1.71	1.78
	N1*B*—H1*B*	O1*U*	1.92	1.77	1.96
	N1*B*—H1*B*	O1*T*	2.13	2.00	1.96
4,4′-Bipyridine	O1*A*—H11*A*	O2*B*	1.755 (19)	1.68	1.78
	N1*A*—H1*A*	N10*S*	2.047 (18)	1.92	1.96
	O1*B*—H11*B*	O2*A*^{ii}	1.81 (2)	1.71	1.78
	N1*B*—H1*B*	N1*T*^{iii}	2.100 (18)	2.01	1.96
N,*N*-dimethylpiperazine	N1—H1	O2^{iv}	1.98 (2)	1.84	1.92
	O1—H11	N1*S*^{v}	1.81 (2)	1.82	1.82
N-methylmorpholine	O1—H11	O1*S*/N1*S*^{vi}	1.88 (2)	1.81	1.81/1.82
	N1—H1	O2^{vii}	1.925 (16)	1.80	1.92
Piperazine	O1—H11	N1*S*	1.79 (3)	1.74	1.82
	N1—H1	O2^{viii}	2.14 (3)	2.06	1.92
	N1*S*—H1*S*	O1^{viii}	2.30 (3)	2.21	2.03
Morpholine	O1*A*—H11*A*	O1*B*^{ix}	1.97 (2)	1.76	1.87
	N1*A*—H1*A*	O2*B*^{x}	2.033 (18)	1.87	1.92
	O1*B*—H11*B*	N4*S*^{xi}	1.79 (3)	1.69	1.82
	N1*B*—H1*B*	O2*A*^{xii}	2.061 (19)	1.86	1.92

(i) $x, y, z+1$; (ii) $x-1, y, z-1$; (iii) $-x, y-\frac{1}{2}, -z+\frac{1}{2}$; (iv) $x, -y+\frac{1}{2}, z-\frac{1}{2}$; (v) $-x+1, -y, -z$; (vi) $-x+1, -y+2, -z$; (vii) $x, -y+\frac{3}{2}, z-\frac{1}{2}$; (viii) $x, y+1, z$; (ix) $x+\frac{1}{2}, -y+\frac{3}{2}, -z$; (x) $x+\frac{1}{2}, -y+\frac{1}{2}, -z$; (xi) $-x+1, y+\frac{1}{2}, -z+\frac{1}{2}$; (xii) $-x+1, y-\frac{1}{2}, -z+\frac{1}{2}$.

3.3. The paracetamol:4,4′-bipyridine adduct

The O atoms in 1,4-dioxane formally have two lone pairs of electrons, each of which could potentially act as a hydrogen-bond acceptor. In practice, however, motifs in which ethers act as double hydrogen-bond acceptors occur rarely, and so for practical crystal-packing purposes it can be considered to be a centrosymmetric molecule containing two hydrogen-bond acceptors. 4,4′-Bipyridine is similar, although a torsion about the central C—C bond breaks the inversion symmetry. Recrystallization of paracetamol from a solution of 4,4′-bipyridine in ethanol yields a 1:1 co-crystal rather than the hemisolvate obtained with dioxane, a possible effect of the greater basicity of bipyridine.

The crystal structure of paracetamol:bipyridine contains two independent molecules each of paracetamol and bipyridine. Primary bond lengths and angles are normal and have been deposited; hydrogen-bonding parameters are listed in Table 2. As in the dioxane adduct, the paracetamol molecules form $C(9)$ chains through OH···O=C hydrogen bonds (Fig. 3). The two crystallographically independent paracetamol molecules alternate along the chain. The disposition of the molecules within the chains is rather similar to that in orthorhombic paracetamol, except that alternate molecules are rotated through 180° about the chain axis in order to accommodate the bipyridine molecules.

The NH bonds of paracetamol act as hydrogen-bond donors to the aromatic N atoms of the bipyridine molecules, forming a discrete (D) graph set. However, since this crystal is a 1:1 adduct there are insufficient hydrogen-bond donors for the number of acceptors present, and only one of the two N atoms in each bipyridine acts as an acceptor. The result is that there are no hydrogen-bonded pathways connecting the $C(9)$ paracetamol chains. The structure thus consists of a paracetamol backbone with attached bipyridine molecules. These motifs are interconnected by π-stacking between the bipyridine molecules, building up sheets than run parallel to the $(10\bar{1})$ planes.

3.4. The paracetamol adducts with *N*-methylmorpholine and *N*,*N*-dimethylpiperazine

N,*N*-dimethylpiperazine and *N*-methylmorpholine are closely related to 1,4-dioxane by the substitution of one or both O atoms by N—Me; paracetamol forms 2:1 adducts with both compounds, as it does with dioxane. The *N*,*N*-dimethylpiperazine adduct consists of one crystallographically independent paracetamol molecule with the *N*,*N*-dimethylpiperazine residing on a crystallographic inversion centre. The *N*-methylmorpholine adduct is isostructural with this, with the guest molecule disordered about the inversion centre. Primary bond lengths and angles are unremarkable and have been deposited; hydrogen-bonding parameters are listed in Table 2

The crystal structures are similar to those of the dioxane and bipyridine adducts in that the packing can be described with reference to chains of paracetamol molecules. However, rather than $C(9)$ motifs formed through OH···O=C H bonds, the paracetamol molecules define a $C(4)$ graph set through NH···O=C bonds (Fig. 4). The NH moiety of the para-

cetamol now fulfils the role of the OH groups in the dioxane structure, and *N*,*N*-dimethylpiperazine and *N*-methylmorpholine are similar to dioxane with regard to their hydrogen-bonding properties. Therefore, although the nature of the paracetamol chain differs from that of the dioxane adduct, the roles of the *N*-methylmorpholine and dimethylpiperazine molecules are similar, and both act to link paracetamol chains *via* the $D_2^2(6)$ graph set. Overall, this structure consists of a two-dimensional network, although the sheets formed have a corrugated or zigzag appearance in cross section. Alternate regions of the network are approximately parallel to the (310) and (3$\bar{1}$0) planes. Just as in the dioxane adduct, the open structure of Fig. 4 is filled in by symmetry-equivalent networks.

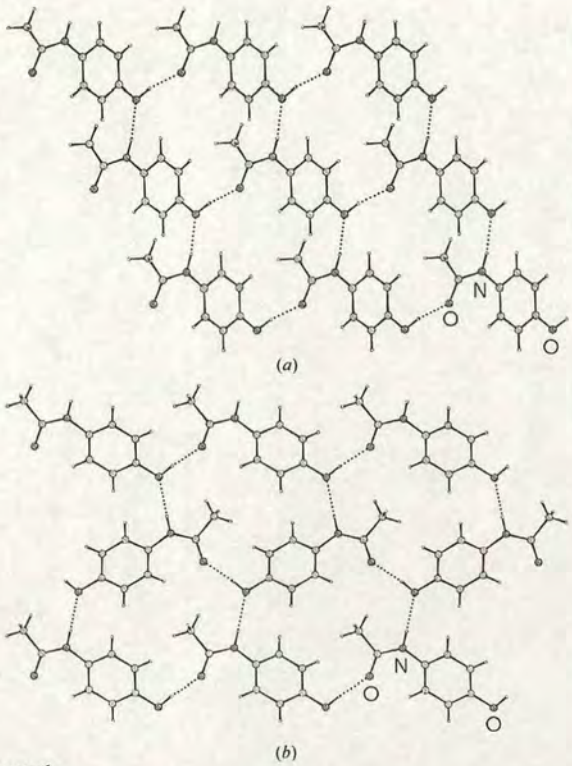

Figure 1
(*a*) Monoclinic paracetamol (Form I) viewed along the *b* axis; the *c* axis runs diagonally from top left to bottom right, so that the *C*(9) chains are established by the *n*-glide. (*b*) Orthorhombic paracetamol (Form II) viewed along the *c* axis; the *a* axis runs horizontally, the *b* axis runs from top to bottom. The *C*(9) chains referred to in the text run from left to right and the *C*(7) chains run approximately vertically. [Colour versions of this and the other figures are available in the online edition of this journal.]

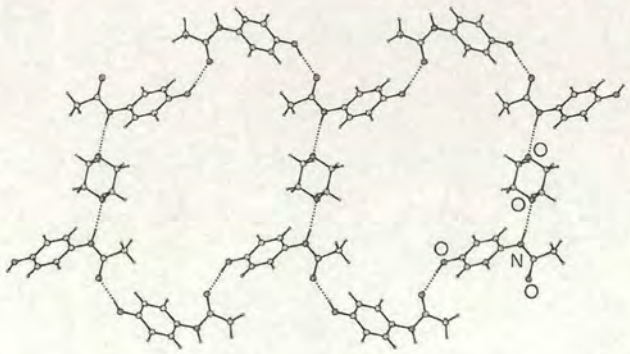

Figure 2
Paracetamol:1,4-dioxane adduct viewed perpendicular to (210); the *c* axis runs horizontally. The *C*(9) chains referred to in the text run from left to right and are linked together by dioxane molecules. The dihedral angles between the amide and phenyl mean planes in the two independent paracetamol molecules are 41.72 (15)° and 39.37 (14)° for molecules *A* and *B*, respectively.

3.5. The paracetamol:morpholine adduct

Morpholine is related to *N*-methylmorpholine by the substitution of the methyl group for hydrogen, and it is unique in this series because the hydrogen-bonding characteristics of the two hetero-centres are not the same: the NH group is a donor and acceptor, the ether O atom potentially a double, but more usually a single, acceptor. The asymmetric unit of the morpholine hemiadduct consists of two crystallographically independent paracetamol molecules (labelled *A* and *B*) and one molecule of morpholine (labelled *S* in the tables). Primary bond lengths and angles are normal and have been deposited; hydrogen-bonding parameters are listed in Table 2.

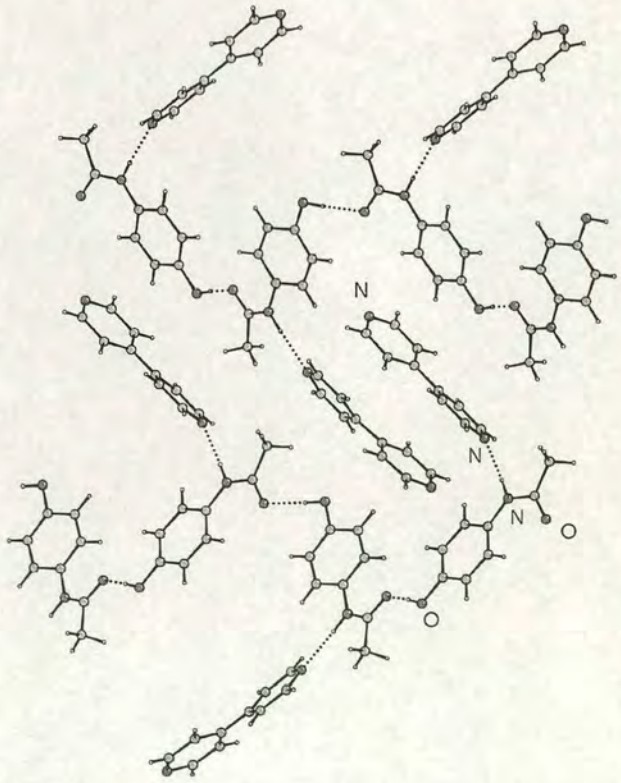

Figure 3
Paracetamol:4,4-bipyridine viewed perpendicular to (10$\bar{1}$); the *b* axis runs from top to bottom. The *C*(9) chains referred to in the text run from left to right and are linked together by a pair of π-stacked bipyridine molecules. The dihedral angles between the amide and phenyl mean planes in the two independent paracetamol molecules are 14.68 (8)° and 13.27 (9)° for molecules *A* and *B*, respectively.

The crystallographically independent paracetamol molecules alternate in the pattern ...*ABABAB*... along a chain formed by ···HNCO···NHCO··· linkages between neighbouring amide groups. Because these molecules are crystallographically independent, these hydrogen bonds formally constitute discrete graphs at the unitary level, although it is clear from Fig. 5 that they are closely related to the *C*(4) graphs observed in the crystal structures of the *N*-methylmorpholine and *N*,*N*-dimethylpiperazine adducts described above. For consistency we continue to use this designation, although it is not formally correct [the binary graph $C_2^2(8)$ takes proper account of symmetry].

The chains are formed by 2_1 operations parallel to *c*, leading to a pairwise alternation of the centres of the paracetamol molecules above and below the chain. This pattern is reminiscent of the structures of the *N*-methylmorpholine and *N*,*N*-dimethylpiperazine adducts, except that in these cases the alternation applies to single molecules. The potential for this arrangement to lead to some steric hindrance between the phenyl groups of neighbouring molecules is avoided by adjacent molecules veering slightly away from each other and an increase in the torsional angle between the phenyl group and amide group from 3.04 (3)° in molecule *B* to 36.03 (6)° in molecule *A*.

Lattice translation along the *b* direction generates further *C*(4) chains, and these are linked together by discrete [*D*] hydrogen bonds in which an OH group from an '*A*' molecule in one chain acts as a donor to an OH group of a '*B*' molecule in a neighbouring chain. This is the only structure in the series in which pairs of paracetamol molecules interact *via* their hydroxyl moieties.

The two sets of hydrogen bonds described above – the *C*(4) chains and the *D* links between chains – form a grid-like network parallel to the (100) planes. The morpholine molecules fit into the cavities of the grid. As in the *N*-methylmorpholine adduct, the amine N atom acts as an acceptor to the OH group of one of the paracetamol molecules (*B*), but this is the only hydrogen-bonding interaction formed by the morpholine. The NH group of the morpholine is in an axial position to accommodate this interaction.

This scheme satisfies all the hydrogen-bonding potential of the two paracetamol molecules, with the exception of the hydroxyl acceptor of molecule *A*. The weakest acceptor in the system (the ether function of the morpholine) does not

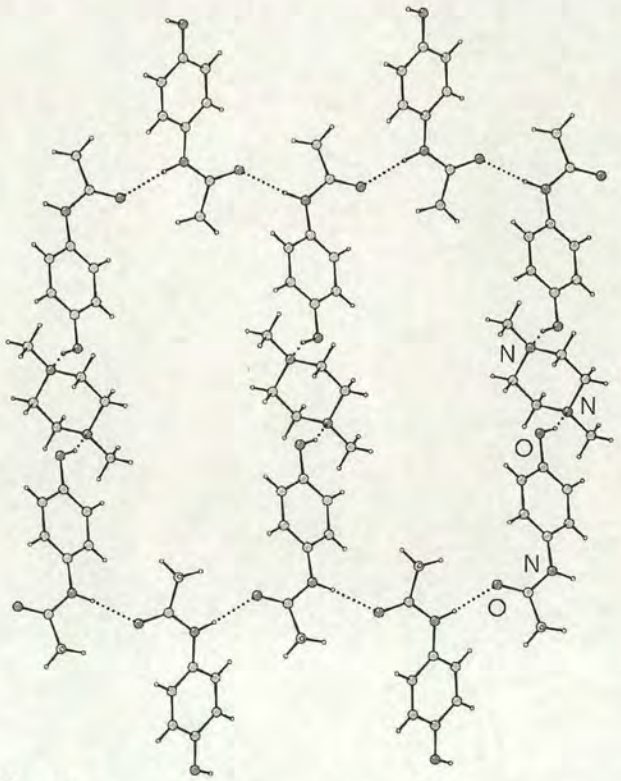

Figure 4
Paracetamol:*N*,*N*-dimethylpiperazine adduct (isostructural to the *N*-methylmorpholine adduct) viewed along the *a* axis; the *c* axis runs from left to right and the *b* axis from top to bottom. The *C*(4) chains referred to in the text run from left to right and are linked together by *N*,*N*-dimethylpiperazine molecules. The dihedral angles between the amide and phenyl mean planes in the paracetamol molecules are 33.75 (7)° and 34.11 (6)° in the *N*,*N*-dimethylpiperazine and *N*-methylmorpholine adducts, respectively.

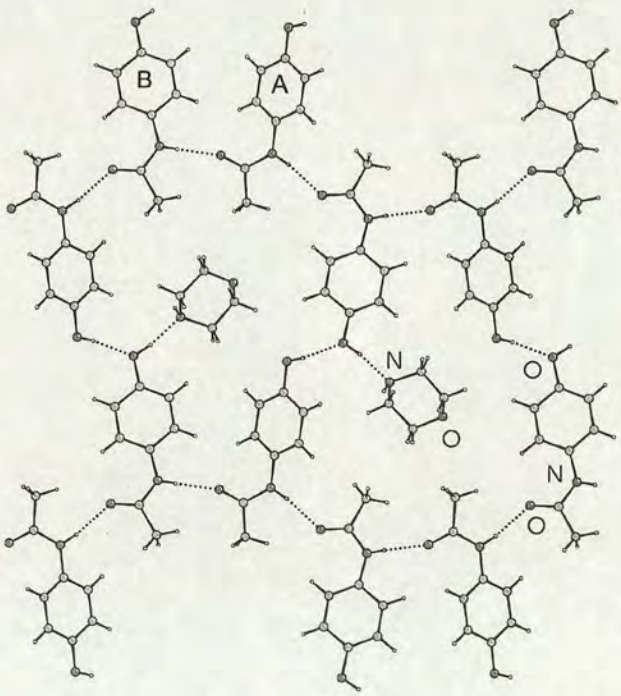

Figure 5
Paracetamol:morpholine adduct viewed along the *a* axis. The *c* direction runs from left to right, the *b* direction up and down. The labels *A* and *B* refer to the crystallographically independent paracetamol molecules referred to in the text. The *C*(4) chains referred to in the text run from left to right and are linked together by hydrogen bonds between opposed OH groups. This forms a grid-like array with the morpholine molecules residing in the grid cavities. The dihedral angles between the amide and phenyl mean planes in the two independent paracetamol molecules are 36.03 (6)° and 3.04 (3)° for molecules *A* and *B*, respectively.

participate in hydrogen bonding at all. A rather surprising feature of this structure, given the excess of acceptors present, is that the NH donor functionality of the morpholine amine moiety is also unsatisfied. However, this is consistent with the relatively long NH···OH hydrogen bonds observed in the piperazine adduct (which is described in the next section) and the generally poor hydrogen-bond-donor ability of secondary amines (see below).

3.6. The paracetamol:piperazine adduct

Piperazine is related to *N*,*N*-dimethylpiperazine by substitution of the two methyl groups by hydrogen. The asymmetric unit of the piperazine adduct, in common with the *N*,*N*-dimethylpiperazine adduct, consists of one paracetamol molecule and a molecule of piperazine on a crystallographic inversion centre. Primary bond lengths and angles are normal and have been deposited; hydrogen-bonding parameters are listed in Table 2. There are $C(4)$ chains, consisting of NH···O=C hydrogen bonds, linked *via* $D_2^2(6)$ motifs consisting of OH···N bonds (Fig. 6). Piperazine is a weak hydrogen-bond donor as well as an acceptor, and the extra NH-donor moiety is satisfied by rotating alternate paracetamol molecules about the $C(4)$ chain axis, leading to *D*-type NH···OH hydrogen bonds. This rotation produces ribbons that run parallel to the *b* axis rather than the infinite two-dimensional networks.

3.7. Differential scanning calorimetry

Decomposition of a co-crystal of paracetamol is a potential strategy for the production of the orthorhombic polymorph. In all cases except for the 4,4′-bipyridine adduct, DSC traces exhibited thermal events attributable to loss of the guest molecule followed by a strong endotherm, corresponding to melting, at 438–444 K. The melting point of monoclinic paracetamol is 442 K (Nichols & Frampton, 1998). The same authors showed that DSC traces for orthorhombic paracetamol show either melting at 430 K or a phase transition to the monoclinic form at the same temperature, depending on the method of preparation. The DSC traces observed in this study can therefore be interpreted in terms of decomposition leading to formation of the monoclinic polymorph.

Thermal decomposition temperatures follow the trend that might be predicted on the basis of the boiling points of 1,4-dioxane (374 K), *N*-methylmorpholine (388 K), morpholine (401 K), *N*,*N*-dimethylpiperazine (404 K) and piperazine (419 K). Two exotherms were observed for the dioxane solvate at 299 K and 338 K, in agreement with the previous study (Fachaux *et al.*, 1995). This is plausibly interpreted as sequential loss of the two crystallographically independent dioxane molecules. Dioxane is readily lost at room temperature from a crystalline sample of this adduct, and the DSC trace of a sample that had been allowed to stand for 10 min showed only one exotherm with an onset temperature of 330 K. Decomposition of the morpholine, *N*-methylmorpholine and *N*,*N*-dimethylpiperazine adducts occur as broad exotherms with onsets at approximately 327, 335 and 373 K, respectively. The DSC trace of the piperazine adduct showed one endotherm at 413 K.

4,4′-Bipyridine sublimes at 578 K under ambient pressure, and it is the least volatile compound to have been studied in this work. The DSC trace of the co-crystal exhibits a weak endotherm at 399 K followed by a strong endotherm at 402 K; no thermal event attributable to the melting of pure paracetamol was observed. The strong endotherm occurs at a similar temperature to the decomposition events observed for the other adducts, and it is likely to correspond to a melting process forming paracetamol solvated by liquid bipyridine (m.p. 374–377 K). Unlike the other solvents studied here, bipyridine is not lost to leave pure paracetamol, because its boiling point is well beyond the temperature of adduct decomposition. It is likely that the small peak corresponds to a phase transition.

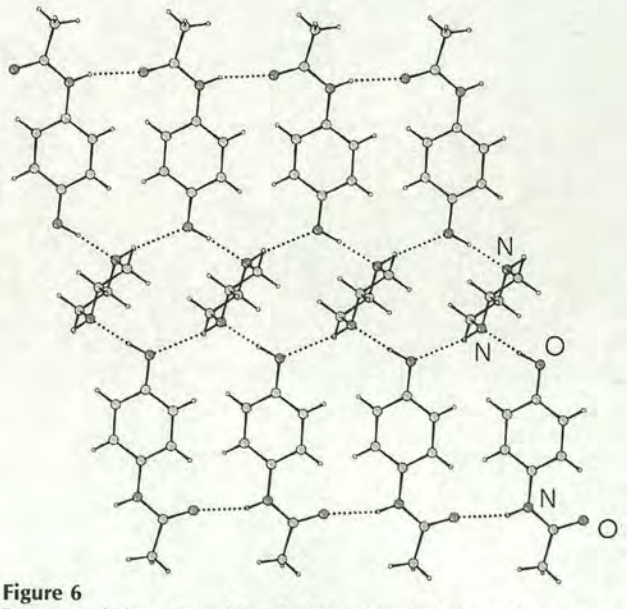

Figure 6
Paracetamol:piperazine adduct viewed perpendicular to (302); the *b* axis runs from left to right. The $C(4)$ chains referred to in the text run from left to right and are linked together by piperazine molecules. The latter also act as weak hydrogen-bond donors. The dihedral angles between the amide and phenyl mean planes in the paracetamol molecule is 33.21 (14)°.

4. Discussion and conclusions

This paper has described the formation of five new paracetamol hemiadducts with 1,4-dioxane, *N*,*N*-dimethylpiperazine, *N*-methylmorpholine, morpholine and piperazine and a 1:1 adduct with 4,4′-bipyridine. This is the first such systematic study of paracetamol co-crystals to have been undertaken. As is to be expected, the crystal structures of all adducts are dominated by hydrogen-bond formation, and comparisons between them were much facilitated by the use of graph-set analysis in the form described in the illuminating review by Bernstein *et al.* (1995).

Although ether oxygen can potentially act as a double acceptor, it rarely does so, and so with the exception of

	Acceptor (O or N in each case)					
Donor (NH or OH)		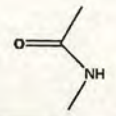	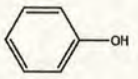	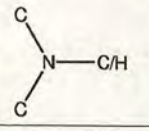	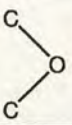	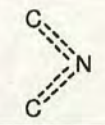
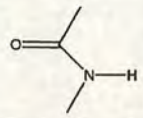	Sample size	1250	14	11	31	40
	Max NH..A /Å	(2.2) *	2.14	2.17	2.19	2.19
	Min NH..A /Å	1.73	1.79	1.80	1.83	1.81
	Mean NH..A /Å	**1.92**	**2.01**	**1.96**	**2.03**	**1.96**
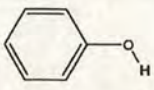	Sample size	49	256	49	53	76
	Max OH..A /Å	2.19	2.20	2.19	2.20	2.18
	Min OH..A /Å	1.60	1.67	1.66	1.62	1.53
	Mean OH..A /Å	**1.78**	**1.87**	**1.82**	**1.90**	**1.81**
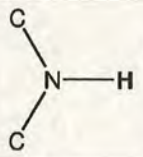	Sample size	5	1 (HOLZOD)	12	4	Not applicable
	Max NH..A /Å	2.17	-	2.20	2.18	
	Min NH..A /Å	2.08	-	2.00	2.11	
	Mean NH..A /Å	**2.13**	**2.03**	**2.14**	**2.13**	

Figure 7
Summary of the results of searches of the CSD (Version 5.23, April 2002) for typical distances (in Å) in hydrogen-bonded systems containing identical functional groups to the paracetamol adducts studied. The distances to H atoms were normalized to typical neutron distances (C—H 1.803, N—H 1.009 and O—H 0.983 Å). Only 'organic' structures where the *R* factor is less than 0.05 with no errors or disorder were included, and ionic or polymeric structures were excluded. The C atoms attached to the amine moieties were specified to be sp^3 hybridized. The donor-H-to-acceptor distance was specified to be 1.50–2.20 Å. The asterisk denotes the limit of search.

morpholine all the guest molecules studied are at least pseudo-centrosymmetric with respect to their hydrogen-bonding properties. The dioxane, *N*-methylmorpholine, *N*,*N*-dimethylpiperazine and piperazine adducts all consist of hydrogen-bonded chains of paracetamol molecules linked together by the guest molecules, which all reside on crystallographic inversion centres. In the bipyridine adduct the chains are linked *via* a pair of π-stacked pyridine rings, though the structure as a whole is still centrosymmetric. The morpholine adduct does not conform to this pattern, although chains of paracetamol are still present. The arrangements of paracetamol chains described in this paper tend to lend themselves to the formation of centrosymmetric crystal structures, and this seems to favour adduct formation in the centrosymmetric guest molecules. It is perhaps significant that we have been unable to prepare an adduct with 1,3,5-trioxane, a molecule closely related to dioxane but which lacks inversion symmetry.

The donor groups that appear in this series are amidic NH, phenol OH and secondary amine NH; the acceptors are amidic O, phenolic O, secondary or tertiary amine N, ether O, and pyridine N. The results of searches of the CSD for typical hydrogen-bond geometries involving these functionalities are shown in Fig. 7; searching criteria are given in the legend to that figure. The pattern of adduct formation observed in this study is quite consistent with the data in Fig. 7 if the reasonable assumption is made that the hydrogen-bond strength is related to the average donor-hydrogen—acceptor distance. The donor group O—H or N—H to acceptor distances observed in this study were normalized to typical neutron values (O—H 0.983 Å and N—H 1.009 Å) to aid ready comparison with typical H-to-acceptor distances derived from our CSD search, and this comparison is made in Table 2. Our hydrogen-bond distances agree tolerably well with typical values; they are often on the short side, as might be expected with low-temperature data.

The strongest hydrogen bonds in Fig. 7 are formed between phenolic OH (as donor) and amide O (as acceptor). These are observed in the $C(9)$ chains formed in structures of both polymorphs of paracetamol. In pure paracetamol, hydrogen bonds are formed between the remaining NH donor and OH acceptor to form $C(7)$ chains, but on adduct formation with 1,4-dioxane and 4,4′-bipyridine it is these, weaker, interactions that break to accommodate the guest molecules, preserving the strongly bound $C(9)$ chains and forming hydrogen bonds between the amide NH of paracetamol and either the ether O or the pyridyl N atoms of the guest molecule. These observations are consistent with the results obtained in the variable-pressure study of monoclinic paracetamol by Boldyreva *et al.* (2000), where the NH···O contacts were found to be more compressible than the OH···O contacts.

Neither dioxane nor bipyridine has any group attached to the donor O or N atoms. All of the other molecules studied carry either hydrogen or methyl groups in these positions, and reference to Fig. 2 or Fig. 3 shows that a structure based on the $C(9)$ paracetamol chains would suffer some steric crowding

between these groups and either the phenyl or the methyl group attached to the amide moiety. In order to avoid steric overcrowding in the morpholine, piperazine, *N*,*N*-dimethylpiperazine and *N*-methylmorpholine adducts, the paracetamol utilizes its NH group as a donor. Fig. 7 shows that the most effective acceptor for this group is amide CO and this explains the formation of *C*(4) paracetamol chains in all four of these structures.

In the structures of *N*-methylmorpholine and *N*,*N*-dimethypiperazine, hydrogen bonds are formed between the OH group of paracetamol and the N or O of the guest molecule. In morpholine and piperazine, both the OH group of paracetamol and the NH group(s) of the guest could act as either donors or acceptors. Fig. 7 shows that secondary aliphatic amines are particularly poor hydrogen-bond donors, and so the hydroxyl group acts as the donor in both cases. In fact, so poor a donor is secondary amine NH that it is left unsatisfied in the morpholine adduct, even in the presence of excess acceptor functions. The weakness of these NH$\cdots$N hydrogen bonds relative to OH$\cdots$O or NH$\cdots$O systems may be a consequence of the size of N relative to O, a feature recently emphasized by Brown (2002). However, in piperazine the NH groups do act as weak donors, and this induces a change in conformation of these *C*(4) chains relative to the *N*,*N*-dimethylpiperazine adduct that condenses the sheets into ribbons.

In the case of morpholine, the *C*(4) chains are linked by the OH group of a paracetamol molecule in one chain acting as a hydrogen-bond donor to a similar group in a neighbouring chain. On the basis of the structures of the other adducts, the role might have been expected to be fulfilled by the ether moiety of the morpholine. Fig. 7 shows that these interactions are of rather similar strength, and this might explain the apparently anomalous behaviour observed in this adduct.

In the 1,4-dioxane adduct, alternate *C*(9) paracetamol chains have reversed polarity. In the adducts based on *C*(4) chains, the resemblance to orthorhombic paracetamol is less obvious, although inspection of Fig. 1(*b*) shows that removal of alternate molecules along the *C*(7) graph followed by a small displacement would yield NH$\cdots$O=C *C*(4) chains. Viewed in this light, desolvation might have been predicted to yield the orthorhombic polymorph of paracetamol, although in practice it was shown by DSC that in all cases except for paracetamol:bipyridine (for which we did not observe desolvation at all) the thermodynamically more stable monoclinic polymorph was formed.

We thank Mrs A. Dawson and Dr A. Parkin for assistance with data collection, and the EPSRC, the Cambridge Crystallographic Data Centre and the University of Edinburgh for funding.

References

Allen, F. H., Kennard, O. & Taylor, R. (1983). *Acc. Chem. Res.* **16**, 146–153.

Bernstein, J., Davis, R. E., Shimoni, L. & Chang, N-L. (1995). *Angew. Chem. Int. Ed. Engl.* **34**, 1555–1573.

Blessing, R. H. (1995). *Acta Cryst.* A**51**, 33–38.

Boldyreva, E. V., Shakhtshneider, T. P., Vasilchenko, M. A., Ahsbahs, H. & Uchtmann, H. (2000). *Acta Cryst.* B**56**, 299–309.

Brown, I. D. (2002). *The Chemical Bond in Inorganic Chemistry*, ch. 7. IUCr Monographs on Crystallography. Oxford University Press.

Bruker (2001). *SMART*. Bruker-AXS, Madison, Wisconsin, USA.

Bruker (2002). *SAINT*. Bruker-AXS, Madison, Wisconsin, USA.

Cooper, R. I., Gould, R. O., Parsons, S. & Watkin, D. J. (2002). *J. Appl. Cryst.* **35**, 168–174.

Fachaux, J.-M., Guyot-Hermann, A.-M., Guyot, J.-C., Conflant, P., Drache, M., Veesler, S. & Boistelle, R. (1995). *Powder Technol.* **82**, 123–128.

Farrugia, L. J. (1999). *J. Appl. Cryst.* **32**, 837–838.

Haisa, M., Kashino, S., Kawaii, R. & Maeda, H. (1976). *Acta Cryst.* B**32**, 1283–1285.

Haisa, M., Kashino, S. & Maeda, H. (1974). *Acta Cryst.* B**30**, 2510–2512.

McGregor, P. A., Allan, D. R., Parsons, S. & Pulham, C. R. (2002). *J. Pharm. Sci.* **91**, 1308–1311.

Nichols, G. & Frampton, C. S. (1998). *J. Pharm. Sci.* **87**, 684–693.

North, A. C. T., Phillips, D. C. & Mathews, F. S. (1968). *Acta Cryst.* A**24**, 351–359.

Sheldrick, G. M. (1997*a*). *SHELXTL*. Bruker-AXS, Madison, Wisconsin, USA.

Sheldrick, G. M. (1997*b*). *SADABS*. Bruker-AXS, Madison, Wisconsin, USA.

Spek, A. L. (2002). *PLATON. A Multipurpose Crystallographic Tool.* Utrecht University, The Netherlands.

Stoe & Cie (1990*a*). *DIF*4. *Diffractometer Control Program.* Stoe & Cie, Darmstadt, Germany.

Stoe & Cie (1990*b*). *REDU*4. *Data Reduction Program.* Stoe & Cie, Darmstadt, Germany.

Watkin, D. J., Pearce, L. & Prout, C. K. (1993). *CAMERON – A Molecular Graphics Package.* Chemical Crystallography Laboratory, University of Oxford, UK.